



Universidad de Cantabria
Departamento de Física Moderna



CSIC - Universidad de Cantabria
Instituto de Física de Cantabria

Caracterización espectral en rayos X del acrecimiento y oscurecimiento en Galaxias Activas

Memoria presentada por la Licenciada

Amalia Corral Ramos

para optar al título de Doctora por la Universidad de Cantabria

2011

Declaración de Autoría

Xavier Barcons Jáuregui, Doctor en Ciencias Físicas y Profesor de Investigación del Consejo Superior de Investigaciones Científicas,

y

Francisco Carrera Troyano, Doctor en Ciencias Físicas y Profesor Titular de la Universidad de Cantabria,

CERTIFICAN que la presente memoria

**Caracterización espectral en rayos X del acrecimiento y oscurecimiento
en Galaxias Activas**

ha sido realizada por **Amalia Corral Ramos** bajo nuestra dirección. Consideramos que esta memoria contiene aportaciones suficientes para construir la tesis Doctoral del interesado

En Santander, a 8 de Noviembre de 2011

Xavier Barcons Jáuregui

Francisco Carrera Troyano

A mi familia y amigos y, ah sí, a Paco...

Agradecimientos

Bueno, una de las pocas ocasiones en las que no sé qué decir, porque hay mucha gente, a la mayoría se me olvidará mencionar, y muchas cosas que agradecerles y que han contribuído a completar, por fin, esta Tesis. Primero, agradecerles a mis padres su apoyo todo este tiempo aún sin saber dónde me metía, y a Paco sobre todo por apoyarme aún sabiendo dónde me metía. Al resto de mi familia, gracias por haceros tanta ilusión tener un científico en la familia, pero Patri, me temo que esto de la ciencia no dá para la casa del callejón del agua todavía, habrá que esperar al Nobel.

A mis directores de Tesis, Xavier y Francisco, no sé ni qué decir. Gracias mil por la paciencia infinita y todo lo enseñado, ya sea de ciencia o de política científica. De lo primero, espero haber aprendido algo, pero de lo segundo, poco ha calado desafortunadamente. Todavía me hace falta aprender de vosotros cómo habéis hecho para sacar el tiempo que habéis sacado para mí y para ésto, gracias infinitas. A Silvia, gracias mil por ejercer de profesora cuando llegué al IFCA. A pesar de las mil preguntas diarias, ni una sola vez me mandaste a tomar por saco. Maite, no sé qué haría el grupo de rayos X sin tí. Perdona que te haya estado dando la lata durante tanto tiempo, no hay jamones suficientes. Gracias a Jose Ramón y María, ciudadanos del mundo, por traer algo de casa para acá y a la vez enseñarme a querer a Cantabria. A Jacobo y a Ángel, sin vosotros y esos locos de microondas y alrededores (no os nombro que sois muchos, leñe), pero sobre todo sin vosotros, esto no habría sido tan divertido.

To the people at the MSSL, thank you all for hosting me, and above all, thanks to Mat Page, without whom I would have never been able to finish this. E molte grazie a tutta la gente dell'OAB, e particolarmente a Roberto, Alessandro e Paola, per tutto l'aiuto e la pazienza sia dentro che fuori dell'osservatorio.

A todos, gracias de las de verdad.

Resumen de la tesis en castellano

El objetivo de este trabajo de Tesis es el estudio de los núcleos activos de galaxias (AGN – del inglés *Active Galactic Nuclei*), que son las fuentes persistentes más brillantes del Universo. Estos objetos se caracterizan principalmente por emitir grandes cantidades de energía a lo largo de todo el espectro electromagnético y por presentar una alta variabilidad en escalas de tiempo muy cortas, lo que implica una dimensiones muy pequeñas para la fuente emisora (del orden de días luz o menor). El único mecanismo físico conocido capaz de reproducir las características observadas de los AGN es el acrecimiento de materia por parte de un agujero negro supermasivo (SMBH – *Super Massive Black Hole*). Gracias a su alto poder de penetración, los rayos X son fundamentales a la hora de entender los procesos físicos que tienen lugar en las regiones más cercanas al SMBH, permitiéndonos estudiar la Física en condiciones extremas, incluyendo efectos relativistas. Además, al tratarse de objetos extremadamente brillantes, pueden ser detectados hasta grandes distancias, permitiéndonos así aprender sobre el Universo temprano y cómo éste ha ido evolucionando.

En la actualidad, y gracias a un gran número de observaciones en distintas longitudes de onda, se cree que hay un SMBH en el centro de todas las galaxias. Esto implica que los AGN no constituyen un tipo de objeto en sí, sino que se trata de un estado por el que atraviesan todas las galaxias durante su crecimiento y que puede ser activado o interrumpido por diferentes factores, como colisiones entre galaxias o brotes de formación estelar.

Existe una amplia evidencia observacional que apunta a que la formación de la galaxia anfitriona del AGN y el crecimiento de su SMBH central tienen que estar estrechamente conectados. Prueba de esto son las correlaciones encontradas entre la dispersión de velocidades de las estrellas del bulbo galáctico y la masa del SMBH, la masa del SMBH y la masa en estrellas del bulbo o la masa del SMBH y la del halo de materia oscura de la galaxia. Las galaxias y los AGN también comparten una característica evolutiva llamada “reducción cósmica” o “cosmic downsizing”. En el caso de los AGN, esto significa que la densidad de los AGN más luminosos alcanza su punto máximo en épocas más tempranas (o mayores desplazamientos al rojo) que los AGN menos luminosos. Las observaciones muestran que, en general, las galaxias más luminosas y masivas formaron sus estrellas en épocas más tempranas que las menos masivas, que muestran una formación estelar más prolongada en el tiempo. Esto implica que algún tipo de proceso tuvo que suprimir la formación estelar en galaxias masivas impidiendo que siguieran creciendo. El mecanismo primario propuesto para explicar este proceso es la influencia del AGN sobre la galaxia anfitriona (AGN feedback).

Objetivos de la investigación

La investigación llevada a cabo durante esta tesis se centra específicamente en el estudio detallado de dos de las cuestiones más relevantes y aún no resueltas sobre la física de los AGN: las desviaciones al modelo unificado de los AGN y las propiedades de la línea de emisión en rayos X $\text{Fe K}\alpha$.

Las versiones más sencillas del **modelo unificado de los AGN** suponen que todos los tipos de AGN comparten la misma estructura y que las diferencias entre ellos se deben simplemente a un efecto de orientación. Según este modelo, el SMBH central está rodeado por un sistema compuesto por un disco de acrecimiento y una corona de electrones altamente energéticos. Se cree que el sistema disco/corona constituye la fuente primaria de emisión de rayos X de los AGN. Sobre este sistema se mueven nubes turbulentas de gas a altas temperaturas, la región de emisión de líneas anchas (BLR – *Broad Line Region*), y más allá, una estructura toroidal, coplanar con el disco de acrecimiento, compuesta de gas molecular frío y polvo. En las partes más externas, se encuentra una región compuesta por nubes de gas templado y menos turbulento que la BLR, la región de emisión de líneas estrechas (NLR – *Narrow Line Region*). La BLR es responsable de las líneas de emisión anchas correspondientes a transiciones permitidas (anchura a media altura o FWHM $> 2000 \text{ km s}^{-1}$) que se observan en los espectros ópticos/UV de algunos AGN. De forma análoga, la NLR es la responsable de las líneas de emisión estrechas. En función de la presencia o ausencia de estas líneas anchas se definen los tipos espectrales ópticos. Los AGN de tipo 1 presentan líneas anchas y estrechas mientras que los de tipo 2 sólo las presentan estrechas. Los tipos intermedios (1.2, 1.5, 1.8 y 1.9) se asignan en función de la relación entre las intensidades de las componentes anchas y estrechas en las líneas permitidas. La hipótesis principal del modelo unificado consiste en que las diferencias observadas entre distintos AGN se deben a diferencias en el ángulo del observador con respecto al eje de la estructura toroidal, es decir, las diferencias se deben a las distintas cantidades de materia atravesadas por la radiación en su camino hasta el observador. De esta forma, los distintos tipos espectrales ópticos del tipo 1 al 2 se explican como una transición continua desde ángulo de observación 0 a 90° , es decir, la BLR va desapareciendo de la vista del observador a medida que su emisión es más y más absorbida por el toro. La implicación más obvia de este modelo sería entonces que los AGN de tipo 1 no deberían presentar absorción significativa en rayos X, mientras que los de tipo 2 deberían mostrar un espectro absorbido en rayos X. Aunque la mayoría de las observaciones son consistentes con este modelo, los muestreos en rayos X suelen detectar un cierto número de AGN que parecen no seguirlo del todo.

La segunda cuestión objeto de esta Tesis es **la línea de emisión en rayos X $\text{Fe K}\alpha$** . Esta línea es la más comúnmente observada en espectros de rayos X de AGN y su estudio puede aportar información sobre las condiciones físicas de las

zonas más cercanas al SMBH. Si es emitida lo suficientemente cerca del SMBH, por ejemplo, debería presentar un perfil ancho relativista a partir del cual se puede extraer información sobre las condiciones dentro de las partes más internas del AGN. Sin embargo, este perfil relativista ha sido detectado y caracterizado sólo en un número limitado de casos, cuando la calidad del espectro de la fuente es muy alta. La línea de emisión Fe $K\alpha$ estrecha, por otra parte, parece ser una característica omnipresente en los espectros de rayos X de AGN locales. Sin embargo, sus propiedades a desplazamientos al rojo medios y altos aún no ha sido caracterizada apropiadamente.

Planteamiento y metodología

Para afrontar el estudio de los dos temas objeto de esta Tesis, la investigación se dividió en dos partes adoptando dos estrategias muy distintas, aunque las dos están basadas principalmente en el uso de espectroscopía de rayos X.

Actualmente existen en funcionamiento un gran número de observatorios espaciales de rayos X como XMM-Newton (ESA), Chandra (NASA), Suzaku (JAXA/NASA), SWIFT (NASA) o INTEGRAL (ESA). Los datos en la banda de rayos X utilizados durante este trabajo de Tesis proceden del observatorio de rayos X de la Agencia Espacial Europea (ESA) XMM-Newton¹. XMM-Newton es el telescopio de rayos X con la mayor área efectiva en funcionamiento, lo que lo convierte en el mejor instrumento actual para llevar a cabo espectroscopía de rayos X.

El modelo unificado de los AGN

Las desviaciones del modelo unificado observadas ponen de relieve la necesidad de estudiar este modelo y sus implicaciones con mayor detalle. Una de las explicaciones propuestas para estas desviaciones se basa en la variabilidad de los AGN. Los AGN son muy variables y las observaciones en distintas longitudes de onda, que dan lugar a distintas clasificaciones espectrales, suelen estar muy separadas en el tiempo. Si el material absorbente que rodea al SMBH varía, como ha sido observado en un gran número de casos, las distintas observaciones, habitualmente no simultáneas, en distintas longitudes de onda podrían estar simplemente viendo distintos estados de absorción.

La estrategia propuesta en esta tesis consiste en la observación simultánea, en rayos X y en el óptico, de una pequeña muestra de AGN que han mostrado una historia de variabilidad en su clasificación óptica a lo largo de los años.

¹<http://xmm.esac.esa.int/>

Además de variar en su tipo espectral, los AGN de la muestra tenían que cumplir algunos requisitos adicionales, como ser lo suficientemente brillantes para poder obtener datos con la suficiente calidad y por tanto poder medir su absorción intrínseca con tiempos de exposición no muy largos (entre 10 y 30 ks en rayos X). Además, debían poder ser observados por XMM-Newton y por los observatorios ópticos terrestres que se han utilizado al mismo tiempo. Una vez adquiridos los datos, el modelo unificado se pondría a prueba comparando la cantidad de absorción en rayos X, obtenida a partir del modelado del espectro en rayos X, con el enrojecimiento óptico obtenido a partir del decremento Balmer de las líneas de emisión ópticas.

La muestra final está compuesta por cuatro fuentes: Mrk 993, Mrk 1018, NGC 7603 y Mrk 6. Se enviaron propuestas de observación a XMM-Newton y a observatorios ópticos terrestres de forma coordinada, permitiendo que las diferencias en las fechas de observación en ambas longitudes de onda fuera como máximo de sólo dos días. Afortunadamente, conseguimos que estos programas de observación fueran aprobados tanto por los comités de asignación de tiempo de XMM-Newton (ESA) como por los correspondientes a los observatorios ópticos terrestres utilizados (principalmente el Centro Astronómico Hispano-Alemán de Calar Alto, CAHA). En el caso de Mrk 1018 y Mrk 6, se pudo realizar una segunda observación óptica alrededor de un mes más tarde con la intención de detectar variabilidad óptica en escalas de tiempo cortas, que podría ser causada por una demora entre la emisión en rayos X y en el óptico debido a la distancia que separa ambas regiones de emisión.

La línea de emisión Fe $K\alpha$

Aunque Fe $K\alpha$ es la línea de emisión más comúnmente observada en AGN, sus propiedades aún son poco conocidas a desplazamientos al rojo medios y altos. La causa principal es que se necesita una calidad muy alta en los espectros de rayos X para poder detectarla y caracterizarla a esas distancias, lo que no es posible con los instrumentos actuales.

La estrategia adoptada en esta tesis fue compilar tantos espectros de rayos X de AGN como fuera posible y que cubrieran un rango muy amplio de distancias y luminosidades. Además, los AGN seleccionados debían haber sido identificados mediante espectroscopía óptica, de forma que los desplazamientos al rojo obtenidos fuesen lo más precisos posibles. Una vez obtenidos los espectros, se promediarían para así obtener un espectro promedio con la suficiente calidad como para detectar características espectrales como la línea de emisión Fe $K\alpha$.

Las muestras utilizadas durante esta Tesis han sido AXIS (*An XMM-Newton International Survey*), XWAS (*XMM-2dF Wide Angle Survey*) y la muestra Lockman

Hole, sumando en total más de 800 AGN. Las dos primeras muestras proceden de detecciones “casuales” por parte de XMM-Newton. Esto quiere decir que estas fuentes no eran los objetivos de la observación pero, gracias al campo de visión cubierto por los instrumentos a bordo de XMM-Newton y a las características de éstos, sus espectros pueden ser extraídos y analizados. Estas dos muestras, compuestas por fuentes con flujos intermedios ($\sim 10^{-14}$ erg cm $^{-2}$ s $^{-1}$), forman parte del programa de identificación de fuentes de rayos X llevado a cabo por el SSC (*Survey Science Center*²), un consorcio internacional compuesto por 10 instituciones en países pertenecientes a la ESA. La tercera muestra corresponde a una de las observaciones más profundas llevadas a cabo por XMM-Newton, compuesta por fuentes con flujos menores ($\sim 10^{-15}$ erg cm $^{-2}$ s $^{-1}$), y para la que también se empleó un gran esfuerzo observacional a la hora de identificar sus fuentes de rayos X mediante espectroscopía óptica. Esta muestra ya había sido utilizada para construir un espectro promedio de AGN (Streblyanska et al., 2005) obteniéndose resultados muy interesantes que desafiaban las predicciones teóricas. El espectro promedio obtenido mostraba una línea de emisión Fe K α extremadamente intensa tanto para los AGN de tipo 1 como 2 (con anchuras equivalentes – *Equivalent Width* – EW \sim 400-600 eV). El objetivo era por tanto utilizar esta muestra para comparar los resultados obtenidos por los diferentes métodos de promediado.

El paso final fue desarrollar un nuevo método para promediar todos estos espectros, maximizando la relación señal-ruido del espectro promedio resultante y a la vez minimizando cualquier contaminación espúrea. De esta forma, las propiedades más relevantes de los espectros de rayos X de AGN, incluyendo la línea de Fe K α , pueden ser identificadas y medidas. Dividiendo nuestra muestra total en diferentes sub-muestras en función de diferentes propiedades, como la luminosidad o la distancia, la dependencia de las características espectrales de estas propiedades también puede ser estudiada. Para probar la eficiencia y restricciones del método, se usaron un gran número de datos simulados. Estas simulaciones se usaron también para construir un espectro promedio simulado con el que comparar los espectros reales y así detectar cualquier desviación significativa entre unos y otros.

Aportaciones originales

La investigación presentada en esta tesis ha contribuído significativamente al conocimiento de la naturaleza física de los AGN, principalmente en rayos X, aunque también en el óptico.

En el caso de las galaxias Seyfert que cambian de tipo, la estrategia observa-

²<http://xmmssc-www.star.le.ac.uk/>

cional propuesta, la observación simultánea en diferentes longitudes de onda, se aplicó por primera vez al estudio de fuentes de este tipo. Para llevar a cabo este estudio se presentaron varias propuestas de observación en concurrencia competitiva internacional a los observatorios XMM-Newton y CAHA de forma coordinada. Estas propuestas fueron aprobadas por los comités correspondientes de asignación de tiempo y seleccionadas con la más alta prioridad.

En el caso del estudio de la línea de emisión $\text{Fe K}\alpha$, se desarrolló un método completamente nuevo para obtener un espectro promedio de rayos X usando espectros de calidad baja a media. Además, se empleó el uso extensivo de datos simulados para comprobar la fiabilidad de este método. A partir de estas simulaciones, se extrajo también un procedimiento de estimación de la significación de los resultados obtenidos.

Los resultados obtenidos durante este trabajo de Tesis han sido presentados en varios congresos y revistas internacionales (Corral et al., 2005, 2008, 2011a,b).

Conclusiones

Galaxias Seyfert que cambian de tipo espectral

Nuestras observaciones simultáneas en rayos X y en el óptico muestran que una absorción variable podría explicar los cambios espectrales en tres de nuestras fuentes: Mrk 6, NGC 7603 y Mrk 1018. Sin embargo, no es éste el caso para **Mrk 993**. En este último caso, la densidad de columna de Hidrógeno derivada de los rayos X no es suficiente para ser la responsable del enrojecimiento medido en el óptico. El alto decremento Balmer medido debe ser en este caso una propiedad intrínseca de esta fuente en vez de estar causado sólo por oscurecimiento, en contra de las predicciones del modelo unificado más sencillo (Corral et al., 2005). Dada su baja luminosidad en rayos X, las condiciones en la BLR para esta fuente podrían ser significativamente distintas de las de otros AGN más brillantes, por ejemplo, dando lugar a líneas anchas más débiles. En el caso de **Mrk 1018**, el espectro óptico observado es el de un AGN de tipo 1, consistente con la no detección de absorción en rayos X. El cambio espectral en este caso podría ser debido a un cambio en la cantidad de absorción en escalas de tiempo del orden de años, un tipo de variabilidad ya observada en varios AGN. Los resultados de las observaciones simultáneas de **Mrk 6** y **NGC 7603** también parecen cumplir las predicciones del modelo unificado. Sin embargo, ambas fuentes muestran una variabilidad muy compleja en el óptico, ambas han sido monitoreadas durante años y, en ambos casos, se necesitan uno o varios absorbentes ionizados (y variables, en el caso de Mrk 6) con muy alta densidad de columna para ajustar adecuadamente sus espectros en rayos X. Además, sus líneas de emisión anchas en el óptico muestran dos picos, por lo que estas fuentes pertenecen al grupo de

emisores de líneas dobles (DPEs – *Double-peaked emitters*). El modelo más aceptado para explicar esta emisión doble es emisión por parte del disco de acrecimiento en vez de por la BLR propiamente dicha, por lo que el perfil de estas líneas se vería enormemente afectado por cualquier cambio en el continuo ionizante, lo que es algo común en AGN. Nuestros resultados son consistentes con un escenario en el que estas líneas son producidas por chorros de materia parcialmente ionizada y expulsada a grandes velocidades sobre el disco de acrecimiento. De esta forma, cambios en el continuo ionizante implicarían cambios en las condiciones en el sistema disco/BLR produciendo un cambio en la absorción ionizada en rayos X y a su vez, variabilidad en el perfil de las líneas de emisión dobles (Corral et al., 2011a).

En resumen, las galaxias Seyfert que cambian de tipo no constituyen un tipo de fuente en sí, sino que parecen estar compuestas por una mezcla de diferentes tipos de fuentes que, muy probablemente, muestran unos tipos de absorción muy complejos y variables. Salvo por una de nuestra fuentes, Mrk 993, los resultados obtenidos concuerdan con las predicciones del modelo unificado de los AGN. Por lo tanto, se debe ser cauto a la hora de extraer resultados procedentes de observaciones no simultáneas en distintas longitudes de onda.

Espectro de rayos X promedio de los AGN

Para estudiar las propiedades promedio de los espectros de rayos X de los AGN, las diferentes muestras usadas se dividieron en AGN de tipo 1 y 2.

1. **Muestra a flujos intermedios (AXIS+XWAS):** Tanto los AGN de tipo 1 como 2 presentan una línea de emisión estrecha Fe $K\alpha$, consistente con Fe neutro o poco ionizado, con una EW del orden de 100 eV. Consistentemente, el espectro promedio de los AGN de tipo 1 requiere, además de la línea de emisión, una cantidad de reflexión neutra consistente con la EW de la línea y con que ambas componentes procedan de material neutro y localizado lejos de la fuente central. No se detecta ninguna contribución significativa de una posible componente ancha relativista a la emisión Fe $K\alpha$ pero se estima un límite superior a su EW de 400 eV con un nivel de confianza de 3σ (Corral et al., 2008). En el caso de los AGN de tipo 2, dada la menor calidad del espectro resultante debido a un número menor de fuentes, no se detectaron componentes adicionales al espectro promedio salvo por la línea de emisión estrecha.
2. **Muestra a flujos débiles (Lockman Hole):** Contrariamente a los resultados presentados en Streblyanska et al. 2005, se encontraron resultados muy similares a los correspondientes a la muestra anterior. El límite superior a una contribución relativista a la línea de Fe $K\alpha$ es en este caso incluso más restrictivo, ~ 240 eV. Las diferencias entre los resultados presentados en Stre-

blyanska et al. 2005 y los presentados en esta Tesis parecen deberse a una diferencia en el método de promediado. El método desarrollado para esta Tesis trata mucho más cuidadosamente el continuo bajo la línea. Además, durante el proceso de promediado presentado en Streblyanska et al. 2005 se usaron espectros agrupados, lo que puede distorsionar el perfil de la línea Fe $K\alpha$ haciendo que esta se ensanche hacia bajas energías simulando un perfil relativista. En el caso de los AGN de tipo 2, probablemente debido a una mayor cantidad de AGN altamente oscurecidos en este caso, fue necesario añadir un absorbente neutro cubriendo sólo parte de la fuente central a la hora de ajustar el espectro promedio.

3. **Muestra total (AXIS+XWAS+Lockman):** Las dos muestras anteriores se combinaron para obtener espectros promedios de los AGN de tipo 1 y 2. Los resultados del análisis de estos espectros fueron muy similares a los correspondientes a las muestras por separado. Los AGN de tipo 1 presentan una línea de emisión estrecha Fe $K\alpha$ acompañada por la cantidad de reflexión esperada, mientras que para los de tipo 2, a parte de la línea, sólo se detectaron los efectos de la absorción fotoeléctrica neutra. El límite superior para la contribución relativista a la línea, en el caso de los de tipo 1, se estimó en 370 eV con un nivel de confianza de 3σ .
4. **Dependencia de la línea estrecha Fe $K\alpha$:** La muestra total también se utilizó para construir sub-muestras con el fin de analizar la dependencia de las características espectrales con el flujo, el desplazamiento al rojo y la luminosidad de las fuentes. No se encontró dependencia significativa de los espectros promedio con el flujo o el desplazamiento al rojo de las fuentes. Lo que sí se observa es un decremento de la EW de la línea estrecha a medida que la luminosidad aumenta. Este efecto es conocido como efecto Baldwin en el óptico y como efecto Iwasawa-Taniguchi en rayos X. En el caso de los AGN de tipo 1, también se observa una aparente disminución de la cantidad de reflexión a medida que la luminosidad aumenta. Este resultado apoya el modelo en el que el radio interno del toro aumentaría al aumentar la luminosidad de la fuente disminuyendo así la cantidad de reflexión y por consiguiente, la intensidad de la línea de emisión (Corral et al., 2011b).

Los resultados más importantes de nuestro análisis de las propiedades de la línea Fe $K\alpha$ son por tanto los siguientes:

- La línea de emisión estrecha Fe $K\alpha$ es una característica omnipresente de los espectros de rayos X también a altos desplazamientos al rojo, como lo es en el universo local. Nuestros resultados están en completo acuerdo con análisis similares presentados recientemente para AGN cercanos (de La Calle Pérez et al., 2010) o más distantes (Chaudhary et al., 2010).

- La componente relativista a la línea Fe $K\alpha$, si está presente, debe presentar una EW < 300 - 400 eV. Ese resultado está de acuerdo con modelos teóricos recientes que estiman una EW máxima ~ 300 eV (Ballantyne, 2010).
- La EW de la línea estrecha así como la cantidad de reflexión parecen decrecer a medida que la luminosidad aumenta, como se encuentra que sucede también para AGN locales.

Futuras líneas de investigación

Los resultados del estudio de las galaxias Seyfert que cambian de tipo, salvo en un caso, están de acuerdo con las versiones más sencillas del modelo unificado de los AGN combinado con absorbentes complejos y probablemente variables. Estos resultados nos muestran también la importancia de estudiar un tipo de fuente en particular, los emisores de líneas dobles o DPEs. En el caso de la línea de emisión de Fe $K\alpha$, nuestros resultados no sólo están de acuerdo con predicciones teóricas sino que parecen confirmarse con recientes estudios. A pesar de ello, la dependencia de esta emisión con otras características de los AGN así como la posible contribución de una componente relativista a ésta no están todavía bien delimitadas.

Estudio detallado de los DPEs en rayos X

De las cuatro galaxias Seyfert que cambian de tipo estudiadas, dos han resultado ser DPEs. El origen de esta emisión doble sigue siendo objeto de debate. Existen diferentes modelos propuestos para explicar esta emisión: un SMBH binario, chorros de materia en forma bicónica, una colección de nubes anisotrópicamente iluminadas y el mencionado anteriormente, emisión por parte de un disco de acrecimiento truncado en su parte interior. Aunque el modelo de emisión del disco es el más ampliamente aceptado, ninguno de estos modelos es capaz de reproducir todas las propiedades observacionales de estas fuentes.

Los DPEs se observan con más frecuencia en AGN radio-brillantes (la mayoría mostrando un espectro de tipo 1.5 en el óptico) pero no en fuertes emisores en radio. Si la emisión procede del disco, ¿por qué no se observan estas líneas en todos los AGN de tipos 1 a 1.5? Además, la potencia que puede ser extraída del disco se ha encontrado que es insuficiente para dar lugar a líneas tan intensas en muchos casos, es decir, el disco requiere iluminación extra para producir estas líneas. ¿De dónde proviene esta iluminación extra?

Una solución promettedera a todos estos problemas fue propuesta por Cao and Wang 2006. En ese trabajo los autores proponen que la emisión de estas líneas se debe a chorros de materia ionizada muy densa y expulsada a gran velocidad sobre

el disco de acrecimiento. Una de las mejores maneras de comprobar esta hipótesis es buscando este material ionizado en el espectro de rayos X, donde aparecería dejando trazas de absorbente ionizado con grandes densidades de columna. De hecho, las dos DPEs encontradas en nuestra muestra requieren un absorbente ionizado con grandes densidades de columna a la hora de ajustar sus espectros de rayos X.

Aunque los rayos X podrían resolver de una vez por todas los mecanismos de emisión de los DPEs, los estudios realizados a DPEs en rayos X se han limitado hasta ahora a datos de baja calidad y con una resolución espectral moderada. Sin embargo, se necesitan espectros de alta calidad para detectar absorbentes ionizados y aún mejor calidad y resolución espectral para caracterizar las propiedades de este absorbente. El instrumento RGS (*Reflecting Grating Spectrometer*) a bordo de XMM-Newton cumple los requisitos de resolución adecuados, pero se necesitan tiempos de observación extremadamente largos para obtener la calidad suficiente como para detectar estos absorbentes.

Los pasos propuestos a seguir para el estudio de estas fuentes son los siguientes:

- Compilar todos los espectros de rayos X de resolución moderada de DPEs en archivo procedentes de observaciones propuestas, es decir, que no procedan de detecciones casuales, para así asegurar una alta calidad de los espectros. Mediante el análisis individual de estas fuentes y su comparación con una muestra de referencia de no DPEs de la misma calidad, se podría comprobar si existen diferencias entre espectros de alta energía de DPEs y no DPEs.
- Proponer observaciones de larga duración en rayos X de varios de los arquetipos de DPEs más brillantes que aún no han sido observados en rayos X, como por ejemplo Arp 102b, con el objeto de obtener datos de la suficiente calidad con alta resolución espectral.
- Promediar espectros de rayos X de alta resolución espectral en archivo (del tipo RGS) para poder identificar si existen características de absorción distintas de este tipo de fuentes.

Dependencia de la emisión Fe $K\alpha$

Aunque el trabajo realizado durante esta Tesis ha ayudado a caracterizar la contribución de la emisión Fe $K\alpha$ hasta altos desplazamientos al rojo en los AGN de tipo 1, algunas preguntas continúan aún sin respuesta. La dependencia de esta emisión con las propiedades intrínsecas de las fuentes sigue poco delimitada, así como las características de una posible contribución relativista a esta emisión. En el caso de los AGN de tipo 2, el menor número de fuentes, y por consiguiente menor calidad en el espectro promedio resultante, así como la contribución de la

absorción hacen que no sea posible derivar resultados concluyentes. Para abordar estos problemas se proponen los pasos siguientes:

- Para aumentar la cobertura del espacio de parámetros se podría usar la correlación de los catálogos de fuentes de XMM-Newton³ o Chandra⁴ con catálogos espectroscópicos ópticos como el SDSS (Sloan Digital Sky Survey⁵). Por ejemplo, el catálogo de XMM-Newton ha sido correlacionado con el SDSS DR7 (*Data Release 7*) obteniéndose más de 30000 identificaciones a partir de las cuales se pueden seleccionar grandes muestras completas de AGN de forma uniforme.
- Para estudiar una posible contribución relativista a la línea Fe K α , los mejores candidatos serían AGN con luminosidades en el rango 10^{44} - 10^{45} erg s⁻¹, como se deriva del modelo teórico presentado en Ballantyne (2010).
- Para delimitar la dependencia de las características espectrales con las propiedades de las fuentes (como la luminosidad, la masa del SMBH o la tasa de acrecimiento), se necesitan datos en diferentes longitudes de onda. En la actualidad existen varios proyectos multifrecuencia en marcha, como las muestras COSMOS⁶, CDFS⁷ (*Chandra Deep Field South*) o ALHAMBRA⁸.
- Para aumentar el número de AGN de tipo 2, los catálogos de rayos X anteriormente mencionados podrían usarse para seleccionar AGN en rayos X duros (> 5 keV por ejemplo), que al verse menos afectados por oscurecimiento son los más eficientes para detectar este tipo de fuentes. Estas muestras seleccionadas a alta energía podrían a su vez completarse mediante el uso de datos en el IR, también menos afectado por oscurecimiento, para así construir muestras completas de AGN de tipo 2 lo suficiente mente grandes.
- A largo plazo, la misión de rayos X en fase de estudio ATHENA (ESA), podría permitirnos por primera vez el estudio individual de esta línea a altos desplazamientos al rojo.

³<http://xmm.esac.esa.int/xsa/>

⁴<http://cxc.harvard.edu/csc/index.html>

⁵<http://www.sdss.org/>

⁶<http://cosmos.astro.caltech.edu/>

⁷<http://www2.astro.psu.edu/niel/cdfs/cdfs-chandra.html>

⁸<http://alhambra.iaa.es:8080/alhambra/>



Universidad de Cantabria
Departamento de Física Moderna



CSIC - Universidad de Cantabria
Instituto de Física de Cantabria

X-ray spectral signatures of accretion and obscuration in Active Galaxies

A dissertation submitted in partial fulfillment of the requirements for the degree
of Doctor of Philosophy in Physics

by

Amalia Corral Ramos

2011

*“The fact that an opinion has been
widely held is no evidence whatever
that it is not utterly absurd.”*

Bertrand Russell

*“In the beginning there was nothing,
which exploded.”*

Terry Pratchett (*Lords and Ladies*)

“Hey, ho, let’s go!”

The Ramones

Contents

1	Introduction	1
1.1	Motivation	2
1.2	Active Galactic Nuclei	3
1.2.1	General Properties	4
1.2.2	Physical Properties	8
1.2.3	The AGN paradigm	13
1.2.4	The AGN spectrum	19
1.3	Goals of the Thesis	24
1.3.1	Testing unified models	24
1.3.2	Constraining the Fe K α emission	25
2	X-ray data	27
2.1	X-ray observations	27
2.2	XMM-Newton	29
2.2.1	Spacecraft	31
2.2.2	X-ray Mirrors	31
2.2.3	Instruments	33
2.3	Data reduction	35
2.3.1	Pipe-line processing	36
2.3.2	Spectral extraction	37
2.4	Spectral analysis	43
2.4.1	Spectral models	44
3	Changing Type Seyfert galaxies	51
3.1	Introduction	52
3.2	Mrk 993	53
3.2.1	Previous observations	53
3.2.2	X-ray data	54
3.2.3	Optical data	57
3.2.4	Discussion and results	62
3.3	Mrk 6	64
3.3.1	Previous observations	64
3.3.2	X-ray data	65
3.3.3	Optical data	70
3.3.4	Discussion and results	74
3.4	NGC 7603	75
3.4.1	Previous observations	75
3.4.2	X-ray data	75
3.4.3	Optical data	79
3.4.4	Discussion and results	83

3.5	Mrk 1018	83
3.5.1	Previous observations	83
3.5.2	X-ray data	84
3.5.3	Optical data	87
3.5.4	Discussion and Results	87
3.6	Conclusions	87
4	The average X-ray spectrum of distant AGN	93
4.1	Introduction	93
4.2	Averaging method	95
4.2.1	Assembling the data	95
4.2.2	Bringing the individual spectra to a common frame	98
4.3	Testing the method	99
4.3.1	Fitting the spectra	106
4.4	Medium flux sample: AXIS+XWAS	108
4.4.1	Sample description	108
4.4.2	Average spectra	112
4.5	Faint sample: Lockman Hole	122
4.5.1	Sample description	122
4.5.2	Average spectra	122
4.6	Discussion and Results	131
5	Conclusions and future work	141
5.1	Conclusions of this thesis	141
5.1.1	Changing-type Seyfert galaxies	141
5.1.2	Average Fe K α emission	143
5.2	Potential extensions of this work	145
5.2.1	Further exploring the Broad Line Region	145
5.2.2	Further constraining the Fe emission	147
	Bibliography	149

List of Figures

1.1	Spectral energy distribution of the first discovered quasar	4
1.2	AGN optical spectral types	8
1.3	X-ray power law absorbed by a range of neutral column densities . . .	12
1.4	X-ray power law absorbed by ionised absorbers	13
1.5	X-ray reflection from a cold illuminated slab	14
1.6	X-ray reflection from ionised material	15
1.7	AGN unification model	17
1.8	Type 1 AGN X-ray spectral components	20
1.9	Fe $K\alpha$ emission line profiles	22
1.10	Fe $K\alpha$ emission line for MCG -6-30-15	22
2.1	Earth atmosphere opaqueness	28
2.2	The XMM-Newton observatory	30
2.3	XMM-Newton spacecraft	32
2.4	XMM-Newton effective area	34
2.5	EPIC-pn light path	35
2.6	XMM-Newton data reduction: source masking	41
2.7	XMM-Newton data reduction: source and background region	42
2.8	Soft-excess emission models	48
3.1	Mrk 993: X-ray best-fit model	55
3.2	Mrk 993: optical spectra	58
3.3	Mrk 993: optical spectra and best-fit model	60
3.4	Mrk 993: optical spectra zooming on the H_α and H_β regions	61
3.5	Ward et al. (1988) Fig. 4	64
3.6	Mrk 993: XMM-Newton light curves	65
3.7	Mrk 6: 2-10 keV power law model extrapolation	66
3.8	Mrk 6: EPIC-pn data corresponding to the three <i>XMM-Newton</i> ob- servations	69
3.9	Mrk 6: X-ray best-fit model	70
3.10	Mrk 6: optical spectra	71
3.11	Mrk 6: optical spectra and best-fit model	73
3.12	NGC 7603: 2-10 keV power law model extrapolation	77
3.13	NGC 7603: X-ray best-fit models	78
3.14	NGC 7603: optical spectra	80
3.15	NGC 7603: optical spectra and best-fit model	82
3.16	Mrk 1018: 2-10 keV power law model extrapolation	85
3.17	Mrk 1018: X-ray best-fit model	86
3.18	Mrk 1018: optical spectra	88

3.19	Mrk1018: Optical spectral fit in the H_β (top) and H_α (bottom) regions. Solid line correspond to the best-fit model. Dashed line correspond to each Gaussian component.	89
4.1	Averaging method diagram	96
4.2	Simulated model: p_0 , type 1 AGN, AXIS	101
4.3	Simulated model: $pha * p_0$, type 1 AGN, AXIS	102
4.4	Simulated model: $pha * zpha * p_0$, type 1 and type 2 AGN, AXIS+XWAS	104
4.5	Simulated model: $p_0 + \text{gaus}$, type 1 AGN, AXIS+XWAS	105
4.6	Simulated model: $pha * zpha * (p_0 + \text{gaus})$, type 2 AGN, AXIS+XWAS .	107
4.7	Simulated model and confidence contours: $pha * zpha * p_0$, type 1 and type 2 AGN, AXIS+XWAS	109
4.8	AXIS+XWAS sample properties	111
4.9	AXIS+XWAS sample, intrinsic absorption distribution	113
4.10	AXIS+XWAS sample, type 1 and type 2 AGN average spectra	114
4.11	AXIS+XWAS sample, type 1 and type 2 AGN average spectra to simulated continuum ratio	115
4.12	AXIS+XWAS sample, best fit for type 1 and type 2 AGN	120
4.13	Lockman Hole sample properties	123
4.14	Lockman Hole sample, Intrinsic absorption distribution	124
4.15	Lockman Hole sample, type 1 and type 2 AGN average spectra	125
4.16	Lockman Hole sample, type 1 and type 2 AGN average spectra to simulated continuum ratio	126
4.17	Lockman Hole sample, best fit for type 1 and type 2 AGN	129
4.18	AXIS+XWAS and Lockman Hole samples, luminosity vs redshift	132
4.19	Total sample, average spectra for type 1 and type 2 AGN	133
4.20	Total sample, average spectra to simulated continuum ratio for type 1 and type 2 AGN	134
4.21	Total sample, best fit for type 1 and type 2 AGN	137
4.22	Luminosity sub-samples, average spectra for type 1 AGN	139

List of Tables

3.1	Summary of the simultaneous observations	53
3.2	Mrk 993: X-ray best-fit spectral parameters	56
3.3	Mrk 993: optical best-fit spectral parameters	62
3.4	Mrk 6: X-ray best-fit spectral parameters	67
3.5	Mrk 6: X-ray best-fit spectral parameters for the join fit	69
3.6	Mrk 6: optical best-fit spectral parameters	72
3.7	Mrk 6: luminosity and fluxes for the three XMM-Newton observations	74
3.8	NGC 7603: X-ray best-fit spectral parameters	79
3.9	NGC 7603: optical best-fit spectral parameters	81
3.10	Mrk 1018: X-ray best-fit spectral parameters	86
3.11	Mrk 1018: optical best-fit spectral parameters	90
3.12	Summary of the Changing-type Seyfert galaxies sample analysis	92
4.1	Broadening of narrow features caused by the averaging process	103
4.2	AXIS+XWAS sample, best-fit spectral parameters	121
4.3	Lockman Hole sample, best-fit spectral parameters	130
4.4	Total sample, best-fit spectral parameters	138
4.5	Luminosity sub-samples best-fit spectral parameters	140

Introduction

Contents

1.1 Motivation	2
1.2 Active Galactic Nuclei	3
1.2.1 General Properties	4
1.2.2 Physical Properties	8
1.2.3 The AGN paradigm	13
1.2.4 The AGN spectrum	19
1.3 Goals of the Thesis	24
1.3.1 Testing unified models	24
1.3.2 Constraining the Fe K α emission	25

Active Galactic Nuclei (AGN) are the brightest persistent emitters in the Universe. They emit huge amounts of energy over the entire electromagnetic spectrum. They are also characterised by variability on short-time scales, which implies a small emitting region. The only known astrophysical environment capable of reproducing those properties is accretion onto a super massive black hole (SMBH). X-rays, given their penetrating ability, are key to understand the physical processes that take place in such extreme environments, and allow us to test Physics in the extreme relativistic regime. Besides, given the large amount of radiation emitted by this kind of sources, they can be detected up to large distances and thus allow us to learn about the early Universe and how it has evolved across cosmic time.

In this chapter a summary of our current knowledge about AGN most relevant to this thesis work is presented. In Sect. 1.1, some of the current open questions about AGN are listed including the ones that are the subject of this thesis work. In Sect. 1.2, the observational characteristics of these kind of sources are presented as well as physical processes that could produce their emission and the theoretical models suggested to explain it. Finally, in Sect. 1.3, the strategy adopted in this work to address the questions formulated in Sect. 1.1 is presented.

1.1 Motivation

Nowadays, it is widely believed that there is a SMBH at the centre of all galaxies (Magorrian and Tremaine, 1999; Kormendy and Richstone, 1995). Therefore, AGN are no longer considered as a class of object but as a state all galaxies go through at some point of their evolution and that can be triggered by different mechanisms, such as galaxy mergers or star formation.

Although it is uncertain how the host galaxy and its central SMBH interact, very compelling evidence has been presented in recent years supporting that galaxy formation and SMBH growth must be tightly linked. There is a well-established correlation between SMBH mass and the galaxy bulge stellar velocity dispersion (the M - σ_* relation, Gebhardt et al. 2000; Ferrarese and Merritt 2000; Tremaine et al. 2002; Greene and Ho 2006). Besides, the SMBH mass has been found to be proportional to the stellar mass in the host galaxy bulge and even to that of the galaxy dark matter halo (Graham et al., 2001; Ferrarese, 2002). AGN and “normal” galaxies also share an evolutionary feature called “cosmic downsizing” (Ueda et al., 2003; Hasinger et al., 2005; Bongiorno et al., 2007). This means that the number density of the most luminous AGN peaks at higher redshifts than for less luminous AGN. In the case of normal galaxies, it is found that the most massive ones form stars at earlier epochs, i.e., the most luminous and massive galaxies form all their stars more rapidly, whereas less massive galaxies have a more prolonged star formation till later cosmic times (Cowie et al., 1996; Gavazzi and Scodeggio, 1996). In a hierarchical scenario where dark matter halos grow with cosmic time, this means that star formation in massive galaxies must be terminated by some process to prevent them from keeping growing. Feedback from AGN has been proposed as the primary mechanism to shape the stellar content of massive galaxies.

The sky in X-rays shows a diffuse emission of cosmic origin: the cosmic X-ray background (CXB, Giacconi et al. 1962). This radiation has been largely resolved into discrete sources thanks to X-ray surveys (Worsley et al., 2005; Hickox and Markevitch, 2006). At hard energies (> 2 keV), the dominant emitters of the CXB are found to be AGN, so the CXB is the integrated emission of AGN across cosmic time. Since AGN are believed to emit energy by accreting material and their SMBH growth is connected to that of the galaxies that host them, studying the CXB implies to study the evolution of galaxies and accretion in the Universe. CXB synthesis models make use of the AGN unified model (Antonucci, 1993) in order to reproduce its shape and intensity (Gilli et al., 2007; Treister et al., 2009). This model states that all AGN share a common structure (central engine surrounded by material with similar geometry) and the differences between different AGN types are attributable mainly to an orientation effect, i.e., to differences in the amount of intervening material. However, a number of AGN have been found that appear not to follow the simplest ver-

sion of this unified model, thus challenging the CXB synthesis model assumptions.

There still are many open issues regarding the physics of AGN and their description as a population. The number of absorbed sources and its evolution across cosmic time are still poorly known as well as their dependence on the source's properties such as the luminosity. As mentioned above, the way the host galaxy evolution determines the SMBH formation and viceversa (AGN feedback) is still not well understood or characterised. AGN unified models have to be revised to get a better picture of what it is going on at the centre of active galaxies. Besides, one of the most commonly observed features of AGN X-ray spectra, the Fe $K\alpha$ emission line, is expected to show a relativistic profile when emitted close to the SMBH, but this emission has only been observed in a limited amount of cases (high quality data are needed to detect it). Moreover, how common narrow Fe $K\alpha$ emission lines are and their properties, although much more commonly observed, have only been constrained at low redshifts.

This thesis work is focused on shedding some light upon the last two issues: AGN unified models and Fe $K\alpha$ emission.

1.2 Active Galactic Nuclei

At the beginning of the 20th century, galaxies were still considered as “nebulae” since their extragalactic nature had not been proved yet. In order to clarify their nature, [Fath \(1909\)](#) carried out a series of observations using an optical telescope. Most of the galaxies observed showed a spectrum with stellar absorption lines consistent with a collection of different stars. However, the spectrum of NGC 1068 showed absorption but also emission lines similar to those of a gaseous nebulae.

It was not until the work of [Seyfert \(1943\)](#), that the study of “galaxies with nuclear emission lines” began. A fraction of the galaxies observed emitted bright emission lines at their centres attributable to highly ionised species, and some of them showed very broad emission lines. Their nuclei were compact and bright, sometimes many times brighter than the host galaxy. From then on, this kind of galaxies were known as Seyfert galaxies. Nonetheless, the beginning of the study of AGN came from radio observations. Since the work of Jansky in 1932, many radio astronomers contributed to this field constructing large catalogues of “quasi-stellar radio sources” (quasars), and suggesting the non-thermal nature of their emission. Similarly to quasars, “quasi stellar objects” (QSOs) were discovered. These objects also appeared as point-like sources with high brightness but, in this case, without significant radio emission (compared to the emission at other wavelengths). [Schmidt \(1963\)](#) demonstrated that the optical observed emission lines were redshifted nebular lines, thus confirming their extragalactic nature and implying extremely high luminosities.

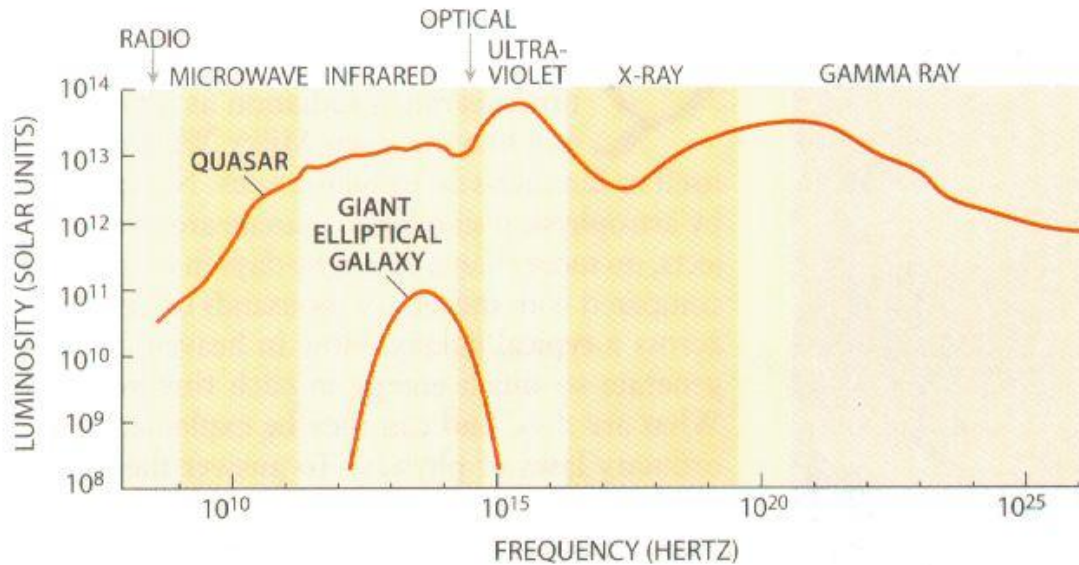


Figure 1.1 Spectral energy distribution (SED) of the first discovered quasar, 3C273, compared against the SED of a giant elliptical galaxy, the most luminous “normal” galaxies.

Nowadays, quasars and QSOs are considered the distant and high luminosity analogs of Seyfert galaxies. The same very energetic physical phenomena are believed to take place at the centres of all of them, and they are all considered “active galaxies”, or AGN.

1.2.1 General Properties

AGN emit vast amounts of energy over the entire electromagnetic spectrum (from radio to γ -rays) with bolometric luminosities ranging from 10^{41} to 10^{48} erg s^{-1} . The bulk of this emission appears to arise from an unresolved compact region in the nucleus. Besides, AGN emission varies in very short time scales, which implies that the emitting source is very small. This, along with the huge amount of energy emitted, supports the now widely held assumption that the source of power in AGN is accretion onto a SMBH. This point and its implications are discussed in more detail in Sect. 1.2.2.

AGN emission is relatively flat from the far IR to hard X-rays. The representation of the emitting power versus frequency is called Spectral Energy Distribution (SED). As an example, the SED corresponding to a quasar is plotted against the one corresponding to a “non-active” galaxy in Fig. 1.1. AGN SEDs can be very different among particular objects although they can be roughly modelled by using a power law over a narrow wavelength range. However, as the observational

data improved, AGN spectra turned out to have a far more complex spectrum than that. The focus of this thesis is the optical and X-ray spectra of AGN, which are discussed in more detail in Sect. 1.2.4. In this section, only a brief description of the continuum emission is given for every relevant wavelength range.

1. **Radio emission:** About 10-20% of AGN are radio-loud (RL). This means that their radio loudness parameter (R, which corresponds to the radio (5GHz) to optical (B-band) flux ratio) is larger than 10, according to the current classification. Radio emission for radio-quiet (RQ) AGN can be 100 to 1000 times weaker than for RL AGN. The continuum spectrum of the RL AGN emission takes the form of a power law coming from synchrotron radiation. In all cases, radio emission is not a significant fraction of the bolometric luminosity, not even for RL AGN.
2. **IR emission:** The integrated emission over the IR bands amounts to $\sim 30\%$ of the bolometric luminosity. The continuum shape is characterised by a broad bump between $\sim 2\text{-}200 \mu\text{m}$ and a minimum around $1 \mu\text{m}$. This emission is consistent with thermal emission from dust at different temperatures, and the $1\mu\text{m}$ minimum would correspond to the sublimation radius, i.e., to the maximum temperature in which dust could survive (1000-2000 K depending on the composition of the dust grains).
3. **Optical/UV emission:** The main feature of the UV/optical spectra of AGN is the big blue bump (BBB). The big blue bump can be reproduced by a multi-blackbody spectrum with a maximum temperature of $\sim 10^{5\pm 1}$ K. The BBB usually corresponds to the peak of AGN luminosity and it can encompass up to $\sim 50\%$ of the bolometric luminosity. The relative strengths of the IR and big blue bump vary but they are generally comparable. Strong emission lines are present in AGN spectra. Another bump is usually found between 2000 and 4000 \AA , but we now know that it is not a real continuum feature but a blend of emission lines.
4. **X-ray emission:** AGN X-ray emission can be approximated to first order by a power law. In flux density units, it is expressed as

$$F_\nu \propto \nu^{-\alpha} \quad (1.1)$$

where F_ν is the flux density, ν is the frequency and α is the spectral index. This power law extends from ~ 1 keV to over 100 keV and has a typical spectral index ranging from 0.8 to 1. In X-rays, the power law is usually expressed in photon units

$$F_E \propto E^{-\Gamma} \quad (1.2)$$

where F_E is the photon flux per unit energy, E is the photon energy and Γ is called the photon index ($\Gamma = \alpha + 1$). RL AGN usually display flatter photon

indices than RQ AGN. High energy data (above 10 keV) suggest the presence of an exponential cut-off at energies 80-300 keV, and a bump which peaks around 30 keV. Sometimes, an excess emission over the power law shape at soft energies is detected, and in other cases, the emission at soft energies appears suppressed. X-ray emission, which is one of the main topics of this thesis, is thought to originate from the immediate vicinity of the SMBH and the accretion disk around it.

5. **γ -ray emission:** Some RL AGN, known as Blazars, emit most of their bolometric luminosity above 100 MeV. They are characterised by a non-thermal continuum spectrum, a flat radio spectrum, strong variability and optical polarisation. Blazars exhibit a double-peaked SED, the lower frequency peak due to synchrotron emission and the higher frequency one to Comptonisation.

1.2.1.1 Classification

AGN classification has become more and more complex throughout the years as different kinds of AGN were discovered. Historically, RL and RQ AGN have been classified in a different way. RQ AGN are classified depending on their optical spectral properties and their luminosity (Osterbrock, 1989). In the low luminosity regime, RQ AGN are called Seyfert galaxies whereas high luminosity RQ sources are called QSOs. In the beginning, the difference between Seyferts and QSOs was established as a function of the host galaxy being visible or not (the host galaxy is supposed to be outshined by the nuclear emission in QSOs). Currently, the dividing parameter between Seyferts and QSOs is the absolute magnitude ($M_V < -23$ for QSOs) or the luminosity ($L_X > 10^{44}$ erg s⁻¹ for QSOs). RL classification is somewhat more complex. RL AGN are classified depending on their spectral properties in the optical but also on their radio morphology (Fanaroff and Riley, 1974). RL AGN radiation is believed to be linked to the emission of collimated jets of plasma from the active nucleus. These jets would be responsible for the formation of extended structures that are called radio lobes and that can outshine nuclear emission at radio frequencies. To add more complexity to this classification scheme, the terms QSO and quasar are now accepted to describe a RL or a RQ AGN. Here we describe briefly the different AGN types most relevant for this thesis as they are usually classified in the literature.

◇ Radio-quiet AGN:

- **Seyfert 1 galaxies (Sy1s)** are those active galaxies that show broad permitted and narrow forbidden emission lines in their optical spectra. To distinguish between broad and narrow lines in active galaxies, given that even narrow lines are broader than for non-active galaxies, a threshold on the full width at half maximum (FWHM) of 1000 km s⁻¹ is usually adopted. Within this kind of AGN, there is another class called narrow line Seyfert 1 galaxies

(NLSy1s), for which the broad permitted lines are also present but they are narrower than for most Sy1s, i.e., they have usually $\text{FWHM} \sim 1000 \text{ km s}^{-1}$, whereas Seyfert galaxies usually show broad lines of $\text{FWHM} > 2000 \text{ km s}^{-1}$. NLSy1s are believed to be accreting at very high rates and to have low mass SMBH.

- **Seyfert 2 galaxies (Sy2s)** only show narrow emission lines in their optical spectra, both permitted and forbidden lines. The intermediate types (type 1.2, 1.5, 1.8, and 1.9 AGN) refer to the relative strength of narrow and broad line components (Osterbrock, 1981).
- **QSOs** are the brighter version of Seyfert galaxies and, in the same way as Seyfert galaxies, they are divided into type 1 and type 2 QSOs.
- **LINERS (low ionisation nuclear emission-line region galaxies)** are the least luminous AGN. They appear similar to type 2 AGN in the optical, but the relative strengths of certain low ionisation lines are much higher than they are for Seyfert galaxies (for example, $[\text{OII}]\lambda 3727$ to $[\text{OIII}]\lambda 5007$ line ratio is $\simeq 1$ for LINERS whereas it is ≤ 0.5 for Sy1s).

◇ **Radio-loud AGN:**

- **FR-I radio galaxies** have low radio power and their radio surface brightness profiles decrease outwards. In the optical and UV, only narrow lines are detectable.
- **FR-II radio galaxies** have high luminosities (they are very powerful radio sources) and their radio surface brightness profiles increase dramatically outwards as they reach the end of the extended structures. In the optical they can show a spectrum similar to a Seyfert 1 or a Seyfert 2 galaxy and accordingly, they are called broad line radio galaxies (BLRG) or narrow line radio galaxies (NLRG), respectively.
- **RL quasars** are usually included within the BLRG, the only difference being that, in the case of RL quasars, the continuum emission of the nucleus dominates over the extended radio emission.
- **Blazars** encompass BL Lacs and optical violent variables (OVVs), and they show no emission lines or very weak ones in their optical spectra, respectively. They also show strong variability at all wavelengths.

In X-rays surveys, a simplified classification is usually adopted. Most AGN types (excluding LINERS or Blazars) are divided into **type 1 AGN** and **type 2 AGN** depending on the presence or absence of broad permitted lines in their optical spectra, respectively. For simplification, this classification is adopted throughout this thesis work whenever the data in use come from X-ray surveys. In Fig. 1.2 sample optical spectra for each class of AGN are shown.

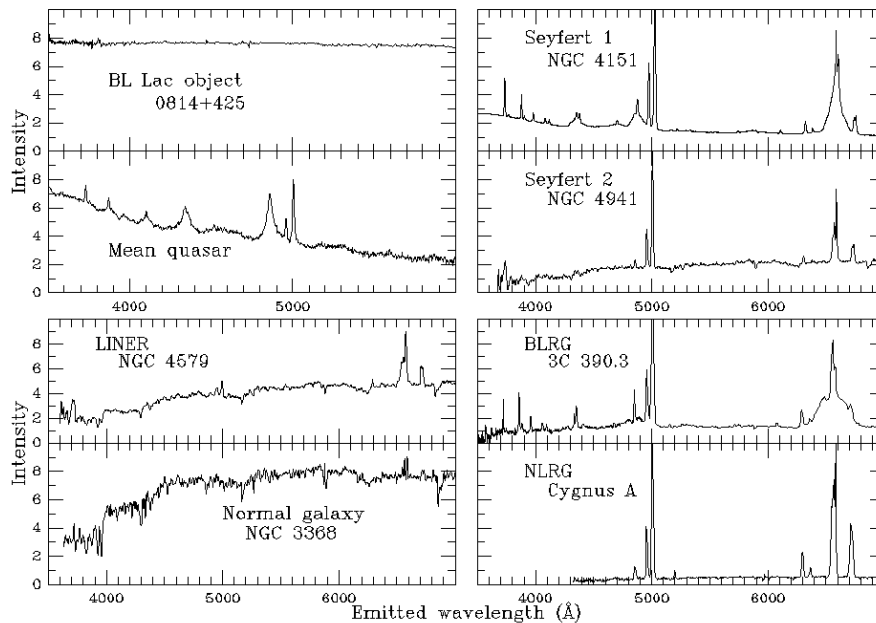


Figure 1.2 AGN optical spectral types from Bill Keel's gallery (<http://astronomy.ua.edu/keel/agn/spectra.html>).

1.2.2 Physical Properties

The source power of an AGN is believed to come from accretion onto a SMBH. There is no other known physical mechanism capable of releasing such amount of energy from the inferred size of the emitting source (it must be of the order of light days or less, as inferred from its rapid variability). In this Thesis, only the observational properties of AGN have been presented so far. Although there is a wide variety of AGN types and spectral properties among them, all share some common characteristics. The emission comes from an unresolved small source at the galaxy nucleus, they vary in short-time scales and they emit with an almost flat spectrum from the IR to the hard X-rays. In the case of some RL AGN, they also emit significant amounts of energy at radio and γ -rays wavelengths. In this section, the main physical mechanisms that are thought to cause this emission are discussed.

1.2.2.1 Accretion onto a SMBH

We have strong evidence for the presence of SMBH at the centre of galaxies:

- Assuming that the material responsible for the emission of broad optical/UV emission lines is gravitationally bound, then the mass must be very high. High masses are derived by using a method called reverberation mapping of the broad emission lines (see [Peterson and Bentz 2006](#) for a review on reverberation mapping).

- Velocity dispersion of stars increase towards the nucleus implying a high concentration of mass there (see for example [Yu and Lu 2004](#)).
- The observed X-ray variability leads to an efficiency in converting matter to energy that can not be achieved by thermonuclear processes ([Salpeter, 1964](#); [Fabian, 1979](#)). Matter/antimatter annihilation would produce a γ -ray dominated spectrum, which is not observed.
- A large central mass has also been derived from water maser emission ([Neufeld et al., 1994](#)).

The minimum mass of the accreting SMBH can be estimated by assuming spherical accretion of fully ionised hydrogen and hydrostatic equilibrium. In this case, the gravitational force inwards equals the continuum radiation force outwards:

$$F_{rad} = \frac{L\sigma_e}{4\pi r^2 c} \quad (1.3)$$

$$F_{grav} = \frac{GMm_p}{r^2} \quad (1.4)$$

where F_{rad} and F_{grav} are the forces due to radiation pressure and gravitational potential, respectively, L is the bolometric luminosity, and σ_e is the Thomson cross-section. By equating these two forces we obtain

$$L_{edd} = 1.26 \times 10^{38} \left(\frac{M}{M_\odot} \right) \text{ erg s}^{-1} \quad (1.5)$$

where L_{edd} is the Eddington luminosity ([Eddington, 1913](#); [Rees, 1984](#)) and represents the maximum luminosity for a source of mass M powered by spherical accretion.

Therefore, assuming that an AGN is accreting at the Eddington limit, the minimum mass required is given by

$$M = 8 \times 10^5 \left(\frac{L}{10^{44} \text{ erg s}^{-1}} \right) M_\odot \quad (1.6)$$

This implies minimum masses for accreting SMBH as high as $10^{10} M_\odot$ for the most luminous AGN.

The luminosity released by accretion is defined as

$$L = \eta \dot{M} c^2 \quad (1.7)$$

where η is the efficiency of accretion in converting mass into radiated energy, and \dot{M} is the accretion rate.

In a more realistic scenario, a spherical cloud of infalling matter cannot be directly accreted by a SMBH. This matter needs to lose its angular momentum in order to be accreted. This is achieved by forming a flat accretion disk ([Lynden-Bell,](#)

1969). Within this structure, matter loses angular momentum via viscous drag so that it can fall onto the accretion disk and liberate energy. This energy is liberated by heating the disk which then, assuming that the disk is optically thick, emits thermal photons in the optical/UV band, which is believed to be the origin of the BBB.

For a non-rotating Schwarzschild SMBH, the last stable orbit for the matter in the accretion disk before falling onto the SMBH is $6R_S$, where R_S is the Schwarzschild radius ($R_S = 2GM/c^2$, where GM/c^2 is called the gravitational radius, is the distance for which the escape velocity of the infalling material equals the speed of light). This produces an efficiency in converting matter to radiated energy of ≤ 0.06 . For a rapidly rotating Kerr SMBH, the innermost stable orbit (ISCO) extends to $\sim R_S$ and the maximum efficiency (for a maximally rotating SMBH) can reach $\eta \simeq 0.46$.

1.2.2.2 Primary X-ray emission

The basic physical phenomena underpinning X-ray continuum emission mechanisms are bremsstrahlung, synchrotron and inverse Compton scattering.

- **Bremsstrahlung emission:** (German for “braking radiation”) occurs when a charged particle is deflected by the electrostatic field of an ion. When a charge is accelerated or decelerated, it emits radiation, the amplitude of which is proportional to the charges of the two interacting particles. Thermal bremsstrahlung is the name given when instead of a single charged particle, the radiation comes from a plasma of thermal particles. This kind of radiation is usually observed in regions of hot gas, like the intracluster gas in galaxy clusters. In AGN, this radiation could originate in a hot ionised gas close to the central SMBH.
- **Synchrotron emission:** is the radiation coming from charged relativistic particles moving in a magnetic field. If the particles’ energy spectrum has a power law shape, a non-thermal synchrotron radiation with a power law spectrum is emitted as a result of the superposition of the individual particle power laws. If the photons emitted interact again with these particles, they can either be absorbed preferentially at low energies or they can gain energy through inverse Comptonisation. This is called Synchrotron self-Comptonisation. These kinds of processes are believed to take place in AGN jets.
- **Inverse Compton scattering:** When low energy photons interact with high energy electrons, the former gain energy. In AGN, UV/optical photons coming from the accretion disk surrounding the SMBH are thought to be up-scattered by relativistic electrons in a corona around the disk, producing a power law X-ray spectrum. This process is called **Comptonisation** when it

is caused by the multiple inverse Compton scattering by energetic electrons (Zdziarski et al., 1994). Inverse Compton scattering by a thermal electron corona also predicts an exponential cut-off at the energy of the thermal electron corona (> 100 keV). This is the process believed to be the source of the primary X-ray emission of AGN.

To these continuum emission processes, partially ionised atoms should also be added. Atomic transitions in the form of emission lines, radiation recombination continua and other features are also seen in high resolution X-ray spectra of hot astrophysical plasmas. However, the energy budget contained in such spectral features is normally modest and the X-ray emission is dominated by the continuum.

1.2.2.3 X-ray reprocessing

The primary X-ray power law spectrum is then reprocessed by material surrounding the central source through different physical mechanisms. Depending on the energy of the X-rays and the state of the material, a significant fraction of the primary emission can be absorbed or scattered.

- **Photoelectric absorption by neutral material:** For an X-ray photon of energy E , the probability of being photoelectrically absorbed by a neutral atom is

$$P(E) = 1 - e^{-\sigma(E)N_H} \quad (1.8)$$

where $\sigma(E)$ is the photoelectric absorption cross-section, and N_H is the Hydrogen-equivalent column density, which accounts for the contribution of the various atomic species for a given abundance pattern. When an incident power law is absorbed by neutral material, the resulting spectrum contains different absorption edges corresponding to the different ionisation potentials for each species within the absorbing material. Therefore, the effective cross-section of this process depends on the abundances in the absorbing material. Column densities over 10^{20} cm $^{-2}$ are needed to produce a detectable effect in X-rays at redshift zero. For higher redshifts, as the emission and, consequently, the intrinsic absorption, are shifted towards lower energies, larger and larger column densities would be needed in order to be detectable. In Fig. 1.3, the effects of cold absorption with different column densities over an incident power law of $\Gamma = 2$ are shown.

- **Absorption by ionised material:** If the absorbing material is partially ionised, the absorption pattern depends not only on the abundances and the column density but also on the degree of ionisation of the material. This material, usually called **warm absorber**, will normally be only partly ionised so the absorption could preferentially occur at certain energies. For example, this kind of absorber could be transparent at low and high energies but not at intermediate energies and result in a curved spectrum caused by the photons lost at intermediate energies. This material could be also so ionised that

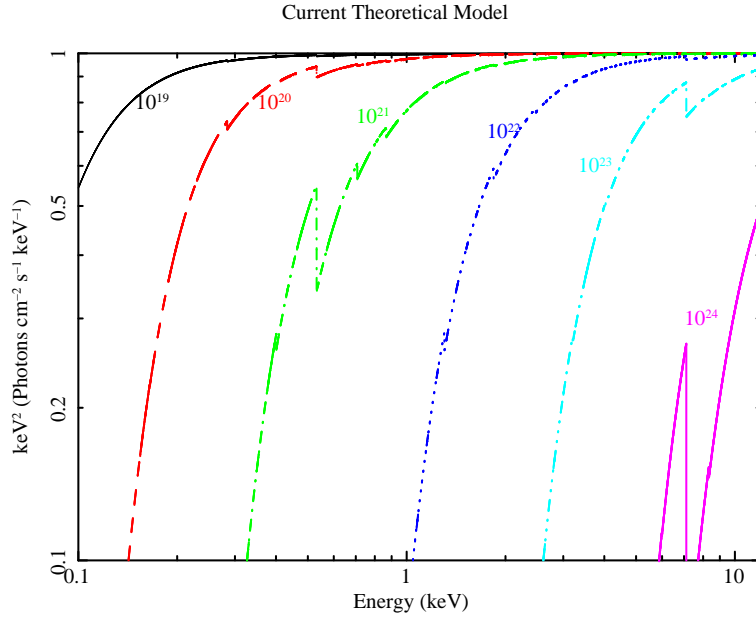


Figure 1.3 X-ray power law ($\Gamma = 2$) absorbed by a range of column densities. The numbers represents the value of the different column densities in cm^{-2} units.

its spectral features would be undetectable. In Fig. 1.4, we show how an incident power law ($\Gamma = 2$) is affected by ionised absorption from material with different ionisation parameters. The ionisation parameter ζ is a measure of the ionisation state of the material

$$\zeta = \frac{4\pi F}{n_H} \quad (1.9)$$

where F is the total illuminating flux and n_H is the hydrogen number density.

- **X-ray reflection** does not refer to an individual physical process but to a combination of different ones. When the incident power law illuminates cold material, there are a number of interactions that can occur: photons can be Compton scattered to lower energies or they can be absorbed (photoelectric absorption, as described above) and then re-emitted by fluorescent line emission or by Auger de-excitation. The fluorescent yield is the probability that a photoelectric absorption is followed by fluorescent line emission instead of the Auger effect. It is different for different atomic species and it also depends on the ionisation state of the ion that absorbs the X-ray photon. The intensity of a fluorescence emission line depends also on the abundance of the absorbing ion. Besides, low energy X-ray photons are more likely to be absorbed than scattered, whereas high energy photons are more likely to be Compton back-scattered. Therefore, the resulting “reflected” spectrum shows, roughly, a bump between 5-50 keV and a series of emission lines

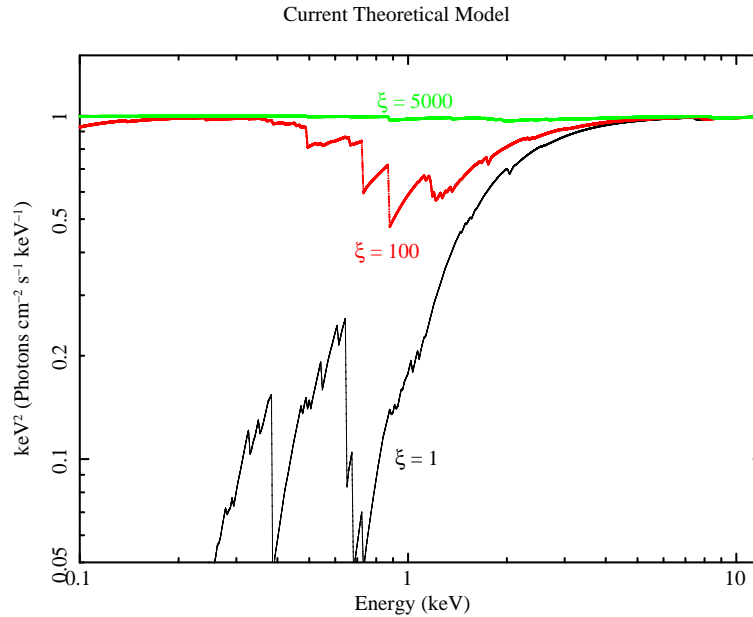


Figure 1.4 X-ray power law ($\Gamma = 2$) absorbed by ionised absorbers with different ionisation parameters (ξ).

at lower energies (see Fig. 1.5). The resulting incident plus reflected spectrum would display a flattening on the spectral slope at high energies caused by the reflected component. If the reflecting material is partially or totally ionised (like the accretion disk), the shape of the reflected spectrum depends on the ionisation state of the reflecting material. For highly ionised material absorption effects could be reduced at low energies (see the discussion about ionised absorption above) and for totally ionised material, emission lines will not be produced. In Fig. 1.6, different reflected spectra for different ionisation parameters are shown.

1.2.3 The AGN paradigm

A great variety of AGN types and properties have been presented so far, but all of them are believed to share the same basic phenomena at their centres. In order to reconcile both theory and observations, unified models for AGN were developed.

The first unification was proposed for RQ AGN (Antonucci, 1993). In this model, the differences between AGN types were explained as caused by the different viewing angle between the rotation axis of the accretion disk and the observer. The central SMBH plus accretion disk and corona structure is surrounded by hot and dense clouds of gas (the broad line region, BLR, responsible for the broad permitted lines) and further away by a dusty molecular torus with a planar geometry (responsible for the absorption in X-rays and the obscuration in the optical) and

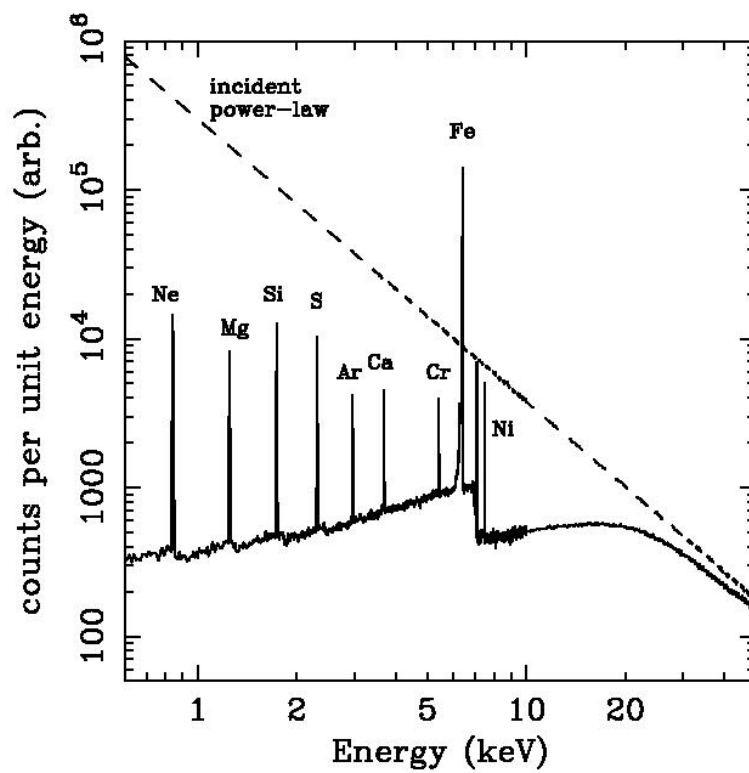


Figure 1.5 X-ray reflection from a cold illuminated slab. Dashed and solid lines represent the incident power law and the reflected spectrum (Fabian et al., 2000).

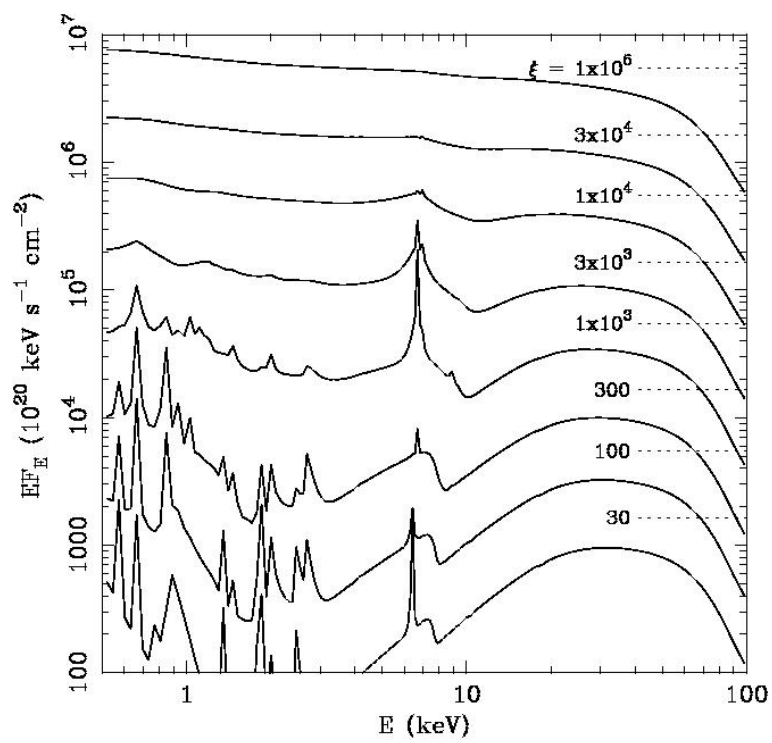


Figure 1.6 X-ray reflection from ionised material as a function of the ionisation parameter ζ (Fabian et al., 2000).

beyond this torus, colder clouds of gas (the narrow line region, NLR, responsible for the narrow emission lines). In this way, the observational differences between type 1 to type 2 AGN and the intermediate types are explained as a continuum transition in the viewing angle from 0 to 90°.

The second unification was the RQ/RL AGN unification (Urry and Padovani, 1995). In this case and besides the previous mentioned structure, the relativistic jet is included, so that AGN radio emission depends on the inclination angle between the observer to the jet. This model also explains Blazar emission by relativistic beaming of the jet emission pointing directly towards the observer.

A visual representation of the AGN paradigm is presented in Fig. 1.7, and its principal components are

- **SMBH** at the centre with mass in the range $10^6 - 10^{10} M_{\odot}$.
- **Accretion disk:** Within $\sim 10^{-3}$ pc from the nucleus, there is a geometrically thin, optically thick accretion disk with a maximum temperature $\sim 10^{5\pm 1}$ K composed of hot dense plasma of infalling matter. As the matter falls losing angular momentum via viscous drag, it heats and emits thermal radiation in the optical/UV band and it produces the BBB.
- **Corona:** Over the innermost parts of the accretion disk, there is a hot ($T \sim 10^9$ K) corona of very energetic electrons that are responsible for the inverse Compton scattering of the thermal photons emitted from the disk. This results in the primary X-ray power law emission.
- **Broad line region (BLR):** Clouds of gas moving rapidly in the gravitational potential of the SMBH. This is the region where broad permitted lines observed in the optical/UV band arise from. From reverberation mapping of the broad emission lines, the size of the BLR is estimated to range between ~ 0.01 - 0.1 pc. From the absence of broad forbidden lines, its typical density has to be $> 10^8 \text{ cm}^{-3}$, and from the emission lines width, the velocity of the gas is the range 1000 - 30000 km s^{-1} .
- **Torus:** A toroidal structure that extends from 1 to 100 pc and that contains both cold gas and dust. This structure is believed to be Compton thick, very likely formed by blobs of gas, and to obscure the direct emission for high viewing angles, although it can also scatter part of this emission into our line of sight.
- **Narrow line region (NLR):** Clouds of gas with smaller turbulence than the ones in the BLR (a few hundreds of km s^{-1}) and with lower densities ($10^3 - 10^6 \text{ cm}^{-3}$); they are responsible for the narrow emission lines in the optical/UV band. This region is much further away from the nucleus than the BLR (~ 100 pc) and displays a biconical shape. When this emission extends

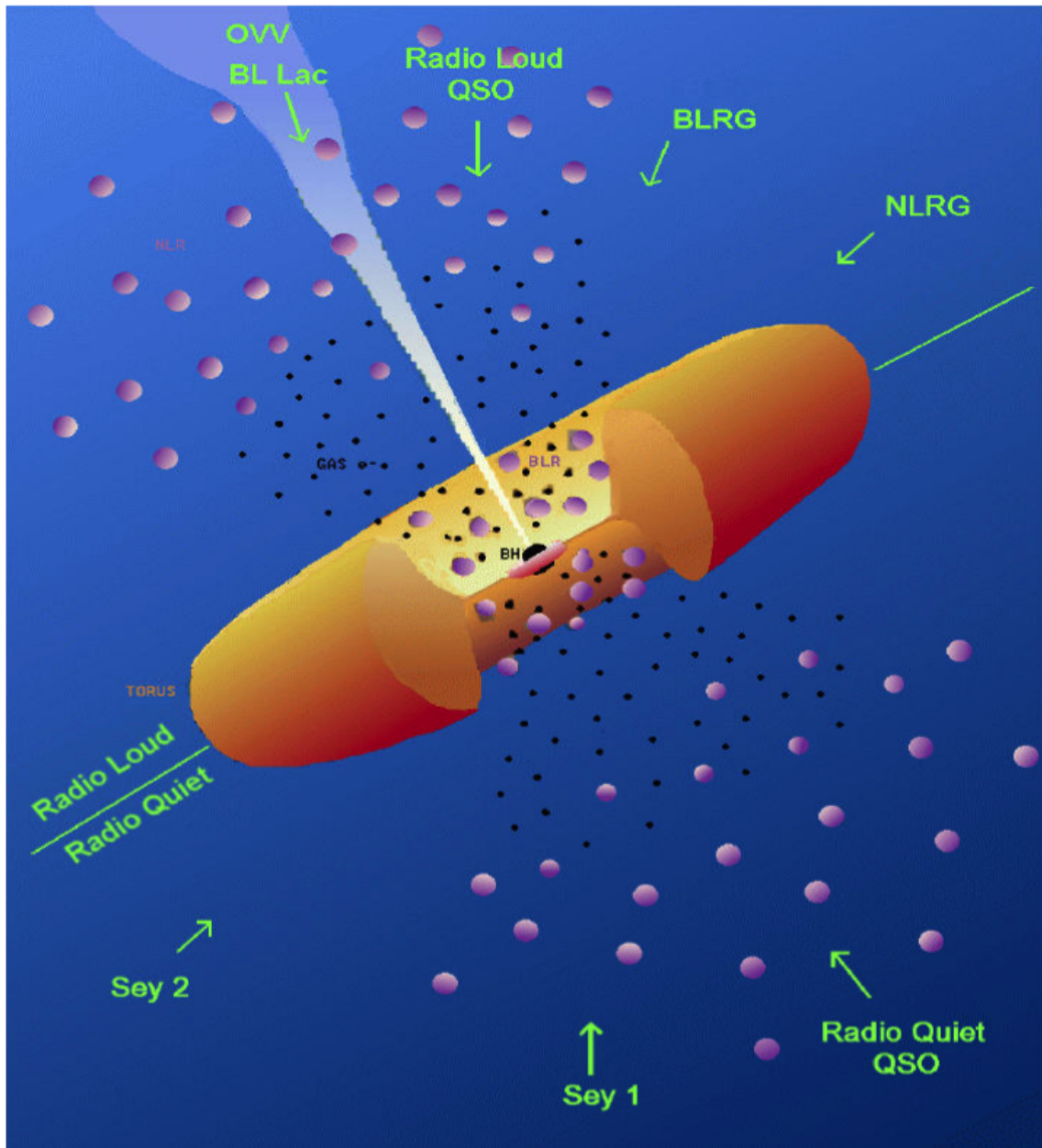


Figure 1.7 AGN unification model adapted from Urry and Padovani (1995).

a few kpc into the host-galaxy ionised gas, it is called the extended narrow line region (ENLR).

- **Relativistic jet:** its is supposed to form by the emission of very energetic particles along the poles of the disk. The relativistic jets are responsible for the radio emission in RL AGN.

The predictions of this model are usually in agreement with observations. X-ray absorption seems to increase as optical obscuration increases (see for example [Smith and Done 1996](#), [Nandra and Pounds 1994](#), [Bassani et al. 1999](#) and [Risaliti et al. 1999](#)), and Sy2 galaxies usually show more dust emission than Sy1s ([Granato et al., 1997](#)). Unified models have also been strongly supported by the discovery of “hidden type 1 nuclei” at the centre of type 2 AGN, i.e., AGN showing only narrow emission lines in their optical spectra are found to have broad emission lines when observed in polarised light (see for example [Antonucci and Miller 1985](#)). The proposed explanation is that the BLR is obscured by the torus but some BLR photons are scattered towards our line of sight and scattered radiation is polarised. Hidden broad lines have also been found in type 2 AGN when observed in the IR, less affected by obscuration, and the inferred optical depths from the IR correspond to the expected optical extinction ([Ward et al., 1991](#)). The ENLR emission has been found to display a biconical shape, which is consistent with anisotropic obscured emission from a type 1 nucleus shaped into a biconical shape by the toroidal structure.

In the case of RL AGN, Blazar emission is explained by relativistic beaming of the jet emission, which also accounts for their rapid variability and the lack of emission lines in their optical spectra because they are swamped by the bright beamed emission.

However, there are also optical and X-ray observations that deviate from this unified model. Unabsorbed type 2 AGN and absorbed type 1 AGN are occasionally found in X-rays surveys (see for example results from [Fiore et al. 2001](#), [Page et al. 2001](#), [Tozzi et al. 2001](#), [Mainieri et al. 2002](#), [Brusa et al. 2003](#), [Page et al. 2003](#), [Perola et al. 2004](#), [Mateos et al. 2005a](#), [Pappa et al. 2001](#), [Panessa and Bassani 2002](#), [Barcons et al. 2003](#) and [Carrera et al. 2004](#)). Even sources for which the BLR appears to be absent have been recently discovered ([Panessa et al. 2009](#), [Bianchi et al. 2008](#)), discarding optical reddening as the physical cause for their type 2 optical classification.

A possible explanation for the existence of absorbed type 1 AGN could be that, since an important fraction of the X-ray photoelectric absorption may arise fairly close to the nucleus, where dust cannot survive ([Granato et al., 1997](#)), the intrinsic column density derived from X-rays would be larger than the one derived from optical reddening when assuming a Galactic gas-to-dust ratio.

Several explanations have been suggested for unabsorbed type 2 AGN (Pappa et al., 2001): the source might be Compton-thick, i.e., the intrinsic absorption is so large that most of the direct emission is suppressed and we only see scattered light; the central engine might be obscured in the optical by an ionised dusty absorber (with little effect on X-rays); and, finally, the difference is an intrinsic property, i.e., the properties of the BLR are unrelated to orientation/absorption. For example, the BLR could disappear due to a decrease of the continuum emission (Guainazzi et al. 2005, Matt et al. 2003) or could be optically thick, which would change the intrinsic Balmer decrements used to derive the optical reddening (Emerson, 1999). All this highlights the importance of adding to the simplest unified schemes the dependence on the AGN intrinsic properties such as the SMBH mass, its spin, the accretion rate, and the host-galaxy morphological type.

An additional possibility is that since the X-ray and optical observations are almost invariably non-simultaneous, they could map the same AGN in a different “absorption” state. That means that the amount of absorbing material (both in the X-rays and in the optical) would vary on scales from months to years. Variations in X-ray absorption have been reported on such times scales (Risaliti et al., 2002) or even in shorter time scales (Elvis et al. 2004, Risaliti et al. 2007, Risaliti et al. 2007). Also variations in the optical spectral type on these scales have been reported for a number of AGN (Aretxaga and Terlevich, 1994). In that scenario, simultaneous X-ray and optical observations would reveal an amount of X-ray photoelectric absorption consistent with the dust reddening of the BLR as mapped by the optical spectroscopy.

1.2.4 The AGN spectrum

This section is focused on the X-ray and optical spectra of AGN. The main observed characteristics and the physical information that can be extracted from them are discussed here.

1.2.4.1 X-ray spectrum of AGN

The **RQ type 1 AGN** X-ray spectra are characterised by a power law shape with a photon index usually in the range 1.8-2. As X-ray data have improved, new components have been found to contribute to these spectra. Warm absorption signatures are usually found in $\sim 50\%$ of AGN (see Komossa and Hasinger 2003 for a review). Many AGN also show a feature called “soft-excess”. Soft-excess emission refers to excess emission below 2 keV above the extrapolated hard (above 2 keV) power law emission. The origin of this emission in type 1 AGN is still a matter of debate. At first, it was proposed that soft-excess emission corresponds to the hard tail of the optical/UV BBB, but this is not supported by the observations. Its inferred temperature is too high for a disk orbiting a SMBH and it seems not to depend on the intrinsic luminosity or SMBH mass. Other proposed explanations

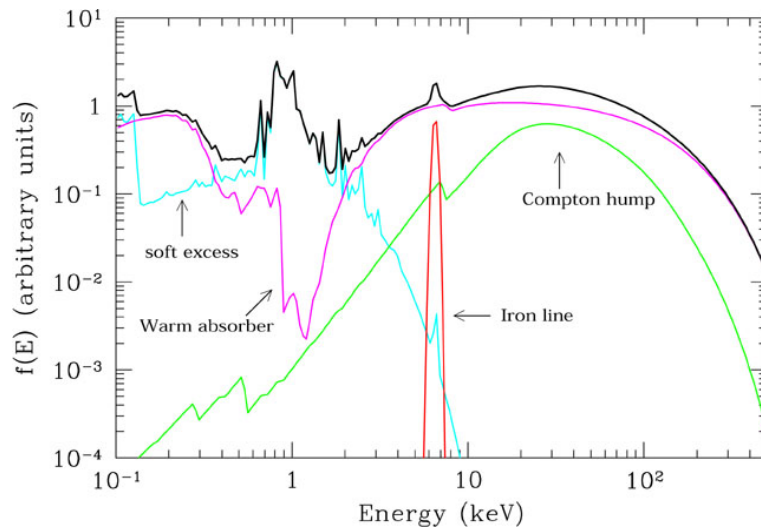


Figure 1.8 AGN X-ray spectral components for a type 1 AGN (Risaliti and Elvis, 2004).

range from a different kind of continuum emission (Porquet et al., 2004; Abramowicz et al., 1988) to atomic processes (Crummy et al., 2006; Middleton et al., 2007). Some AGN show a flattening of the spectral slope at high energies, consistent with a reflection component whether it comes from neutral or ionised reflection. An example of the typical components observed in a type 1 AGN X-ray spectra is shown in Fig. 1.8.

In the case of **type 2 AGN**, to measure the intrinsic photon index is more difficult due to the contribution of neutral absorption. Type 2 AGN usually show significant amounts of neutral absorption in their X-ray spectra so that, in low quality data, the measured photon index results to be flatter than for type 1 AGN when this absorption is not properly accounted for (see Fig. 1.3). As the amount of absorbing material increases, the X-ray continuum is more and more suppressed. If the intrinsic column density reaches values above 10^{24} cm^{-2} the direct continuum is completely suppressed below 10 keV and only reflected emission is observed, which usually amounts only to a few % of the direct emission. These AGN are called “Compton thick sources”. Type 2 AGN also display soft-excess emission, but in this case its origin is more clear. Recent works that make use of grating X-ray spectroscopy, resolved this emission into many emission lines consistent with photoionised clouds (Guainazzi and Bianchi, 2007). The location of this gas is likely the NLR, since its morphology observed in X-rays seems to be coincident with the one derived from high resolution O[III] images (Bianchi et al., 2006), extending from 0.1 to 1 kpc in some cases.

1.2.4.2 The Fe $K\alpha$ emission line

Another striking feature in AGN X-ray spectra is the Fe $K\alpha$ emission line. This line is produced via fluorescent emission when an electron in the K-shell of an Iron atom is pulled out by an X-ray photon. If the excited atom then decays by one of the L-shell electrons dropping to the K-shell, a line photon is emitted. The line central energy increases as the level of ionisation of Iron increases, from 6.4 keV for neutral Iron to 6.7 and 6.9 keV for highly ionised He- and H-like Iron. The relative abundance of Iron and its high fluorescent yield lead to a probability of seeing Iron fluorescent line emission much higher than for any other species. Other lines that can also be observed (but with lower intensities) are the Fe $K\beta$, Ni $K\alpha$, and Cr $K\alpha$ (at 7.06, 7.78, and 5.41 keV, respectively).

Narrow Fe $K\alpha$ emission is associated with emission far from the central engine and is accompanied by the corresponding reflection component. The line and reflection component characteristics can be used to estimate the origin, geometry and ionisation state of the reflecting material (Murphy and Yaqoob, 2009; Yaqoob et al., 2010). In heavily absorbed AGN, the Fe $K\alpha$ shows an extremely high equivalent width (EW, > 1 keV in most cases) as a result of the continuum suppression.

When this line is emitted close to the SMBH, in the accretion disk, its shape is expected to display relativistic effects. The line shows two peaks, due to Doppler effect, an enhancement of the blue peak, due to relativistic beaming, and a very broad red tail, due to gravitational redshift. From its relativistic shape, several important properties of the central engine can be obtained, such as the SMBH spin, the disk inclination angle and the disk inner and outer radii (see Fig. 1.9 and Fabian et al. 2000 for a review). Such relativistically broadened emission lines have been detected in a number of AGN but the line properties have only been constrained in a small number of cases (see Miller 2007 for a review). An example of real data for the most studied Fe $K\alpha$ relativistic line, the one observed in the Seyfert 1 galaxy MCG 6-30-15, is shown in Fig. 1.10.

1.2.4.3 Optical spectrum of AGN

Optical spectra of **type 1 AGN** show a blue continuum, very broad permitted emission lines, and narrow forbidden emission lines. The mechanism for line emission in the BLR and the NLR is believed to be photoionisation and then radiative recombination. A supporting evidence is, for example, the correlation between the continuum and the broad emission line variations. Whereas the physical conditions within the NLR are well reproduced by plasma physics diagnostics, the BLR structure and physical conditions are much more difficult to model. The BLR was usually represented by a spherical cloud of dense and hot gas stratified in density and temperature. However, this simple model is not able to reproduce the broad line shapes and line ratios. High ionisation and low

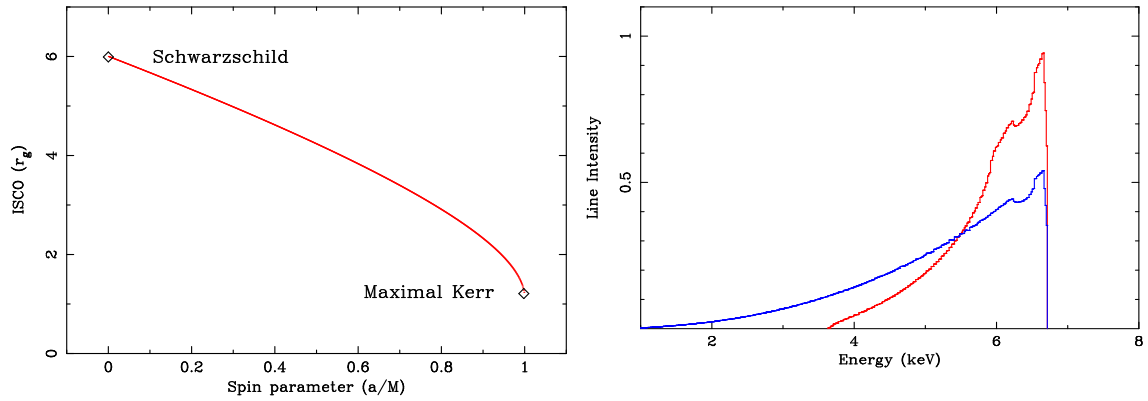


Figure 1.9 *Left*: Dependence of the inner disk radius on the SMBH spin. *Right*: Fe $K\alpha$ profiles for a non-rotating Schwarzschild black hole (red) and a maximum-rotating Kerr black hole (blue) (Miller, 2007).

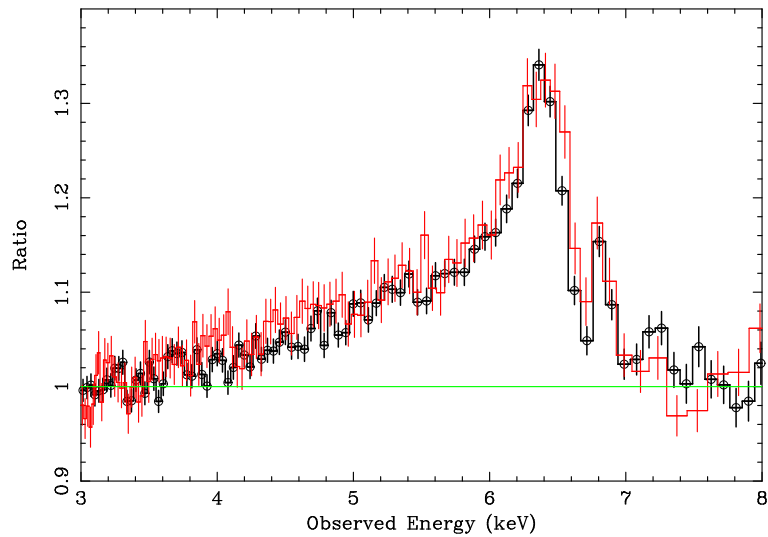


Figure 1.10 Real X-ray data from MCG -6-30-15 (Miller, 2007).

ionisation lines seem to arise from matter with very different properties, and the shape of some lines seems to be composed of emission from different regions. Current models assume that the BLR is indeed composed by a number of clouds of high density and temperature (see [Gaskell 2009](#) for a review).

As the intervening absorption increases, the intermediate AGN types appear. Type 1.2 AGN show both narrow and broad permitted lines, the latter dominating the emission. Type 1.5 AGN also show broad and narrow permitted lines but the broad lines are less intense than for type 1.2 AGN. Types 1.8 and 1.9 AGN correspond to an optical spectrum for which very weak or not broad $H\beta$ line is present, respectively. Finally, **type 2 AGN** only show narrow permitted and forbidden emission lines ([Osterbrock, 1989](#)).

There are also some cases in which a low luminosity AGN nucleus is outshined by the starlight from the host galaxy. It can also happen that a luminous nuclear starburst may hide the nuclear emission. In those cases, the existence of an AGN at their centres and the intervening absorption is inferred from observations at other wavelengths.

Some AGN, RL type 1.5 AGN preferentially, show broad permitted lines that display a double-peaked profile. These are called “double-peaked emitters”. The origin of the double-peaked broad line emission is unclear. Several explanations have been proposed: a binary SMBH ([Gaskell, 1983](#)), a biconical outflow of matter ([Zheng et al., 1990](#)), a collection of anisotropically illuminated clouds ([Wanders et al., 1995](#)), and emission from the accretion disk ([Chen and Halpern, 1989](#)). However, all of these models fail to reproduce one or more of the observed line characteristics.

1.2.4.4 The Balmer decrement

Among the emission lines in AGN optical spectra, the Hydrogen Balmer lines are the most relevant at low redshifts. The likelihood of any of the Balmer series transitions is determined by atomic physics, so that the ratios between the intensities of these lines are known and they are called **Balmer decrements**. This name refers to the decreasing intensity from H_α to H_β to H_γ and so on. Assuming case-B recombination and optically thin photoionised plasma ([Osterbrock, 1989](#)), the intrinsic Balmer decrement corresponding to the H_α to H_β ratio is $R_{int}=2.87$. This value is found in HII regions, which have typical densities $\sim 10^4 \text{ cm}^{-3}$ and temperatures $\sim 10^4 \text{ K}$. However, given the different conditions within the BLR and the NLR (higher densities and temperatures, and a harder ionising continuum), different values are expected in these cases. For the NLR, a value of $R_{int}=3.1$ is usually adopted. The larger value is caused by the contribution of collisional excitation (and the presence of a partially ionised region) to the H_α emission ([Gaskell and Ferland, 1984](#)). In the case of the BLR, the high

density makes the collisional, optical-depth and radiative-transfer effects no longer negligible (Baldwin, 1997). As a result, a higher value for R_{int} is obtained (from 3.2 to 3.5 depending on the author). A value of $R_{int} = 3.4$ (from Carrera et al. 2004 and Ward et al. 1988) is adopted for the BLR throughout this thesis work.

However, when studying real sources, these ratios vary from source to source sometimes reaching very high values (> 10). The usual explanation is dust-reddening. Micron-sized dust grains absorb the optical emission and this absorption depends on the wavelength of the radiation. This is called “reddening” because bluer light is more absorbed than redder light so that the absorbed spectra looks redder. It also affects the Balmer ratios by increasing their values. The amount of absorbing gas can be derived from the measured Balmer ratios by making some assumptions.

Assuming a standard interstellar extinction curve (Osterbrock, 1989), the colour excess can be expressed as

$$E(B - V) = a \log \frac{R}{R_{int}} \quad (1.10)$$

where R_{int} is the intrinsic Balmer decrement, R is the measured Balmer decrement, and a is a constant that depends on the Balmer lines in use. For the $H\alpha$ to $H\beta$ ratio, $a=2.07$.

Assuming a standard Galactic gas-to-dust ratio, the absorbing column density, N_H can be derived. In the case of the work presented by Bohlin et al. (1978), the resulting correlation is

$$N_H(\text{cm}^{-2}) = 5.8 \times 10^{21} E(B - V) \quad (1.11)$$

This value can be then compared to the one obtained by X-ray spectroscopy.

1.3 Goals of the Thesis

The subject of this thesis work is the study two of the still open and much relevant issues about AGN physics: AGN unified models and Fe $K\alpha$ emission.

1.3.1 Testing unified models

As discussed in Sect. 1.2, although unified models are supported by most of the observations, the existence of deviations from these models calls for further investigations. The proposed strategy of this thesis work is to study the “variability explanation” for the AGN optical/X-ray mismatches. To this end, we selected a small sample of AGN that have been shown to vary in their optical spectral type over time. We observed them simultaneously in the optical (by using ground-based telescopes) and in X-rays (by using the XMM-Newton X-ray

observatory). Besides their change in the optical spectral type, the selected AGN must fulfil other requirements. They must be bright enough in X-rays so that a short (10 ks to 30 ks) X-ray observation would be sufficient to accurately measure their intrinsic hydrogen column densities. This also imposes some constraints on the *XMM-Newton* visibility window. They also have to be simultaneously observable at both wavelengths.

The proposed test to the unified models is to compare the amount of X-ray absorption (obtained by fitting the X-ray spectra) with the optical reddening (obtained from the Balmer decrement of the optical emission lines).

The studied sample is composed of 4 sources: Mrk993, Mrk 1018, NGC 7603 and Mrk 6. Observational proposals were submitted to *XMM-Newton* and to ground-based telescopes in a coordinated way, so that both observations for each AGN were carried out as much as two days apart from each other. For Mrk 1018 and Mrk 6, a second optical observation was performed about 1 month later than the first one. This was done to search for optical variability in short-time scales. This variability could be caused by a time lag between the X-ray and the BLR emission due to the distance between both emitting regions. The results of the observational campaigns and data analysis are presented in Chapter 3.

1.3.2 Constraining the Fe $K\alpha$ emission

As mentioned in Sect. 1.2, although being the most common feature in X-ray spectra, how common Fe $K\alpha$ emission is and its properties are still unknown at medium to high redshifts.

In order to search for Fe line emission in distant AGN and then study its shape, we compiled as many X-ray AGN spectra as possible covering a wide range in redshifts and luminosities. AGN must be identified by optical spectroscopy, which has proved to be the most reliable way of obtaining cosmological redshifts. Then, a new method is developed to average all the spectra minimising any spurious contamination in order to identify and quantify the most relevant features and to study their dependence on the source properties. This method is tested by the extensive use of simulated data.

The samples used in this work, the development of the method and the results are presented in Chapter 4. Finally, in Chapter 5 we summarise the conclusions achieved in this work.

CHAPTER 2

X-ray data

Contents

2.1 X-ray observations	27
2.2 XMM-Newton	29
2.2.1 Spacecraft	31
2.2.2 X-ray Mirrors	31
2.2.3 Instruments	33
2.3 Data reduction	35
2.3.1 Pipe-line processing	36
2.3.2 Spectral extraction	37
2.4 Spectral analysis	43
2.4.1 Spectral models	44

In this chapter the main tools and methods to reduce and analyse X-ray spectra are presented.

In Sect. 2.1, a brief description of the history of observational X-ray astronomy and main results is presented. In Sect. 2.2, the X-ray observatory XMM-Newton, from which our data have been obtained, is described. In Sects. 2.3 and 2.4, the Science Analysis Software (SAS) used in data reduction and the XSPEC software used in spectral fitting are presented, along with the fundamentals of the spectral models used.

2.1 X-ray observations

X-rays observations are limited to rockets and satellites due the Earth atmosphere's lack of transparency in the X-ray energy band (below 100 keV, see Fig. 2.1). Even under these circumstances, after World War II it was already known that the Sun emits in X-rays. However, X-ray astronomy did not properly begin until the 1960s, when an American team led by Nobel laureate Riccardo Giacconi launched a rocket with the aim of measuring X-ray emission coming from the Moon. This team finally did not detect Moon emission but something unexpected and much more interesting. They discovered X-ray emission coming from a source in the constellation of Scorpius (named Sco X-1 afterwards) and,

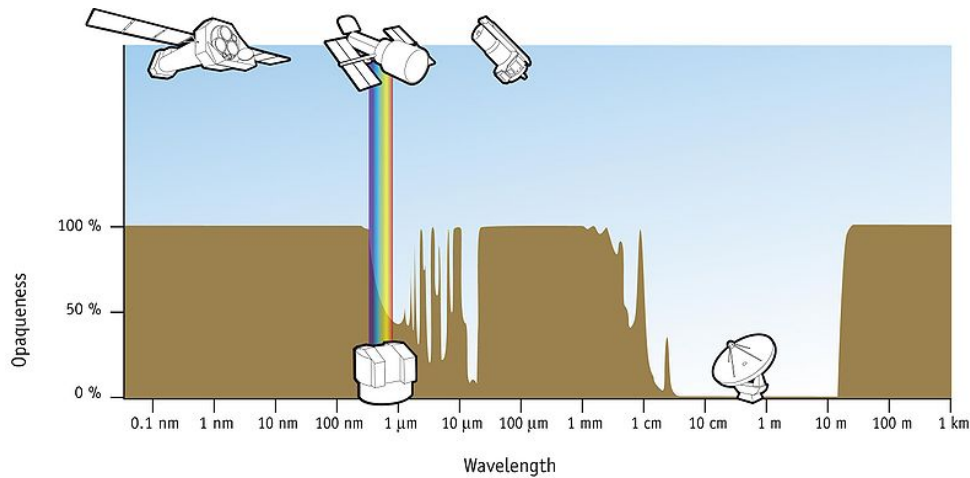


Figure 2.1 Earth atmosphere opacity as a function of wavelength. Copyright 2009© NASA (Space Telescope Science Institute) and ESA (Hubble European Space Agency Information Centre under Contract NAS5-26555).

moreover, diffuse X-ray emission coming from all directions in the sky. This was surprising, since they expected fluxes from celestial sources further than the Sun to be too low to be detected. A new class of stellar system had been discovered (an X-ray binary) and new physical processes had to be invoked in order to explain it. X-ray astronomy had begun.

Since then, a number of X-ray missions have been launched in order to study X-rays from outside our Solar system. Thanks to them, we know today that X-ray emission is ubiquitous among all classes of objects. The first satellite entirely dedicated to celestial X-ray astronomy was Uhuru (NASA, 1970-1973). Uhuru (also known as Small Astronomical Satellite, SAS-1) performed the first uniform all-sky survey cataloguing 339 sources and discovering the diffuse emission from clusters of galaxies. From UHURU data it was also found that the X-ray emission from binary X-rays sources must come from material infalling onto massive compact sources such as neutron stars or black holes. A few years later, the first fully imaging X-ray telescope was launched: EINSTEIN (NASA High Energy Astrophysical Observatory 2, HEAO-2, 1978-1981). Its unprecedented sensitivity and imaging capability allowed for the first time to carry out medium and deep surveys, discovering a large number of serendipitous sources, and to study X-ray sources in both a spectroscopic and morphological way. During the 1980s, other missions were launched with the aim of studying known sources. One of them was EXOSAT (ESA, 1983-1986) which allowed, in particular, the study of variability in X-ray sources due to its long orbital period.

In the 1990s, ROSAT (A Germany/US/UK collaboration, The Roentgen Satellite, 1990-1999) completed, for the first time and with a sensitivity 1000 times better

than that of UHURU, an all-sky imaging survey in the soft X-ray band (0.1-2.5 keV) cataloguing ~ 150000 objects. Also launched in the 1990s, the ASCA satellite (Advanced Satellite for Cosmology and Astrophysics, Japan/US, 1993-2001) allowed for the first time to perform X-ray spectroscopy with a good spectral resolution thanks to its CCD detectors, the first to be used in a X-ray satellite. One of the discoveries facilitated by ASCA data was the existence of broad relativistic Fe emission lines, probing the strong gravity regime near black holes. Two years after ASCA, RXTE (NASA, Rossi X-ray Timing Explorer, 1995 to present) was launched. The main goal of this mission is to observe X-ray variability in a wide energy band and with moderate spectral resolution. This mission permitted the study of Gamma Ray Burst (GRB) afterglows and the more accurate measurement of their origin, which could not be done by using gamma-ray observatories. This also was performed by BeppoSAX (Italy/Netherlands, 1996-2002), delivering position for GRBs with errors of the order of arc minutes, the most accurate at the time. Thanks to the broad energy range covered by BeppoSAX instruments, broad band X-ray spectroscopy with moderate spectral resolution was possible for the first time.

On 1999, Chandra (NASA, Advanced X-ray Astrophysics Facility – AXAF, later renamed in the honour of Subrahmanyan Chandrasekhar, 1999 to present) and XMM-Newton (ESA, X-ray Multi-Mirror Mission, 1999 to present) were both launched. Both constitute the best X-ray missions built to date. Chandra has an unprecedented angular resolution ideal to perform high quality imaging. XMM-Newton has a larger effective area, the largest to date, thus more appropriate to perform spectroscopy over faint X-ray sources.

Two more satellites carrying X-ray telescopes were launched only a few years ago: SWIFT (NASA/UK/Italy, 2004 to present) and Suzaku (Japan/US, 2005 to present). SWIFT is designed to study GRBs, but as it observes the sky, it also performs a hard X-ray survey. Suzaku is an X-ray mission that covers a broader energy range than Chandra and XMM-Newton but it has a smaller effective area.

2.2 XMM-Newton

The X-ray data used during this thesis work come from observations performed by XMM-Newton, the ESA X-ray Multi-Mirror Mission. XMM-Newton was launched by an Ariane 504 on December 10th 1999 as the second of “cornerstone” missions defined in ESA’s Horizon 2000 programme.

Most of the observing time on XMM-Newton is “Open time”, i.e., observations can be requested by any observer during the annual call for proposals. These proposals are then evaluated and selected as a function of their potential scientific



Figure 2.2 Artist's impression of XMM-Newton (ESA/Ducros). Copyright 2009© European Space Agency. All rights reserved.

output. The XMM-Newton Science Operations Centre (SOC)¹, located at the European Space Astronomy Centre (ESAC) in Villafranca (Madrid, Spain) is responsible for the XMM-Newton science operations from the reception of the proposals to the delivery of calibrated data to the observers. In addition, the Survey Science Centre (SSC)², a consortium of 10 institutes within the ESA member states, is in charge of the construction of the *XMM-newton* Serendipitous Source catalogue³, the largest X-ray source catalogue ever produced. The SSC also collaborates with the SOC in the pipe-line processing of the data and in the development of the science analysis software.

XMM-Newton is describing a highly elliptical orbit with a period of about 2 days, with a apogee/perigee of $\sim 115000/6000$ km, which allows long uninterrupted exposure times. Its three sets of X-ray mirrors provide XMM-Newton with the largest effective area ever achieved in current or past X-ray imaging missions. Among the scientific instruments it carries, there are three CCD cameras (The European Photon Imaging Camera – EPIC), two grating spectrometers (the Reflection Grating Spectrometers – RGS), and an optical/UV telescope (the Optical Monitor – OM), the first flown on a X-ray observatory, which allows simultaneous photometric observations in the optical/UV and X-ray band. All XMM-Newton instruments operate simultaneously. The data used in this Thesis come from the EPIC instrument.

2.2.1 Spacecraft

The XMM-Newton satellite is composed of four modules (see Fig. 2.3): **The Focal Plane Assembly**, containing the focal-plane scientific instruments: two Reflection Grating Spectrometer (RGS), one EPIC-pn and two EPIC-MOS imaging detectors; **The Telescope Tube**, with a length of 6.8 m and composed of two halves; **The Mirror Support Platform**, carrying the three mirrors assemblies, the Optical Monitor (OM) and the two star-trackers; and **The Service Module**, which carries the spacecraft subsystems and associated units, the two solar-array wings, the sun shield and the antennas.

2.2.2 X-ray Mirrors

The three mirror assemblies are each one composed of 58 nested Wolter I grazing-incidence mirror pairs. They are designed to perform X-ray imaging maximising the effective area over the full covered energy range and specially around 7 keV, the rest-frame energy range for the Fe K α emission line (see Fig. 2.4).

¹<http://xmm.esac.esa.int/>

²<http://xmmssc-www.star.le.ac.uk/>

³<http://xmmssc-www.star.le.ac.uk/Catalogue/2XMM/>

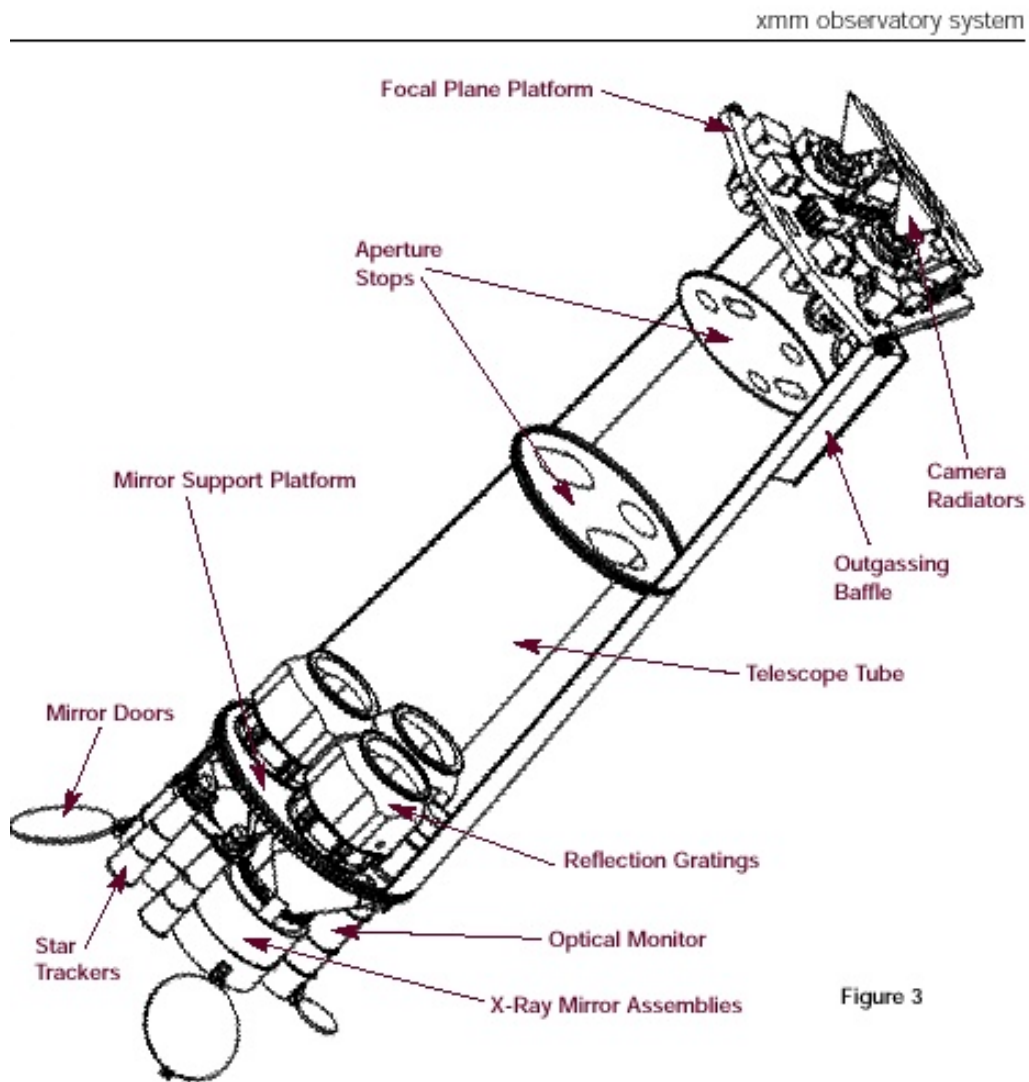


Figure 2.3 Schematic design of XMM-Newton spacecraft. Copyright 2009© European Space Agency. All rights reserved.

X-rays cannot be focused by normal refraction using lenses or reflection, as in the optical band, due to their high penetrating power. Instead, grazing incidence is used, i.e., X-rays are focused by reflection under small angles of incidence (Trümper and Hasinger, 2008, Chapter 6). Three basic types of two-mirror systems were proposed by Hans Wolter in 1952: Wolter I and Wolter II, composed by a paraboloid and a hyperboloid and Wolter III, using a paraboloid and an ellipsoid. XMM-Newton mirrors, as most of the current X-ray astronomy telescopes, follow the Wolter I configuration with a focal length of 7.5 m.

The three light beams coming from the three X-ray telescopes are directed to 5 different instruments: the EPIC-pn camera, the two EPIC-MOS cameras and the two RGS. For one of the telescopes, all the light is focused on the EPIC-pn camera, see Fig. 2.5 for the light path. For each of the remaining two, about half of the incident flux is diverted by the RGS gratings towards one of the RGS detectors and approximately the other half to one of the EPIC-MOS.

2.2.3 Instruments

The scientific instruments on board of XMM-Newton are the EPIC camera (composed of three CCD detectors) the two RGS detectors and the detectors for the OM. The detectors main characteristics are listed in Table 2.1. Each of these detectors works independently at the same time during an standard observation.

- **EPIC camera** The EPIC camera is composed of three CCD arrays, two of them using Metal Oxide Semi-conductor CCDs (EPIC-MOS1 and EPIC-MOS2, six CCDs each) and the other one using pn CCD (EPIC-pn, nine CCDs). This camera is able to perform high sensitive imaging observations in the 0.15-15 keV range with moderate spectral and angular resolution. It also includes a filter wheel comprising three different filters named Thin1, Medium and Thick. These filters are designed to block photons from the IR, visible and UV, since the CCD detectors are sensitive also at those wavelengths. Since EPIC CCDs operate in photon counting mode, the resulting data has the form of tables containing position, time and energy information per received event. In this way and from a single observation, images, spectra and light curves can be obtained. There are different science modes, with different FOVs and time resolutions, depending of the window size: full frame, partial window and timing mode. For the full window imaging mode, with a FOV of $\sim 30'$ in diameter, besides the intended target, about 50-200 “serendipitous” sources are detected. This means that data can also be extracted for these serendipitous sources thus maximising the scientific output of each observation. This is the instrument used to obtain the data used in this Thesis.
- **RGS** Each RGS unit consists of an array of reflection gratings which diffract the X-rays to a stripe of nine CCD detectors. The RGS are designed to per-

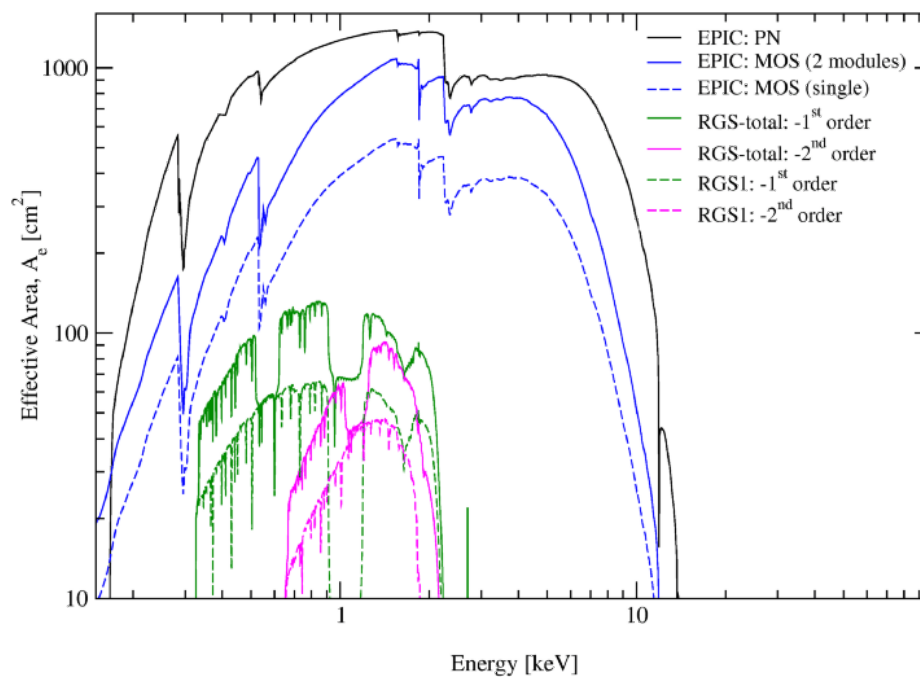


Figure 2.4 The net effective area of all XMM-Newton X-ray telescopes, EPIC and RGS (from "XMM-Newton Users Handbook", Issue 2.9, 2011. ©ESA: XMM-Newton SOC).

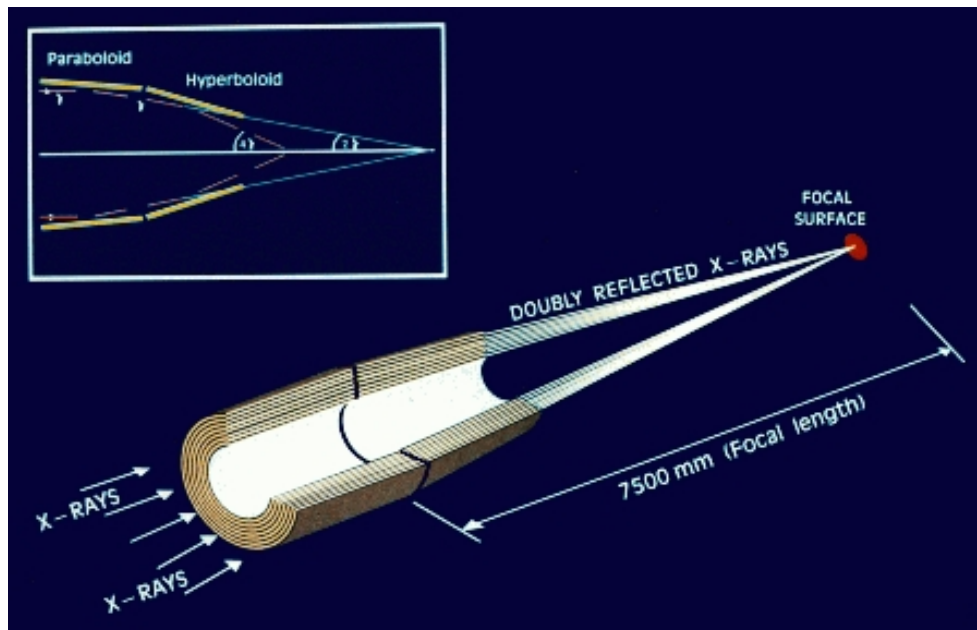


Figure 2.5 Light path for the EPIC-pn camera on board of XMM-Newton. Copyright 2009© European Space Agency. All rights reserved.

form high spectral resolution in the 0.35-2.5 keV energy band.

- **OM** The OM telescope is a 30 cm Ritchey-Chretien telescope with a focal length of 3.8 m. The OM instrument consists of two redundant filter wheels with 6 broad band filters (3 in the optical and 3 in the UV band) and two gratings (UV and optical), and two redundant CCD detectors.

2.3 Data reduction

X-ray data reduction was carried out by using the Science Analysis Software (SAS)⁴. SAS consists of a collection of tasks, scripts and libraries designed to reduce and analyse XMM-Newton data and developed jointly by the Science Operations Centre (SOC) and the Survey Science Centre (SSC).

The X-ray data used in this thesis work come from the EPIC camera, so the discussion in this section is restricted to EPIC pipe-line and EPIC data reduction tasks.

⁴<http://xmm.esac.esa.int/sas/current/howtouseas.shtml>

Table 2.1 XMM-Newton instrument characteristics

Instrument	EPIC – MOS	EPIC – pn	RGS	OM
Bandpass	0.15 – 12 keV	0.15 – 15 keV	0.35 – 2.5 keV	180 – 600 nm
OTV	5 – 135 ks	5 – 135 ks	5 – 135 ks	5 – 145 ks
Sensitivity ⁽¹⁾	$\sim 10^{-14(2)}$	$\sim 10^{-14(2)}$	$\sim 8 \times 10^{-5(3)}$	20.7 mag
FOV	30'	30'	5'	17'
PSF(FWHM/HEW)	5''/14''	6''/15''	N/A	1.4''/2.0''
Pixel size	40 μ m (1.4'')	150 μ m (4.1'')	81 μ m (9×10^{-3} Å)	0.476513''
Timing resolution	1.75 ms	0.03 ms	0.6 s	0.5 s
Spectral resolution	~ 70 eV	~ 80 eV	0.04/0.025 Å	350

OTV: Orbital target visibility, total time available for science per orbit. FOV: Field of view.

(1): After 10 ks. (2): In units of $\text{erg cm}^{-2} \text{s}^{-1}$. (3): OVII 0.57 keV line flux in $\text{photon cm}^{-2} \text{s}^{-1}$ for an integration time of 10 ks.

2.3.1 Pipe-line processing

The sets of data that are made available for the observer after a successful observation are:

- **The observation data files (ODF)**, that contain the raw data corresponding to each instrument, instruments' housekeeping files and files related to the conditions during the observations.
- **The pipe-line products (PPS)**, that include images and exposure maps in different bands, source lists and the calibrated event lists for each EPIC detector and exposure.

The most relevant EPIC files contained in the pipe-line products are the following:

- Images for each detector and exposure in the following energy bands: 0.2-0.5 keV (band 1), 0.5-2.0 keV (band 2), 2.0-4.5 keV (band 3), 4.5-7.5 keV (band 4), 7.5-12.0 keV (band 5) and the full 0.2-12.0 keV energy band (band 8).
- Exposure maps in the different energy bands, which contain the angular efficiency of the instruments after taking into account spatial quantum efficiency, filter transmission, mirror vignetting, and field of view.
- Sensitivity map, which contains the point source detection upper limits, in units of count rate.

- Detection masks obtained from the images and representing the sky area used in source detection.
- Source lists containing the X–rays sources on the observation detected above a certain likelihood threshold.
- Calibrated event lists, which are FITS tables with angular, time and energy information for each registered event at each CCD. From the calibrated event lists, images, spectra and light curves can be extracted by filtering in spatial coordinates, energy or time, respectively. The tasks used during the pipe-line process to construct the calibrated event lists are `epchain` (for EPIC-pn) and `emchain` (for EPIC-MOS), which in turn, are composed of individual tasks. If the reduction process has to be started from the ODFs, the pipe-line process can be reproduced by the observer by using the same tasks. Both `epchain` and `emchain` perform similar sub-chain loops over all CCDs, performing event selection and calibration in time and energy. They also identify the patterns of the events, i.e., a number representing the number of pixels in which an event is distributed and the way it is distributed.

A set of calibration files is also needed in order to reduce the data. These calibration files and the analysis software are periodically updated, so, in the case of significant changes being produced since the observation date, the observer is advised to start the reducing process from the ODFs.

2.3.2 Spectral extraction

Two different extraction processes were used in this thesis work. The first one, a manual process, was used to extract the X–ray spectra of the Seyfert galaxies presented in Chapter 3. The second one, a semi-automated process, was used in order to extract the X–ray spectra of the serendipitous sources in the AXIS (An International XMM-Newton Survey) and in the XWAS (XMM-2dF Wide Angle Serendipitous Survey) surveys presented in Chapter 4.

2.3.2.1 Manual process

In this case pipe-line produced event lists are used. The main steps in the process are as follows:

1. **Filtering high background intervals:** Since XMM-Newton orbit crosses the Earth radiations belts, a certain amount of the exposure time during an observation can be affected by high background intervals, i.e., periods or major incidence of low energy protons. In order to identify these periods and filter them out, a light curve is extracted for each exposure by using the SAS task `evselect`. This task performs event selection over event lists according to a number of input parameters which refer to columns in the table. Since the purpose is to identify events that are actually due to particles and not

to X-rays, high energy single events are selected ($E > 10$ keV, `PATTERN == 0`). After a visual inspection of these light curves, the time intervals showing count rates values lower than a certain value (0.4-1.5 depending on the source and the quality of the observation) are selected and then used to filter the event lists, again using `evselect`, resulting in “clean” event lists.

2. **Source and background regions:** Once the clean event lists are extracted, images in the full 0.2-12 keV energy range are produced. To do that, `evselect` is used by selecting all events corresponding to those energies and with a certain pattern selection depending on the EPIC camera: single, double, triple and quadruple events for EPIC-MOS (`PATTERN <= 12`) and only single and double for the EPIC-pn (`PATTERN <= 4`). The source and background regions are selected, by visually inspecting these images, as circular regions, taking into account that the background region should be in a source free region and its resulting “backscale” size at least two times the source region size in order to allow a better background subtraction. The “backscale” is a measure of the region solid angle taking into account the CCD gaps and bad pixels within the extraction region.
3. **Spectral extraction:** The previous source and background regions are fed into `evselect` in order to accumulate all the events per energy channel within those regions thus obtaining source and background spectra. Additional filters are also applied during the spectral extraction to improve the spectral quality: `#XMMEA_EM` for the MOS and `FLAG == 0` for the pn.
4. **Response matrices:** The next step is to produce the calibration response matrices. Spectral fitting requires, in addition to the source and background spectra, a file containing a characterisation of the EPIC detector response. In the case of *XMM-Newton* that can be obtained as the product of the Redistribution Matrix File (RMF) times the Ancillary Response File (ARF). The RMF matrix, created by using the SAS task `rmfgen`, describes the spectral dispersion as a function of energy and channel. The ARF, created by using `arfgen`, contains the effective area as a function of energy. Both RMF and ARF depend on the extraction region so they must be extracted for each single spectrum.
5. **Checking for pile-up:** In the case of bright sources, as the Seyfert galaxies studied in Chapter 3, the detector can interpret as an individual event all photon incidences in the same pixel during a read-out CCD cycle. As a result, the interpreted energy of this “event” is registered as the sum of the individual energies of the actual events. This is called photon pile-up. A significant pile-up contribution can be avoided by shortening the read-out time. That was done for the Seyfert galaxies discussed on Chapter 3 by reducing the EPIC window sizes during the observations. Besides, the pile-up fraction was evaluated after the observations by using the SAS task `epatplot`. This

task performs pattern statistics over an observation and compares it with the expected pattern distribution. By using that, the pile-up fraction for our Seyfert galaxies was estimated and found to be insignificant.

6. **Merging spectra:** In the case that MOS 1 and MOS 2 observations were performed with the same filter, spectra from both instruments can be added in order to improve the signal to noise ratio (SNR) in the resulting spectra. This process is carried out as follows: Source and background counts are added together separately simply by adding the counts at each corresponding channel. To scale the resulting added source and background spectra properly, the exposure times are summed and the backscals weighted with the corresponding exposure times as follows:

$$SET = SET1 + SET2 \quad (2.1)$$

$$BET = BET1 + BET2 \quad (2.2)$$

$$SB = \frac{SB1 * SET1 + SB2 * SET2}{SET} \quad (2.3)$$

$$BB = \frac{BB1 * BET1 + BB2 * BET2}{BET} \quad (2.4)$$

where: SET, SET1 and SET2 are the exposure times corresponding to the resulting source spectrum, and each of the input source spectra; BET, BET1 and BET2 are the exposure times for the resulting background spectrum and each input background spectra; SB, SB1 and SB2 are the backscals of the resulting source spectrum and each of the input source spectra; BB, BB1 and BB2 are the backscals of the resulting background spectrum and each input background spectrum. To obtain the response matrix corresponding to the resulting added spectra, two FTTOOLS⁵ are used: `marfrmf`, that multiplies the RMF and the ARF in order to obtain a single response matrix for each input source spectrum, and `addrmf`, that adds together the two single response matrices for the two input source spectra.

2.3.2.2 Semi-automated process

New sets of refinalised ODFs were made available for the observations used to construct the AXIS and XWAS samples presented in Chapter 4. Therefore, instead of using pipe-line products, the tasks `epchain` and `emchain` were run over these new ODFs in order to obtain calibrated event lists for each exposure and detector. In the case of the AXIS sample, new observations performed since the definition of the sample were also added and the reduction was performed as well from the new ODFs.

⁵http://heasarc.gsfc.nasa.gov/ftools/ftools_menu.html

In this case the extracting process is significantly different from the manual process described previously. On the one hand, the sources in the AXIS and XWAS samples are serendipitous sources, which implies for most of them a small number of counts in their spectra and therefore, the need for a more careful background subtraction. This cannot be achieved in an fully automated way. On the other hand, both samples are composed of a large number of sources, some of them with more than one XMM-Newton observation, which discards manual spectral extraction. An intermediate approach was selected, the main steps being as follows:

1. **Filtering high background:** As in the manual process, light curves are extracted for each exposure and instrument. However, instead of individually inspecting each light curve, Good Time Interval (GTI) tables are automatically created via the SAS task `tabgtigen` by selecting an upper limit of 0.4 counts per second above 10 keV in the count rate. These GTI tables are then used to filter the event list via `evselect`.
2. **Source lists:** In the case of the AXIS sample and the sky fields for which new observations were added resulting in more than one observation of the same field, the old source lists used to define the sample were improved in the following way:
 - (a) Combined EPIC-pn images, detection masks and exposure maps of all the observations in different energy bands were created by using `emosaic`, the SAS task designed to add EPIC images.
 - (b) A preliminary source list is created using the previous files and the SAS task `eboxdetect`, a source detection task. First `eboxdetect` is run in local mode, which means that the source detection is performed by searching for excess counts over the background by using a box that slides over the images and taking into account the exposure maps.
 - (c) The resulting source list is used as input to `esplinemap` to create a background map for each energy band by masking out the sources in the input source list.
 - (d) The source list obtained from `eboxdetect` run in local mode, the background maps, exposure maps and images are introduced to `eboxdetect` that is run this time in map mode. In map mode, the source detection is performed by taking into account the local background maps, which results in an improvement of the detection sensitivity.
 - (e) The final source list is created by using `emldetect`. This task performs a source detection algorithm based on maximum likelihood PSF fits to the source counts distribution by using the images, exposure maps and background maps in the different X-ray bands.

Since not all the sources in the source lists are observed in all EPIC detectors during the same observation (a source detected in the EPIC-pn data could

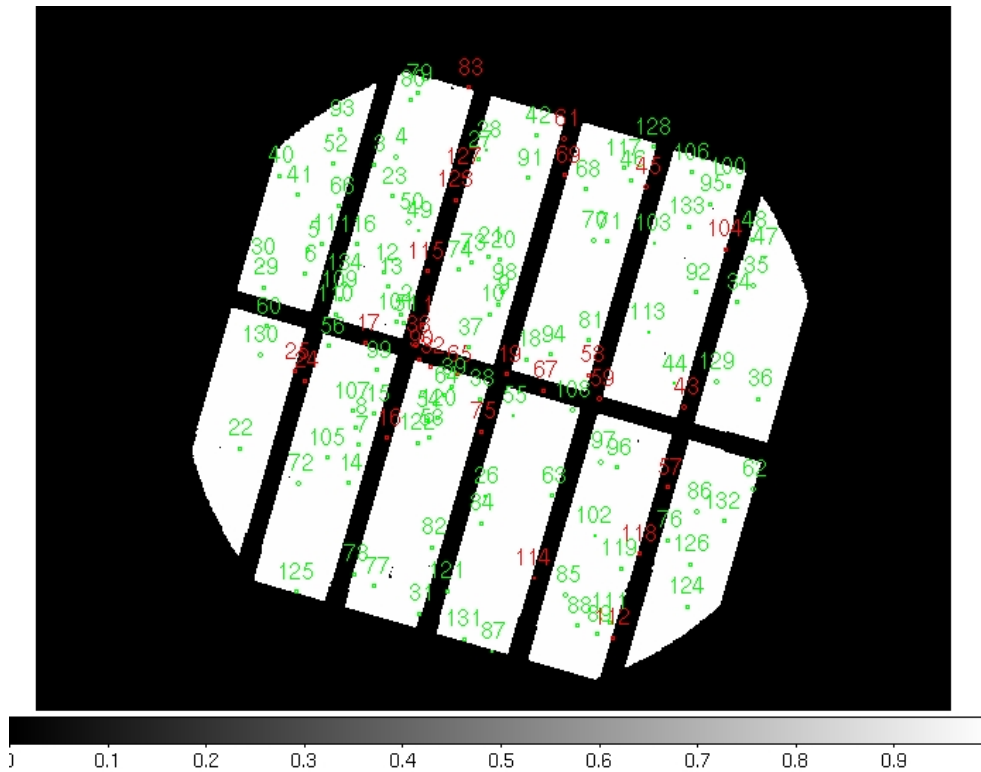


Figure 2.6 An example of source masking corresponding to an AXIS field and EPIC-pn camera. Sources in red are filtered out from the source list due to the source position falling in CCD gap or out of the FOV.

fall within a MOS gap or out of the MOS field of view, for example), for each exposure, camera and observation a source extraction list is created by removing the sources whose spectra can not be extracted in that case (see Fig. 2.6).

3. **Source and background regions** As a first approximation, source and background regions are created by using the SAS task `region`. This task uses the source list to create source and background regions in the following way: circular source regions are created with radii depending on the encircled energy fraction (a 80% was selected in our case) and background regions as annuli centred at the source position with inner radius the source region radius and outer radius three times that value. `region` also creates “holes” in the background regions in the case of other sources fall within these area (see Fig. 2.7). These regions are then optimised via the SAS task `eregionanalyse`. This task uses the source and background region and the exposure maps to optimise the source region centre and radius so as to maximise the SNR. Finally, source and background backscales are checked in order to prevent background regions from being too small.

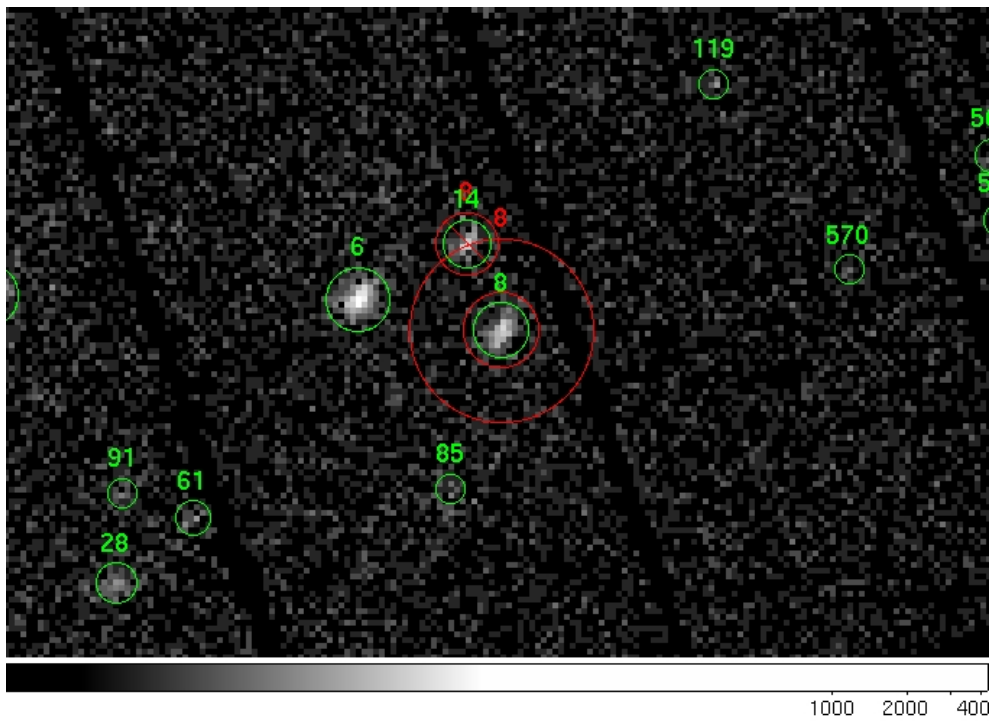


Figure 2.7 An example of source and background region. Green regions correspond to optimised source extraction regions. Red region correspond to the constructed background region for source numbered 8.

4. **Spectral extraction and response matrices** are extracted for each source, camera, exposure and observation in the same way as it is described for the manual process.
5. **Merging spectra:** For each observation, MOS 1 and MOS 2 data corresponding to the same source are merged together, if filters are the same, following the process described for the manual process. In the case of different observations, the same method is used for spectra corresponding to the same source, EPIC camera and only if the observations have been performed with the same filter and the source falls within the same CCD at a similar off-axis angle.

2.4 Spectral analysis

In order to fit the extracted X-ray spectra, XSPEC software was used. XSPEC was developed at Cambridge University as a mission-independent general analysis program for X-ray spectral data (Arnaud, 1996). XSPEC manipulates theoretical models, X-ray source and background data, and calibration data. Before entering the data, the X-ray spectra are grouped into a certain minimum number of counts per energy bin. Since X-ray spectra are in counts per channel, a minimum number of 20 source plus background counts should be selected in order to be able to use χ^2 minimisation technique which requires Gaussian statistics. In the case of XMM-Newton data, the input files for XSPEC are as follows:

- Grouped source spectrum: a FITS file containing four columns: energy channel, number of counts, quality and grouping. The quality and grouping columns are introduced during the grouping process and give XSPEC the necessary information to use this grouping during the spectral fit.
- Background spectrum: FITS file corresponding to the extracted background spectrum. In this case, only the columns corresponding to energy channel and counts are necessary since the information about the grouping is already contained in the source spectra. XSPEC performs a background subtraction by using these two spectra and assigns error bars assuming Poisson statistics.
- Calibration files: these files contain the detector response, which is proportional to the probability that an incoming photon of energy E will be detected as a count in channel I . In our case, the detector response is the product of the RMF and ARF matrices.

The input spectrum – expressed in counts per channel $C(I)$ – does not represent the actual incident spectrum – in monochromatic photon flux as a function of energy $f(E)$ – but the incident spectrum after entering the detector and therefore modified by the detector response $R(I, E)$:

$$C(I) = \int_0^{+\infty} f(E)R(I, E)dE \quad (2.5)$$

Since this equation cannot be inverted in an analytical way, a spectral fit is used. A model spectrum $M(E)$, usually described in terms of a few parameters, is selected and a predicted $Cp(I)$ is computed and compared to the observed $C(I)$. The fit statistic used to compare $C(I)$ and $Cp(I)$ is χ^2 . In this way, the model parameters are varied so as to minimise the χ^2 value of the fit:

$$\chi^2 = \sum \frac{(C(I) - Cp(I))^2}{\sigma^2(I)} \quad (2.6)$$

where $\sigma(I)$ is the error for channel I estimated by Poisson statistics.

A “rule of thumb” for a good fit is to obtain a value of the reduced χ^2 ($\chi^2/\text{d.o.f}$, where d.o.f is the number of degrees of freedom) close to 1. To obtain the errors in the model parameters, their values are varied until a certain $\Delta\chi^2$ is reached. In the case of errors at 90% confidence level for one varying parameter, for example, the tabulated value for the critical $\Delta\chi^2$ is 2.71.

2.4.1 Spectral models

Several spectral models have been implemented in XSPEC in order to fit X-ray spectra taking into account the physical process that may take place (see Sect. 1.2.2). In this section only the models that have been used in our spectral analysis are summarised. In the case of models that include redshift effects, the model parameters refer to their rest-frame values.

There are different kinds of models according to the way they have to be used: additive models (`powerlaw`, `gauss`, `Laor`, `diskline`, `pexrav`), multiplicative models (`phabs`, `pcabs`, `edge`, `absori`, `siabs`, `xion`, `swind1`), and convolution models (`kdblur`). Beyond these models there is also another kind of model called “table model”. This kind of model can be additive, multiplicative or a convolution but they do not have an analytical form. A table model is a file that contains a N-dimensional grid of model spectra, for a model with N parameters, with each element of the grid corresponding to a different set of values for the N input parameters. During the spectral fit, XSPEC interpolates on the grid to obtain the best-fit parameters.

2.4.1.1 Additive models

The additive models more commonly used in our analysis are:

- **Power Law:** `powerlaw`, `zpowerlw`

The `powerlaw` and `zpowerlaw` additive models correspond to a single power law model and a redshifted power law, respectively. The model parameters are the photon index (Γ), the normalisation at 1 keV (K , in units of photons $\text{keV}^{-1} \text{cm}^{-2} \text{s}^{-1}$), and, in the case of `zpowerlaw`, the redshift (z):

$$\text{powerlaw} : M(E) = KE^{-\Gamma} \quad (2.7)$$

$$\text{zpowerlaw} : M(E) = K[E(1+z)^{-\Gamma}]/(1+z) \quad (2.8)$$

– **Gaussian emission lines:** `gauss`, `zgauss`

Simple redshifted (`zgauss`) or not (`gauss`) additive Gaussian profiles:

$$\text{gauss} : M(E) = N \frac{1}{\sigma\sqrt{2\pi}} e^{-\frac{(E-E_L)^2}{2\sigma^2}} \quad (2.9)$$

$$\text{zgauss} : M(E) = N \frac{1}{(1+z)\sigma\sqrt{2\pi}} e^{-\frac{(E(1+z)-E_L)^2}{2\sigma^2}} \quad (2.10)$$

where N is the line flux (total photons $\text{cm}^{-2} \text{s}^{-1}$ on the line). σ and E_L are the line width and central energy in keV.

– **Relativistic lines:** `laor`, `diskline`

An emission line from an accretion disk around a maximally rotating black hole (`laor`, [Laor 1991](#)) and around a non rotating black hole (`diskline`, [Fabian et al. 1989](#)). Model parameters are : line energy (E , in keV), power law dependence of emissivity (a , which scales as R^{-a} and R^a , for `laor` and `diskline`, respectively), inner and outer accretion disk radii (R_{in} , R_{out} in units of GM/c^2), inclination angle (i , in degrees) and normalisation (in photons $\text{cm}^{-2} \text{s}^{-1}$ in the line).

– **Neutral reflection:** `pexrav`

Additive model that represents an exponentially cut-off power law spectrum reflected from neutral material ([Magdziarz and Zdziarski, 1995](#)). The output spectrum is the sum of the cut-off power law and the reflection component not including fluorescence lines. The opacities are from [Balucinska-Church and McCammon \(1992\)](#). H and He are assumed to be fully ionised. The parameters are the photon index for the incident power law (Γ), the cutoff energy, the reflection scaling factor (R), redshift (z), abundance of elements heavier than He, Iron abundance, cosine of inclination angle (i) and normalisation. The usual varying parameters in the spectral fits are R and the normalisation unless the value for the inclination angle can be measured at the same time, which is not always possible. We restricted R to negative values during our spectral analyses in order to obtain the reflection component alone. Then the reflection fraction, R , turns to out be the actual reflection normalisation.

2.4.1.2 Multiplicative models

Models describing absorption around a SMBH are represented by multiplicative models. The absorption models used in our analysis are:

– **Photoelectric absorption:** `phabs`, `zphabs`

A photoelectric absorption multiplicative model coming from neutral material at redshift 0 (`phabs`) or redshift z (`zphabs`), the only parameters in this case are the hydrogen column density in units of 10^{22} cm^{-2} (N_H) and the redshift:

$$\text{phabs} : M(E) = e^{-N_H \sigma(E)} \quad (2.11)$$

$$\text{zphabs} : M(E) = e^{-N_H \sigma(E(1+z))} \quad (2.12)$$

where $\sigma(E)$ is the photo-electric cross section, not including Thomson scattering. This cross section assumes chemical abundances and ion abundances as those in our Galaxy. Different abundance patterns are available for selection. The table from [Anders and Grevesse \(1989\)](#) was selected in our case.

– **Partial covering absorption:** `pcfabs`, `zpcfabs`

A partial covering fraction neutral absorption (`pcfabs`) and its reshifted version (`zpcfabs`). This is a multiplicative model whose analytical form assumes that there is a neutral material surrounding the source that partially absorbs its emission whereas the rest of it is unabsorbed. The parameters in this case are N_H (in units of 10^{22} cm^{-2}) and the covering fraction (f):

$$\text{pcfabs} : M(E) = f e^{-N_H \sigma(E)} + (1 - f) \quad (2.13)$$

$$\text{zpcfabs} : M(E) = f e^{-N_H \sigma(E[1+z])} + (1 - f) \quad (2.14)$$

Abundances were selected in the same way as for the `phabs` and `zphabs` models.

– **Ionised absorption:** `edge`, `zedge`, `absori`, `siabs`

The multiplicative models `edge` and `zedge` are often used to account for the absorption edges of the most commonly observed ionised elements, such as Oxygen (Oxygen absorption edges from OVII and OVIII, at 0.74 and 0.87 keV respectively, and FeI K at 7.1 keV, which have been detected in a large number of Seyfert galaxies [Reynolds 1997](#)). The model parameters are the threshold energy (E_C) and the absorption depth (τ) at that energy.

$$\text{edge} : M(E) = \begin{cases} 1 & E \leq E_C \\ e^{[-\tau(E/E_C)^3]} & E \geq E_C \end{cases} \quad (2.15)$$

And for the redshifted absorption edge:

$$\text{zedge} : M(E) = \begin{cases} 1 & E \leq E_C \\ e^{[-\tau(E(1+z)/E_C)^3]} & E \geq E_C \end{cases} \quad (2.16)$$

Siabs (Kinkhabwala et al., 2003) is a more sophisticated table model which represents single-ion absorption for a low density photoionised plasma. This model takes into account absorption edges but also resonance absorption lines for each ionised species. The model parameters are the atomic number of the species (Z), the number of electrons (z), the ion column density (N_{ion} in cm^{-2}), the redshift, the velocity shift with respect to that redshift (v), and the velocity width (σ_v). It also has three additional parameters that describe the way the grid is interpolated: minimum and maximum energies for internal grid (EMIN and EMAX) and the number of energy bins (SPECBINS).

Absori is an ionised absorber multiplicative model, based on that of Done et al. (1992) and developed by Magdziarz and Zdziarski (1995), that consists of a superposition of absorption edges that depends on the ionisation state of the material. Photoionisation rates are from Reilman and Manson (1979), who employ the Hartree-Slater approximation (accurate to about 5%), and recombination rates are from Shull and van Steenberg (1982). The cross sections are extrapolated with E^3 above 5 keV. The parameters corresponding to this model are power law photon index (Γ), hydrogen column density ($N_{\text{H}i}$, in units of 10^{22} cm^{-2}), temperature, ionisation parameter ($\xi=L/nr^2$, where L is the X-ray luminosity, n the electron density and r the distance of the absorber to the emitting source), redshift (z) and Iron abundance of the ionised absorber. The usually varying parameters in the spectral fits are $N_{\text{H}i}$ and ξ .

2.4.1.3 Soft-excess emission models

In Sect. 1.2.4, a commonly observed feature in X-ray AGN spectra, the “soft-excess” emission, is described. For unabsorbed AGN, its nature is still unclear so that very different models have been proposed to describe it. For featureless soft-excess emission, continuum emission processes are usually invoked (see for example Porquet et al. 2004; Abramowicz et al. 1988). This seems not to be the case for the Seyfert galaxies presented in Chapter 3. Two competitive models, that are based on atomic processes, have been successful in reproducing more complex soft-excess emission: relativistically blurred ionised reflection from an accretion disk (XSPEC model: `kdblur(zpo+reflion)`, Ross and Fabian 2005) and velocity smeared ionised absorption from a disk wind (XSPEC model: `swind1(zpo*xion)`, Gierliński and Done 2004).

– **Relativistically blurred ionised reflection:** `kdblur(zpo+reflion)`

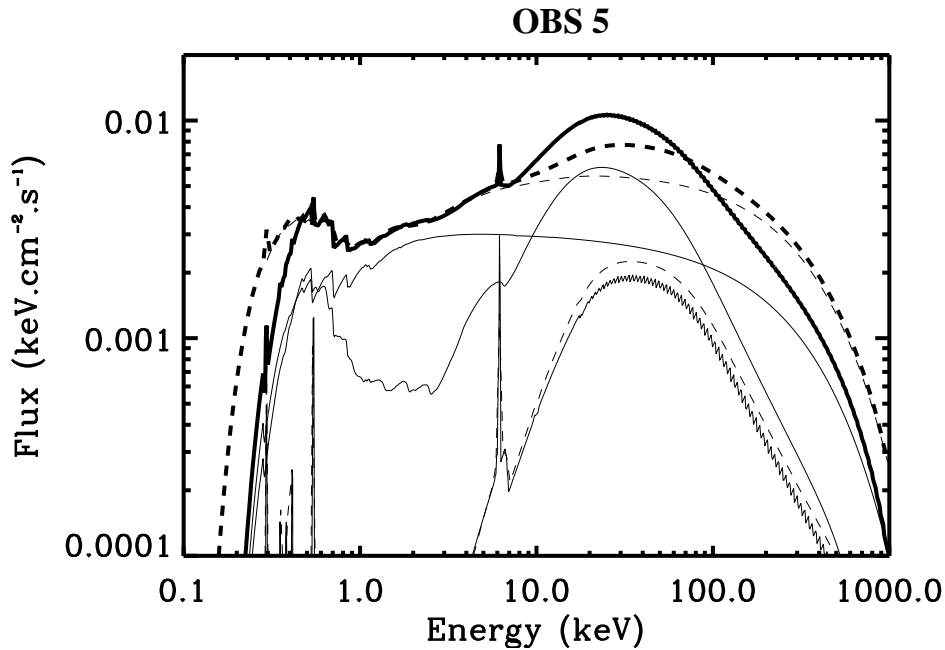


Figure 2.8 Smeared ionised absorption model (thick dashed line) and relativistically blurred reflection model (thick solid line) applied to the same data (from [Petrucci et al. 2007](#)). The thin solid and dashed lines correspond to the different components for each model. Both models also include neutral reflection.

This model assumes that the incident power law is reflected on an accretion disk modelled as a semi-infinite slab of optically thick cold gas of constant density. As described in Sect. 1.2.2, the reflected spectrum consists of a Compton component and fluorescence lines. Since the reflection is produced close to the SMBH, the relativistic effects are simulated by convolving the resulting power law plus reflected component spectrum with a Laor profile, which assumes a maximum rotating SMBH. This would produce a blurring of the spectral features so that the fluorescence emission lines blend and produce the soft-excess emission observed.

The reflected component is modelled with the additive table model `reflion`. The `reflion` model is a self-consistent reflection model from an ionised accretion disk ([Ross and Fabian, 2005](#)). The emergent ("reflected") spectrum is calculated for an optically-thick atmosphere (such as the surface of an accretion disk) of constant density illuminated by radiation with a power law spectrum. This additive model includes both the reflection hump produced by Compton scatter as well as fluorescence line emission. The parameters of this model are the abundance of iron relative to solar value (abundances of other elements are fixed at solar values, [Morrison and McCammon 1983](#)), the photon index of the incident power law (Γ), the ionisation parameter of the disk (ξ), the redshift, and the normalisation of the

reflected spectrum.

The relativistic blurring is represented by the convolution model `kdblur`. This model smooths a spectrum by relativistic effects from an accretion disk around a maximum rotating black hole (Laor, 1991). The model parameters are the power law dependence of emissivity (a , scaling as R^{-a}), inner and outer radii (in units of GM/c^2) and the inclination (degrees).

– **Velocity smeared ionised absorption:** `swind1(zpo*xion)`

As the previous model, this model is composed of an incident power law plus accretion disk reflection but in this case, the reflection model assumes hydrostatic balance within the disk rather than constant density. The resulting incident plus reflected spectrum is then absorbed by optically thin material, instead of being relativistically blurred as in the previous model. In order to reproduce the featureless soft-excess emission, this material, besides being partially ionised, must have strong velocity gradients so that Doppler smearing removes lines and edges. This suggests that the origin of the ionised material is an accretion disk wind. The soft-excess emission in this case would be “apparent” and caused by the spectral curvature produced by the ionised absorption.

The disk reflection is modelled by using `xion`. This model describes the reflected spectra of a photoionised accretion disk or a ring assuming hydrostatic balance (Nayakshin and Kallman, 2001). The default geometry is that of a lamppost, with free parameters of the model being the height of the X-ray source above the disk (h_X), the ratio of the X-ray source luminosity to that of the disk, the accretion rate (\dot{m} , in Eddington units), cosine of the disk inclination angle ($\cos i$), the inner and outer radii of the disk (in Schwarzschild radii, $R_S=2GM/c^2$), the incident power law photon index (Γ), the redshift, the Fe abundance relative to Solar, and the exponential high energy cut-off of the incident power law (in keV). The total disk spectrum also includes relativistic smearing of the spectrum for a non-rotating black hole (Fabian et al., 1989).

To model the ionised absorption, the model `swind1` is used. This model represents ionised absorption by a partially ionised material with large velocity shear. It approximates this by using XSTAR⁶ kn5 photoionisation absorption model grids (calculated assuming a micro-turbulent velocity of 100 km/s), and then convolving this with Gaussian smearing absorption by partially ionised material with large velocity shear. The model parameters are the ionised absorber column density (N_{Hi} in units of 10^{22} cm^{-2}), its ionisation parameter (ξ), the Gaussian width for velocity smearing (in units of v/c) and the redshift.

⁶<http://heasarc.gsfc.nasa.gov/xstar/xstar.html>

These two models, relativistically blurred ionised reflection and velocity smeared ionised absorption, turn out to be statistically indistinguishable at the energies covered by XMM-Newton (see Fig. 2.8). Therefore, sensitive enough data at higher energies would be needed to distinguish between them.

Changing Type Seyfert galaxies

Contents

3.1	Introduction	52
3.2	Mrk 993	53
3.2.1	Previous observations	53
3.2.2	X-ray data	54
3.2.3	Optical data	57
3.2.4	Discussion and results	62
3.3	Mrk 6	64
3.3.1	Previous observations	64
3.3.2	X-ray data	65
3.3.3	Optical data	70
3.3.4	Discussion and results	74
3.4	NGC 7603	75
3.4.1	Previous observations	75
3.4.2	X-ray data	75
3.4.3	Optical data	79
3.4.4	Discussion and results	83
3.5	Mrk 1018	83
3.5.1	Previous observations	83
3.5.2	X-ray data	84
3.5.3	Optical data	87
3.5.4	Discussion and Results	87
3.6	Conclusions	87

In this chapter the optical and X-ray spectral analysis of a small sample of Seyfert galaxies which have been reported to exhibit optical spectral type changes is presented. Our intention is to explore whether the mismatches reported so far between the optical and X-ray classifications of AGN are due to intrinsic properties or just due to variability, i.e., to the non-simultaneity between observations in different spectral bands.

The chapter is organised as follows: in Sect. 3.1 the sample and our observational strategy are presented. In each following section, a detailed description

of the spectral analysis and results is given for a different source in the sample. Finally in Sect. 3.6 a summary of the main results obtained is presented. Errors are at 90% confidence unless otherwise stated and a standard cosmology ($\Omega_m=0.3$, $\Omega_\lambda=0.7$, $H_0=70 \text{ km s}^{-1} \text{ Mpc}^{-1}$) is assumed.

3.1 Introduction

In the framework of the simplest version of the unified model for Active Galactic Nuclei (AGN) there are two basic AGN types, type 1 and type 2 AGN (Antonucci, 1993). Within this scenario, broad line obscuration and X-ray absorption both arise in the same material, the torus, so the differences between AGN types are solely due to differences in the inclination subtended between the line of sight and the symmetry axis of the torus. In this way, type 1 AGN would present broad permitted (FWHM $> 2000 \text{ km s}^{-1}$) and narrow forbidden emission lines in the optical and little (if any) absorption in the X-rays. This is because we are seeing the central engine face-on and, therefore, we see the Broad Line Region (BLR) unobscured by the molecular torus. On the contrary, type 2 AGN should display significant absorption in the X-ray band and only narrow lines in their optical spectra, as we do not see the BLR but only the Narrow Line Region (NLR). According to this model, intermediate types are predicted depending on the inclination angle so that the strength of the broad permitted lines decreases as the absorption in the X-ray band increases. Such behaviour has been confirmed by many observations (see for example Smith and Done 1996, Nandra and Pounds 1994, Bassani et al. 1999 and Risaliti et al. 1999).

However, as discussed in Chapter 1, several observations have shown that this is not always true. Unabsorbed type 2 AGN and absorbed type 1 AGN are occasionally found in X-ray surveys. Among the proposed explanations for these mismatches, there is “the absorption variability hypothesis”. Optical and X-ray observations could be observing the same source in different absorption states. Variations in the intrinsic absorption of AGN as well as in the optical spectral types have been indeed reported in the literature (see for example Risaliti et al. 2002; Risaliti and Elvis 2004; Elvis et al. 2004; Risaliti et al. 2007 for X-ray absorption variations, and Aretxaga and Terlevich 1994 for optical spectral type variations). The aim of the work that is described in this chapter is to test this variability hypothesis.

Therefore simultaneous X-ray and optical spectroscopy appears to be a mandatory strategy to solve the mystery of the AGN with mismatched optical and X-ray spectral properties. To this goal, we have constructed a sample of optical spectrally variable Seyfert galaxies starting with the Aretxaga and Terlevich (1994) compilation, which consists of 11 AGN. Out of the 11 sources, we have down-selected those that can be observed simultaneously by XMM-Newton and

Table 3.1 Summary of the simultaneous observations

Source	XMM – Newton observation date	X – ray flux 2 – 10 keV ($\text{erg cm}^{-2} \text{s}^{-1}$)	Optical observation dates	Magnitude B
Mrk 993	23 Jan 2004	1.3×10^{-12}	23 Jan 2004	14.4
Mrk 6	27 Oct 2005	1.5×10^{-11}	1 Nov 2005 27 Nov 2005	14.9
NGC 7603	14 Jun 2006	1.9×10^{-11}	4 Aug 2006	14.0
Mrk 1018	7 Aug 2008	1.5×10^{-12}	31 Jul 2008 2 Sep 2008	14.3

the Calar Alto observatory (CAHA). We also checked the quality of the optical spectra from which the spectral type variations were derived and finally excluded a few local, heavily studied AGN.

In this way, we ended with a sample of 4 *bona-fide* changing type AGN: **Mrk 993, Mrk 6, NGC 7603 and Mrk 1018**. By performing simultaneous X-ray/optical spectroscopy of these sources, we can distinguish whether the apparent mismatches are due to intrinsic properties of the BLR or are caused by variations in the source absorption properties. Doing this in a well-defined sample is very important to assess whether these type-changing sources represent an important fraction of the overall AGN population, as it seems since several of the brightest and best observed AGN show these spectral changes.

These 4 galaxies were proposed to be observed by XMM-Newton and from ground-based optical telescopes quasi-simultaneously. In two cases, a second optical observation, taken ~ 1 month later, was also carried out. In this way, we can search for optical variability, if any, within the time scale in which the BLR would respond to changes in the ionisation continuum, as mapped by the X-ray emission. A summary of these observations is shown in Table 3.1.

3.2 Mrk 993

3.2.1 Previous observations

Mrk 993 is a Seyfert galaxy at redshift $z=0.015537$ (Huchra et al., 1999). Its central super massive black hole (SMBH) mass has been estimated from the host galaxy stellar velocity dispersion to be $M_{\text{BH}} \sim 2 \times 10^7 M_{\odot}$ (Wang et al., 2007). Its AGN bolometric luminosity, estimated from its [OIII] luminosity, is $L_{\text{bol}} \sim 2.6 \times 10^{44} \text{ erg s}^{-1}$, which leads to an Eddington ratio of $L/L_{\text{Edd}} \sim 0.1$.

This AGN has a long record of type changes on scales of months to years. It was first classified as a Seyfert 2, based in a spectrum obtained by Osterbrock in August 1983 (Tran et al. 1992 later refined the classification of that spectrum to a Seyfert 1.9). A further unpublished spectrum obtained by L. Kay and J. Miller in October 1988 (quoted by Goodrich 1989) showed no trace of narrow components in the permitted lines, which classified this object as a classical Seyfert 1. Tran et al. (1992) also conducted 3 observations in 1991 (February, September and December), when Mrk 993 had developed a strong (and variable in scales of \sim months) H_β broad component on top of a very strong H_α component, converting it into a Seyfert 1.5. Tran et al. (1992) argued that variations in the extinction along the line of sight are the most likely explanation for these changes.

3.2.2 X-ray data

Mrk 993 was observed with XMM-Newton during revolution 755 on January 23rd 2004 (Observation ID: 0201090401). Only data from the EPIC instruments, MOS1, MOS2 and pn was used, which were operated in Full Window (imaging) mode with Thin1 filters.

The data were pipeline-processed with the XMM-Newton Science Analysis Software (SAS) version 5.4.1. In all further work, including generation of calibration files, version 6.0.0 of the SAS was used. The calibrated event lists were filtered in the time domain to avoid background flares. The resulting good time intervals were 15.8, 15.8 and 14.6 ks for the MOS1, MOS2 and pn, respectively.

Source spectra were extracted in circular regions of 40 arcsec radii for all detectors. The background spectra were taken in circular source-free regions of 87 arcsec radii near the galaxy, avoiding CCD gaps. We selected single, double, triple and quadruple events in the MOS1 and MOS2 ($PATTERN \leq 12$) and only single and double events in the pn ($PATTERN \leq 4$). In the EPIC-pn spectra, only events with the highest spectral quality were included (i.e., $FLAG=0$). We generated redistribution and effective area matrices using SAS tasks `rmfgen` and `arfgen`. Finally, the spectra were binned to have at least 30 counts per bin in order to use the χ^2 statistic to fit the data.

The fitting was performed jointly to the MOS1, MOS2 and pn spectra with XSPEC (Arnaud, 1996) in the spectral range 0.2-12 keV. First, an absorbed power law was fitted with the hydrogen column density (model `phabs*zpowerlaw`) fixed at the Galactic value in the direction of Mrk 993 ($5.56 \times 10^{20} \text{ cm}^{-2}$, Dickey and Lockman 1990). That gave a poor fit ($\chi^2/\text{d.o.f.} = 508/321$). Then an intrinsic photoelectric absorption component was added (model `zphabs`), resulting in a substantial improvement of $> 99.99\%$ in terms of the F-test ($\chi^2/\text{d.o.f.} = 351/320$), with a column density of $N_H \sim 7 \times 10^{20} \text{ cm}^{-2}$.

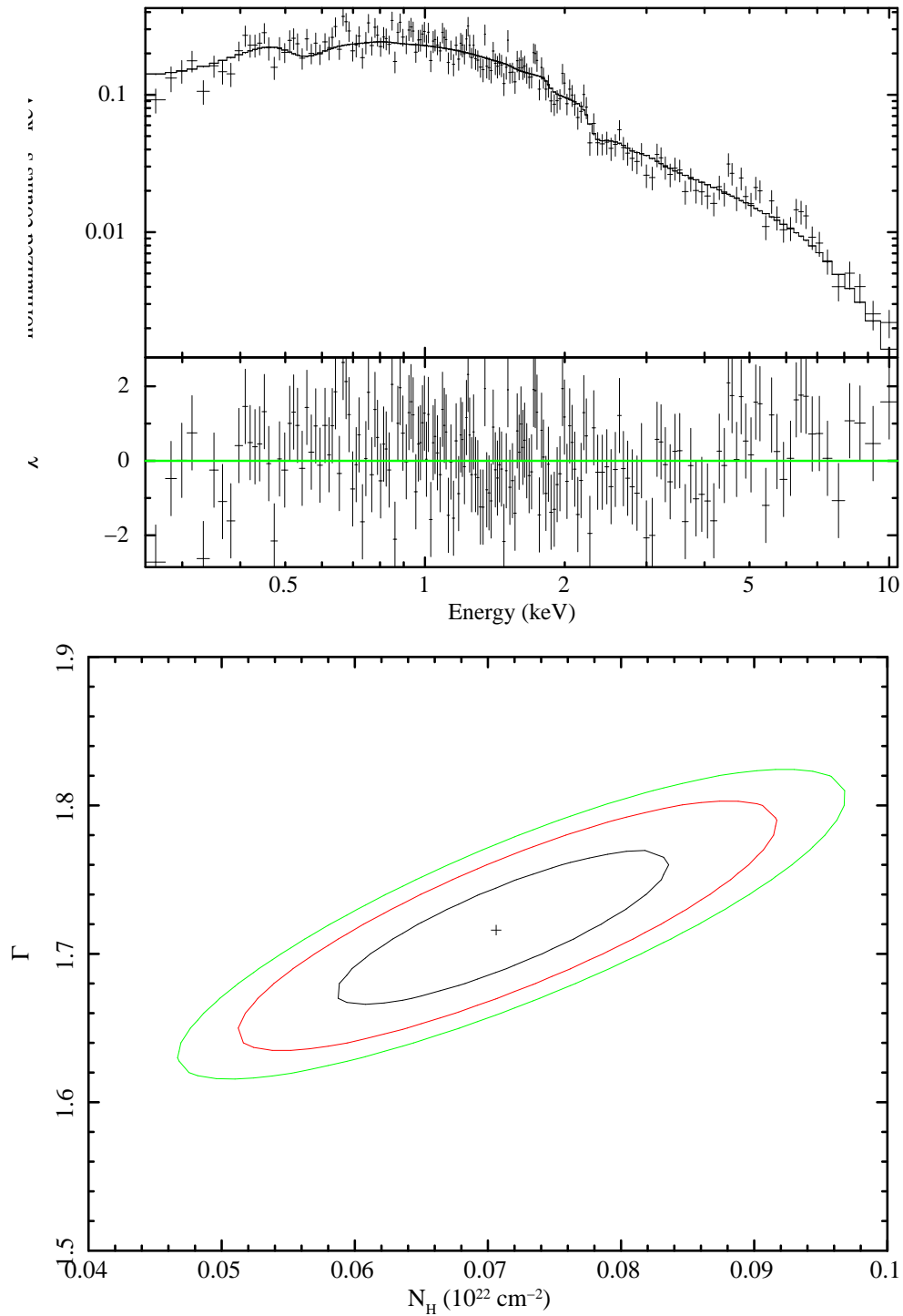


Figure 3.1 **Mrk 993**: EPIC-pn best-fit model, data and residuals (top) and confidence contours 1σ , 2σ , and 3σ (bottom) for the best-fit model: `pha*zpha*po`. N_H represents the intrinsic column density and Γ is the photon index.

Table 3.2 **Mrk 993**: X-ray spectral parameters corresponding to the best-fit model: `phabs*zphabs*zpowerlaw`.

Γ	N_{H} (10^{20} cm^{-2})	Flux 2 – 10 keV ($10^{-12} \text{ erg cm}^{-2} \text{ s}^{-1}$)	($\chi^2/\text{d.o.f.}$)
1.69 ± 0.04	7.2 ± 1.1	1.34 ± 0.02	351/320

The residuals of the fit (see Fig. 3.1) corresponding to the pn only are suggestive of the presence of various emission lines (at ~ 2 , ~ 4.6 and ~ 6.4 keV). Each of these features were modelled using Gaussian profiles but they are of $< 80\%$ significance in F-test terms, if we consider together the MOS1, MOS2 and pn, and at most $\sim 98\%$, if we consider only the pn. Given this very limited significance, we do not pursue the use of these features any further.

To search for an ionised absorber, whose features are commonly detected in Seyfert galaxies, two models were tried: `absori` (Done et al. 1992, Zdziarski et al. 1995), which provides a simple superposition of absorption edges dictated by the photo-ionisation state of the absorber, and the more sophisticated model `siabs` (Kinkhabwala et al., 2003), where both the absorption edge and the resonance absorption lines are included for a single ion species. In model `absori` the variable parameters were the absorber temperature, the overall chemical abundance and the ionisation parameter, and, in the model `siabs`, the absorber column density and the ion species (for C, S, Si, Mg and O). None of these models introduced significant improvements in the fit for any values of the parameter space explored. Specifically, for the model `absori`, the best fit gave a hydrogen column density of $\sim 7 \times 10^{20} \text{ cm}^{-2}$ and an ionisation parameter of ~ 0 , i.e. we are led to the neutral absorber previously discussed. For the model `siabs` we looked for the spectral features that could arise in ionised species. Given the spectral range of our data the more representative absorption edges correspond to Oxygen, but the best fitted models (including the other ion species) gave a significance $< 90\%$ in the improvement of χ^2 and correspond to nearly or totally neutral ions. For Oxygen ions we found that, a 3σ upper limit, for the ion column density (N_{ion}) is $< 3 \times 10^{17} \text{ cm}^{-2}$. We therefore conclude that no significant ionised absorption is present in the source.

The best-fit model `phabs*zphabs*zpowerlaw` – a single power law at the source redshift photoelectrically absorbed by neutral gas at the same redshift as well as by a fixed amount of gas from our Galaxy – and the unfolded spectrum for the pn are represented in Fig. 3.1. The corresponding values to the fit are shown in Table 3.2.

3.2.3 Optical data

Mrk 993 was observed, simultaneously to XMM-Newton, on January 23rd 2004 with the 3.5 m telescope at the Calar Alto Observatory (CAHA). The TWIN double spectrograph was used with central wavelengths of 4500 Å and 6700 Å for the blue and the red channels respectively. In total, six exposures of 1000 s were obtained, three with the slit oriented in the direction of the major axis of the galaxy and the other three in the direction of the minor axis. Only the three former exposures were considered in our analysis, as in this case the light from the host galaxy can be subtracted (this will be discussed later).

A standard reduction procedure for long slit spectra, that uses the IRAF package, was used to reduced and combine the three exposures. The resulting spectrum is shown in Fig. 3.2. The reduction included debiasing, flat-fielding, wavelength calibration with arc lamps, and flux calibration using a standard star and the standard extinction curve for the observatory. The wavelength calibration (fitted to a fourth order polynomial) gave residuals of 0.02 Å for both the blue and the red spectra. The measured spectral resolution (FWHM of unblended arc lines) was 1.5 Å for the blue and 1.3 Å for the red. The statistical errors were propagated along the whole process. Since the slit was not aligned with the parallactic angle ($\sim 30^\circ$ apart), a certain amount of light may have been lost, preferentially in the blue. This probably affected the continuum shape so we have to be cautious about extracting directly information from it.

The spectral fitting was carried out using the QDP fitting routines via χ^2 minimisation. A broad H_α component ($H_\alpha(b)$) is evident, in addition to narrow H_α ($H_\alpha(n)$) and N[II] doublet components. The H_β broad component ($H_\beta(b)$), if any, is very weak. To search for it, the blue and the red spectra were fitted simultaneously in the range 4800-5050 (which includes H_β and the narrow emission line [OIII] λ 4958) and 6500-6800 Å (which includes H_α and the [NII] $\lambda\lambda$ 6548,6583 and [SII] $\lambda\lambda$ 6716,6730 doublets) using a linear component to represent the continuum emission and a Gaussian profile for each emission line. Line widths and central energies for the emission lines were fitted according to the following restrictions:

- Broad H_α and H_β velocity widths and redshifts were tied down to the same.
- Narrow H_α and H_β velocity widths and redshifts were also tied down to the same value. This value was allowed to be different from the one for the broad components, as this improved the quality of the fit substantially.
- [OI] λ 6300 and λ 6365 were fitted independently.

The resulting Balmer decrements turned out to be quite large: ~ 13 for the NLR and ~ 20 for the BLR, the intrinsic values being ~ 3 and ~ 3.4 , respectively. However, the influence of the host galaxy in the resulting optical spectrum was not yet considered, and it can be seen clearly in Fig. 3.2 that it is strongly affecting

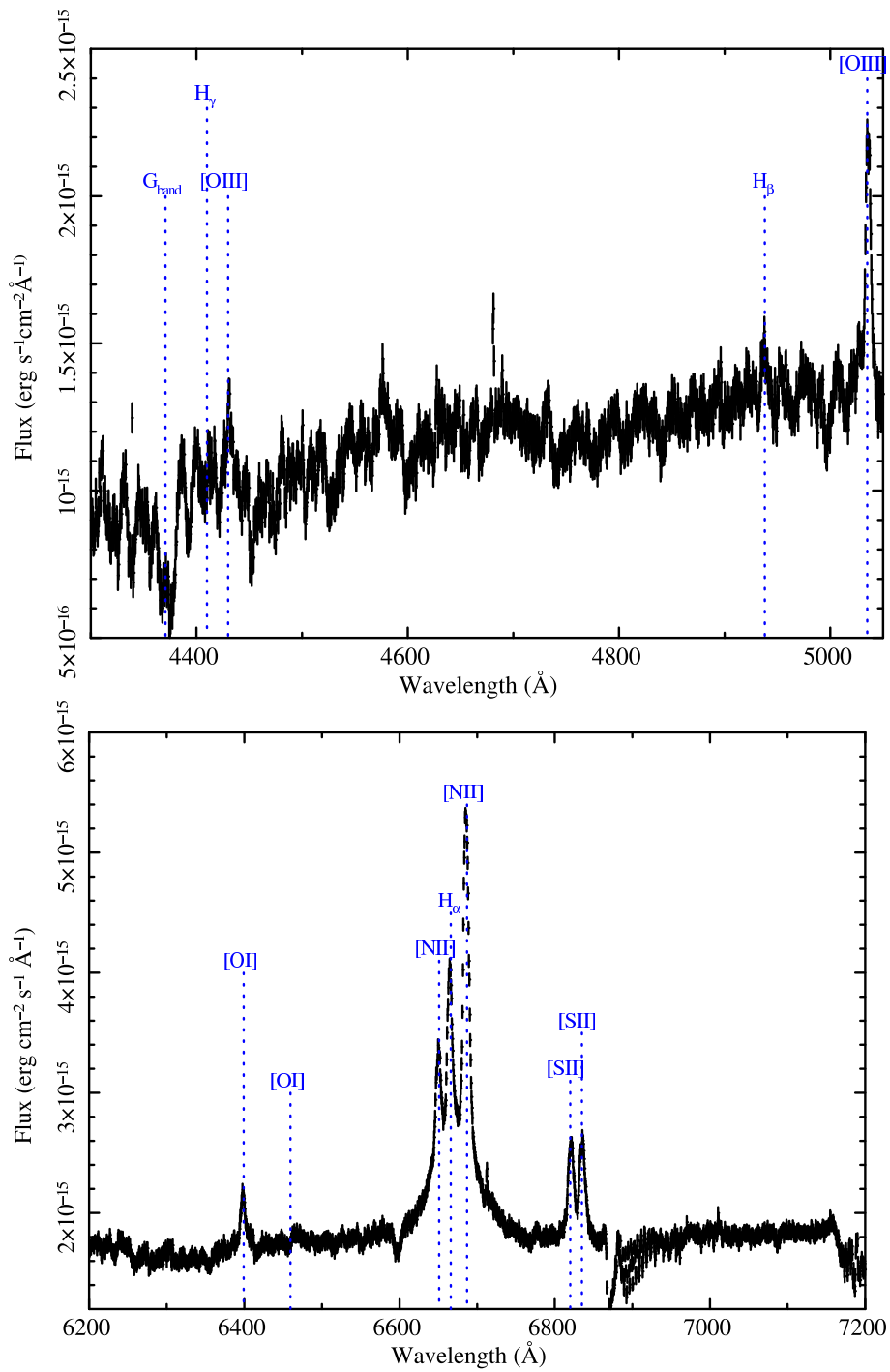


Figure 3.2 Mrk 993: CAHA 3.5m TWIN optical spectra. Blue (top) and red (bottom) bands.

the continuum shape.

Some authors (Mouri and Taniguchi 2002, Ivanov et al. 2000) have reported the possibility that Mrk 993 has a nuclear starburst. Ivanov et al. (2000) suggested, based on observations in the CO band, that Mrk 993 might have a circumnuclear starburst but they did not use it in their analysis because its spectrum had a low signal to noise ratio. Ivanov et al. (2000) classified Mrk 993 as ‘host dominant’, i.e., a galaxy that probably presents a circumnuclear starburst that hides the BLR. It has also to be pointed out that the host galaxy is an emission line galaxy, displaying narrow emission lines such as H_α and the [NII] doublet, so the measured line intensities must be affected by this. Therefore, it is extremely important to obtain a host galaxy spectrum that represents the actual emission of the galaxy instead of using a template.

To take this into account the spectrum of the host galaxy was extracted in order to subtract it from the obtained total (AGN+galaxy) spectrum as follows. First, for each exposure the AGN+galaxy spectrum and the galaxy spectrum are extracted from the same CCD image independently. The galaxy spectrum is extracted by shifting the CCD image along the cross dispersion direction and by following the same spectral trace as for the AGN. Then the galaxy spectrum is corrected for the rotation curve (by shifting the wavelength direction to the nuclear frame) and all the galaxy spectra are combined. The errors were not propagated in this complicated process, but instead were estimated by computing the standard deviation in a line-free region of the final spectrum. Once we had the AGN+galaxy and the galaxy spectra, the galaxy contribution is re-scaled by using absorption lines from the host galaxy (e.g., G-band, Ca H). These absorption lines are used as a reference to rescale the galaxy spectrum so that the final ‘‘pure’’ AGN spectrum does not show absorption lines. Finally, the rescaled galaxy spectrum is subtracted from the AGN+galaxy spectrum. The final spectra are shown in Fig. 3.3 and Fig. 3.4. This time, the presence of a broad H_β component is much more clear than for the non-subtracted spectrum. The spectral fitting was performed in the same way as for the non-subtracted spectra of Fig. 3.2, obtaining the line intensities listed on Table 3.3.

In order to compute the errors in the Balmer decrement, the model was modified so that the Balmer decrement was a fitting parameter itself, and then we searched for the minimum χ^2 . The measured values and the corresponding errors at 90% confidence level are the following:

$$\frac{H_\alpha}{H_\beta}(\text{NLR}) = 5.88 \pm 0.13, \quad \frac{H_\alpha}{H_\beta}(\text{BLR}) = 8.99 \pm 0.02$$

The line at 5007\AA of the [OIII] doublet was just missed by our setup. To compute it, a ratio to [OIII] $\lambda 4958$ of 3 was assumed, a relation which holds with almost no exception (Osterbrock, 1989). Using the Balmer decrement of the NLR to correct

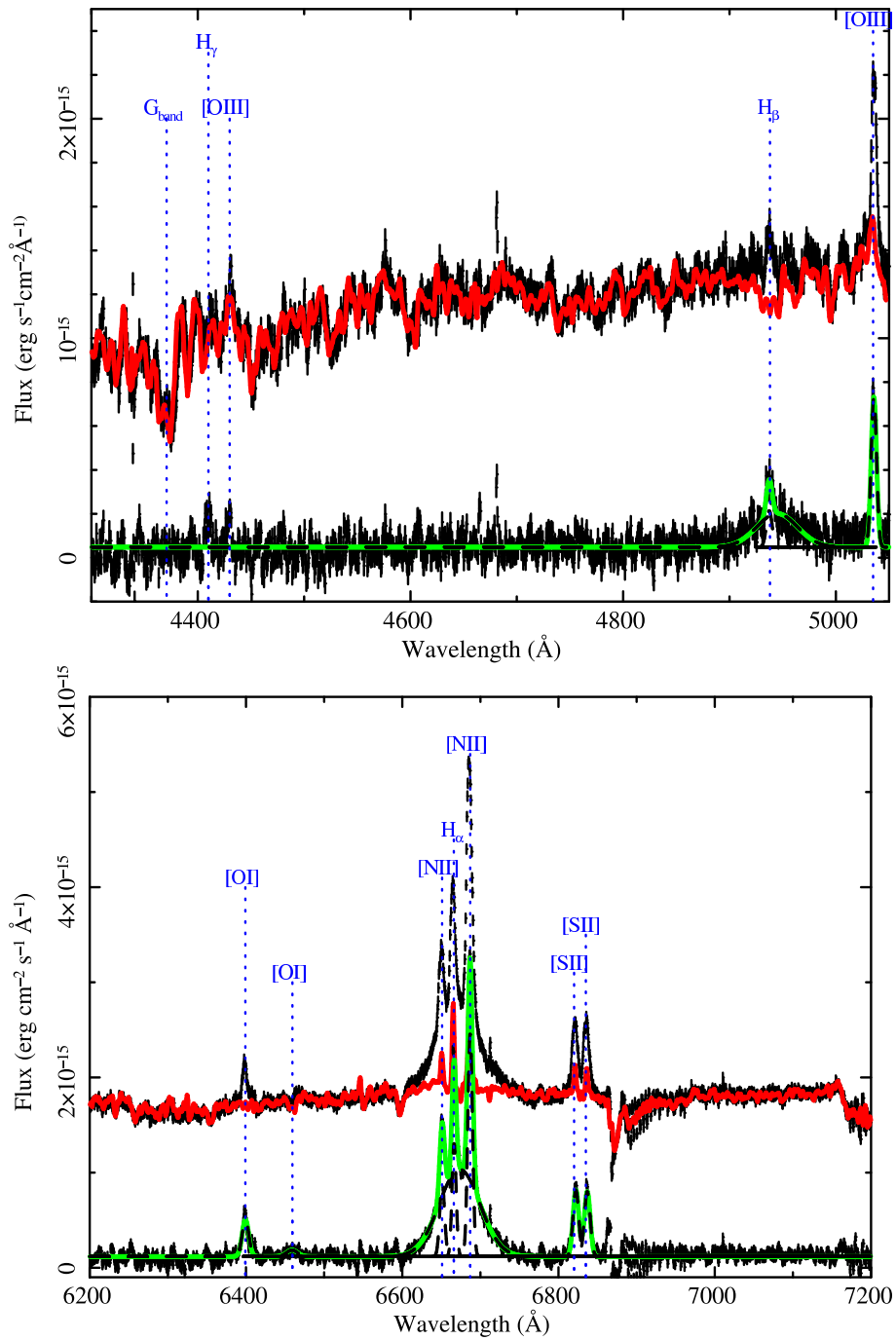


Figure 3.3 **Mrk 993**: Original and galaxy-subtracted optical spectra for each band (blue and red bands correspond to top and bottom panels, respectively), as well as the galaxy model (red line) and the fitted continuum plus emission lines models (green line) to the AGN emission.

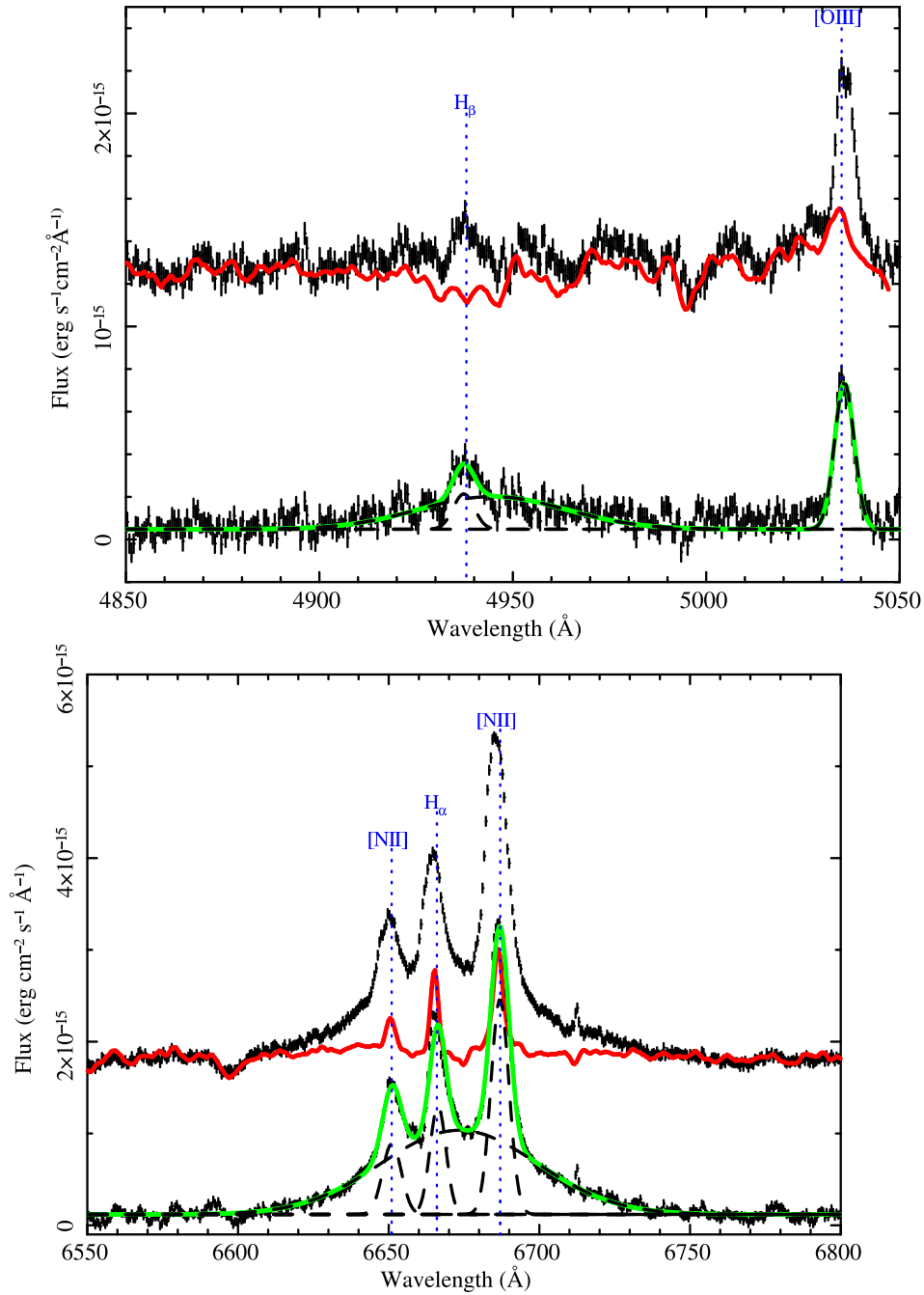


Figure 3.4 Mrk 993: Zooming on the H α and H β regions of Fig.3.3: original and galaxy-subtracted optical spectra for each band (blue and red bands correspond to top and bottom panels, respectively), as well as the galaxy model (red line) and the fitted continuum plus emission line models to the AGN emission (green line).

Table 3.3 **Mrk 993**: Optical line intensities and FWHM corresponding to the galaxy subtracted spectrum.

Line	Intensity($10^{-15}\text{erg cm}^{-2} \text{s}^{-1}$)	FWHM(km s^{-1})
$\text{H}_\beta(\text{n})$	1.4 ± 0.2	385 ^a
$\text{H}_\beta(\text{b})$	6.1 ± 1.1	2800 ^b
$[\text{OIII}]\lambda 4958$	6.1 ± 0.2	390 ± 20
$[\text{NII}]\lambda 6548$	6.06 ± 0.30	370 ± 20
$\text{H}_\alpha(\text{n})$	8.40 ± 0.02	385 ± 12
$\text{H}_\alpha(\text{b})$	60.5 ± 0.3	2800 ± 30
$[\text{NII}]\lambda 6583$	18.6 ± 0.2	365 ± 5
$[\text{SII}]\lambda 6718$	5.7 ± 0.3	376 ± 12
$[\text{SII}]\lambda 6730$	6.2 ± 0.2	376 ± 14

^a Fixed at the same $\sigma(\text{km s}^{-1})$ as $\text{H}_\alpha(\text{n})$

^b Fixed at the same $\sigma(\text{km s}^{-1})$ as $\text{H}_\alpha(\text{b})$

the narrow line intensities for reddening and following Baldwin et al. (1981), the following line ratios are measured:

$$\log \frac{[\text{OIII}]\lambda 5007}{\text{H}_\beta} = 0.63, \quad \log \frac{[\text{NII}]\lambda 6583}{\text{H}_\alpha} = 0.51$$

$$\log \frac{[\text{SII}]\lambda\lambda(6716 + 6730)}{\text{H}_\alpha} = 0.31, \quad \log \frac{[\text{OI}]\lambda 6300}{\text{H}_\alpha} = -0.19$$

These values place clearly the object in the AGN zone in line diagnostic diagrams (Osterbrock, 1989), thus confirming that our measured line intensities are not very much affected by a possible host galaxy or starburst contribution.

3.2.4 Discussion and results

We found that the Balmer decrement was ~ 6 for the NLR. From this value the hydrogen column density can be estimated assuming a standard gas-to-dust-ratio (Bohlin et al., 1978) resulting in a value of $N_{\text{H}} \sim 3 \times 10^{21} \text{cm}^{-2}$. However, the Balmer decrement of the BLR is found to be ~ 9 which, under the assumption of a *standard* case-B recombination and optically thin plasma Balmer decrement of ~ 3.4 applicable to most Seyfert 1 galaxies, corresponds to a column density of $N_{\text{H}} \sim 5 \times 10^{21} \text{cm}^{-2}$. On the other hand, the intrinsic column density derived from the X-ray data turned out to be $N_{\text{H}} \sim 7 \times 10^{20} \text{cm}^{-2}$ with an upper limit at 3σ confidence level of $N_{\text{H}} < 9 \times 10^{20} \text{cm}^{-2}$.

Three possible explanations to this apparent discrepancy were suggested by Pappa et al. (2001): the galaxy is Compton-thick, there is a dusty warm absorber and finally, the obtained Balmer decrement is real and an intrinsic property of the BLR.

To examine the first possibility a Fe K_{α} Gaussian emission line was added to the model for the X-ray spectra. We only got a marginally significant ($\sim 98\%$) detection of the line in the pn spectrum with an equivalent width of ~ 270 eV. The measured flux in X-ray band 2-10 keV was 1.34×10^{-12} erg cm $^{-2}$ s $^{-1}$. Even considering the “detection” of the Fe line as real and using the three dimensional diagnostic diagram proposed by Bassani et al. (1999), this small value versus the F_X to F([OIII] λ 5007) ratio (~ 10) clearly rejects a Compton-thick scenario.

The second possibility was studied by searching for spectral features that must appear in the X-ray spectrum if a dusty warm absorber is present. As we saw in Sect. 3.2.2, we did not find evidence for an ionised absorber. Komossa and Bade (1998) predicted that a dusty warm absorber would smooth the oxygen edges but then we should see a C K-edge at 0.28 keV. There is nothing in our X-ray spectra that supports the presence of a significant absorption edge at 0.28 keV, although we cannot be completely sure since the EPIC-pn calibration it is not good enough below 0.3 keV.

The last possibility is that the Balmer decrement is an intrinsic property of the BLR. Ward et al. (1988) found a correlation between the Balmer decrement and the F_X to $F(H_{\beta})$ ratio for a large sample of Seyfert 1 galaxies. Despite the unlikely applicability of the case-B recombination and the likely optical thickness of the BLR clouds, they found an intrinsic Balmer decrement for the BLR of 3.5. They conclude that the differences in the Balmer decrements are due to nuclear reddening rather than being an intrinsic property of the BLR. However, when we represent Mrk 993 in that diagram (see Fig. 3.5) it has a Balmer decrement that place it formally $> 3\sigma$ above that correlation (solid line). If we compare this value with the Ward et al. (1988) sample, Mrk 993 has a deviation from the fit which is larger than at least 90% of the sample. A similar result was found by Carrera et al. (2004) for the object RXJ133152.51+111643.5 and a much more extreme result was also found by Barcons et al. (2003) for the Seyfert 1.8/1.9 galaxy H1320+551. Both authors consider the possibility of non-simultaneity in the X-ray and optical observations as a possible way to resolve this discrepancy. This is certainly not our case, since our data were taken simultaneously so the results must represent the real absorption state of Mrk 993 at the time of the observation. We are therefore forced to conclude that the Balmer decrement of this source cannot be explained by obscuration but it has to be an intrinsic characteristic of the BLR. A possible explanation is the BLR being optically thick. At high densities other physical processes besides photoionisation become important, changing the intrinsic Balmer ratios and making the Balmer decrements unreliable as reddening indicators.

There is, however, a caveat we have to consider. There could be a lag between

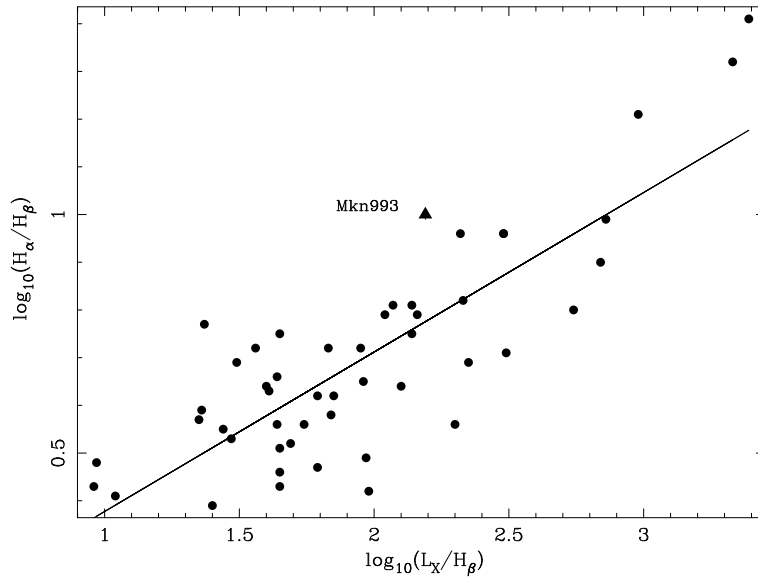


Figure 3.5 Ward et al. (1988) Fig. 4 and the fitted relation (solid line)

changes in the ionisation spectrum –X-rays– and the optical emission lines due to the distance from the ionising source and structure of the BLR (recombination times might be significant). To estimate the source variability, we extracted the light curves for the pn and the MOS instruments. After correcting for the background we obtained the curves shown in Fig. 3.6. By fitting the data to a constant model, we found that variability is not significant ($< 90\%$). Therefore, this result does not lend support the previous optical-lag explanation. However, our data extends only to hours while the expected lag could be of up to few days (see for example Dietrich et al. 1998), so our measurements of the X-ray variability cannot completely discard this possibility.

In short, unless the source varied significantly (for which we have no evidence) and there is a time lag between the variations of the ionising continuum and the state of the BLR, we have to conclude that Mrk 993 is not an obscured Sy1 due to orientation effect but the Balmer decrement must be an actual characteristic of the BLR.

3.3 Mrk 6

3.3.1 Previous observations

Mrk 6 is a radio loud Seyfert galaxy at redshift $z=0.018813$ (Gallimore et al., 1999). Its SMBH mass has been estimated from the broad line widths to be $M_{\text{BH}} \sim 6.3 \times 10^7 M_{\odot}$ (Wang et al., 2006). Its AGN bolometric luminosity, estimated from its [OIII] luminosity, is $L_{\text{bol}} \sim 2.6 \times 10^{44} \text{ erg s}^{-1}$, which leads to an Eddington ratio of $L/L_{\text{Edd}} \sim 0.03$.

This source has changed its type from a Sy1 to Sy2 and finally to a Sy1.5 state

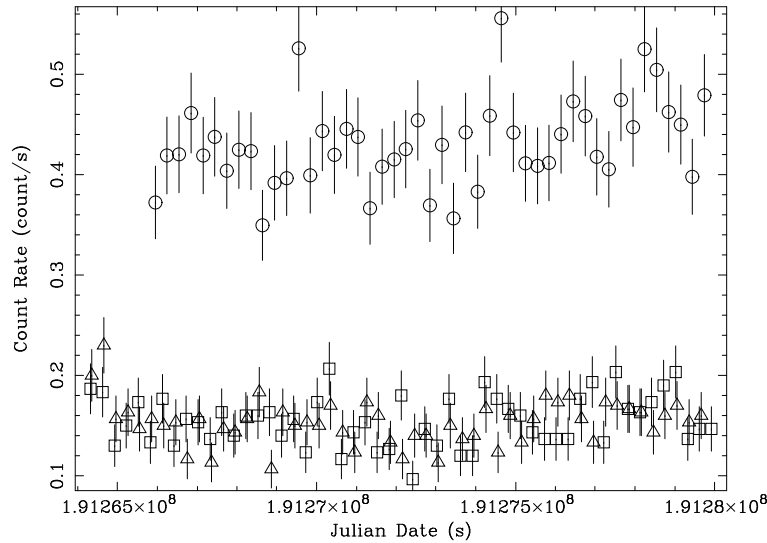


Figure 3.6 **Mrk 993**: Light curves for MOS1(squares), MOS2(triangles) and pn(circles) instruments, after background subtraction, corresponding to the 0.2-10 keV band.

(Doroshenko and Sergeev, 2003). It has been spectroscopically monitored in the optical for about 30 years (Doroshenko and Sergeev 2003, Sergeev et al. 1999). Sergeev et al. (1999) found that the variations of the H_{α} and H_{β} fluxes are delayed relative to the continuous flux variations by about 18 days.

There is also one first XMM-Newton observation (Immler et al., 2003) whose results were in clear opposition to the (non-simultaneous) optical data, the inferred absorbing column density being much higher than that was expected from its measured Balmer decrement. However, the intrinsic column density was derived from a double partial covering model that invokes a extremely complex structure of the inner region around the central engine. On the contrary, Schurch et al. (2006) modelled the X-ray data, from the former and a second XMM-Newton observations in this case, by a more physically motivated multi-layer ionised absorber that would also account for the X-ray variability of this source.

3.3.2 X-ray data

The new XMM-Newton observation of Mrk 6 was performed during revolution 1077 on October 27th 2005 (Observation ID: 0305600501). Only EPIC data were considered in our analysis due to the small number of counts collected in the RGS spectra. EPIC cameras were in full frame, for the pn, and large window, for the MOS1 and MOS 2, imaging mode with Thin1 filters.

Data reduction was carried out in the same way as for Mrk 993 but SAS version was 7.0.0 in this case. After filtering for high background intervals, the

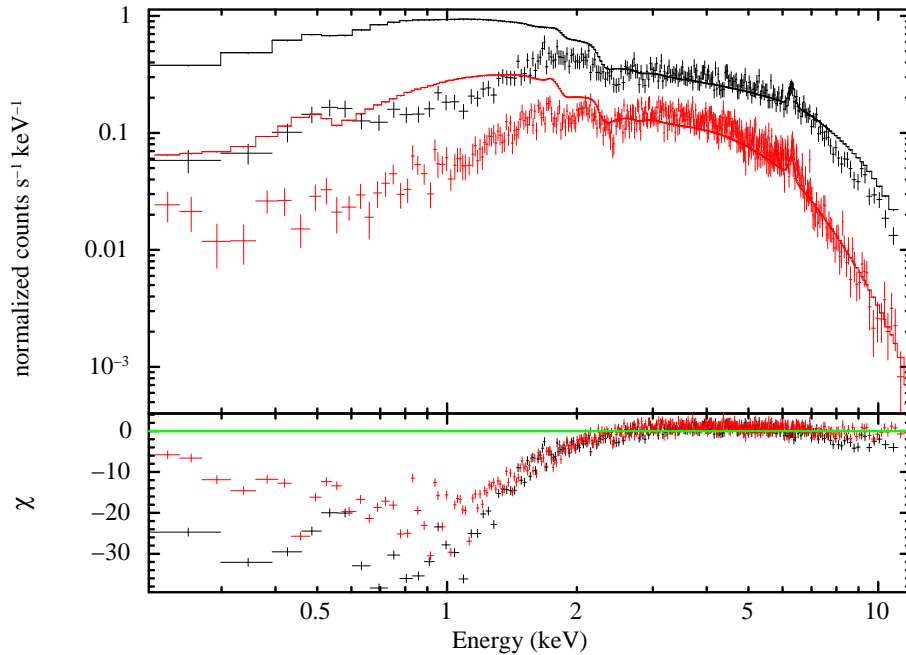


Figure 3.7 **Mrk 6**: 2-10 keV power law model extrapolated to the whole 0.2-12 keV energy range. Solid line corresponds to the fitted $\text{pha}(z\text{po}+z\text{gauss})$ model.

clean exposure times were 6 ks for the pn, and 14 ks for each MOS detector. Source spectra were extracted using circular regions of 40-60 arcsec radii (pn-MOS). To obtain background spectra, nearby source-free circular regions were selected. MOS 1 and MOS 2 data were merged into a single spectrum. Finally, the spectra was binned to at least 30 counts per bin in order to use the χ^2 statistic during the spectral fit.

The spectral fit was performed using XSPEC v12 (Arnaud, 1996), in the 0.2-12 keV energy band jointly for pn and MOS detectors. As a starting point, a simple power law model plus photoelectric absorption from our own Galaxy in the direction of Mrk 6 ($6.39 \times 10^{20} \text{cm}^{-2}$, Dickey and Lockman 1990) was fitted, resulting in a very poor fit ($\chi^2/\text{d.o.f} = 4156/962$), with an extremely flat photon index of $\Gamma \sim 1$ and displaying complex residuals around the model at low energies. In order to better constrain the continuum shape, a power law model was fitted in the 2-10 keV range but a very flat photon index was still obtained ($\Gamma \sim 0.8$). The extrapolation of this model to the whole 0.2-12 keV energy band is shown in Fig. 3.7. We can see a narrow emission line around 6.4 keV, presumably Fe $K\alpha$ from neutral Iron. Fitted as a Gaussian, a value for its equivalent width (EW) of ~ 100 eV is obtained. In the following, this Gaussian fit is included in all models. Besides, we can see that residuals become larger at low and high energies. Low energy residuals are likely due to absorption whereas the high energy residuals along with the flat photon index could suggest a reflection component.

Table 3.4 **Mrk 6**: Best-fit parameters for our 2005 XMM-Newton observation. XSPEC model: pha*zpha(absori(t)(absori(p)*zpo+zpo)+zgaus)

Γ	N_{H} (10^{21} cm^{-2})	$N_{\text{H}}(\text{t})$ (10^{22} cm^{-2})	$\zeta(\text{t})$	$N_{\text{H}}(\text{p})$ (10^{22} cm^{-2})	$\zeta(\text{p})$	Covering fraction (%)	$\chi^2/\text{d.o.f}$
$1.57^{+0.08}_{-0.08}$	$1.6^{+0.5}_{-0.2}$	8^{+3}_{-3}	2100^{+1100}_{-800}	$3.5^{+0.4}_{-0.5}$	5^{+4}_{-4}	91 ± 15	920/956

As next step, photoelectric neutral absorption at the source redshift was included, significantly improving the fit but still being an unacceptable fit ($\chi^2/\text{d.o.f} = 1810/961$). The complex spectral shape at low energies could be also due to ionised absorption, which is a common characteristic in Seyfert galaxies. To model that, the XSPEC `absori` model (Zdziarski et al., 1995) was used, in addition to the neutral absorption and resulting in an improvement on the fit of $> 99\%$ as measured by F-test, but still not resulting in an acceptable fit ($\chi^2/\text{d.o.f} = 1657/959$), and the residuals still suggesting additional absorption. Two models assuming additional ionised absorption were tried, one assuming that the additional absorber covers completely the source, as the previous one, and another one assuming that the additional ionised absorber covers only partially the central source ($\chi^2/\text{d.o.f} = 1062/957$ and $920/956$, respectively). The later, besides its lower value of χ^2 , gives less correlated residuals at low energies. Therefore, we selected this model as our best-fit model for Mrk 6: a power law absorbed by neutral material from our Galaxy and its host galaxy and two layers of an ionised absorber, one of them completely covering the central source and the other one only partially covering it. A narrow emission line is also included corresponding to neutral to low ionisation Iron. The full spectral XSPEC model is: pha*zpha(absori(t)(absori(p)*zpo+zpo)+zgaus) and the best-fit parameters are shown in Table 3.4. The total covering ionised absorber – `absori(t)` – is a highly ionised absorber with a column density twice as large as the one for the partial covering absorber – `absori(p)` – which is nearly neutral given its low value for the ionisation parameter.

In order to better model the high energy region, the results presented for the Mrk 6 BeppoSAX data in Malizia et al. (2003) and Immler et al. (2003) were used. The spectral fit was repeated using the best-fit model plus a Compton reflection component, modelled by `pexrav` in XSPEC (Magdziarz and Zdziarski, 1995) and with the reflection parameter fixed at the values reported in Immler et al. (2003) ($\Gamma=1.81$, $R=1.21$, $\text{cosi}=0.94$), but no significant improvement was obtained, likely due to the lack of enough data at high energies. As a safety test, the high energy data from SWIFT¹ satellite high energy instrument BAT, corresponding to the addition of 22 months of observations, were taken into account. EPIC and BAT data were fitted simultaneously with our best-fit model ($\chi^2/\text{d.o.f} = 966/964$) and

¹<http://heasarc.nasa.gov/docs/swift/swift.html>

with our best-fit model plus a neutral reflection component with the reflection parameters fixed at the Immler et al. (2003) values (933/963). The improvement on the fit was significant, $> 99.99\%$ as measured by F-test, but the only significant difference in the spectral parameters was the value of the photon index.

Two layers of ionised absorption were also used by Schurch et al. (2006) to model the data for the previous two XMM-Newton observations carried out on 2001 and 2003. They pointed out that, whereas Mrk 6 X-ray spectra is usually fit by using partial covering neutral absorption, multi-layer ionised absorption is a more physically motivated model and can easily explain, without assuming strange geometry, the complex variability at soft X-rays for this source. In order to test this argument and with the advantage of having new *XMM-Newton* data and therefore, more information in the time domain, the spectra corresponding to the previous 2001 and 2003 observations were extracted. The spectra corresponding only to the EPIC-pn camera and the three XMM-Newton observations are shown in Fig. 3.8 although data from MOS detectors were also used during the spectral fit. It can be seen how the source has varied in its spectral shape but only at low energies, suggesting changes in the absorbing material. We fitted the three data sets at the same time using our best-fit model plus the reflected component in order to search for variable and constant components. The reflection component is needed in this case, i.e. it significantly improves the spectral fit, probably due to the better quality for the longest observation, the one taken in 2003. We find that the neutral absorption along with the emission line, assuming a constant reflection component, are constant along the three observations, as expected if they arise far from the central source. On the contrary, the two ionised absorbers must vary in column density between the three observations, i.e., the fit was significantly worse when any or the two of them were tied together to be the same for different observations. Regarding the ionisation parameters of the absorbers, only the one corresponding to the full covering absorber is needed to vary, the one corresponding to the partial covering and low ionisation absorber being constant. The values obtained for this fit are shown in Table 3.5 and our 2005 spectra fitted with this best-fit model is shown in Fig. 3.9.

A simple explanation for this behaviour is that the total covering ionised absorber, much more dense and ionised and probably located closer to the central engine, varies as the source flux varies. The partial covering one, almost neutral and likely placed farther from the central source, is less affected by the nuclear emission. The variation in column density and covering fraction, although small for the latter, could be due to the patchy structure of this absorber resulting in different covering fractions and computed column densities as the clouds move around the central source.

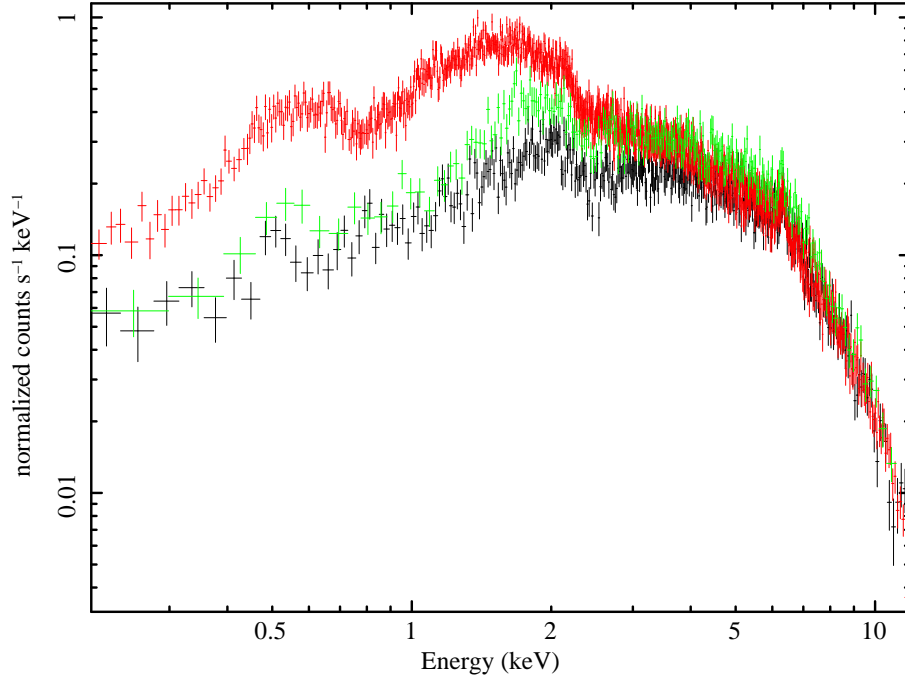


Figure 3.8 **Mrk 6**: EPIC-pn data corresponding to the three XMM-Newton observations. Black, red and green data correspond to 2001, 2003 and 2008 observations, respectively.

Table 3.5 **Mrk 6**: Best fit parameters for the joint fit of the three XMM-Newton observations. XSPEC model: `pha*zpha(absori(t)(absori(p)*zpo+zpo)+zgaus+pextrav)`

Observation	N_{H} (10^{21} cm^{-2})	$N_{\text{H}}(\text{t})$ (10^{22} cm^{-2})	$\zeta(\text{t})$	$N_{\text{H}}(\text{p})$ (10^{22} cm^{-2})	$\zeta(\text{p})$	Covering fraction (%)
2001	$2.00^{+0.14}_{-0.20}$	13^{+3}_{-2}	3000^{+600}_{-500}	$4.3^{+0.3}_{-0.2}$	$6.3^{+2.0}_{-1.2}$	93 ± 6
2003	2.00^{a}	$5.1^{+0.8}_{-0.6}$	1600^{+300}_{-200}	$1.51^{+0.09}_{-0.07}$	6.3^{a}	90 ± 6
2005	2.00^{a}	11^{+2}_{-3}	2900^{+900}_{-1000}	$4.1^{+0.2}_{-0.3}$	6.3^{a}	95 ± 6

^a Fixed at the same value for the three observations.

(t) : corresponding to the ionised absorber totally covering the central source.

(p) : corresponding to the ionised absorber partially covering the central source.

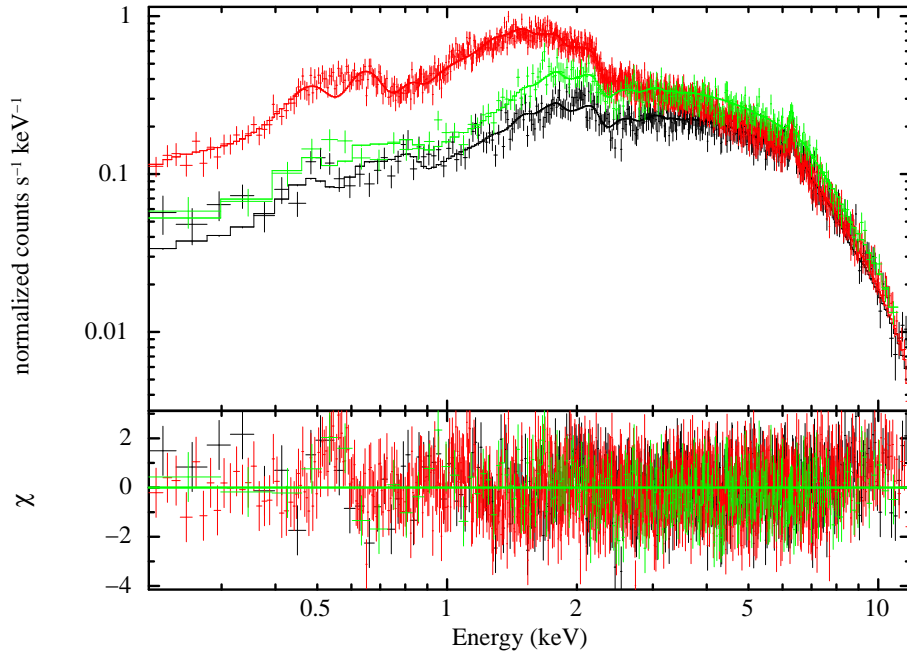


Figure 3.9 **Mrk 6**: best-fit model and data (top) and residuals (bottom) corresponding to the XSPEC model: $\text{pha}(\text{absori}(\tau)(\text{absori}(p)\text{zpo}+\text{zpo})+\text{pexrav}+\text{zgaus})$.

3.3.3 Optical data

Mrk 6 was observed at the 2.2m CAHA telescope on November 1st 2005, only four days after the XMM-Newton observations, with an exposure time of 1800 s. An additional observation was carried out at the same site and with the same instrumental set up about one month later (November 27th) in order to check for possible broad emission line variations within such time scale. As mentioned in Sect. 3.2.4, if there is a time lag between variations in the continuum and the broad lines, even simultaneous observations could catch the source in different states since we are observing different regions in X-rays and in the optical.

The CAFOS spectrograph was used in long-slit mode, with a central wavelength of $\sim 6000 \text{ \AA}$ and a spectral resolution of $\text{FWHM} \sim 6 \text{ \AA}$. As it is described in Sect. 3.2.3, the IRAF package was used to extract the spectra following the same basic procedure. The resulting spectra for the two nights are shown in Fig. 3.10, Mrk 6 being in an optical Sy1.5 state during both nights. As it can be seen in the figure, no significant variations in the broad line profiles seem to be present so only the first observation is considered in the following analysis.

No significant contribution from the host galaxy is detected in the optical spectra of Mrk 6, i.e., no red continuum or stellar absorption bands are observed. Therefore, no host galaxy subtraction was performed in this case. The continuum and the emission lines were fitted at the same time with a model composed of a simple linear component, to reproduce the continuum emission, plus Gaussian

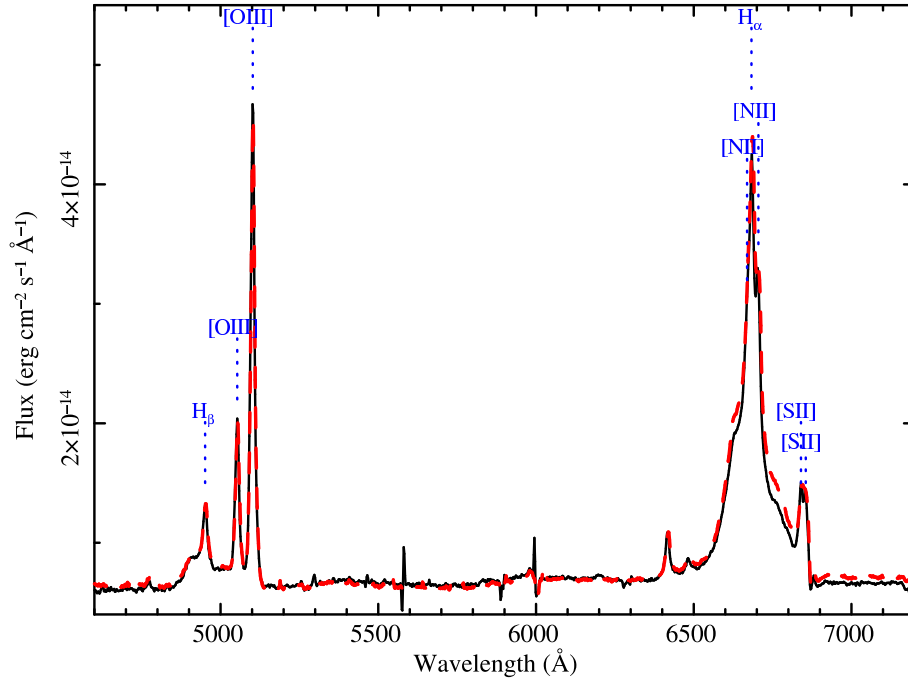


Figure 3.10 **Mrk 6**: CAHA 2.2m CAFOS optical spectra corresponding to the first (solid line) and the second (dashed line) observation.

profiles for each emission line were used in the fit. For the emission lines, both the H_α and H_β regions were fitted at the same time using the following restrictions:

- Emission line velocity widths were tied together for the [OIII], [NII] and [SII] line doublets as well as for the Balmer narrow and broad lines, separately.
- In order to deal with the line blends (as in the H_α region), we forced the doublets line intensity ratios to follow their theoretical relations (Osterbrock, 1989):

$$\begin{aligned} I([\text{OIII}]\lambda 5007)/I([\text{OIII}]\lambda 4958) &= 3 \\ I([\text{NII}]\lambda 6583)/I([\text{NII}]\lambda 6548) &= 3 \\ I([\text{SII}]\lambda 6730)/I([\text{SII}]\lambda 6718) &= 1 \end{aligned}$$

- Central energies for the narrow and broad emission lines were fixed at the same redshift separately.

Broad Balmer lines in Mrk 6 display a complex shape. In order to reproduce this shape two Gaussian lines both for H_α and H_β are needed, one shifted to shorter wavelengths (hereafter blue component) and the other to longer wavelengths (red component) with respect to the central energy defined by the narrow components. The resulting fit for the H_α and H_β regions is shown in Fig. 3.11, and the values

Table 3.6 Mrk 6: Optical line fluxes and FWHM.

Line	Intensity(10^{-14} erg cm $^{-2}$ s $^{-1}$)	FWHM(km s $^{-1}$)
H $_{\beta}$ (n)	$6.1^{+0.4}_{-0.2}$	780 ^a
H $_{\beta}$ (b)blue	$28.4^{+0.9}_{-0.8}$	6000 ^b
H $_{\beta}$ (b)red	$7.7^{+0.4}_{-0.8}$	3680 ^b
[OIII] λ 4958	$21.2^{+0.1}_{-0.1}$	860
[OIII] λ 5007	63.6 ^d	860 ⁺¹⁰ ₋₁₀
[NII] λ 6548	$6.98^{+0.01}_{-0.01}$	610 ^c
H $_{\alpha}$ (n)	$38.2^{+0.1}_{-0.1}$	780 ⁺¹⁰ ₋₁₀
H $_{\alpha}$ (b)blue	213^{+1}_{-1}	6000 ⁺¹⁰ ₋₅₀
H $_{\alpha}$ (b)red	$29.3^{+0.1}_{-0.1}$	3680 ⁺⁷⁰ ₋₆₀
[NII] λ 6583	21.0 ^d	610 ⁺¹⁰ ₋₁₀
[SII] λ 6718	9.5 ^d	550 ^c
[SII] λ 6730	$9.5^{+0.2}_{-0.2}$	550 ⁺²⁰ ₋₂₀

- ^a Fixed at the same σ (km s $^{-1}$) as H $_{\alpha}$ (n) narrow.
^b Fixed at the same σ (km s $^{-1}$) as H $_{\alpha}$ (b) broad for the corresponding wing.
^c Fixed at the same σ (km s $^{-1}$) as the other line in the doublet.
^d Forced to keep the theoretical line ratio for the corresponding doublet.

obtained are listed in Table 3.6. Using the measured line intensities, the following Balmer decrements were computed for the NLR and The BLR:

$$\frac{H_{\alpha}}{H_{\beta}}(\text{NLR}) = 6.3 \pm 0.3, \quad \frac{H_{\alpha}}{H_{\beta}}(\text{BLR}) = 6.7 \pm 0.2$$

However, it has to be noted that the resulting ratio for the H $_{\beta}$ blue to red components is ~ 3.7 whereas it is larger than 7 for the H $_{\alpha}$ broad components. This can be due to Fe II emission line blends, not taken into account during the spectral fit, affecting the fit of the red H $_{\beta}$ component and thus resulting in a larger value for it. The ratio between the H $_{\alpha}$ red and blue components is much better constrained than the one corresponding to the H $_{\beta}$ broad components, likely due to a better constrained continuum. To better compute the Balmer decrement (BD) for the BLR, the H $_{\beta}$ broad components ratio was assumed to be the same as for the H $_{\alpha}$ broad components. From this assumption, an estimate of the intensity of the H $_{\beta}$ red component is obtained and from that, a Balmer decrement for the BLR of BD(BLR)=7.5 \pm 0.3.

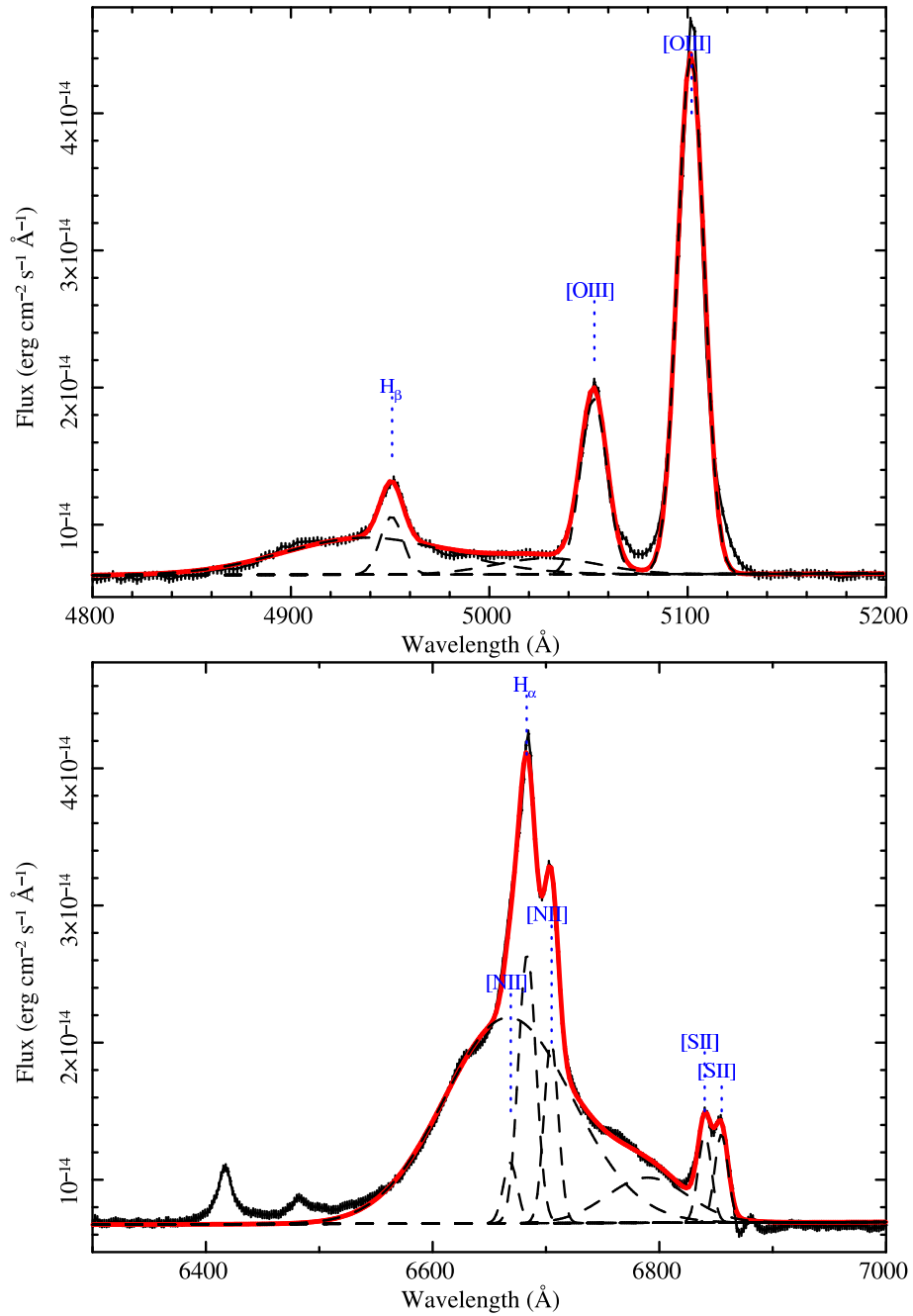


Figure 3.11 **Mrk 6**: Optical spectral fit in the H_β (top) and H_α (bottom) regions. Solid line correspond to the best-fit model. Dashed line correspond to each Gaussian component.

Table 3.7 **Mrk 6**: Luminosity and fluxes for the joint fit of the three XMM-Newton observations.

Observation year	Flux 2 – 10 keV (erg cm ⁻² s ⁻¹)	Luminosity 2 – 10 keV (erg s ⁻¹)
2001	1.22×10^{-11}	9.6×10^{42}
2003	1.44×10^{-11}	1.13×10^{43}
2005	1.65×10^{-11}	1.29×10^{43}

3.3.4 Discussion and results

From the BD computed in the optical, assuming as in Sect. 3.2.4 a standard gas-to-dust ratio, an estimate of the intrinsic column density can be obtained. For the NLR we estimate a $N_H \sim 4 \times 10^{21} \text{cm}^{-2}$. For the BLR and taking into account the two different computed values for the BD, we estimate a $N_H \sim 3.5\text{-}4.1 \times 10^{21} \text{cm}^{-2}$. In X-rays, we measured a $N_H \sim 2 \times 10^{21} \text{cm}^{-2}$ plus almost neutral partial covering absorption of $N_H \sim 4 \times 10^{22} \text{cm}^{-2}$. The distance for this later absorber from the central source is unknown and so it is its corresponding gas-to-dust ratio. Since its ionisation parameter is not zero, it could be close enough to the central source so that part of the dust would have sublimated thus reducing its reddening effect over the BLR. However, the distance of this absorber to the central source should be large enough to allow no variations in its ionisation state within the 4 years between XMM-Newton observations. Feldmeier et al. (1999) estimated a dust sublimation radius for Mrk 6 of ~ 25 light days. Assuming that the partial covering absorber is located within this radius, from its ionisation parameter we estimate a electronic density of $\sim 10^7\text{-}10^8$, consistent with the material being located within the BLR, which is unlikely to contain significant amounts of dust. Immler et al. (2003) found a flux variation of $\sim 60\%$ between the ASCA, BeppoSAX and the first XMM-Newton observation. For this flux variability, the ionisation state of the material located within the BLR could change appreciably. However, by comparing the fluxes for the three XMM-Newton observations, we only find a variation of $\sim 25\%$ (see Table 3.7) that would allow variations in the ionisation parameter between 4.8 and 7.8, well within our computed errors. Therefore, in the case of Mrk 6, the measured amount of X-ray obscuration is consistent with the observed optical spectral type.

The shape of the broad components classified Mrk 6 as a “double-peaked emitter”, although the separation between its red and blue profiles is not as large as for the archetypes 3C 390.3 and Arp 102B. The physical origin of these double-peaked profiles is still a matter of controversy. The most widely accepted scenario is emission from a accretion disk slab. Within this scenario, the line profile is due

to emission from the accretion disk and it would be double-peaked due to Doppler effect. The reason why this double-peaked profile is not seen in all galaxies could be due to the inclination angle, if we see the source face-on we will see a single-peaked profile. Another reason could be radio-loudness. Radio loud sources tend to display broader line profiles, thus allowing us to distinguish the two peaks only if the source is radio loud. Observations supporting this scenario are the variability of the line profiles, that follows what it is expected for a rotating disk, and the fact that double-peaked sources are more often found in Sy1.5 radio-loud objects, although not in powerful radio sources for which the jet emission outshines the disk emission (see [Strateva et al. 2008](#) and references therein). However, there are still many open questions about double-peaked sources, for example why double-peaked profiles are not observed in all radio loud Sy1.5. Besides, the estimated ionising luminosity coming from the disk and computed by using the broad lines fluxes, turns to be too large when compared to the disk luminosity obtained at other wavelengths. Where does the extra-illumination of the disk come from? A model by [Cao and Wang \(2006\)](#) proposes that the origin of the extra-illumination is the presence of jets in RL double-peaked AGN and slower outflows with large column densities ($N_H > 10^{23} \text{ cm}^{-2}$) in the case of RQ double-peaked AGN. The total covering ionised absorber detected in Mrk 6 is consistent with this scenario. However, in order to characterise the properties of these ionised outflows, high quality data with high spectral resolution at low energies are needed. Unfortunately, the RGS data for Mrk 6 do not have enough quality to perform this kind of analysis.

3.4 NGC 7603

3.4.1 Previous observations

NGC 7603 is a Seyfert galaxy at redshift $z=0.029524$ ([Huchra et al., 1999](#)). Its SMBH mass has been estimated from the host galaxy stellar velocity dispersion to be $M_{r_{\text{MBH}}} \sim 1.2 \times 10^8 M_{\odot}$ ([Woo, 2005](#)). Its AGN bolometric luminosity, estimated from the construction of its SED, is $L_{\text{bol}} \sim 4 \times 10^{44} \text{ erg s}^{-1}$, which leads to an Eddington ratio of $L/L_{\text{Edd}} \sim 0.03$.

This source has shown variability from type 1 to 1.9 and back again to 1 over a period of about a decade. It has been spectroscopically monitored in the optical for more than twenty years ([Kollatschny et al., 2000](#)) but there was no good quality spectral information in the X-ray band.

3.4.2 X-ray data

Our XMM-Newton observation of NGC 7603 was performed on June 14th 2006 during revolution 1193 (OBSID: 0305600601). The EPIC-pn camera operated in small window imaging mode, and MOS 1 and MOS 2 cameras, due to the

large count rate for this source, operated in timing mode. Due to that, spectral extraction for the MOS cameras was carried out in a different way as the one described in Sect. 3.2.2, which was applied only to the pn data in this case with a circular extraction region of 60 arcsec. SAS version 7.1.0 was used in this case. In timing mode, the RAWY detector coordinate does not represent spatial information but timing information. So, in order to extract the spectra, instead of using a sky circular region, a rectangular region in detector coordinates is used. Its width represents the actual sky width and its length represents the exposure time. The background region for the pn data was a circular source free region nearby, and for the MOS cameras, a rectangle from the outer CCDs. The resulting good time intervals after removing background flares are 11 ks and 10 ks for the pn, and each MOS detector, respectively. MOS 1 and MOS 2 data were merged together and all the spectra were binned to at least 50 counts per bin in order to use χ^2 statistics.

XSPEC v12 (Arnaud, 1996) was used for the spectral fit. First, a single power law modified by photoelectric absorption was fitted in the 2-10 keV band, obtaining a photon index of $\Gamma \sim 1.9$ ($\chi^2/\text{d.o.f.} = 455/366$). An emission line can be seen around 6.4 keV, the Fe K α line. Modelling it with a Gaussian profile its width turns to be $\sigma \sim 200$ eV (435/363). Trying a Laor (Laor, 1991) relativistic profile for a maximally rotating black hole gives the same fit in terms of χ^2 . The Gaussian profile was kept for simplicity in the following fits, with a measured central energy of $E = 6.37_{-0.10}^{+0.06}$ eV, width $\sigma = 210_{-100}^{+60}$ eV and $\text{EW} = 160 \pm 20$ eV.

The extrapolation of this 2-10 keV power law fit to the whole 0.2-12 keV band is shown in Fig. 3.12. There seems to be a mismatch between pn and MOS data around 2.5 keV and similar features at lower energies. Given that MOS data come from observations in timing mode (most likely less well calibrated than other modes), we decided to perform the rest of the analysis only considering pn data. As it can be seen in Fig. 3.12, there are positive residuals at low and at high energies. The single power law fit gives a poor fit ($\chi^2/\text{d.o.f} = 1528/732$) and no intrinsic absorption was needed.

The low energy residuals when extrapolating the 2-10 power law fit constitute the evidence for a ‘‘Soft-excess’’. Soft-excess is a common feature observed in AGN. As explained in Sect. 2.4.1, featureless Soft-excess emission is usually represented by continuum emission models, like black-body emission. Applying the phenomenological black body model, we obtain a poor fit and residuals at low energies that indicate that the soft-excess is not featureless in this case. Adding ionised absorption (XSPEC `absori` model) to the power law fit in order to reproduce the low energy features did not improve the fit. Models based on atomic processes have been proved to be successful in reproducing this kind of soft-excess emission: velocity-smearred absorption from a disk wind and ionised reflection relativistically-blurred by motion in an accretion disk (see again

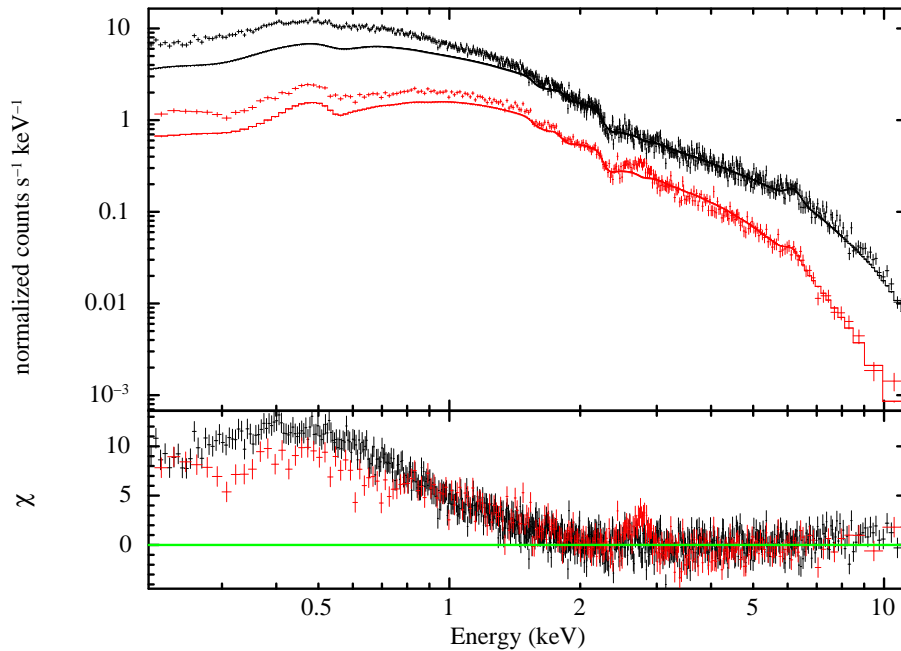


Figure 3.12 NGC 7603: 2-10 keV power law model extrapolated to the whole 0.2-12 keV energy range. Solid line corresponds to the fitted $\text{pha}(\text{zpo}+\text{zgauss})$ model.

Sect. 2.4.1 and Middleton et al. 2007 and Crummy et al. 2006 for the application of each model over the same AGN sample, respectively).

The ionised reflection model described in Crummy et al. (2006) was tried (XSPEC model: $\text{pha}(\text{kdblur}(\text{zpo}+\text{reflion}))+\text{zgauss}$). The resulting fit was acceptable (856/723), but some high energy positive residuals can be still seen. Finally, velocity-smearred absorption from a disk wind described in Middleton et al. (2007) was also tried (XSPEC model: $\text{pha}(\text{swind1}(\text{zpo}*\text{xion}))+\text{zgauss}$). This model turned to be also an acceptable fit that significantly improves the power law fit (820/723). Results for these last two models are shown in Fig. 3.13 and in Table 3.8. Unfortunately, these two models are indistinguishable in the energy range covered by *XMM-Newton*. High quality data at energies above 10 keV is needed since it is above these energies where they become significantly different. As for Mrk 6, data at high energies are available from the SWIFT-BAT instrument. Extrapolating the two models at BAT energies (14-200 keV), the velocity-smearred absorption model appears to reproduce the high energy data better. The measured 14-200 keV BAT flux is $\sim 4.7 \times 10^{-11} \text{ erg cm}^{-2} \text{ s}^{-1}$. The velocity-smearred absorption model extrapolated to BAT energies gives a similar flux of $\sim 4 \times 10^{-11} \text{ erg cm}^{-2} \text{ s}^{-1}$, whereas the relativistically-blurred reflection model underpredicts this flux giving an estimation of the order $\sim 3 \times 10^{-11} \text{ erg cm}^{-2} \text{ s}^{-1}$.

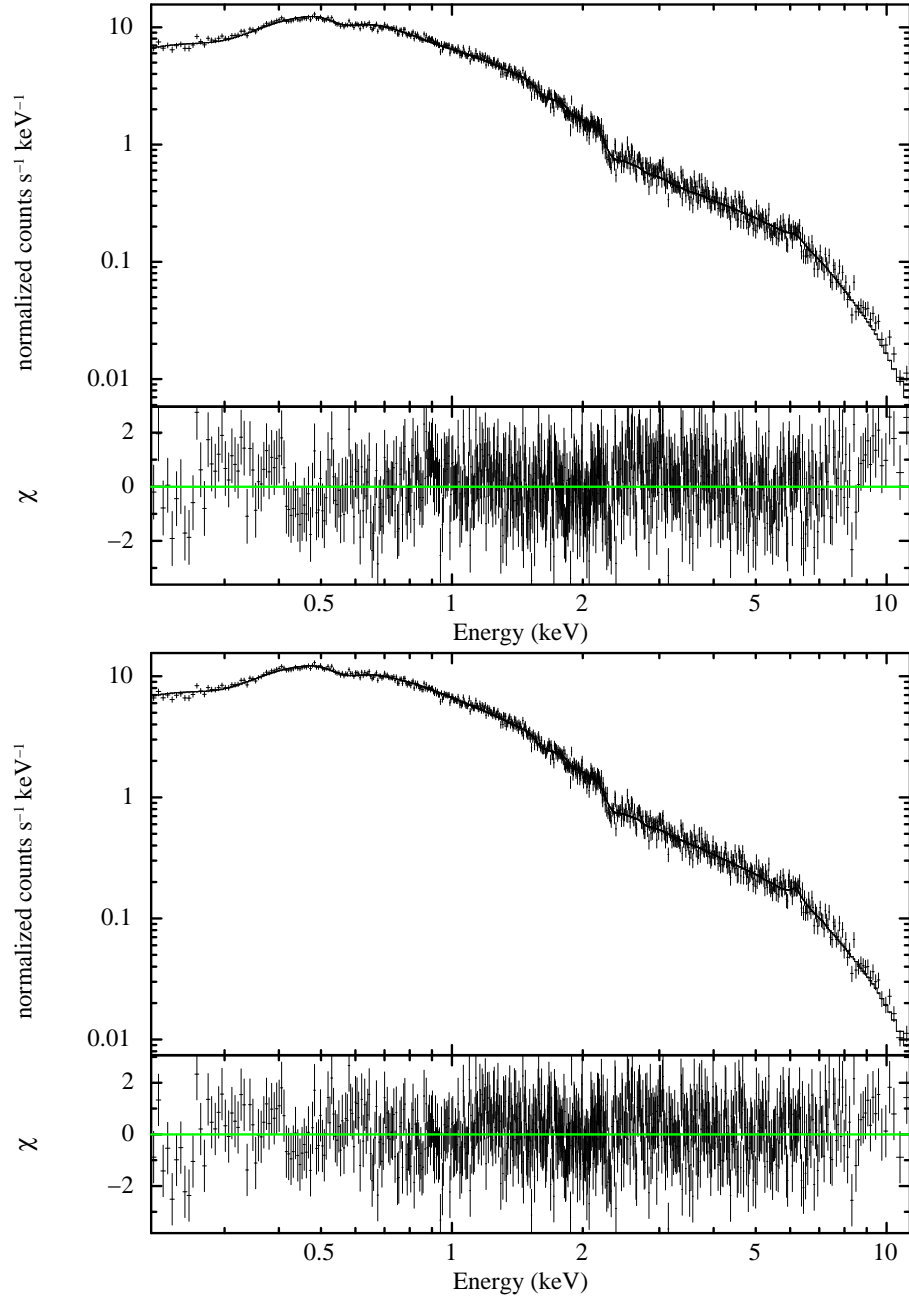


Figure 3.13 **NGC 7603**: best-fit model and data corresponding to the relativistically-blurred ionised reflection (top) and to the velocity-smearing disk wind seen in absorption (bottom) models .

Table 3.8 NGC 7603: X-ray best-fit models and parameters.

Relativistically	blurred	ionised	reflection				
Γ	Em.Ind.	R_{in} (gravitational radii)	i (degrees)	Fe	ζ	Frac (%)	$\chi^2/d.o.f$
$1.86^{+0.12}_{-0.05}$	$8.9^{+0.6}_{-0.8}$	$1.24^{+0.02}_{-1.24}$	$70.7^{+1.2}_{-7}$	$0.43^{+0.05}_{-0.07}$	1100^{+500}_{-500}	$0.8^{+0.4}_{-0.4}$	856/723
Velocity	smeared	ionised	absorption				
Γ	N_{Hi} (10^{22} cm^{-2})	ζ	Ratio				$\chi^2/d.o.f$
$2.093^{+0.007}_{-0.011}$	31^{+5}_{-5}	2500^{+400}_{-200}	$0.6^{+0.4}_{-0.4}$				820/723

Γ : photon index. Em. Ind.: disk's emissivity index; R_{in} : disk's inner radius in gravitational radii; i: inclination in degrees. Fe: Iron abundance of the disk relative to solar. ζ : ionisation parameter. Frac.: ratio of reflected emission to total emission; N_{Hi} : hydrogen column density of the ionised absorber. Ratio: ratio of X-ray to intrinsic disk illumination.

3.4.3 Optical data

Our optical observation of NGC 7603 was carried out at the G.D. Cassino telescope at the Loiano observatory on August 4th 2006. In this case, no later observation was taken. The BFOSC spectrograph in long-slit mode was used with two different grisms with central wavelengths ~ 6000 and 7000 \AA and a spectral resolution $\sim 3\text{\AA}$. The exposure time for each configuration was 900s.

The standard data reduction procedure using IRAF was applied again obtaining the spectrum shown in Fig. 3.14, NGC 7603 being in a Sy1-Sy1.2 state. The continuum in this case is complex, including several emission line blends such as Fe II blends at various wavelengths and also displaying a steep continuum. We fit the spectra using two power laws and 3 broad Gaussian lines, to account for the continuum shape, and one Gaussian line for each emission line. As for Mrk 6, NGC 7606 Balmer emission lines show a complex profile. Two broad Gaussians shifted to shorter (broad blue component) and longer (broad red component) wavelengths are needed in order obtain a good fit. A double-peaked profile, however, it is not as clearly present as for Mrk 6. The shape of NGC 7603 broad emission lines is much more complex and asymmetric than for Mrk 6, as already pointed out in Kollatschny et al. (2000). In that work, the authors reported extreme changes in the broad emission lines both in shape and in amplitude, making NGC 7603 one of the most variable Seyfert galaxies known to date. They even reported a change in the way the BLR responds to changes in the ionising continuum. The H_{β} line intensity was found to correlate with the continuum flux in all epochs, as predicted by photoionisation models. However, during the

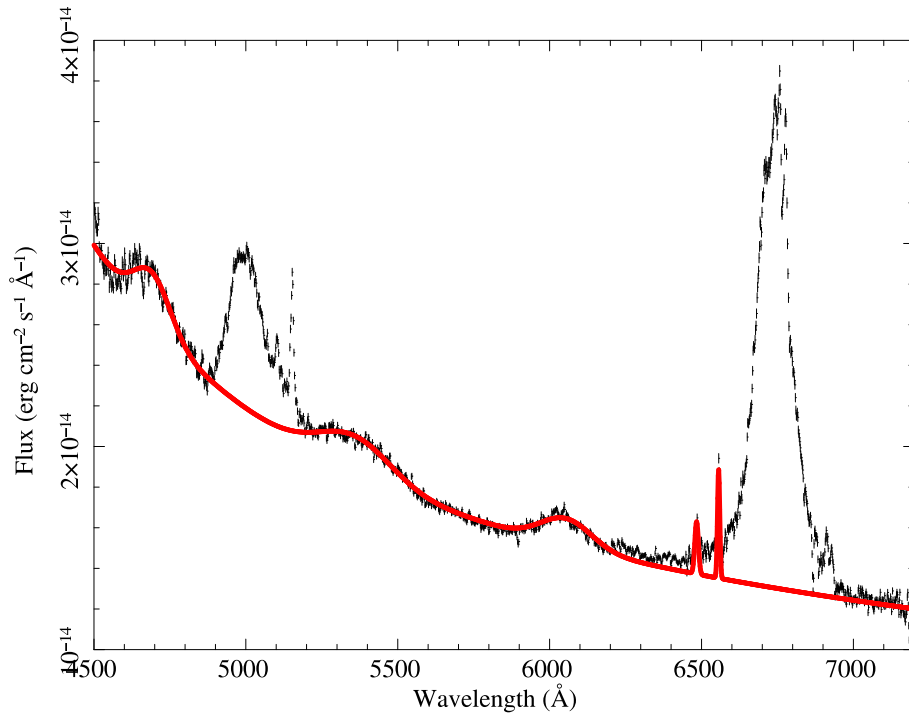


Figure 3.14 **NGC 7603**: Loiano 152cm BFOSC optical spectra. The solid line corresponds to the adopted continuum during the spectral fit.

first half of the monitoring campaign, the BD anti-correlated with respect to the H_{β} intensity, whereas for the last part of the campaign, it remained between ~ 3 -4 despite of the H_{β} intensity variations. The proposed explanations were an intrinsic change of the BLR conditions or a change in the dust absorption.

Given the complexity of the broad lines behaviour in this source, our parametrisation of the broad components must be considered as an estimate since the underlying actual shape could be much more complex than two Gaussian lines. The same restrictions as for Mrk 6 emission line intensities and widths were applied in this case with the only difference being the narrow H_{β} line intensity. Due to the relative weakness of the narrow component respect to the broad one, we were forced to assume the intrinsic Balmer ratio of 3 for the NLR in order to derive an estimate of the narrow H_{β} intensity. The resulting fit is shown in Fig. 3.15 and the values obtained are listed in Table 3.9.

The ratio between the broad blue and red components is found again to be much larger for H_{α} (~ 10) than for H_{β} (~ 1), again likely due to contamination of blended lines for the red component of H_{β} . Using the values in Table 3.9, we obtain a value for the Balmer decrement of the BLR, $BD(BLR)=2.77\pm 0.03$, a value lower even than the expected value for the “case-B” recombination. It is clear then, than the H_{β} red component is very much affected by features of the continuum.

Table 3.9 NGC 7603: Optical line intensities and FWHM.

Line	Intensity($10^{-14}\text{erg cm}^{-2} \text{s}^{-1}$)	FWHM(km s^{-1})
$H_{\beta}(\text{n})$	2.0 ^d	550 ^a
$H_{\beta}(\text{b})\text{blue}$	54.5 ^{+0.6} _{-0.6}	6060 ^b
$H_{\beta}(\text{b})\text{red}$	61.9 ^{+1.0} _{-0.5}	10900 ^b
[OIII] λ 4958	2.56 ^{+0.06} _{-0.06}	690 ^c
[OIII] λ 5007	7.68 ^d	690 ⁺³⁰ ₋₁₅
[NII] λ 6548	2.4 ^{+0.1} _{-0.1}	390 ^c
$H_{\alpha}(\text{n})$	5.9 ^{+0.2} _{-0.3}	550 ⁺³⁰ ₋₂₀
$H_{\alpha}(\text{b})\text{blue}$	293 ⁺¹ ₋₁	6060 ⁺¹⁰ ₋₂₀
$H_{\alpha}(\text{b})\text{red}$	29.8 ^{+0.1} _{-0.1}	10900 ⁺¹⁰⁰ ₋₁₀₀
[NII] λ 6583	7.2 ^d	390 ⁺¹⁰ ₋₂₀
[SII] λ 6718	2.5 ^d	550 ^c
[SII] λ 6730	2.5 ^{+0.2} _{-0.2}	550 ⁺²⁰ ₋₄₀

- ^a Fixed at the same $\sigma(\text{km s}^{-1})$ as $H_{\alpha}(\text{n})$ narrow.
- ^b Fixed at the same $\sigma(\text{km s}^{-1})$ as $H_{\alpha}(\text{b})$ broad for the corresponding wing.
- ^c Fixed at the same $\sigma(\text{km s}^{-1})$ as the other line in the doublet.
- ^d Forced to keep the theoretical line ratio for the corresponding doublet.

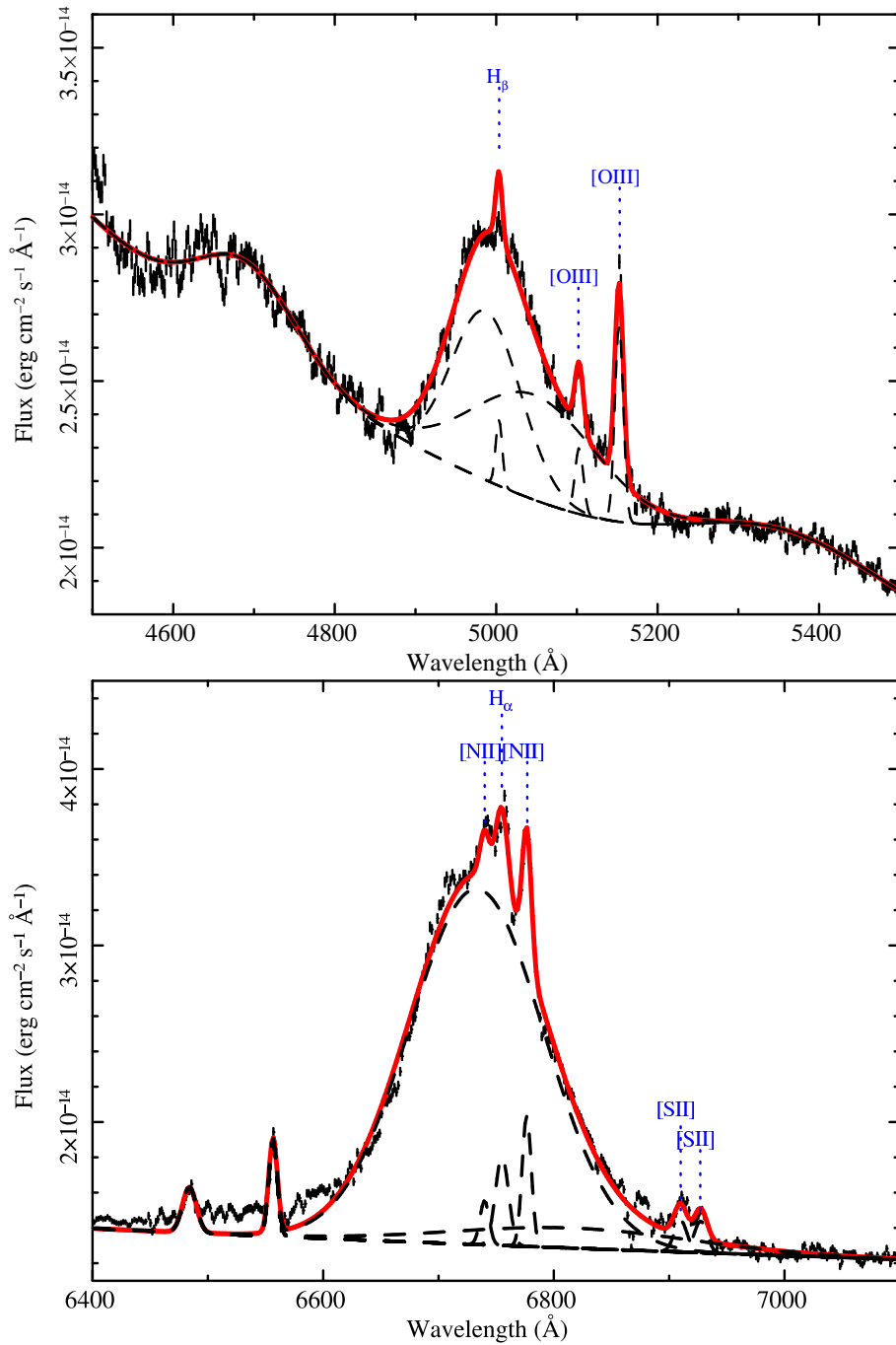


Figure 3.15 NGC 7603: Optical spectral fit in the H β (top) and H α (bottom) regions. Solid line correspond to the best-fit model. Dashed lines correspond to each Gaussian component.

Forcing the blue to red component ratio to be the same as for the H_α component, we obtain $\text{BD}(\text{BLR})=4.79\pm 0.08$. The BD for the NLR is likely larger than the assumed intrinsic value of 3, as it can be seen in Fig. 3.15, so our fit overestimates the narrow H_β component. Leaving the narrow H_β line intensity free and adding the broad and narrow Balmer components, we compute an average Balmer decrement of $\text{BD} \sim 3$ for the BLR, consistent with the values reported in [Kollatschny et al. \(2000\)](#).

3.4.4 Discussion and results

From the BD computed in the optical, assuming as in Sect. 3.2.4 a standard gas-to-dust ratio, an estimation of the intrinsic column density can be measured. We estimate a $N_H < 2 \times 10^{21} \text{cm}^{-2}$ as an average value for the NLR and the BLR. Due to the blending of the H_β broad and narrow components, the derived lower limit for this quantity is consistent with zero. No neutral absorption was measured in the X-ray band with an upper limit at 3σ confidence level of $N_H < 3 \times 10^{20} \text{cm}^{-2}$. Significant amounts of ionised absorption are detected if we consider the velocity-smearred ionised absorption model, but its very high ionisation parameters suggests a practically dust-free region. Therefore, optical and X-ray data give consistent results in this case in terms of intervening absorption. The most likely explanation for the optical changes in this source seems to be a change in the BLR itself.

As in the case of Mrk 6, the optical broad emission lines in NGC 7603 seem to have a double-peaked shape. If we consider the velocity-smearred ionised absorption, this source would also be in agreement with the [Cao and Wang \(2006\)](#) scenario in which double-peaked lines arise from an accretion disk slab illuminated by a high column density outflow. Unfortunately, as for Mrk 6, the low quality of the RGS data do not allow us to further test this scenario.

3.5 Mrk 1018

3.5.1 Previous observations

Mrk 1018 is a Seyfert galaxy at redshift $z=0.042436$ ([Huchra et al., 1999](#)). Its SMBH mass has been estimated from the host galaxy stellar velocity dispersion to be $M_{\text{BH}} \sim 1.2 \times 10^8 M_\odot$ ([Woo, 2005](#)). Its AGN bolometric luminosity, estimated from the construction of its SED, is $L_{\text{bol}} \sim 2.4 \times 10^{44} \text{erg s}^{-1}$, which lead to an Eddington ratio of $L/L_{\text{Edd}} \sim 0.02$.

This AGN was among the first to be classified as a Seyfert 1.9 galaxy by [Osterbrock \(1981\)](#), on the basis of a broad H_α component and absence of any H_β broad component. However, [Cohen et al. \(1986\)](#) conducted new optical and IUE observations of this AGN in 1984 and found only broad H_α and H_β lines, plus a broad

$\text{Ly}\alpha$ line, resulting in an unambiguous Seyfert 1 classification.

3.5.2 X-ray data

Our XMM-Newton observation of Mrk 1018 was performed on August 7th 2008 during revolution 1586 (OBSID: 0554920301), EPIC instrumental configuration being large (MOS cameras) and small (pn) window imaging mode with medium filters. SAS v9.0.0 was used to reduced the X-ray data that, after removing high background intervals, gave clean exposure times of 17 ks and 14 ks for each MOS camera and the pn camera, respectively. There is also another *XMM-Newton observation*, performed in 2005, also belonging to our observational campaign, but which was very much affected by high background intervals leaving only a clean exposure time of 2ks and only in the MOS cameras. These data, due to their poor quality, will be only used to search for variability in a qualitative way.

Source spectra were extracted in circular regions of 40 arcsec radii and background spectra in circular nearby source-free regions of double that size. As for Mrk 6 and NGC 7603, MOS 1 and MOS 2 spectra were merged into a single spectrum. Finally, MOS and pn spectra were binned to at least 50 counts per bin in order to use χ^2 statistics.

First, a single power law modified by photoelectric absorption from our own galaxy ($2.58 \times 10^{20} \text{cm}^{-2}$, [Dickey and Lockman 1990](#)) was fitted on the 2-10 keV band, obtaining a $\Gamma \sim 1.8$ ($\chi^2/\text{d.o.f} = 558/483$). Fitting jointly the 2005 and 2008 gives the same fit, both the source flux and the measured photon index consistent within errors for the two observations. Some positive residuals resembling emission lines can be seen at ~ 6 and 6.7 keV (observed frame). Using narrow Gaussian profiles to fit these lines we obtain significant improvement in the fit ($\chi^2/\text{d.o.f} = 503/477$) and the following line parameters:

$$E = 6.32_{-0.04}^{+0.15} \text{ keV} \quad \text{EW} = 120 \pm 30 \text{ eV}$$

$$E = 7.1_{-0.2}^{+0.4} \text{ keV} \quad \text{EW} = 70 \pm 40 \text{ eV}$$

The lowest energy line likely corresponds to Fe $K\alpha$ emission from neutral Iron. The highest energy one, given the large ratio to the lowest energy one, is unlikely to be Fe $K\beta$ from the same neutral material but more likely, emission from highly ionised Iron. Using a relativistic Laor profile instead of the two Gaussians ([Laor, 1991](#)) also improves the fit ($\chi^2/\text{d.o.f} = 512/477$), but slightly worse than the previous one and leaving positive residuals around 6 keV, so the two-Gaussian fit will be kept in the following models.

Extrapolating this power law fit to the whole energy range, the results shown in Fig. 3.16 are obtained, the source displaying a large soft-excess. Fitting the whole band with this simple model gives a poor fit (1905/970) that does not

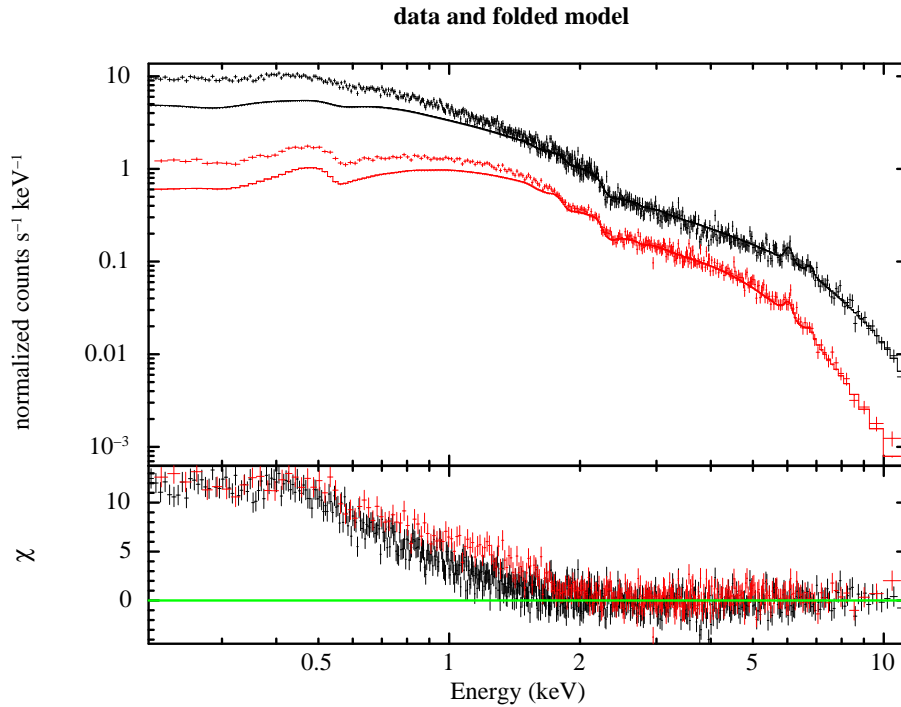


Figure 3.16 **Mrk 1018**: 2-10 keV power law model extrapolated to the whole 0.2-12 keV energy range. Solid line corresponds to the fitted $\text{pha}(\text{zpo}+\text{zgauss}+\text{zgauss})$ model.

improve by adding neutral absorption at the source redshift. Modelling the soft-excess with a black body component gives still a poor fit ($\chi^2/\text{d.o.f} = 1303/968$). The fitted black body temperature is ~ 100 eV. Besides, as in NGC 7603, the residuals at low energies show some structure.

Adding an ionised absorber significantly improves the fit ($\chi^2/\text{d.o.f} = 1356/965$) but now residuals can be appreciated at high energies, and edge-shaped residuals can be still seen at low energies. Multi-layer ionised absorbers have proved successful in reproducing the spectral shape of several Seyfert galaxies (see for example [Blustin et al. 2005](#) and Sect. 3.3.2). We found that adding another ionised absorber significantly improves the fit ($\chi^2/\text{d.o.f} = 1309/966$), the high energy positive residuals, however, remaining the same.

In order to constrain a possible reflection component, data from SWIFT-BAT were taken into account as it was done for Mrk 6 and NGC 7603. A neutral reflection component (XSPEC model `pexrav`) was added so that the extrapolation of our model fitted the high energy flux from SWIFT-BAT. In this way, the neutral reflection fraction was estimated to be $R = 0.18 \pm 0.03$ (fixing the inclination angle to 60 degrees). For the EPIC data, the addition of this component significantly improved the spectral fit ($\chi^2/\text{d.o.f} = 1119/966$). The results for this spectral fit are

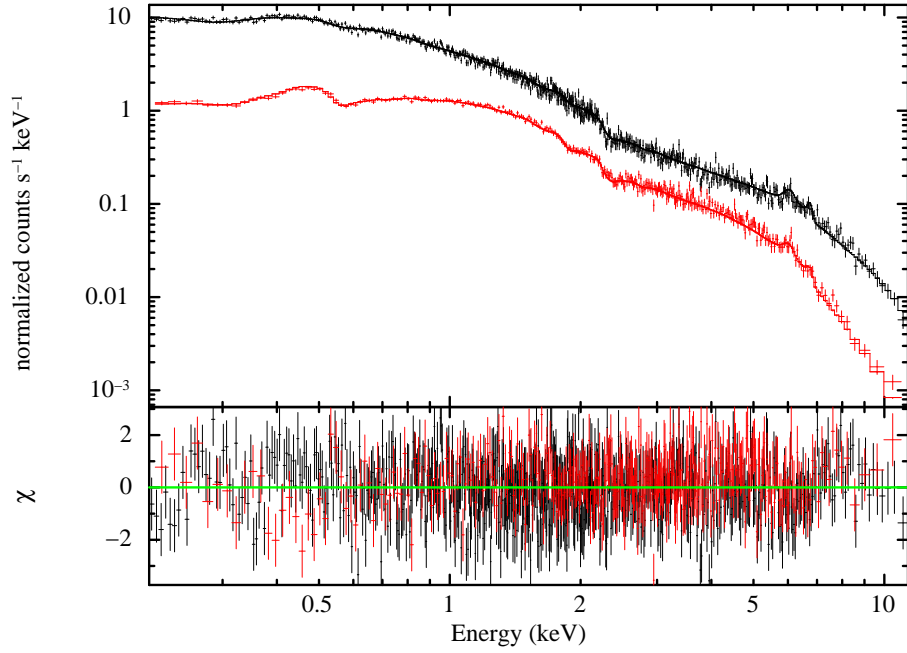


Figure 3.17 **Mrk 1018:** best-fit model and data (top) and residuals (bottom) corresponding to the XSPEC model: `pha(absori(1)*absori(2)zpo+pexrav+zgauss+zgauss)`.

Table 3.10 **Mrk 1018:** X-ray best-fit models and parameters. XSPEC model: `pha(absori(1)*absori(2)zpo+pexrav+zgauss+zgauss)`

Γ	$N_{\text{H}_i}(1)$ 10^{20} cm^{-2}	$\zeta(1)$	$N_{\text{H}_i}(2)$ 10^{21} cm^{-2}	$\zeta(2)$	R	$\chi^2/\text{d.o.f.}$
$2.17^{+0.01}_{-0.01}$	3^{+3}_{-2}	20^{+50}_{-12}	7^{+6}_{-4}	2000^{+3000}_{-100}	0.18 ± 0.03	1119/966

shown in Fig. 3.17 and in Table 3.10.

The relativistically-blurred reflection model (Crummy et al., 2006) was also tried and an acceptable fit was obtained (1142/963). The velocity-smearred disk wind model (Middleton et al., 2007) gives also an acceptable fit (1137/961). However, since these two models are indistinguishable and multi-layer ionised absorbers are commonly detected in high quality X-ray spectra (as it is shown also in Sect. 3.3.2), we selected our two-layer ionised absorber as our best-fit model.

3.5.3 Optical data

Mrk 1018 was observed twice at the 2.2m CAHA telescope on July 31st and September 2nd 2008 with total exposure times of 1800s and 3600s, respectively, divided into two exposures of equal duration each. As for Mrk 6, the spectrograph used was CAFOS in long-slit mode, central wavelength $\sim 6000 \text{ \AA}$ and spectral resolution of 6 \AA .

Following the same method as for the rest of the sample, the IRAF package was used to obtain the spectra shown in Fig. 3.18. It can be seen that the source was in a Sy1-Sy1.2 state during both nights. No significant variations can be seen between the two observations. The second one is of better quality due to the longer exposure time, so we restricted ourselves to this longer observation in our analysis.

In order to fit the continuum and given the spectral features it displays, a model including a third-degree polynomial plus three Gaussian lines was used. As for the rest of the sample, a Gaussian emission line was used to fit each emission line applying the same constraints to line intensities and widths as for Mrk 6. The fit results are summarised in Table 3.11 and shown in Fig. 3.19. From these values the following Balmer decrements are obtained:

$$\frac{H_\alpha}{H_\beta}(\text{NLR}) = 2.9 \pm 0.2, \quad \frac{H_\alpha}{H_\beta}(\text{BLR}) = 3.23 \pm 0.06$$

3.5.4 Discussion and Results

From the Balmer decrement obtained in the optical we estimate that no significant cold absorption is present for this source being in a Sy1-1.2 state during the optical observations. In agreement with that, no intrinsic neutral absorption was needed in the X-ray spectral fit.

3.6 Conclusions

We have conducted simultaneous X-ray and optical observations for a small sample of Seyfert galaxies which have shown variability in their optical spectral class along the years. The main goal was to test, within the Unified model scenario, whether the optical type/ X-ray absorption mismatches reported from several observations are due to intrinsic properties of the sources or due to variability.

The main properties of these four sources and a summary of our conclusions are presented in Table 3.12. The most important conclusion achieved after the detailed study of the small sample of four changing-type Seyfert galaxies is that all of them appear to have a complex absorption environment due to different

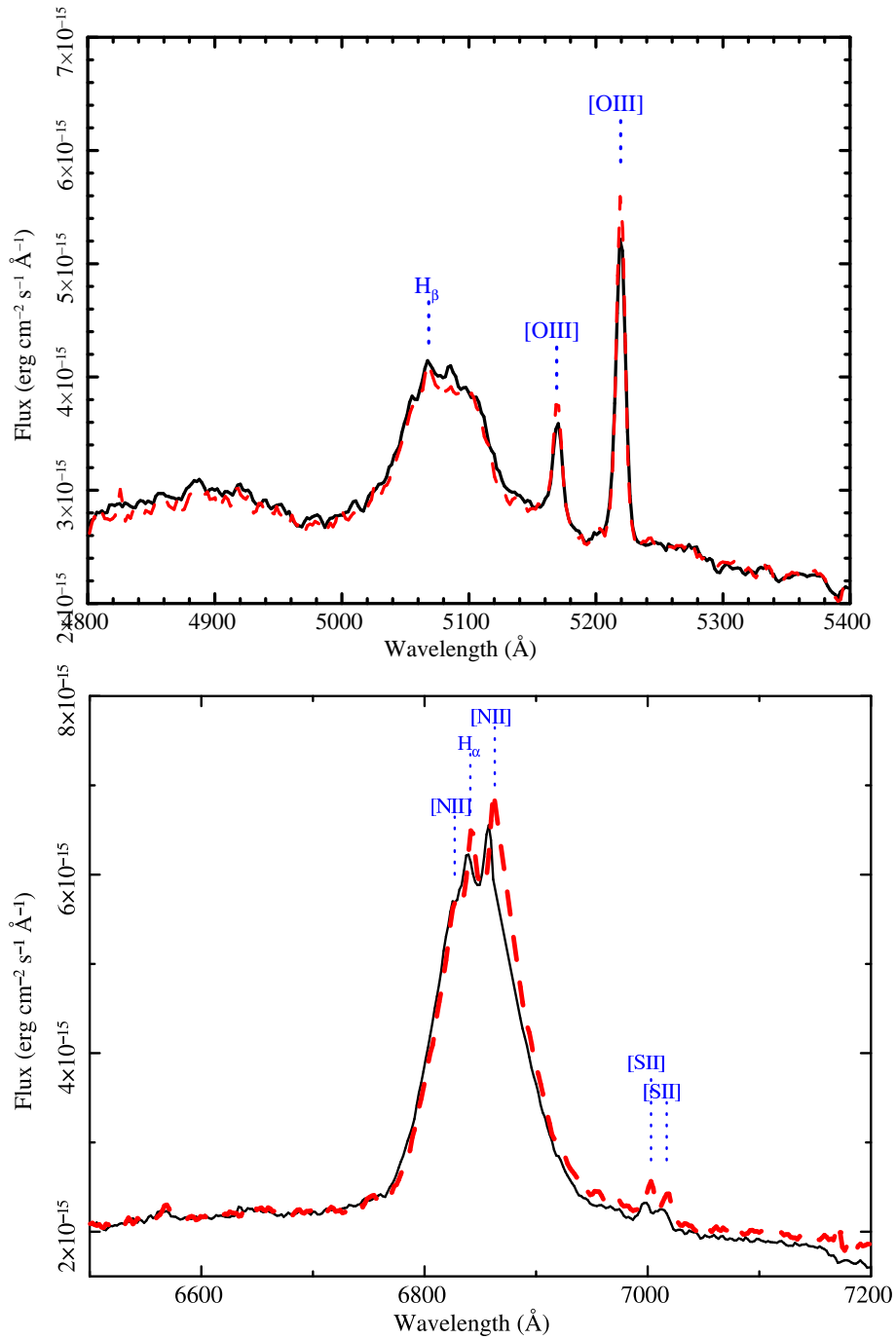


Figure 3.18 **Mrk 1018**: CAHA 2.2m CAFOS optical spectra corresponding to the first (solid line) and the second (dashed line) observation.

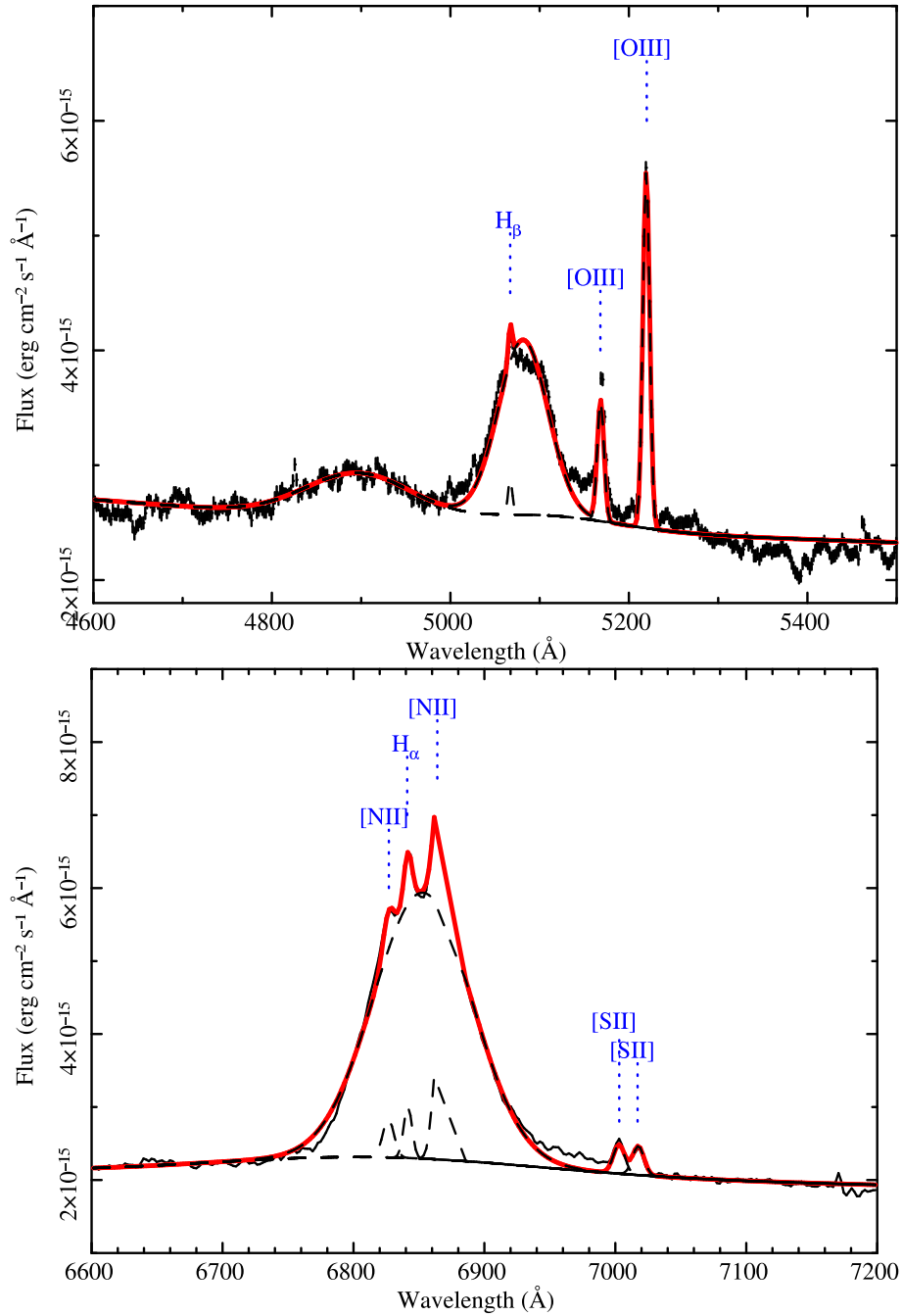


Figure 3.19 **Mrk1018**: Optical spectral fit in the H_β (top) and H_α (bottom) regions. Solid line correspond to the best-fit model. Dashed line correspond to each Gaussian component.

Table 3.11 Mrk 1018: Optical line intensities and FWHM.

Line	Intensity(10^{-15} erg cm $^{-2}$ s $^{-1}$)	FWHM(km s $^{-1}$)
H $_{\beta}$ (n)	1.97 $^{+0.08}$	200 ^a
H $_{\beta}$ (b)	106 $^{+2}_{-1}$	3850 ^b
[OIII] λ 4958	9.91 $^{+0.06}_{-0.08}$	380 ^c
[OIII] λ 5007	29.7 ^d	380 $^{+10}_{-10}$
[NII] λ 6548	5.64 $^{+0.01}_{-0.2}$	360 ^c
H $_{\alpha}$ (n)	5.7 $^{+0.1}_{-0.3}$	200 $^{+20}_{-30}$
H $_{\alpha}$ (b)	342 $^{+1}_{-3}$	3850 $^{+20}_{-10}$
[NII] λ 6583	16.9 ^d	360 $^{+30}_{-20}$
[SII] λ 6718	4.3 ^d	360 ^c
[SII] λ 6730	4.3 $^{+0.2}_{-0.2}$	360 $^{+40}_{-40}$

^a Fixed at the same σ (km s $^{-1}$) as H $_{\alpha}$ (n) narrow.

^b Fixed at the same σ (km s $^{-1}$) as H $_{\alpha}$ (b) broad for the corresponding wing.

^c Fixed at the same σ (km s $^{-1}$) as the other line in the doublet.

^d Forced to keep the theoretical line ratio for the corresponding doublet.

reasons. This complex absorption is most likely at the root of why these objects are spectrally seen at optical wavelengths in different states at different times. Specifically speaking, out of the four studied sources, one of them (Mrk 993) shows a clear discrepancy between optical spectral type and X-ray absorption, if reddening is responsible for the former (Corral et al., 2005). Two other galaxies (NGC 7603 and Mrk 1018) show a spectral type clearly consistent with the amount of X-ray absorption. Our fourth object, Mrk 6, has the most complex behaviour, but we believe that the total amount of dust that can be associated with the absorbers seen in the X-ray spectrum agrees with that needed to produce the amount of reddening seen in the BLR. Variability within the BLR also seems to play a significant role. In the case of Mrk 1018, a change in the amount of cold absorption could explain the changes in its optical spectral classification. In the case of NGC 7603 and Mrk 6, changes in a high column density highly ionised absorber could also explain the changes in their optical broad emission lines within the Cao and Wang (2006) double-peaked emitters scenario. The results of the analysis of Mrk 6, NGC 7603 and Mrk 1018 data presented here are reported in Corral et al. (2011a).

All this probably shows that changing-type Seyfert galaxies are a mixed bag of AGN with complex and variable absorbers, and that in some cases optical spectral type appears to be an intrinsic property of the BLR rather than a byproduct of obscuration.

Table 3.12 Summary of the sample analysis

Source	redshift	L_{bol} (erg s^{-1})	$L_{\text{bol}}/L_{\text{Edd}}$	L_X 2 – 10 keV(erg s^{-1})	X – ray bestfit model
Mrk 993	0.015537	2.6×10^{44}	0.1	7×10^{41}	Single power law
Mrk 6	0.018813	2.6×10^{44}	0.03	1.6×10^{43}	Multilayer ionized absorption
NGC 7603	0.029524	4×10^{44}	0.03	4×10^{43}	Velocity – smeared ionized absorption
Mrk 1018	0.042436	2.4×10^{44}	0.02	3.5×10^{43}	Multilayer ionized absorption

The average X–ray spectrum of distant AGN

Contents

4.1	Introduction	93
4.2	Averaging method	95
4.2.1	Assembling the data	95
4.2.2	Bringing the individual spectra to a common frame	98
4.3	Testing the method	99
4.3.1	Fitting the spectra	106
4.4	Medium flux sample: AXIS+XWAS	108
4.4.1	Sample description	108
4.4.2	Average spectra	112
4.5	Faint sample: Lockman Hole	122
4.5.1	Sample description	122
4.5.2	Average spectra	122
4.6	Discussion and Results	131

In this chapter, a new method to construct a rest-frame X–ray average spectrum and its application to different samples of AGN is presented. The main goal is to characterise the mean Fe $K\alpha$ emission in AGN.

The chapter is organised as follows: in Sect. 4.2 and 4.3 the averaging method and quality checks performed to it are explained. In Sect. 4.4 and 4.5, the resulting average spectra for the different samples are presented. Finally, in Sect. 4.6 the main results from these analyses are summarised along with the results obtained by combining the various samples.

4.1 Introduction

Emission lines are usually seen in the X–ray spectrum of AGN, the Fe $K\alpha$ being the most prominent and best studied one (see Chapter 1). From the line properties, several physical parameters can be inferred: if the line is emitted close enough to the SMBH, in the accretion disk, it shows a broad relativistic profile which is

more pronounced for higher SMBH spin due to the ISCO (*innermost stable circular orbit*) becoming smaller and therefore gravitational redshift (and other General Relativistic effects) being larger (Fabian et al. 1989; Laor 1991).

However, although broad relativistic lines might be common in type 1 AGN, they have been significantly detected and characterised only in a small number of sources (Reynolds and Nowak, 2003), MCG-6-30-15 being the best studied one (Tanaka et al. 1995; Fabian and Vaughan 2003). The number of counts collected in the AGN X-ray spectra turns out to be the limiting factor, since very accurate modelling of the continuum below the line is critical to properly measure the line properties (Guainazzi et al., 2006). Another possibility, somewhat related to the previous one, is that the extreme relativistic blurring along with high inclination angles can both widen and weaken the line making it undetectable (Fabian and Miniutti, 2005).

Several studies have been performed over samples of local AGN in order to characterise Fe K α emission in the local Universe. Nandra et al. (2007) performed a spectral analysis of a sample of 26 type 1 to 1.9 Seyfert galaxies ($z < 0.05$) observed by *XMM-Newton*. They found that a relativistic line is significantly detected in half of their sample ($54 \pm 10\%$) with a mean EW of ~ 80 eV, when fitted as a broad Gaussian. Guainazzi et al. (2006) and de La Calle Pérez et al. (2010) carried out a similar analysis over a larger sample of local type 1 and 2 radio-quiet AGN, excluding highly obscured type 2 sources. They detected relativistic lines in 25% (50% for well-exposed sources) of their sample with an EW $\lesssim 200$ eV. Both studies, although computing a similar average EW, found a high dispersion in the individual values. Nevertheless, this kind of analysis cannot be easily extended to higher redshifts due to the more limited quality of the spectra of distant AGN.

Improving the *Signal to Noise Ratio* (SNR) by averaging as many AGN spectra together as possible is the best solution since spectra of the same type of AGN are expected to display similar spectral characteristics. In recent studies X-ray average spectra for AGN have been constructed but differing results have been obtained. In Streblyanska et al. (2005) (hereafter S05) the results of this kind of analysis are presented for 53 type 1 and 41 type 2 AGN in the pencil beam Lockman Hole *XMM-Newton* deep survey ($z < 4.5$). They found a broad relativistic line in the final average spectra with an EW of 400 and 600 eV for type 2 and type 1 AGN, respectively. Brusa et al. (2005) found qualitatively similar results when stacking the AGN spectra contained in the 1Ms Chandra Deep Field South in 7 different redshift bins from $z = 0.5$ to 4.0, the broad line EW being slightly weaker than in S05 but consistent within errors. Longinotti and de La Calle Pérez (2010), stacked X-ray spectra from a local sample of AGN (extended from the sample of Guainazzi et al. 2006), and found that the EW for the broad relativistic contribution is never larger than 80 eV, either when stacking the whole sample or different sub-samples. Given this apparent divergence of results at high and

low redshifts, it is vital to consider carefully and refine the averaging or stacking method applied to faint object spectra.

A new averaging method is developed here and we apply it to two different but complementary samples of spectroscopically identified AGN. The first one, with more than 700 AGN, comes from two large medium sensitivity surveys: *AXIS (An International XMM-Newton Survey)* and *XWAS (XMM-Newton Wide-angle Survey)*. The second sample, the same as used in S05, corresponds to one of the deepest (> 500 ks) XMM-Newton observations to date (now overtaken by the XMM-Newton ultra deep survey in the CDFS, *Chandra Deep Field South*, [Comastri et al. 2011](#)) and is composed of a smaller number of sources, from medium to faint fluxes, but with a better spectral quality due to the longer exposure time. This latter sample allows us to directly compare the results between the S05 method and the one presented here. Since the samples are composed of low-to-medium quality X-ray spectra, we develop a method that takes into account the effects of the continuum emission around the emission line and the counting statistics, without needing to fit complex models to the individual spectra, but modelling the underlying continuum using simulations. This method is extensively tested and a significance for the emission line detection can be derived from it.

4.2 Averaging method

The main steps of the averaging method presented in this section are schematised in Fig. 4.1.

4.2.1 Assembling the data

The spectra for the *AXIS* and *XWAS* samples were extracted following the automated process described in Sect. 2.3.2.2. The spectral extraction for the Lockman Hole sample is described in [Mateos et al. \(2005b\)](#).

After the spectral extraction and merging procedure (see Sect. 4.4.1 and Sect.4.5.1 for *AXIS+XWAS* and Lockman Hole sample, respectively), only those individual spectra with more than 80 background-subtracted counts in the 0.2-12 keV energy range are considered in the analysis, in order to preserve a minimum spectral quality.

Prior to combining the intrinsic spectra from different sources, we need to obtain the original spectra, i.e., the spectra before they enter the telescope plus detector system. This process is called “unfolding”. As described in Sect. 2.4, X-ray spectra are expressed in photon counts collected at each energy channel. This observed spectrum results from the convolution of the incoming source

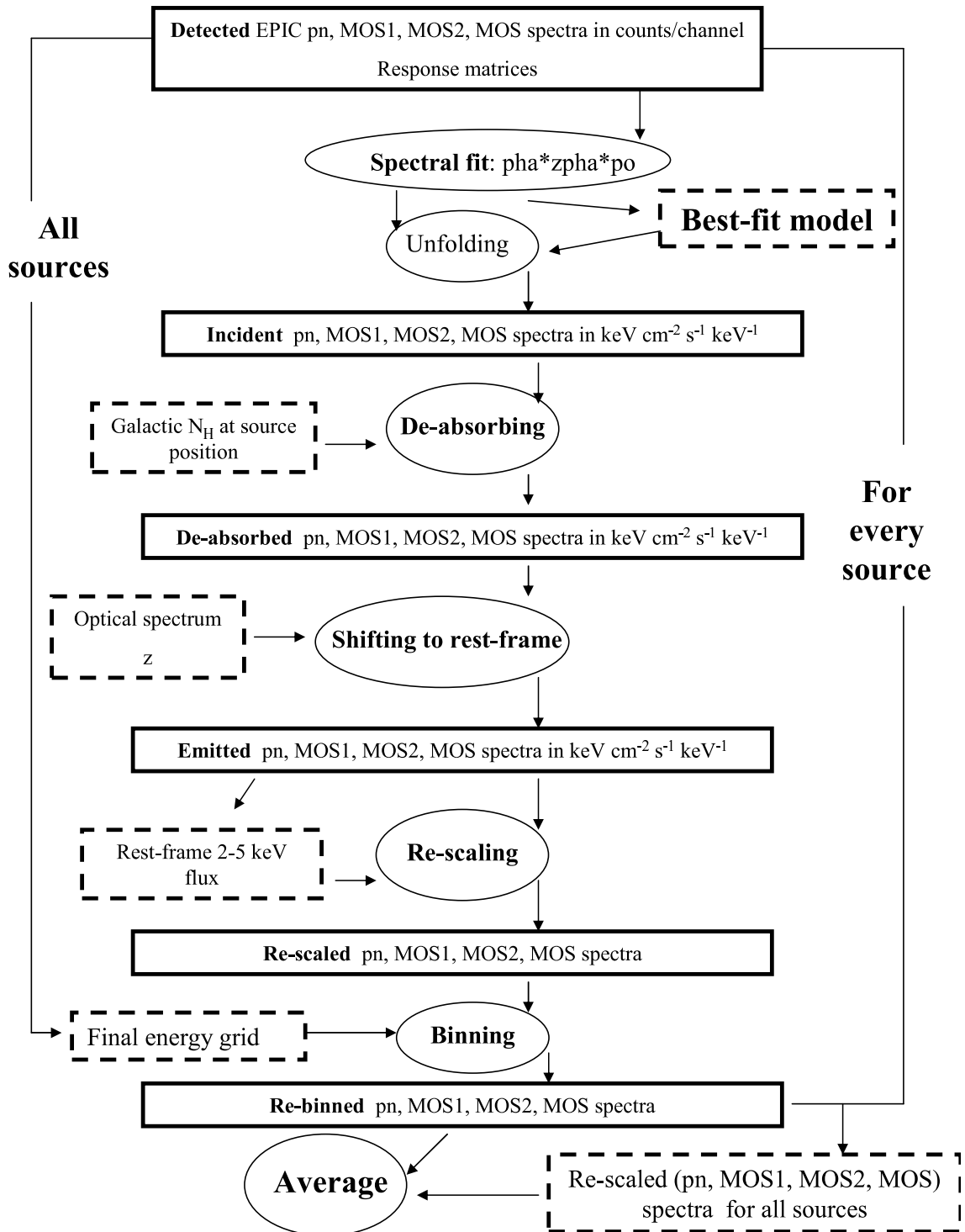


Figure 4.1 Averaging method diagram.

spectrum and the instrumental response represented by the response matrices. To obtain the incident spectrum, a model must be fit and used in conjunction with the response matrices to “unfold” the spectrum. The more similar the model to the actual spectrum, the more similar the “unfolded” spectrum to the actual one. The reason for this is the relatively low spectral resolution of the EPIC detectors ($E/\Delta E \sim 20-50$), which results in spectral features being spread over a wide spectral range, and the strongly varying shape of the effective area as a function of the incoming photon energy (see Sect. 2.2.2).

To obtain the unfolded spectrum for each source, XSPEC v12.4 (Arnaud, 1996) is used (see Sect. 2.4). First, the spectra are grouped to have at least 10 counts per bin in order to ensure a minimal Gaussian behaviour of the errors in the grouped spectra. Then a simple model is fitted. The model consists of a single power law corrected by photoelectric absorption, fixed at the Galactic value for each source position, and intrinsic photoelectric absorption at the redshift of the source. It should be noted that the intention is not to obtain the absolute best-fit parameters but a model good enough to unfold the spectrum without severe biases from the actual spectral shape. In fact, the small number of spectral counts for most of the sources does not allow us to fit a more complex model to the data. To avoid the contribution of any soft excesses each individual spectrum is fitted above 1 keV (rest-frame) leaving the intrinsic hydrogen column density, power law slope and normalisation as free parameters. Then, this “best fit model” is applied to the ungrouped spectrum, obtaining the unfolded spectrum in physical units ($\text{keV cm}^{-2} \text{s}^{-1} \text{keV}^{-1}$) and, to a good approximation, free of instrumental effects (eufspec command in XSPEC).

Below 3 keV, the unfolding process is highly dependent on the model used, due to the shape of the effective area (see Fig. 2.4 in Sect. 2.2.2) and the limited spectral resolution, meaning that caution must be applied in deriving any result from the analysis of the final average spectrum below that energy. Narrow (unresolved) features, both in the model or in the data itself, could also affect the unfolding process above these energies. A narrow emission (or absorption) line, for example, will be widened during the unfolding process if it is not included in the fitting model. Although less significant than the softer ones, these features should be taken into account very carefully, especially around the position where we expect the Fe $K\alpha$ emission line, as they can distort its shape. Given the quality of our spectra, these features cannot be directly fitted on the individual spectra, so their contribution to the continuum around the emission line position is estimated by using simulations, as explained in Sect. 4.3.

4.2.2 Bringing the individual spectra to a common frame

Once all the spectra are in physical units (flux density bins in $\text{keV cm}^{-2} \text{s}^{-1} \text{keV}^{-1}$), they are corrected for Galactic absorption (i. e., we de-absorb the spectrum) via a table model extracted from the `phabs` XSPEC model (see Sect. 2.4.1) as explained in what follows.

Photoelectric absorption affects an incident spectra as shown:

$$F_o(E) = F_e(E)e^{-N_H\sigma(E)} \quad (4.1)$$

where $F_e(E)$ and $F_o(E)$ are the unabsorbed and absorbed (by our own Galaxy) flux density as a function of energy E , N_H is the hydrogen column density and $\sigma(E)$ is the absorption cross section.

To obtain the tabular dependence of the cross section on the energy, we assume power law spectra ($F'(E) \sim E^{-\Gamma}$) of spectral index $\Gamma = 0$, and different values for the hydrogen column density from 10^{19} to 10^{23} cm^{-2} to increase the resolution at the most important absorption edges. Then, we correct each flux density bin in the real spectra by interpolating the corresponding value for $\sigma(E)$ at each energy bin, thus obtaining the observed spectra prior entering our Galaxy. Then, the de-absorbed spectra are shifted to the rest-frame by using the accurate redshifts derived from the optical identifications.

The spectral averaging assumes that each spectrum contributes with the same weight to the final average spectrum and the simplest way to achieve that, without distorting the individual spectral shape, is by dividing each spectrum by a certain value so that every rescaled spectrum has the same flux. Since the differences in spectral shapes could be important, the first issue needed to solve is to select a spectral range to apply a rescaling which is not severely affected by spectral features. It is clear that the energy region where the Fe $K\alpha$ line is expected must be excluded but also lower energy regions due to intrinsic absorption. Besides, higher energies cannot be included either, in order to avoid the contribution of a spectral band where large errors are common. After testing several energy bands within the previous constraints and using simulated data, the 2-5 keV band is selected to rescale the spectra. Tests with our simulations show that this band recovers the input spectral shape in the most accurate way while minimising the errors. We then proceed by summing the fluxes in the 2-5 keV rest-frame band for each spectrum (S) and dividing each spectrum by S so that all the rescaled spectra have unity 2-5 keV rest-frame integrated flux:

$$S = \sum_{E>2}^{E<5} S_i \Delta \varepsilon_i \quad (4.2)$$

where S_i , $\Delta \varepsilon_i$ and are the flux density values (in $\text{keV cm}^{-2} \text{s}^{-1} \text{keV}^{-1}$) and widths

(in keV) at the energy bin i .

Although now rescaled, each spectrum is expressed on a different energy grid because of the different channel sizes at different energies and shifting to rest-frame. In order to achieve some uniformity in the errors of the average spectrum across the whole energy band, we construct a new energy grid for the final average rest-frame spectrum ensuring a minimum number of real source counts (~ 1000) in each new bin. To define these new bins, we use the individual source spectra as measured in counts. We first shift these spectra in counts to the rest frame, rebin them to a common energy grid composed of narrow bins (bin widths = 40 eV) and add them all together. We then group the narrow bins so as to distribute the counts in the most uniform way and so that each new bin contains at least 1000 real source counts. This grid is used to distribute the rescaled flux density values for each individual spectrum in the following way:

$$S'_j = \sum_{i \subset j} \frac{S_i \Delta \varepsilon_i f_{ij}}{\Delta' \varepsilon_j} \quad (4.3)$$

$$f_{ij} = \frac{\min(\varepsilon_{imax}, \varepsilon'_{jmax}) - \max(\varepsilon_{imin}, \varepsilon'_{jmin})}{\Delta \varepsilon_i} \quad (4.4)$$

where S'_j , $\Delta' \varepsilon_j$ and S_i , $\Delta \varepsilon_i$ are the flux density values (in $\text{keV cm}^{-2} \text{s}^{-1} \text{keV}^{-1}$) and widths (in keV) of the new and old bins, respectively, and f_{ij} represents the fraction of the old bin i that covers the new bin j .

Once we have de-absorbed, brought to rest-frame, rescaled and rebinned the individual spectra, we simply average them using an un-weighted standard mean. Because of the quite large dispersion in the redshift distribution, high energies are only significantly accessed by a few high-redshift objects. We do not take into account those spectral ranges that are not significantly covered by at least 10 individual spectra. The individual errors are propagated as Gaussian during the entire process, the final errors being computed in the following way:

$$Error_j = \frac{\sqrt{\sum_{i \subset j}^N \sigma_i^2}}{N} \quad (4.5)$$

where σ_i is the individual error corresponding to the spectrum i at the bin j and N is the number of spectra contributing to bin j .

4.3 Testing the method

In order to distinguish between real spectral features and artifacts from both the averaging process and/or the individual spectral shape around a possible

emission line, extensive tests of the method described in previous section are carried out by using simulated spectra. Our strategy can be summarised as follows: we simulate N times each source and background spectrum, including Poisson counting noise, keeping the same 2-8 keV observed flux and exposure time as in the real spectrum along with the same calibrations files. We then apply to the simulated spectra exactly the same averaging method as for the real spectra and compare it with the input spectra. We also explore how the assumed spectral model, noise and number of simulations affect the final averaged simulated specific spectra.

First, 10 simulations for each source are performed, in order to reduce both noise and spurious features, using a single power law model with $\Gamma = 1.9$ constant (XSPEC model: `po`). The resulting average spectrum for type 1 AGN in the AXIS sample is shown in Fig. 4.2. We fit a power law between 2 and 10 keV obtaining a $\Gamma(2-10 \text{ keV})=1.89\pm 0.01$ and we do not detect any significant deviations from the model. A similar result is obtained for the type 2 AGN and the remaining samples. In order to disentangle systematic effects from those induced by the noise, simulations are also conducted with largely increased fluxes and also without including noise. The results are equivalent, with smaller errors in Γ .

Our method includes the correction for Galactic absorption for each source, so we want to test how this correction affects the average spectrum. We then simulate 10 times each source with a power law model ($\Gamma = 1.9$) modified by Galactic absorption at each source position (XSPEC model: `pha*po`). The resulting average spectrum, again for the type 1 AGN in the AXIS sample, is shown in Fig. 4.3. We again measure $\Gamma(2-10 \text{ keV})=1.89\pm 0.01$ and do not detect any significant deviations. We can conclude that the correction for the Galactic absorption does not affect the results significantly.

Once we had tested that the method and that counting statistics do not significantly affect the results, we have to test how other spectral features propagate through our averaging and analysis procedures. It is well known that intrinsic absorption, along with warm absorption and reflection components, can significantly affect the continuum below the Fe emission lines. Unfortunately, the spectral quality of most of our spectra does not allow us to fit complex models and subtract them in order to obtain a pure emission line spectrum. Besides, the unfolding procedure itself can also affect the spectra due to the shape of the effective area and the spread of the redistribution matrix, i.e., the low spectral resolution (see Sect. 2.2), although it has been tested that this does not significantly affect the spectral shape above 3 keV.

In order to quantify the effect of intrinsic absorption, we use the “best-fit model” we obtain for the real spectra (an absorbed power law XSPEC model: `pha*zpha*po`), but assuming $\Gamma=1.9$, and simulate 10 times each source, Fig. 4.4.

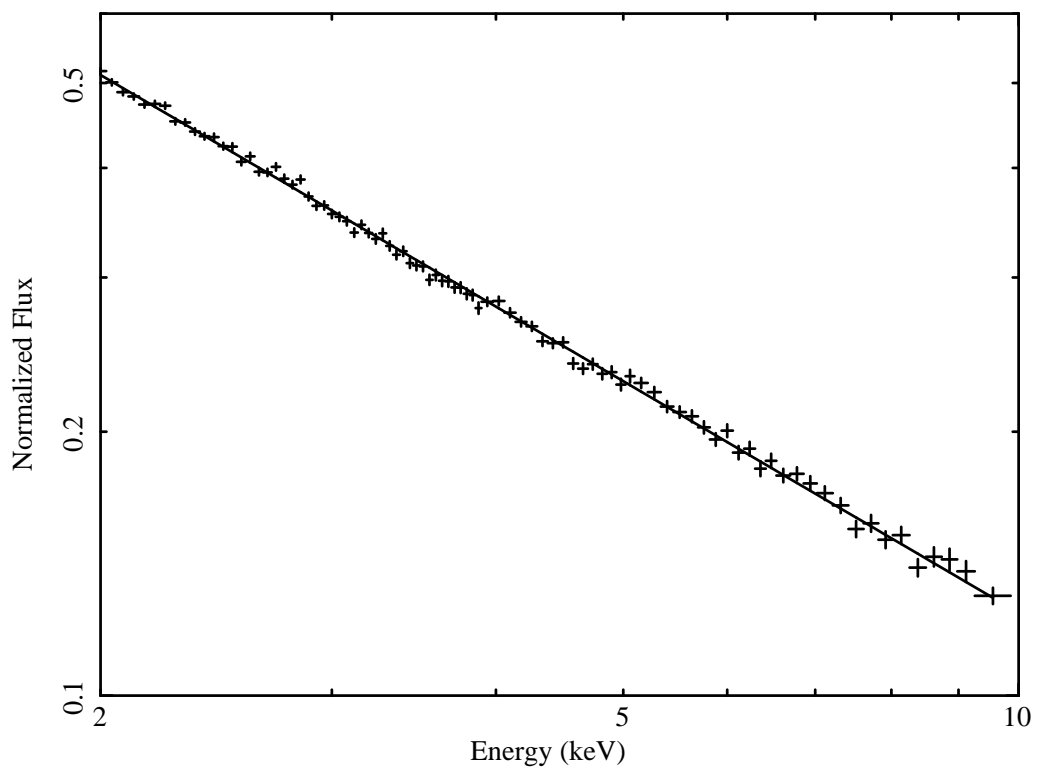


Figure 4.2 **Model:** p_0 , type 1 AGN, AXIS. Simulated average spectrum corresponding to 10 simulated spectrum for each real spectrum and a simple power law model, $\Gamma=1.9$.

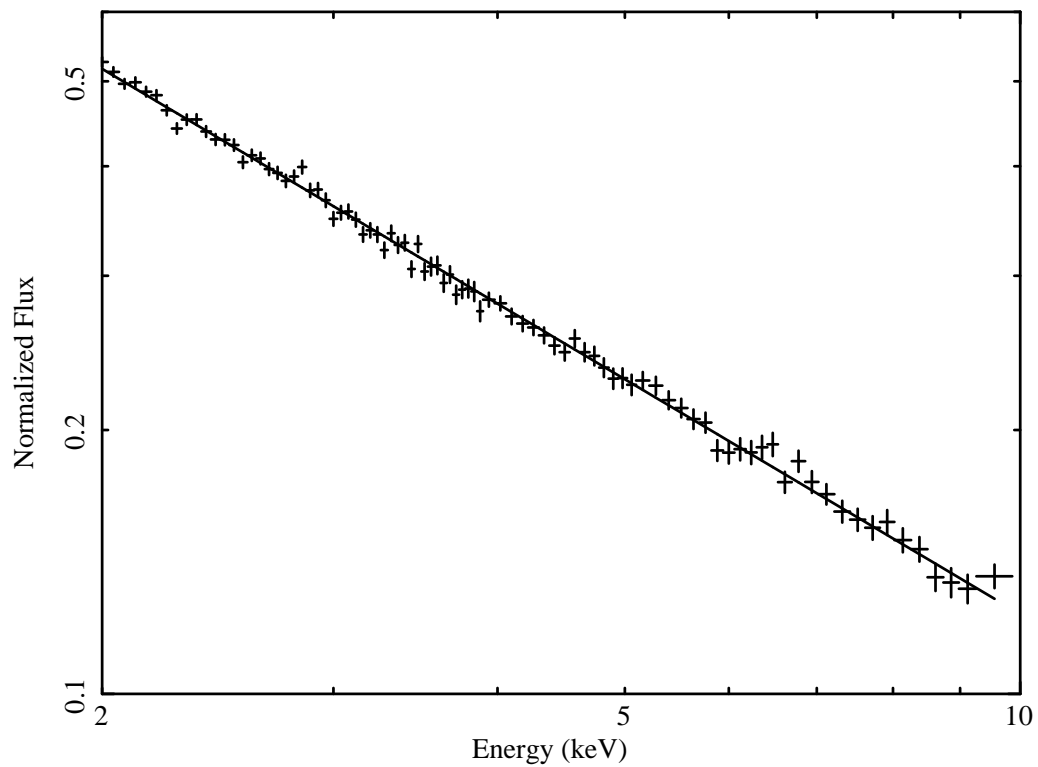


Figure 4.3 **Model:** pha*po, **type 1 AGN, AXIS.** Simulated average spectrum corresponding to 10 simulated spectra for each real spectrum and a power law ($\Gamma=1.9$) plus Galactic absorption model.

Table 4.1 Broadening of narrow features across the full averaging process.

Sample and AGN type	Gaussian widening (eV)
AXIS + XWAS	
Type 1 AGN	100
Type 2 AGN	80
Lockman Hole	
Type 1 AGN	120
Type 2 AGN	100

Type 1 and type 2 AGN from AXIS+XWAS are shown separately this time since the amount of absorption is often much higher for type 2 AGN, thus affecting more dramatically the spectral shape of the latter. We can see broad features above 4 keV, and we measure a $\Gamma(2-10 \text{ keV})=1.81(1.33)\pm 0.01(0.02)$ for type 1 (type 2) AGN, the much lower value obtained for type 2 AGN being due to the larger amount of absorption. Therefore, the average spectrum is affected by the intrinsic absorption above 3 keV and it has to be accounted for very carefully. For example, in the case of type 2 AGN, the observed “broad hump” around the position of the Fe $K\alpha$ line can mimic a broad emission line or a red tail for a relativistic line. Therefore, the amount of absorption has to be taken into account when fitting this emission line in the real data.

To test how narrow features are treated by our method, we simulate a power law plus an intrinsically unresolved emission line ($\sigma = 0$) at 6.4 keV. To avoid the contribution from the noise, we do not include Poisson noise this time and increase the source flux by a large factor. In this way we can measure solely the effects due to the process and the redshift distribution over a narrow feature. We simulate once each source, using a power law plus a Gaussian emission line (XSPEC model: `po+gaus`) with the following parameters: $\Gamma=1.9$, $E = 6.4 \text{ keV}$, $\sigma = 0$ and $EW = 200 \text{ eV}$, rest-frame values. The result is presented in Fig. 4.5 for the case of type 1 AGN in the AXIS+XWAS sample. We can see how the process and the EPIC spectral resolution widen the line giving a value of $\sigma \simeq 100 \text{ eV}$, but we recover the initial values for the remaining parameters (Γ , E and EW). We perform this test also for type 2 AGN within the AXIS+XWAS and for type 1 and 2 AGN within the Lockman Hole sample obtaining the values presented in Table 4.1. This widening of narrow features is due to the different redshifts distribution for the different samples and the spectral resolution at different energies, and must be subtracted in quadrature from fitted values in the real average spectrum.

At this point we still need to quantify how absorption could affect the shape

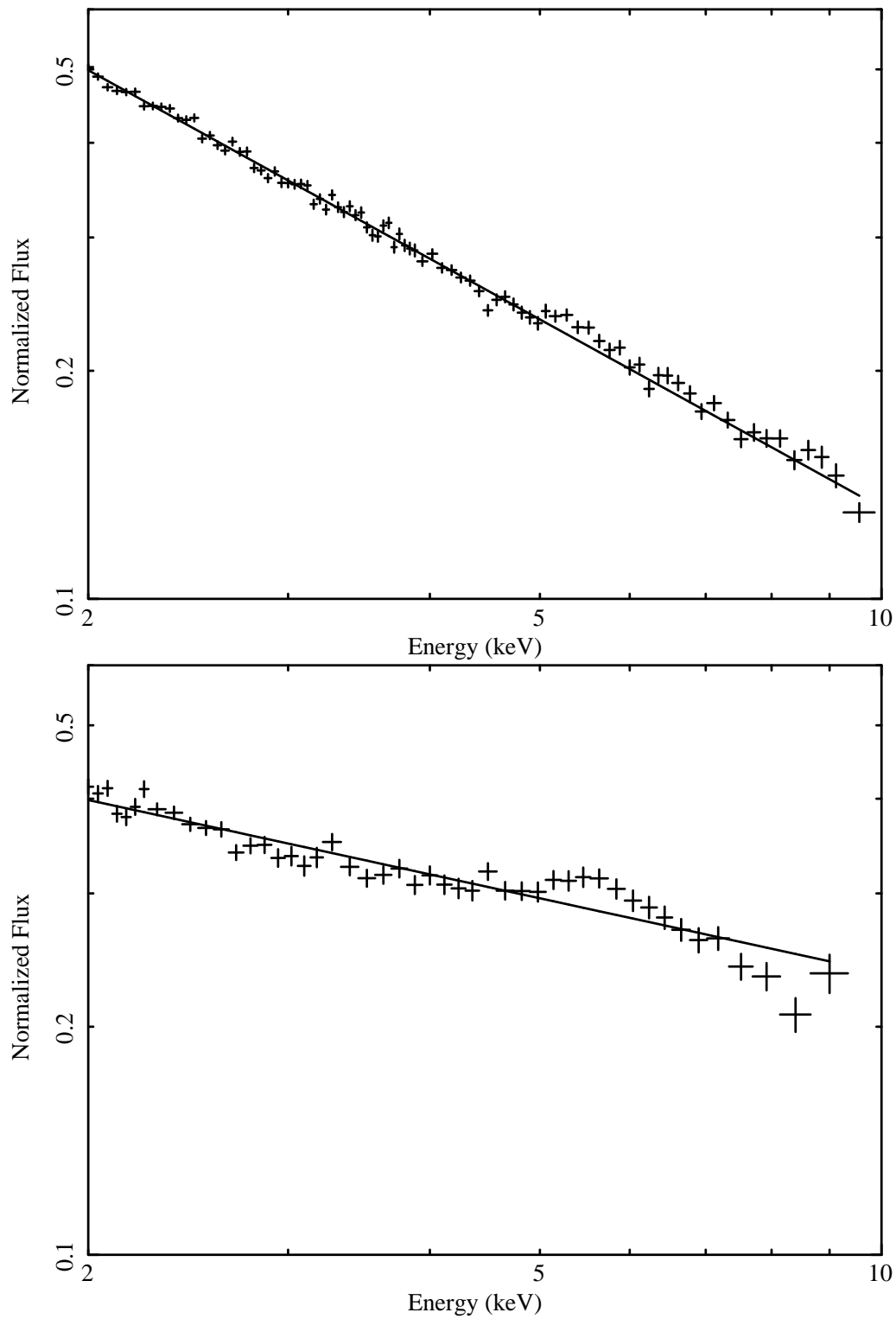


Figure 4.4 **Model:** $\text{pha} * \text{zpha} * \text{po}$, **type 1 (top) and type 2 (bottom) AGN, AXIS+XWAS.** Simulated average spectrum corresponding to 10 simulated spectrum for each real spectrum and a power law ($\Gamma=1.9$) plus Galactic absorption and intrinsic absorption model.

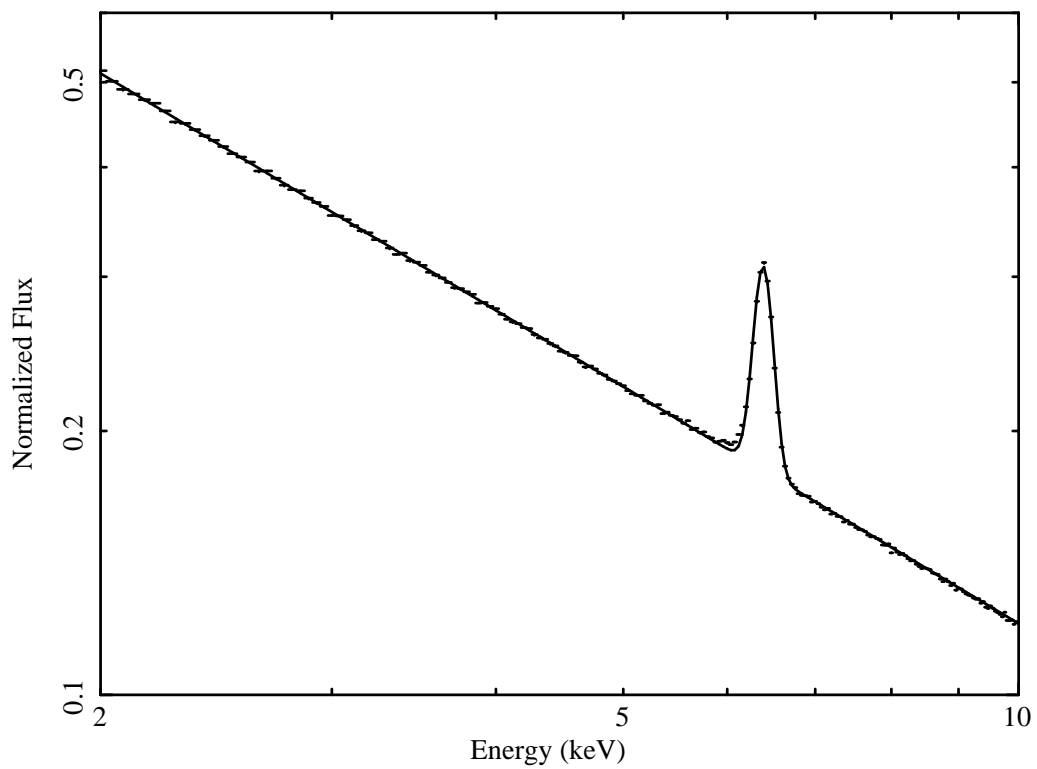


Figure 4.5 **Model:** `po+gaus`, **type 1 AGN**, **AXIS+XWAS**: Simulations without noise corresponding to $E=6.4$ keV, $\sigma = 0$ and $EW=200$ eV, rest-frame values.

of an emission line. To measure this, we add a Gaussian emission line to the “best-fit model” with $\Gamma = 1.9$ and run the simulations using this model (XSPEC model: `pha*zpha*(po+gaus)`). Fig. 4.6 (top) shows the simulations for a Gaussian line centred at $E = 6.4$ keV with $\sigma = 200$ eV and $EW = 200$ eV (rest-frame values) along with the simulations for the “best-fit model” (XSPEC model: `pha*zpha*po`) in the case of type 2 AGN within the AXIS+XWAS sample. We can see that the line shape appears distorted towards low energies mimicking a broad tail, but this feature is also present in the `pha*zpha*po` simulations. If we fit a power law in the 2-10 keV range, excluding the emission line region (4-7 keV), and compute the ratio between the `pha*zpha*(po+gaus)` model and this power law, we obtain the ratio shown in Fig. 4.6 (central). The line shape is clearly distorted and some residuals below 6 keV can be seen. This effect, if not treated properly, could mimic that of a relativistically broadened emission line. Notwithstanding, if we use the simulations without a line as the underlying continuum to obtain the ratio, Fig. 4.6 (bottom), we find that the process slightly widens the line due to the unfolding and the different energy resolutions at different energies, but it does not vary the line shape nor its EW , recovering the input parameters within errors. We also tested that changing the line width, EW and central energy do not affect significantly our conclusions, always recovering the input values within errors when using the `pha*zpha*po` simulations as the underlying continuum.

4.3.1 Fitting the spectra

In order to minimise the distortion introduced by the averaging method and the intrinsic absorption in the search for a possible emission line, we decided to use the “best-fit” simulated continuum described in the previous section as an underlying continuum for our real average spectrum. In this way, all systematic effects are accounted for.

Each real spectrum is simulated 100 times (instead of 10), including Poisson counting noise and keeping the same 2 to 8 keV observed flux, exposure time and calibration matrices as in the real data. We use the “best-fit model” (absorbed power law with power law index, intrinsic absorption and normalisation as free parameters) obtained when fitting the individual spectra and we apply to the simulated spectra exactly the same averaging method as for the real data. By simulating 100 times each source we are able to reduce spurious features as well as to construct 100 absorbed power law simulated continua. From these 100 simulated continua we can estimate the significance in the detection for any feature in the real average spectrum. By removing the 32 and 5 most extreme values for each simulated continuum at each energy bin, we compute the normalised flux intervals that encompass 68% and 95% of the simulated values, respectively. Therefore, a spectral excursion above or below these limits is detected at the 1σ or 2σ level, respectively. Other spectral components or features, not taken into

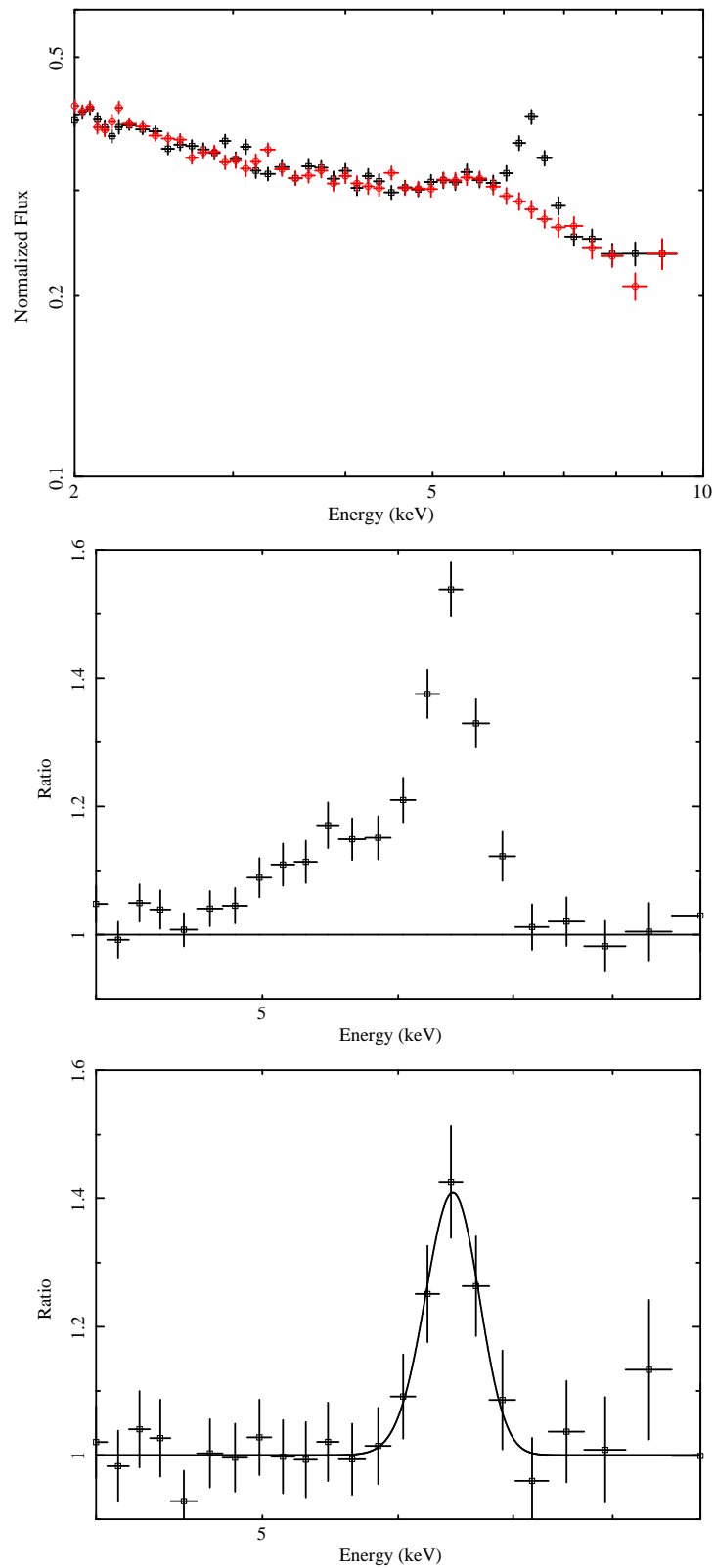


Figure 4.6 *Top panel*: **Model**: $\text{pha}*\text{zpha}*(\text{po}+\text{gaus})$, **type 2 AGN, AXIS+XWAS**. Simulated average spectrum corresponding to 10 simulated spectra for each real spectrum (squares) and the “best-fit model” continuum (circles). *Central Panel*: Simulations $\text{pha}*\text{zpha}*(\text{po}+\text{gaus})$ to power law ratio. *Bottom Panel*: Simulations $\text{pha}*\text{zpha}*(\text{po}+\text{gaus})$ to “best-fit model” continuum ratio.

account in our simulations could contribute to the underlying continuum in the real spectra. However, our continuum accounts for the absorbed power law and for all the effects introduced by the averaging process.

The simulated continua and 1σ and 2σ limits in each bin for the type 1 and type 2 AGN in the AXIS+XWAS sample are shown in Fig. 4.7. For this 100-simulations continuum we fit a power law between 2 and 10 keV obtaining $\Gamma=1.96\pm0.01$ and 1.44 ± 0.06 for type 1 and type 2 AGN in the AXIS+XWAS sample, respectively, close to the mean value for the real samples. Although the continuum shape does not show prominent features, the confidence contours display an increasing dispersion towards high energies and around the position where the Fe $K\alpha$ line is expected to fall. This is likely due to the internal EPIC background, that also contains Fe fluorescence emission from the detectors. This emission is shifted to higher energies when shifting the spectra to rest-frame, thus increasing the errors. Therefore, this must be taken into account when fitting a possible broad line as it could be very much affected by these continuum features.

4.4 Medium flux sample: AXIS+XWAS

4.4.1 Sample description

The AXIS (*An XMM-Newton International Survey*, Carrera et al. 2007) and XWAS (*XMM-2dF Wide Angle Serendipitous Survey*, Esquej et al. in preparation) samples were constructed from serendipitous *XMM-Newton* observations as part of the XID (*X-ray follow-up & Identification*) program carried out by the SSC (*XMM-Newton Survey Science Centre*). The XID program involves the identification of X-ray sources by optical spectroscopy and catalogue searches, which allows accurate measurements of source redshifts and class (stars, normal galaxies, AGN, etc). As stated in Chapter 2, sources classified as AGN were basically divided among two groups, type 1 and type 2 AGN depending on the presence or absence, respectively, of broad permitted emission lines (velocity widths $\geq 1400 \text{ km s}^{-1}$) in their optical spectra.

AXIS is a 4.8 deg^2 survey (~ 40 *XMM-Newton* fields) accessible from the northern hemisphere comprising more than 1000 X-ray sources of which ~ 400 are identified by using a large variety of ground-based optical telescopes. In our analysis, only the *XMM-Newton* fields within the XMS (*XMM-Newton Medium Survey*), 25 *XMM-Newton* fields, were taken into account. XMS (Barcons et al., 2007) is a sub-sample of AXIS used to construct flux-limited samples selected at different X-ray energy bands at medium fluxes, where the bulk of the CXB comes from. However, we do not impose any flux constrain in our source selection. All the identified AGN within the XMS fields are extracted, following the automated procedure described in Sect. 2.3.2.2, and all the available public *XMM-Newton*

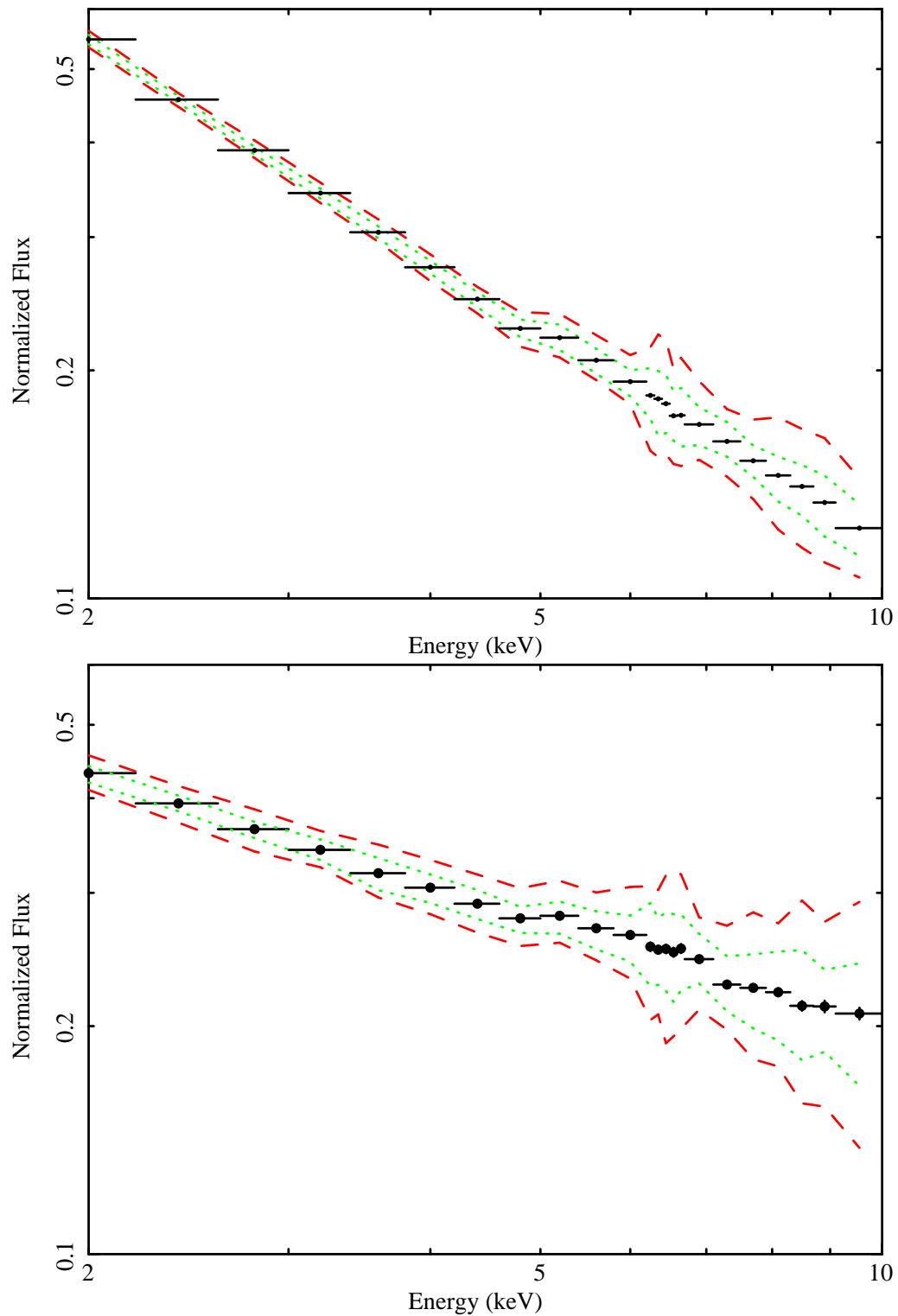


Figure 4.7 **Model:** `pha*zpha*po`, **type 1 (top) and type 2 (bottom) AGN, AXIS+XWAS.** Average continuum with 100 simulations (circles) along with the 1σ (dotted line) and 2σ (dashed line) confidence limits.

observations of those fields at the time of our analysis are used, ending up with more than 600 spectra corresponding to ~ 350 unique X-ray sources.

XWAS is a wide-area ($> 11 \text{ deg}^2$) survey in the southern hemisphere composed of more than 3000 sources with X-ray fluxes above $\sim 10^{-14} \text{ erg cm}^{-2} \text{ s}^{-1}$. The optical identifications were carried out by using the 2dF optical multi-fibre spectrograph on the AAT (*Anglo-Australian Telescope*) so they are restricted to brighter optical magnitudes than those in the AXIS sample, but it contains a larger number of identified sources given the larger area. Again, and following the automated procedure described in Sect. 2.3.2.2, all the identified AGN are extracted obtaining more than 2000 spectra corresponding to ~ 700 unique X-ray sources.

After the spectral extraction, MOS1 and MOS2 spectra corresponding to the same source, observation and filter are merged. If there is more than one observation of the same source and since individual source variability is not expected to significantly affect the results, the spectral quality is improved by merging the spectra for the same source, observed with the same EPIC camera, at a similar off-axis angle on the same CCD chip and with the same filter. If filter, CCD chip or off-axis were significantly different, the spectra were kept separate (see Sect. 2.3.2.1 for a detailed description of the merging procedure). The resulting individual EPIC pn and MOS spectra, even if corresponding to the same source, are treated as separate contributions to the final average spectrum, since they are effectively statistically independent.

Finally, and as stated in Sect. 4.2.1, only individual spectra (pn or MOS) containing more than 80 counts in the total band (0.2-12 keV) are retained, in order to preserve a minimum spectral quality in the sample. This provided a sample of 606 optically identified type 1 and 117 type 2 AGN corresponding to more than 1000 individual EPIC pn and MOS spectra. Out of these ~ 700 sources, most of them were observed only once, but some of them (~ 100) were observed 2 to 6 times. Note that, having more than one observation does not mean having more than one spectrum, since the final number of spectra used depends on the spectral merging procedure. The counts and redshift distributions, along with the flux distribution in the standard hard (2-10 keV) band, are shown in Fig. 4.8. It should be noted that we do not intend to construct a complete or flux-limited sample in any way, but to collect as many counts as possible in order to obtain a high SNR average spectrum. Therefore the sample comprises objects having a wide range of X-ray luminosities and redshifts. Fluxes are, however, mostly concentrated in the 10^{-14} - $10^{-13} \text{ erg cm}^{-2} \text{ s}^{-1}$ flux range.

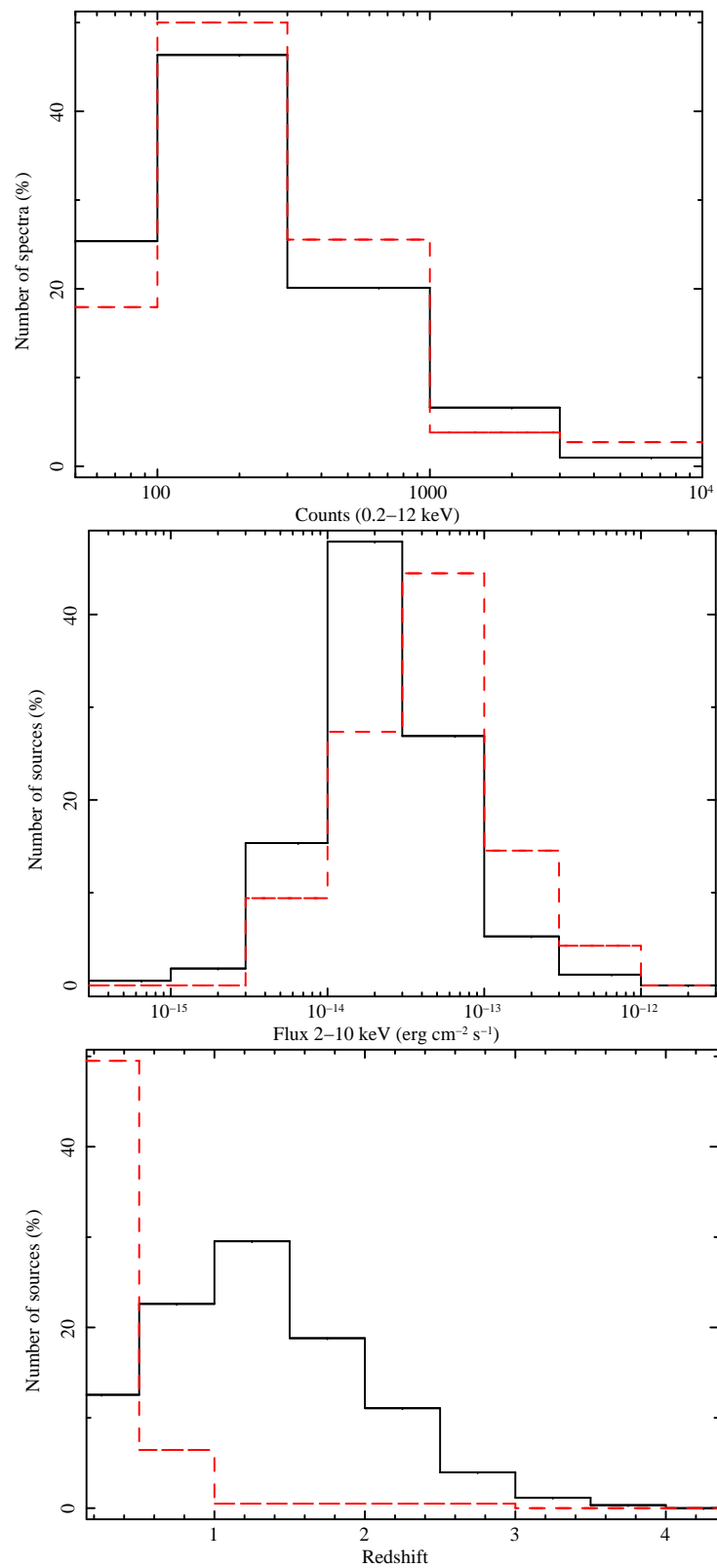


Figure 4.8 **AXIS+XWAS sample:** Counts (top), flux (central) and redshift (bottom) distributions for type 1 (solid line) and type 2 (dashed line) AGN.

4.4.2 Average spectra

From the individual spectral fitting procedure included in the averaging process (Sect. 4.2), we obtain the intrinsic column density distribution shown in Fig. 4.9. It should be noted that the intrinsic absorption measured from the individual spectra could be actually larger due to the limited spectral quality and the fact that we are computing the power law slope and the intrinsic column density at the same time. This could affect the individual fitted values but it should not affect the final average spectral shape for moderate amounts of intrinsic absorption, as it is shown in Sect. 4.3. After applying the averaging method, we obtain the average spectra shown in Fig. 4.10 along with the simulated continuum and confidence contours (the latter already shown in Fig. 4.7). Fitting a power law between 2 and 10 keV, excluding the 4-7 keV range where the Fe line would be present, we obtain a value of $\Gamma = 1.92 \pm 0.02$ and $\Gamma = 1.37 \pm 0.05$ for type 1 and type 2 AGN, respectively, the lower value for type 2 AGN due to the larger amount of absorption (see Fig. 4.9). We clearly see a narrow emission feature around 6.4 keV and also an excess of emission from 5 to 10 keV for type 1 AGN and from 4 to 9 keV for type 2 AGN, but only the narrow peak being well above the 2σ upper continuum level. In Fig. 4.11, the ratio of the average spectrum to simulated continuum is presented around the position of the emission line.

In order to check whether a number of “extreme” sources are responsible for the observed emission features, a safety test is performed. We remove in each energy bin all the spectra that deviate more than 3 times the standard deviation from the average value. The resulting average spectrum shows the same overall shape as for the whole sample, the 5 to 10 keV emission residuals being smaller than the ones in Fig. 4.10, but consistent within errors. This could be due either to the fact that we are actually removing the sources that show more prominent emission in that range, or we are simply reducing the noise by removing the lowest quality spectra. In any case, the differences we find are not significant.

Assuming that the simulated continuum represents the actual underlying continuum below the emission features, we measure a total excess emission with EW of ~ 600 eV between 5 and 10 keV for type 1 AGN and ~ 300 eV between 4 and 9 keV for type 2 AGN. Obviously, this value may correspond to the addition of multiple components in this range. As can it be seen in Fig. 4.10, a relativistic profile is not obviously present in the resulting average spectra.

We perform a spectral analysis of the average spectrum using XSPEC v12.4. We exclude energies above 15 keV where the errors were very large and also energies below 3 keV to avoid the contribution of soft features that can be due to the unfolding procedure. As mentioned in Sec. 4.2.1, the spectral shape below 3 keV is highly dependent on the model used to unfold the spectra. Therefore, the apparent “soft-excess” below 2 keV and the “absorption” feature around 2.5 keV

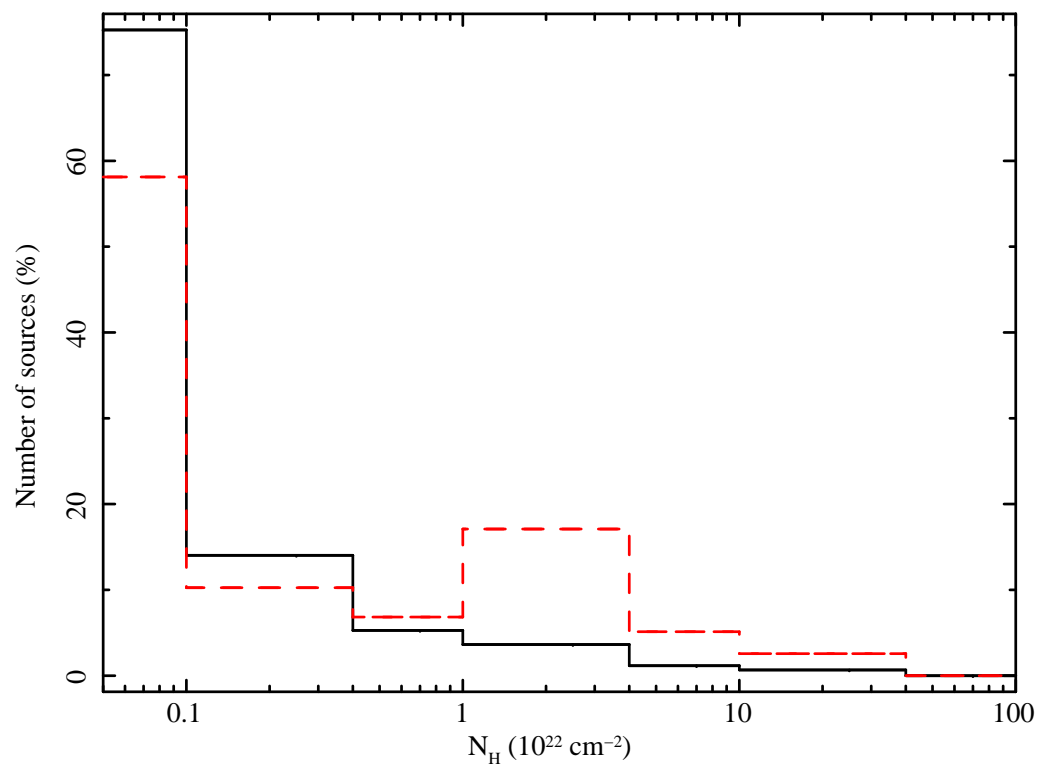


Figure 4.9 **AXIS+XWAS sample:** Intrinsic absorption distribution for type 1 (solid line) and type 2 (dashed line) AGN using the “best-fit” model: $\text{pha} * \text{zpha} * \text{po}$ with Γ , intrinsic absorption and power law normalisation as free parameters.

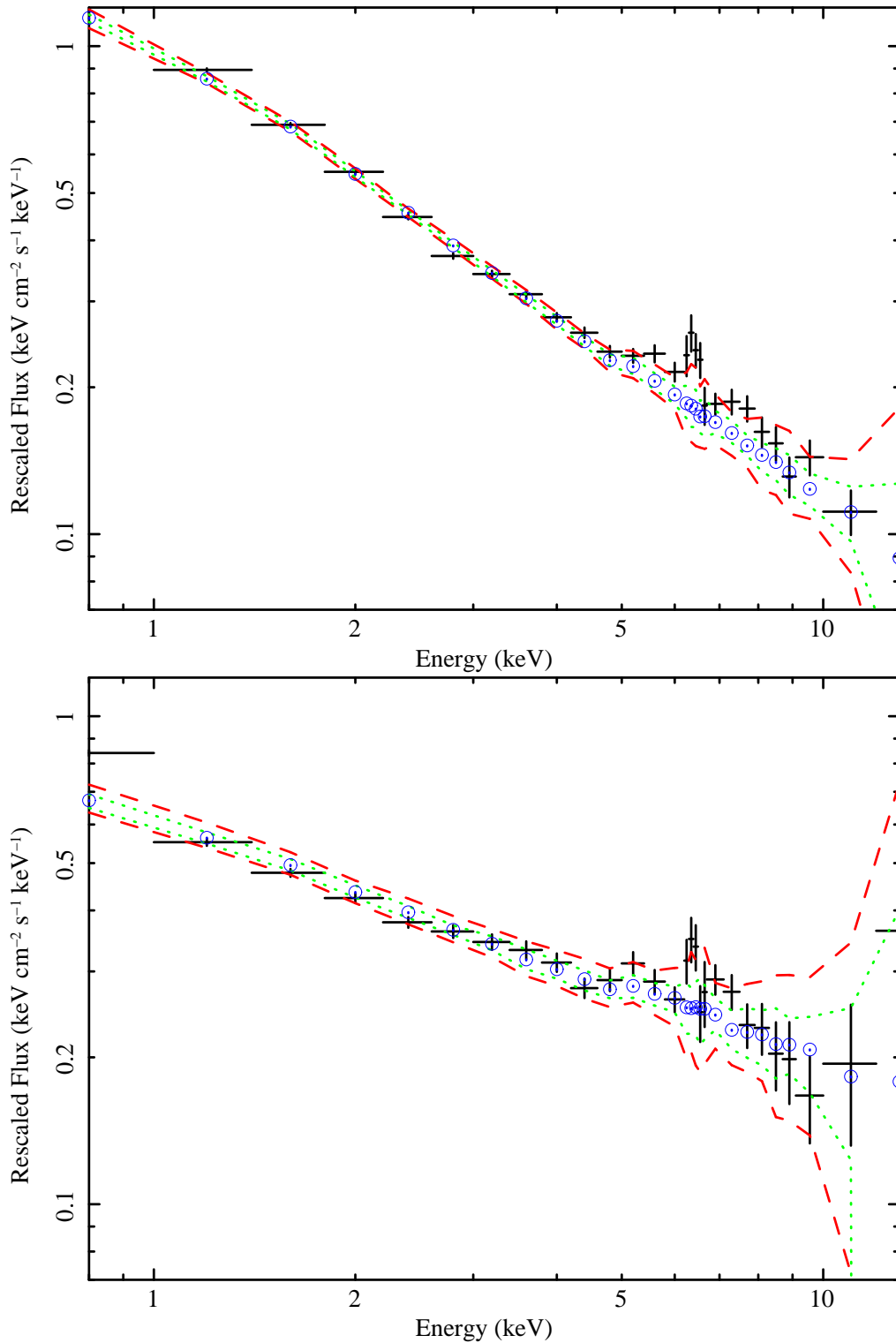


Figure 4.10 **AXIS+XWAS sample** Type 1 (top) and type 2 (bottom) AGN average spectrum (error bars) along with the 100-simulations continuum (open circles) and 1σ (dotted line), 2σ (dashed line) confidence limits.

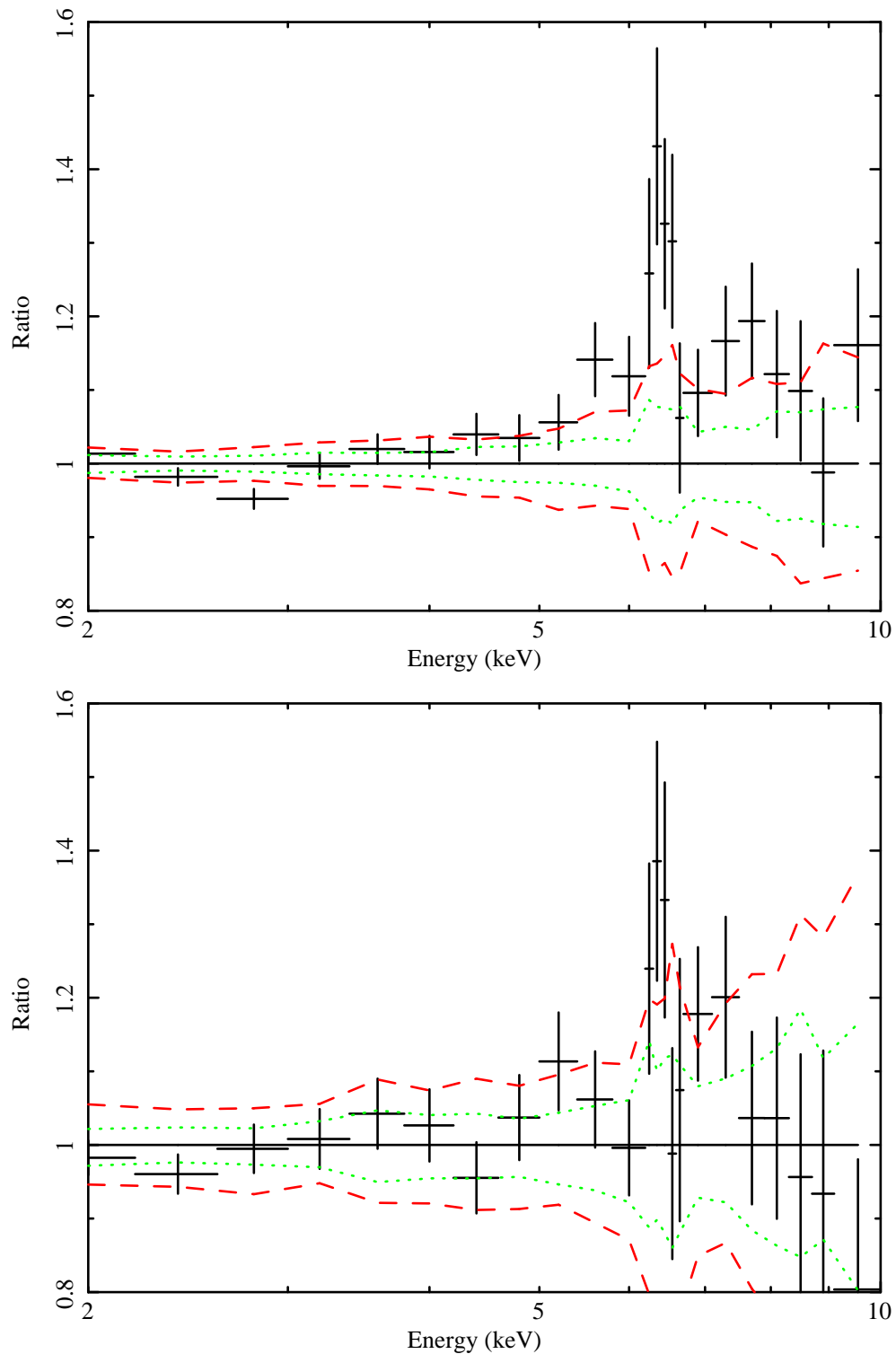


Figure 4.11 **AXIS+XWAS sample** Type 1 (top) and type 2 (bottom) AGN average spectrum to 100-simulations continuum ratio (error bars) along with 1σ (dotted line) and 2σ (dashed line) confidence limits.

could be due to the averaging process and we refrain from assigning them any physical meaning. In any case, the “soft-excess” accounts only for less than 5 % of the soft flux, and the “absorption” feature is barely significant.

For simplicity we define a “baseline model” composed of the following two components:

- A table model computed from the simulated continuum, with no free parameters. As explained in Sect. 4.3, this should account for the average over the whole sample of absorbed power law. Leaving the continuum’s normalisation to vary does not significantly change the results, so we fix it to prevent an unphysical broad line fitting multiple spectral bumps at the cost of having an unjustified small continuum.
- A narrow Gaussian line with energy and normalisation as free parameters. The line width, also a free parameter, is constrained to be below 200 eV. Given the artificial broadening introduced by the EPIC response and the averaging process, $\simeq 100$ eV, this limit ensures that a narrow line is modelled (see Sect. 4.3).

Using this baseline model only we obtained a poor fit ($\chi^2/\text{d.o.f} = 41/18$) for type 1 AGN, but the narrow line is detected at $> 3\sigma$ significance level ($\Delta\chi^2 > 14.16$ for 3 additional parameters) with an EW ~ 200 eV. On the other hand, this baseline model gave a good fit for type 2 AGN ($\chi^2/\text{d.o.f} = 19/18$), the narrow line also detected at $> 3\sigma$ significance level but with an EW ~ 100 eV, although some residuals can be seen around the narrow line position. In both cases, the line is centred around 6.4 keV so it corresponds to neutral or low-ionisation Fe $K\alpha$, i.e it likely comes from distant and cold material such as the putative torus in the Unified Schemes (Antonucci, 1993). Observations have shown that a narrow emission line corresponding to Fe $K\alpha$ is an ubiquitous feature in local AGN X-ray spectra (Page et al. 2004; Nandra et al. 2007). We confirm and extend this important result to the distant Universe.

Since the baseline model only is not a good fit for type 1 AGN, new models are tried by adding additional components. It has been claimed that complex absorption and high-density ionised absorbers can mimic the red tail of a broad relativistic line (Reeves et al. 2004; Turner et al. 2005). Ionised absorbers are often observed in AGN, but we find that adding cold (partially or totally covering the primary source) or warm (absorber, Zdziarski et al. 1995) absorption does not improve the fit at all.

Given the positive residuals at high energies for type 1 AGN, the next step is to fit a reflected component from neutral material (pexrav model, Magdziarz and Zdziarski 1995). We obtain an improvement on the fit of $>3\sigma$ significance level

($\chi^2/\text{d.o.f} = 14/15$), for a reflection fraction $R \simeq 0.5$ ($\Omega/2\pi \sim 0.5$, where Ω is the solid angle subtended by the reflector to the primary X-ray source) and inclination angle $i \simeq 60$ deg, assuming solar Fe abundance. It should be noted that we fit a reflection model for a given inclination angle to a spectrum that corresponds to a mixture of different reflection components with different inclination angles. Unfortunately, the quality of the average spectrum does not allow us to recover the inclination angle distribution for the sample so as to obtain an angle-average model. Leaving the Fe abundance free only results in a slightly higher value for it and no significant improvement of the χ^2 . Adding relativistic blurring to the reflected component (kdblur convolution model using a laor profile) does not improve the fit. Note that the amount of reflection along with the measured narrow Fe $K\alpha$ EW are consistent with reflection from distant Compton-thick matter, such as the torus, for type 1 AGN (Reeves, 2003).

We also try to fit a reflected component from an ionised disk (reflion model, Ross and Fabian 1993). We obtain quite a good fit ($\chi^2/\text{d.o.f} = 19/16$), slightly worse than the previous one, the disk being in a low-ionisation state. Modifying it by relativistic blurring, we obtain a similar goodness of fit ($\chi^2/\text{d.o.f} = 15/16$, all kdblur parameters fixed to their default values) as derived for the neutral reflection. However, looking at this model in detail, we find it provides only an upper limit for the ionisation parameter ($\xi < 30$, neutral to low ionisation disk), that pegs at the lower limit permitted by the model. Moreover, the effect of the relativistic blurring is to smear the emission lines to the point that the resulting shape is almost identical to the pexrav model. Besides that, the fit does not depend on the remaining disk parameters and, allowing them to vary, results in unreasonable values, like an inclination angle for the disk much higher than 60 deg, at odds with the Unified AGN model. Therefore, we cannot distinguish (in terms of $\Delta\chi^2$) between neutral reflection from distant material and ionised reflection from a low-ionisation accretion disk. However, the computed parameters for the neutral reflection component, as well as the central energy for the narrow Fe $K\alpha$ line and its EW (6.36 keV and 90 eV, respectively), favour the neutral reflection scenario rather than the ionised one (Reeves et al. 2001; George and Fabian 1991). Furthermore, the relativistically blurred low-ionisation disk reflection just seems to be mimicking the neutral reflection shape instead of actually fitting relativistic features.

As a safety test, we check whether the measured reflected component could be due to the dispersion in the power law indices, since a mixture of power laws should not result in a perfect power law shape. To this end, we simulate a Gaussian distribution of power law indices similar to the one presented in Mateos et al. (2005a), with a mean spectral slope of 1.9 and an intrinsic dispersion of 0.23. We find that the deviation from a power law shape for the resulting average spectrum is too small to account for the observed residuals above 5 keV, thus supporting our reflection component hypothesis.

We also attempt to fit the broad residuals by using a relativistic line model (1aor model, [Laor 1991](#)). Leaving the line energy to vary results in an unreasonable value of ~ 8 keV so, after trying several values between 6.4 and 6.9 keV, we fix it to 6.4 keV. We find that the fit does not depend on the emissivity index nor the inner or outer radii. The only relevant parameter appears to be the inclination angle, but again, leaving it free to vary results in an unphysically large value (> 80 deg) for type 1 AGN. Requiring such a large value for the inclination angle implies that the relativistic line is trying to fit the continuum as well as the broad residuals. We therefore fix the inclination angle to 30° , a typical value for type 1 AGN ([Antonucci 1993](#), [Nandra et al. 2007](#), [Guainazzi et al. 2006](#)). We obtain in this way a barely acceptable fit ($\chi^2/\text{d.o.f} = 26/17$), significantly worse than the neutral reflection model.

In the case of type 2 AGN, the simple baseline model seems to be a good fit. Adding a relativistic line ($\text{EW} \sim 400$ eV) or a reflection component does not significantly improve the fit ($< 99\%$ significance level). Besides, as it can be seen in [Fig. 4.11](#), the excess emission over the continuum level in this case is barely significant, being below the 2σ confidence level.

The best-fit parameters corresponding to the models that significantly improve the “baseline model” fit are shown in [Table 4.2](#). The fit corresponding to the “baseline model” plus neutral reflection, which appears to be the only physically plausible case for type 1 AGN, is shown in [Fig. 4.12](#) along with the baseline model fit for type 2 AGN. As it can be seen there are still some positive residuals above ~ 7 keV. These residuals could contain the contribution of the Fe emission from the detectors shifted to high energies when shifting the spectra to their rest-frame. Besides, they could be also due to additional components, like a reflection component in the case of type 2 AGN, which are not taken into account in the spectral fit due to their low significance, note that error bars are compatible with the upper 2σ limit.

Adding a relativistic line to the “baseline model” plus cold reflected component in type 1 AGN does not improve the fit significantly. We compute an upper limit for the EW of any broad relativistic line (for a Laor line centred at 6.4 keV) of < 400 eV at 3σ confidence level, a value significantly below the 560 eV reported in S05. The reasons for these differing results could be as follows:

- Differences in the sample characteristics. The sample studied in S05 is composed of faint sources (average flux $\sim 10^{-14}$ erg cm $^{-2}$ s $^{-1}$) whereas ours is composed of medium flux sources (average flux $\sim 5 \times 10^{-14}$ erg cm $^{-2}$ s $^{-1}$). The S05 X-ray spectra are of overall better quality than ours, having more than 200 counts in the 0.2-10 keV band, but their sample only com-

prises ~ 100 AGN whereas ours is composed of more than 700 sources. The sources in S05 are of course more distant and luminous on average, so we are presumably dealing with different source populations. Higher-luminosity sources would be expected to have lower EW, however, due to the Iwasawa-Taniguchi effect (see Sect. 4.6).

- Differences in the stacking method: The method we have developed takes into account all the possible contributions to the underlying continuum. As can be seen in the simulations (see Sect.4.3), broad residuals can appear due to dispersion in the underlying continuum. The subtraction of the continuum has been dealt with in a less detailed way in S05, and this could result in an overestimation of the broad line EW. Besides, stacking grouped spectra, as in S05, can introduce features such as a broad red tail in an emission line as showed in [Yaqoob \(2006\)](#).

Our results shown here favour the second explanation, as we discuss in the following section.

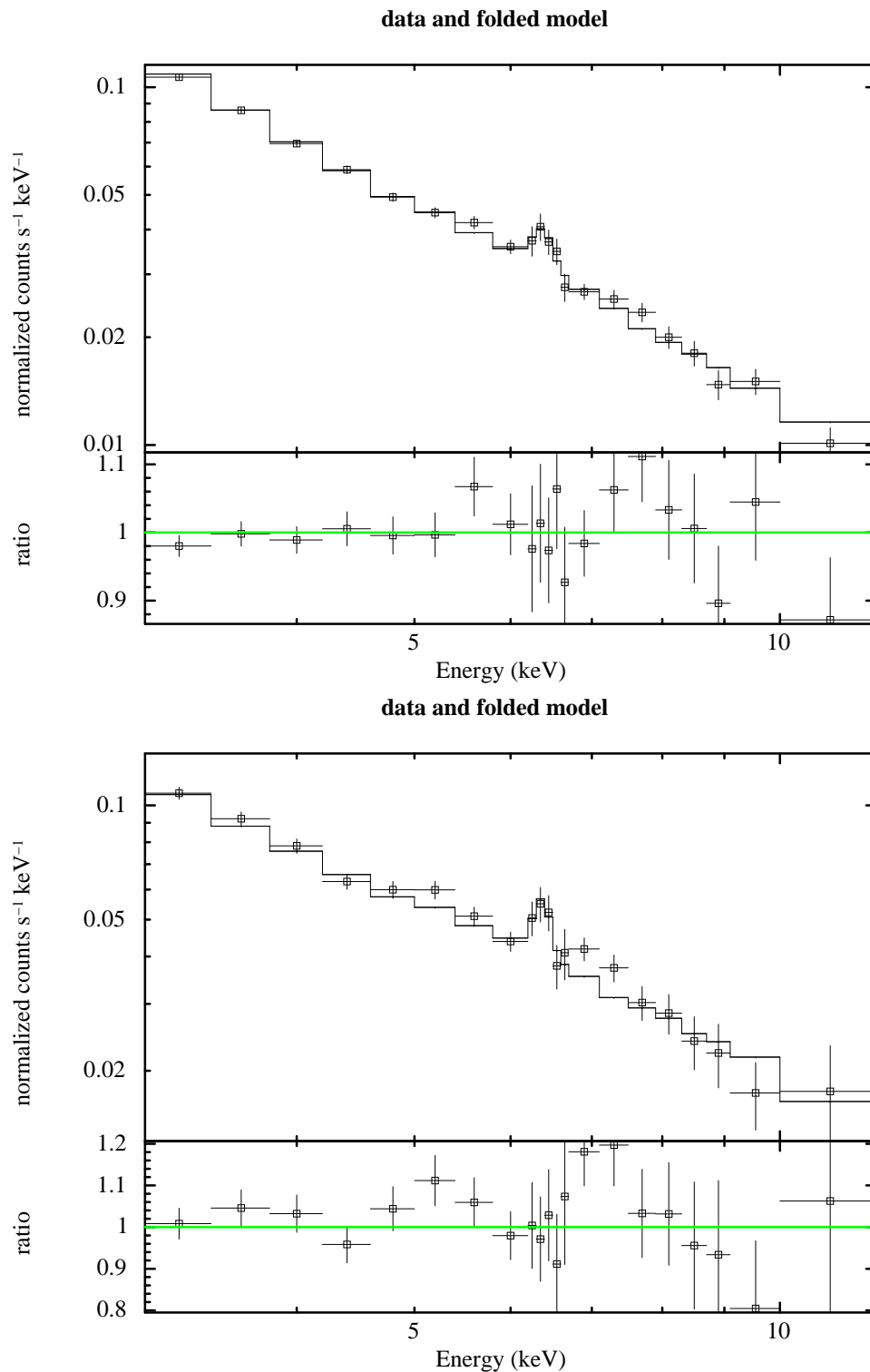


Figure 4.12 **AXIS+XWAS sample**: Spectral fit corresponding to the best-fit model for type 1 (top) and type 2 (bottom) AGN.

Table 4.2 Best fit parameters for the spectral fit to the **AXIS+XWAS sample** average spectra.

Model	E_{gaus} (keV)	σ_{gaus} (eV)	EW_{gaus} (eV)	Reflection Factor	Inclination Angle (deg)	Ionization Parameter (erg cm s^{-1})	EW_{laor} (eV)	$\chi^2/\text{d.o.f}$
Type 1 AGN								
Baseline model	6.34 ⁿ	200 ^p	200 ⁿ	41/18
Baseline model + pextrav	6.36 ^{+0.05} _{-0.05}	80 ⁺⁶⁰ ₋₈₀	90 ⁺³⁰ ₋₃₀	0.50 ^{+0.15} _{-0.20}	60 ⁺¹⁵ ₋₂₀	14/15
Baseline model + kdblur(reflion)	6.37 ^{+0.04} _{-0.04}	80 ⁺⁴⁰ ₋₄₀	80 ⁺²⁰ ₋₂₀	...	30 ^f	, < 30	...	15/16
Baseline model + Laor	6.37 ^{+0.06} _{-0.06}	10 ⁺¹⁰ ₋₁₀	50 ⁺³⁰ ₋₂₀	350 ⁺⁷⁰ ₋₉₀	26/17
Type 2 AGN								
Baseline model	6.36 ^{+0.06} _{-0.07}	< 60 ^p	100 ⁺⁵⁰ ₋₅₀	19/18

Model parameters not displayed correspond to default values.

ⁿ poor fit does not allow error calculation.

^p fit parameter pegged at hard limit.

^f fixed parameter.

4.5 Faint sample: Lockman Hole

4.5.1 Sample description

The Lockman Hole sample corresponds to one of the deepest observations carried out by XMM-Newton (now superseded by the ultra-deep survey in the CDFS, [Comastri et al. 2011](#)). The Lockman Hole region has an extremely low Galactic hydrogen column density, $N_H = 5.7 \times 10^{19} \text{ cm}^{-2}$ and therefore must be transparent to soft X-rays. The X-ray spectra were obtained by adding 17 XMM-Newton observations taken at different epochs so that the resulting clean exposure time was > 500 ks. In this case, all the available spectra for the same source and camera (pn or MOS) were merged provided that the source did not fall close to a CCD gap or too close to the border of the FOV. A detailed description of the spectral extraction for this sample is presented in [Mateos et al. \(2005b\)](#). The source identifications were also carried out by using optical spectroscopy. In this case, and in order to be able to directly compare our results with the ones presented in S05, no selection is made about the number of counts in the individual spectra but we try to compile the same spectral data used in S05. Our sample however, is slightly smaller comprising 49 type 1 (out of 53 in S05) and 35 type 2 AGN (out of 41 in S05). Given the nature and stability of our averaging method, we do not expect this difference to significantly affect the comparison between the two methods.

The counts and redshift distributions, along with the flux distribution in the standard hard (2-10 keV) band, are shown in [Fig. 4.13](#).

4.5.2 Average spectra

We apply again the method described in [Sect. 4.2](#), obtaining the intrinsic absorption distribution shown in [Fig. 4.14](#) and the average spectra shown in [Fig. 4.15](#) along with the simulated continuum and confidence levels. Fitting a power law between 2 and 10 keV, excluding the 4-7 keV range, we obtain a value of $\Gamma = 1.81 \pm 0.04$ and $\Gamma = 1.07 \pm 0.04$ for type 1 and type 2 AGN, respectively. We obtain a much lower value of Γ than we obtained for the AXIS+XWAS type 2 AGN. We see a narrow peak around 6.4 keV and some excess emission from 5 to 10 keV but not clearly above the 2σ confidence limit so again, there is no evidence for a broad relativistic line profile. The measured power law slope for type 2 AGN is extremely flat, implying a larger amount of absorption than for type 2 AGN in the AXIS+XWAS sample (compare [Fig. 4.9](#) with [Fig. 4.14](#)). Besides, the type 2 average spectrum displays a stronger “bump” between 4 and 6 keV, also what it looks like a stronger narrow line at 6.4 keV, that could be due to this large amount of absorption, as we discussed in [Sect. 4.3](#) (see [Fig. 4.6](#)). Assuming the simulated continuum represents the actual underlying continuum below the emission features, we measure a total excess emission with EW of ~ 700 eV

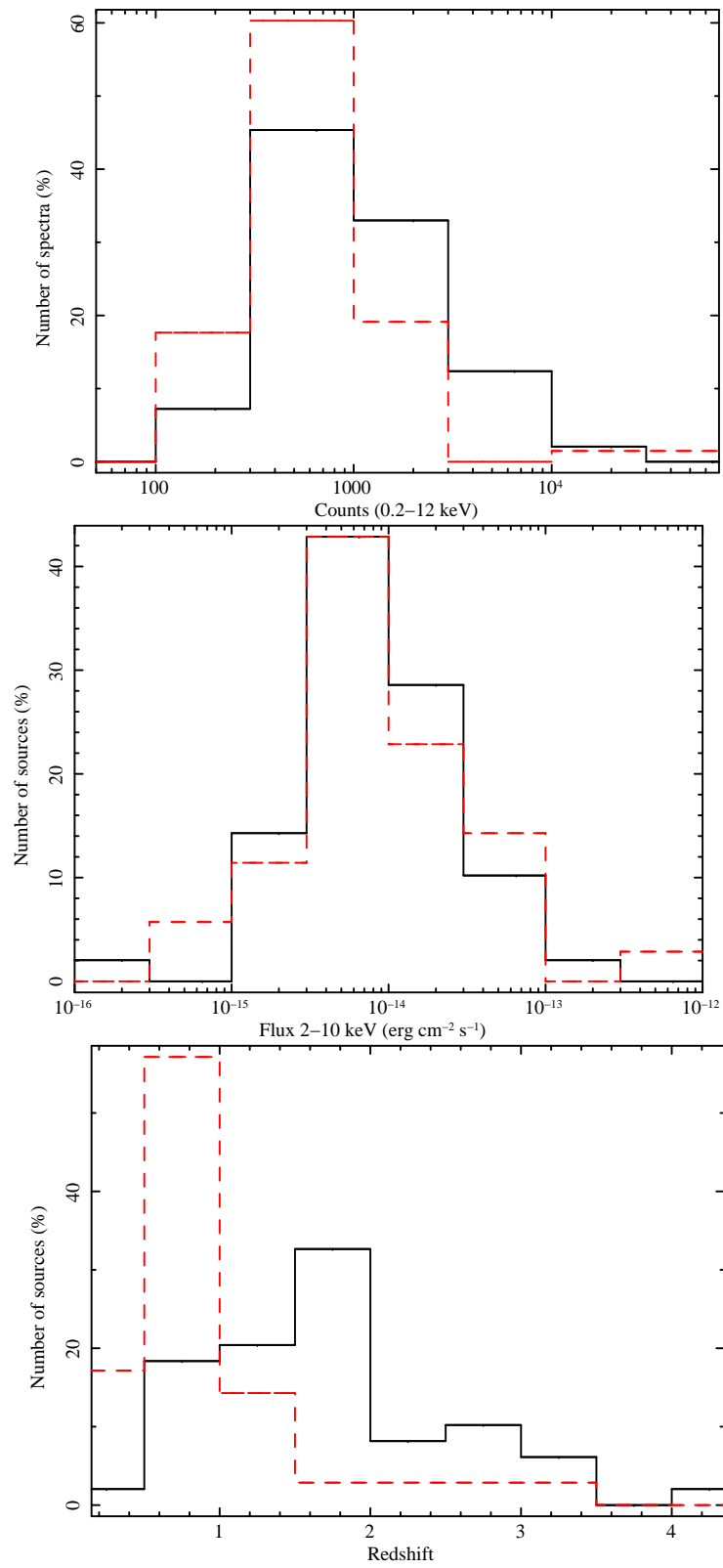


Figure 4.13 **Lockman Hole sample:** Counts (top), flux (central) and redshift (bottom) distributions for type 1 (solid line) and type 2 (dashed line) AGN.

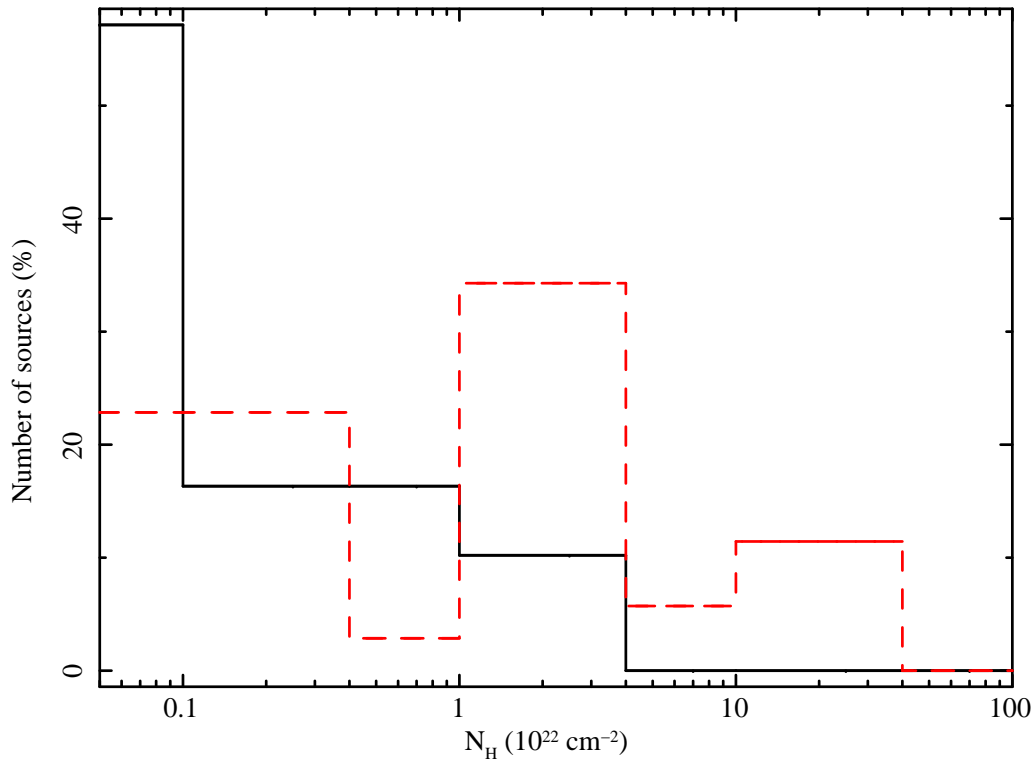


Figure 4.14 **Lockman Hole sample**: Intrinsic absorption distribution for type 1 (solid line) and type 2 (dashed line) AGN using the “best-fit” model: $\text{pha}*\text{zpha}*\text{po}$ with Γ , intrinsic absorption and power law normalisation as free parameters.

between 5 and 10 keV for type 1 AGN and ~ 1 keV between 4 and 9 keV for type 2 AGN. In Fig. 4.16, the average spectrum to simulated continuum ratio is presented around the position of the emission line.

A similar spectral analysis as for the AXIS+XWAS sample is carried out, constructing a baseline model composed of the 100 simulations continuum and a narrow line. This simple baseline model is not a good fit neither for type 1 AGN ($\chi^2/\text{d.o.f} = 50/18$) nor for type 2 AGN ($\chi^2/\text{d.o.f} = 43/18$), but in both cases the narrow line is detected at $> 3\sigma$ confidence level. This narrow line is centred around 6.4 keV, as in the AXIS+XWAS sample, so it likely corresponds to neutral material emitted far from the central source. We measure an EW of ~ 160 eV for type 1 AGN and a larger value for type 2 AGN of ~ 300 eV. This larger value for type 2 AGN could be due to the fact that for a larger amount of absorption, the direct emitted continuum is more suppressed whereas the narrow emission line, that given its width and central energy is likely emitted farther from the central source, is not suppressed. However, we are not taking into account in this model the “bump” which might be attributable to reflection or other phenomena and thus can reduce this EW.

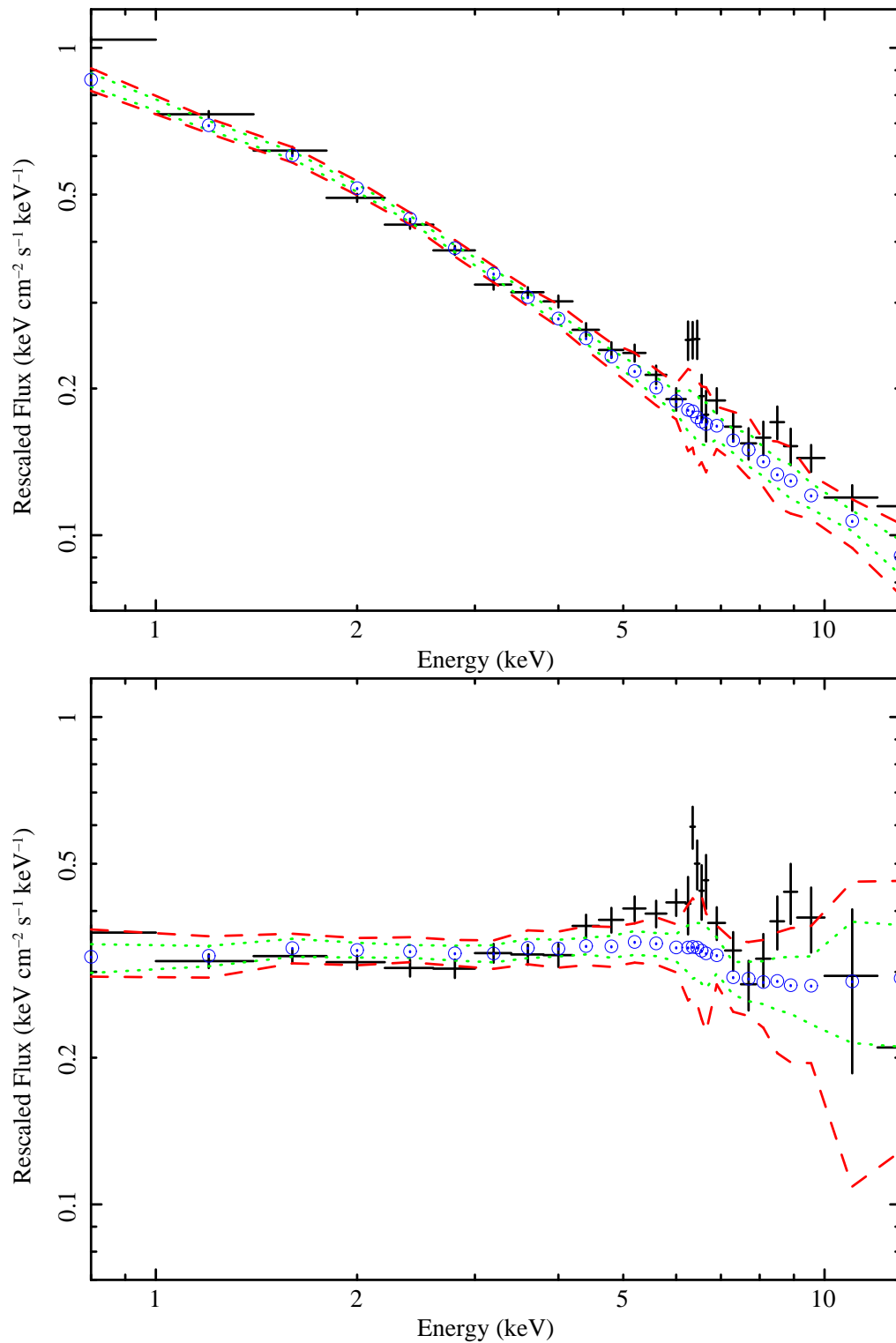


Figure 4.15 **Lockman Hole sample:** Type 1 (top) and type 2 (bottom) AGN average spectrum (error bars) along with the 100-simulations (open circles) continuum and 1σ (dotted line), 2σ (dashed line) confidence limits.

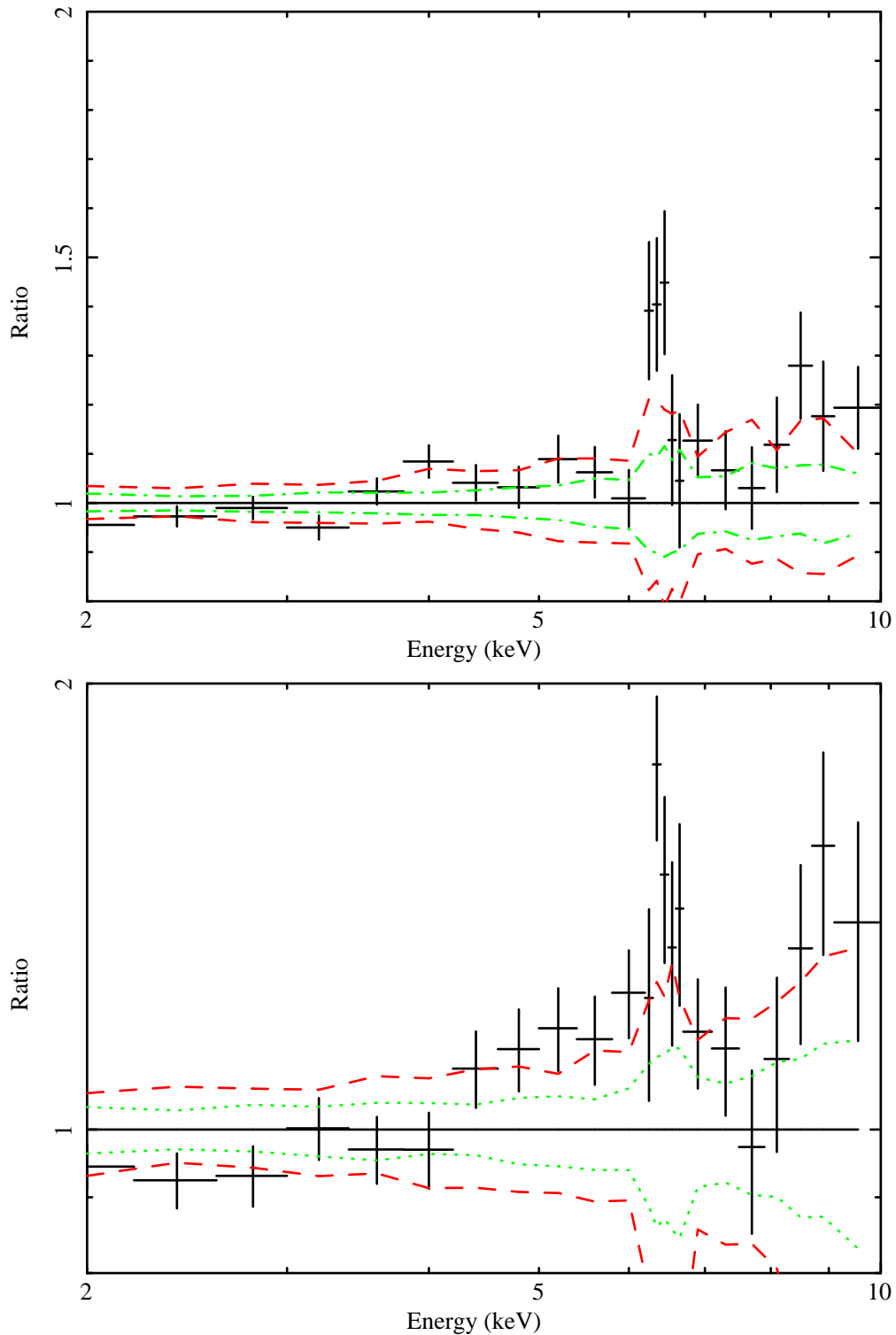


Figure 4.16 **Lockman Hole sample:** Type 1 (top) and type 2 (bottom) AGN average spectrum to 100-simulations continuum ratio (error bars) along with 1σ (dotted line) and 2σ (dashed line) confidence limits.

We then proceed by adding the same additional components as in the AXIS+XWAS sample. We find that for type 1 AGN, a reflected component (`pexrav` XSPEC model) significantly improves the fit ($\chi^2/\text{d.o.f} = 23/16$), obtaining a reflection fraction $R \simeq 0.6$ but just an upper limit for the inclination angle of $i < 80$ deg. We compute an EW for the narrow emission line of $\text{EW} \sim 90$ eV, in agreement with what is expected for the measured amount of cold reflection. Neither adding ionised or neutral, partial or total absorption nor a relativistic line, significantly improves the fit. We find a similar good fit ($\chi^2/\text{d.o.f} = 26/15$) when trying ionised reflection modified by relativistic blurring (model `kdblur(reflion)`). Nevertheless, as it happened with type 1 AGN in the AXIS+XWAS sample, the ionisation parameter pegs at its minimum value, implying neutral reflection, and the relativistic blurring appears to be smearing the emission lines included in `reflion` to the point that the overall resulting shape turns out to be very similar to the one obtained when using the neutral reflection (`pexrav` model). We therefore conclude that the best-fit model in the case of type 1 AGN corresponds to the baseline model plus a neutral reflected component and a narrow Fe K α emission line. From this model, we estimate an upper limit from the contribution of a relativistic line of 240 eV at 3σ confidence level, much lower than the value of 560 eV reported on S05. Our conclusion is that the value presented in S05 could be overestimated due to a less sophisticated treatment of the continuum and the effect of using grouped spectra during the averaging process (Yaqoob, 2006).

The situation is far more complex for type 2 AGN due to the larger amount of intrinsic absorption, larger in average than the absorption of type 2 AGN in the AXIS+XWAS sample. This absorption affects the average continuum and spectrum due to the way we rescale the spectra. We rescale the spectra by using the 2-5 keV rest-frame flux. If the sources are absorbed by a large column density ($N_H > 10^{22} \text{ cm}^{-2}$), part of the 2-5 keV flux will be suppressed (see Fig. 1.3 in Chapter 1), increasing the rescaling factor. Therefore, the contribution of each individual spectrum when mixing highly absorbed spectra will not be the same in the sense that the most absorbed spectra will have the largest weights in the average. On the other hand, the much higher SNR in the average spectrum could be allowing us a better measurement of the absorption than for the individual spectra, so we might be simply “seeing” absorption in the average spectrum which we are not able to measure in the individual spectra. Since the amount of intrinsic absorption used to construct the simulated continuum comes directly from the spectral fit to the real data, the simulated absorption could be different from the actual absorption in the real data. As a result, the “broad hump” in the 4-7 keV energy range turns out to be more pronounced for the real data than for the simulated continuum, although still within the 2σ limits, and the simulated continuum turns out not to be a good representation of the actual underlying continuum in this case. There is not a straightforward solution to all this. Fixing the power law index in order to compute better the intrinsic absorption in the real data could distort the spectra shape around the emission line (since the actual

spectral shape could be quite different from a simple power law shape), whereas excluding the spectral region affected by absorption and the emission line region when rescaling the spectra will leave a too narrow energy range.

Considering all that, we decide to fit a partial covering model as a baseline model instead of using the simulated continuum. In this way we can very roughly account for the mixture of power law slopes with different amounts of absorption. We obtained an intrinsic hydrogen column density of $\sim 3 \times 10^{23} \text{ cm}^{-2}$ and a covering fraction of $\sim 70\%$. The intrinsic column density is much larger than the average computed by fitting the data individually ($\sim 3 \times 10^{22} \text{ cm}^{-2}$), but consistent with having underestimated the actual amount of absorption when fitting the real data (probably due to the fact that we are leaving Γ free when fitting the spectra) and, at the same time, assigning the largest weights to the most absorbed sources. For type 2 AGN within AXIS+XWAS sample, the average absorption is lower, so this effect should be smaller and does not affect significantly our results.

In Fig. 4.17 the best-fits for type 1 (baseline plus reflected component) and type 2 (partial covering power law plus narrow line) AGN are shown. Both spectral fits display some positive residuals above 8 keV. These are likely due to the mentioned Fe emission from the detectors when shifted to the sources rest-frame. In any case, these residuals are consistent with the upper 2σ confidence limits. The parameter values for the baseline model and the best-fit models are presented in Table 4.3.

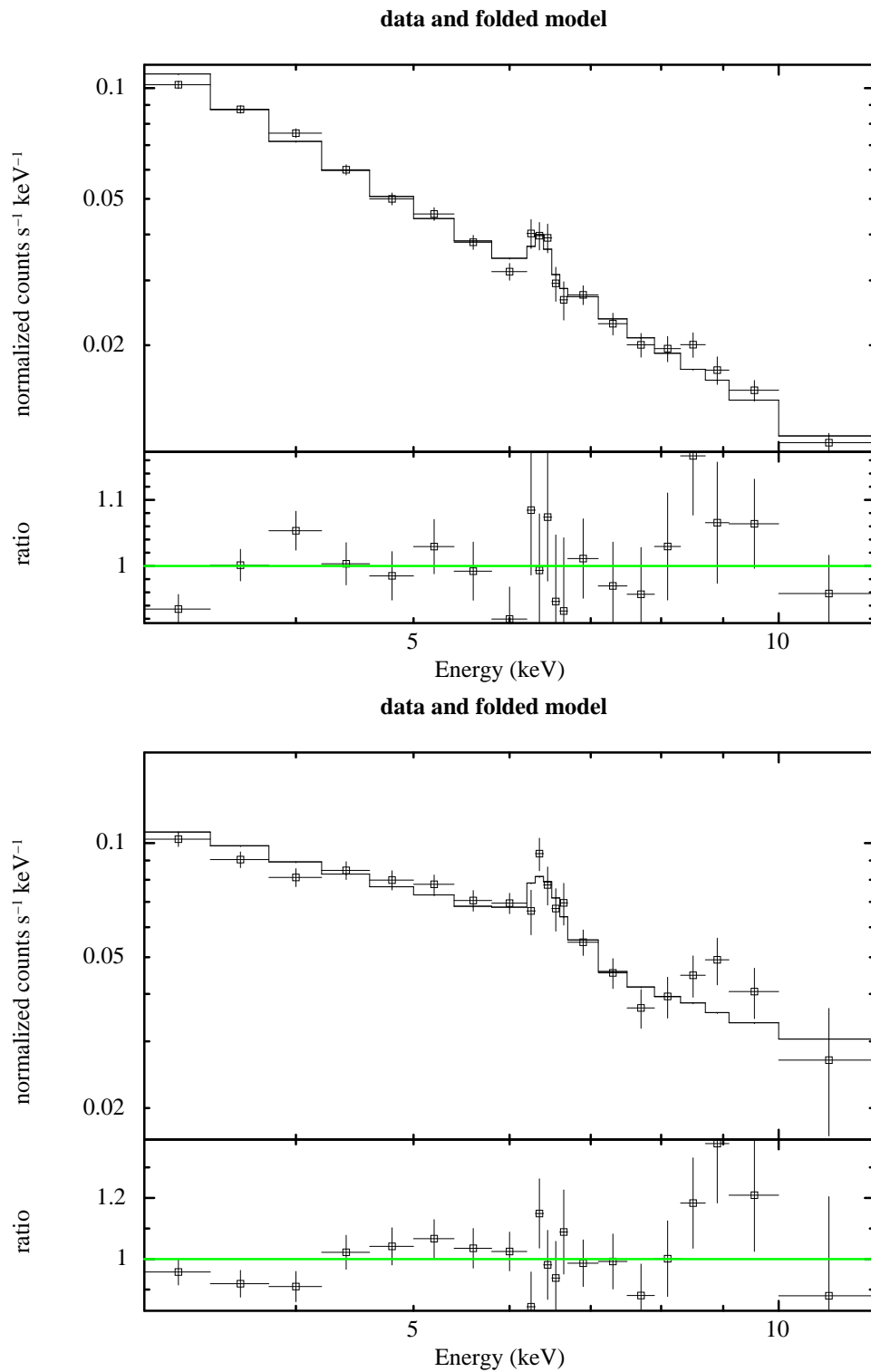


Figure 4.17 **Lockman Hole sample**: Spectral fit corresponding to the best-fit model for type 1 (top) and type 2 (bottom) AGN.

Table 4.3 Best fit parameters for the spectral fit to the Lockman Hole sample average spectra.

Model	E_{gaus} (keV)	σ_{gaus} (eV)	EW_{gaus} (eV)	Reflection Factor	Inclination Angle (deg)	Intrinsic N_{H} (10^{22} cm^{-2})	Covering Fraction	$\chi^2/\text{d.o.f}$
Type 1 AGN								
Baseline model	6.37 ⁿ	160 ⁿ	160 ⁿ	50/18
Baseline model + pextrav	6.36 ^{+0.06} _{-0.06}	< 90	90 ⁺³⁰ ₋₃₀	0.6 ^{+0.2} _{-0.20}	< 80	23/16
Type 2 AGN								
Baseline model	6.36 ⁿ	200 ^p	300 ⁿ	43/18
Partial covering + narrow line	6.4 ^{+0.5} _{-0.5}	< 80 ^p	70 ⁺⁴⁰ ₋₄₀	28 ⁺⁸ ₋₁₀	0.68 ^{+0.08} _{-0.14}	12/14

Model parameters not displayed correspond to default values.

ⁿ poor fit does not allow error calculation.

^p fit parameter pegged at hard limit.

^f fixed parameter.

4.6 Discussion and Results

In order to further improve the SNR of our average spectra, we combined the two samples presented in sections 4.4 and 4.5, obtaining a sample of 655 type 1 and 152 type 2 AGN (see Fig. 4.18). The resulting average spectrum and average spectrum to simulations ratio for type 1 and type 2 AGN are presented in Fig. 4.19 and Fig. 4.20. In this case, we compute a $\Gamma = 1.91 \pm 0.03$ and $\Gamma = 1.30 \pm 0.04$ for type 1 and type 2 AGN, respectively. We again, do not see evidence for a relativistic emission line but only a narrow peak centred around 6.4 keV being well above the confidence limits.

The baseline model resulted in a bad fit for the type 1 and type 2 AGN average spectra. We found that the best-fit model for type 1 AGN is very similar to the one for the AXIS+XWAS sample (baseline plus reflected component), as expected, since we are only adding 41 sources to more than 600, and we estimate an upper limit for the relativistic line of 370 eV at 3σ confidence level. For type 2 AGN, we are adding 35 sources to the 117 in the AXIS+XWAS sample, so in this case the intrinsic absorption became important, as for the Lockman Hole sample only, and we needed to fit a partially covered absorbed power law in order to obtain a good fit. The measured amount of absorption remains the same but the covering fraction decreases to 40%, as the fraction of highly absorbed sources decreases. The best-fit parameters corresponding to the these fits are presented in Table 4.4 and Fig. 4.21.

Given the relatively large number of counts in the final average spectrum (~ 320000 for type 1 AGN, ~ 86000 for type 2 AGN in the 2-10 keV range), we divided the sample into three different bins containing the same number of counts, in order to check for possible spectral variations as a function of redshift, flux or luminosity. The measured narrow Fe K α EW for the different sub-samples is shown in Table 4.5. We do not detect any significant variation with redshift nor with flux, although we marginally detect a correlation of the narrow emission line EW with luminosity. We also detect a drop in the EW at the last redshift bin for type 1 AGN, likely due to the fact that at that redshift bin ($z > 1.7$) the main contributors are high luminosity quasars, whereas there are not enough type 2 sources at high redshifts to see this effect in their case (see Fig. 4.18). As it can be seen from Fig. 4.22 and Table 4.5, the narrow line EW decreases as the luminosity increases, a behaviour previously reported as the Iwasawa-Taniguchi or X-ray Baldwin effect (Iwasawa and Taniguchi, 1993). The errors are however too large to extract conclusive results for type 2 AGN. Note that the tabulated values are maybe slightly higher than the actual values since we are just fitting the baseline model (Sect. 4.4.2) in this case. Several explanations have been proposed to explain this effect:

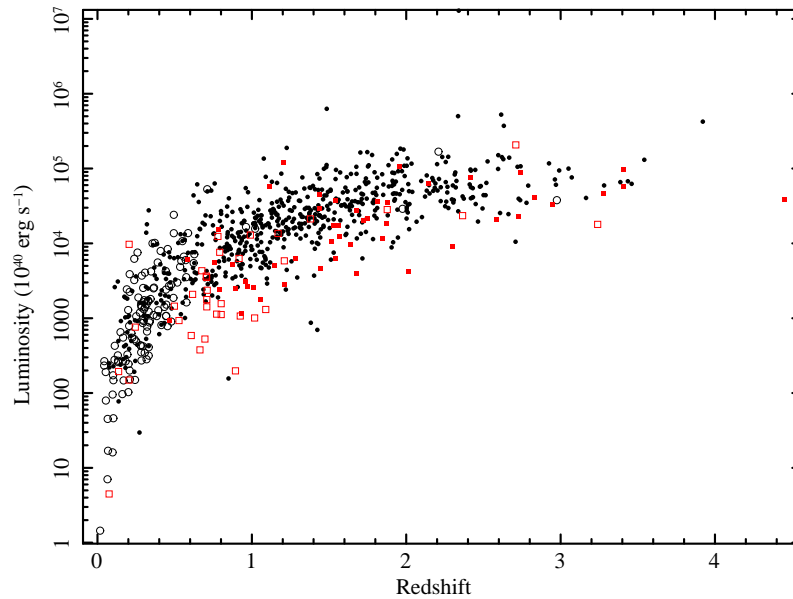


Figure 4.18 **Luminosity versus redshift** for the AXIS+XWAS (circles) and Lockman Hole (squares) samples. Filled and open symbols represent type 1 and type 2 AGN, respectively

- Luminosity-dependent covering fraction of the BLR (Mushotzky and Ferland, 1984), assuming that the emission line is emitted from it. This explanation was proposed to explain the Baldwin effect observed for optical emission lines.
- Contribution of a relativistically broadened component (Nandra et al. 1997, Guainazzi et al. 2006).
- Variation of the ionisation state of the emitting material (Nandra et al., 1997), if the ionisation state of the material became too high, the Fe emission can be suppressed.
- Continuum variability (Jiang et al., 2006), if the line and the continuum are emitted on different scales, the continuum could vary whereas the emission line flux remains constant.
- Luminosity dependent covering fraction of a compact Compton-thick torus, assuming that the emission line is emitted from it, as the luminosity increases the covering fraction of the torus decreases giving a lower EW for the emission line (Page et al. 2004, Bianchi et al. 2007).

Our results point towards the last explanation. The Fe $K\alpha$ central energy and width we measure corresponds to neutral Fe emitted from cold material. Besides, its EW and the presence and amount of cold reflection both suggest emission from Compton-thick material far from the central source. We can also see in Fig. 4.22

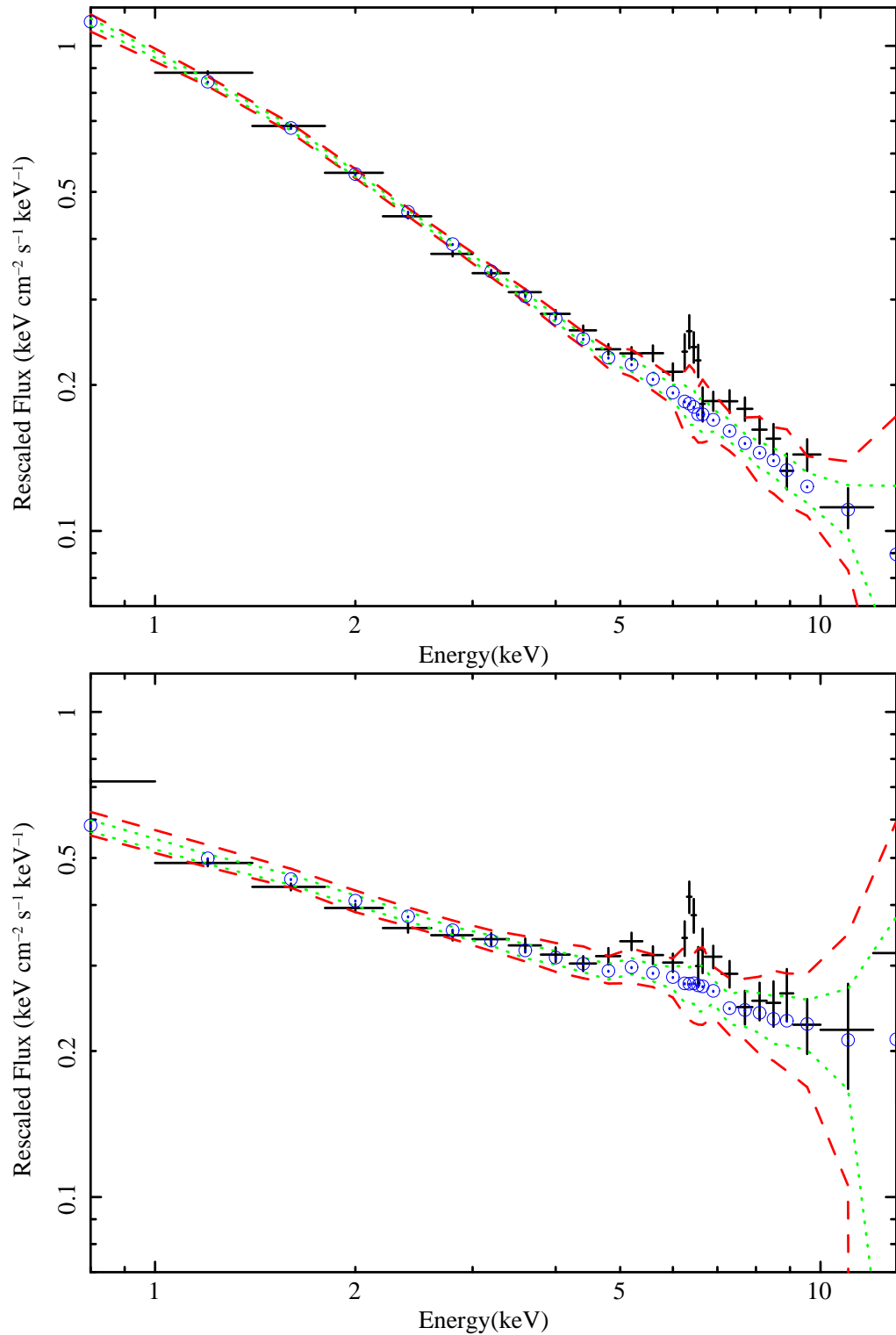


Figure 4.19 **Total sample:** Type 1 (top) and type 2 (bottom) AGN average spectrum (error bars) along with the 100-simulations (open circles) continuum and 1σ (dotted line), 2σ (dashed line) confidence limits.

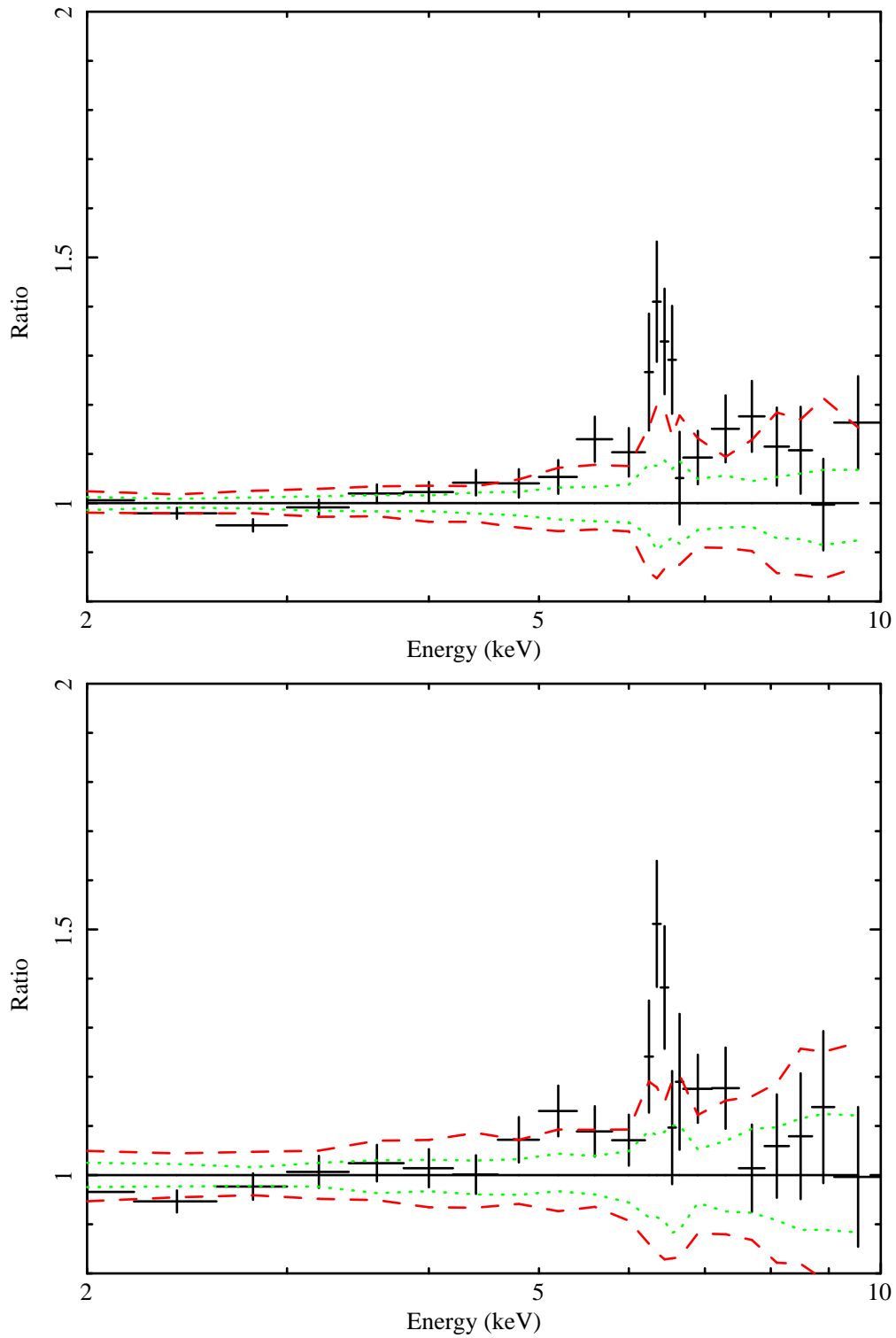


Figure 4.20 **Total sample:** Type 1 (top) and type 2 (bottom) AGN average spectrum to 100-simulations continuum ratio (error bars) along with 1σ (dotted line) and 2σ (dashed line) confidence limits.

that the high energy positive residuals, likely due to the reflection component not fitted in this case, seem to decrease as the luminosity increases, suggesting a decrement in the amount of reflection.

The main results from the work described in this chapter can be summarised as follows:

- We developed a new method to construct an average X-ray spectrum of AGN. This method makes use of medium-to-low quality spectra without needing to fit complex models to the individual spectra but allowing to build a mean spectrum for the whole sample. Extensive quality tests were performed by applying this method to simulated data, and a significance for the detection of any feature over an underlying continuum was derived.
- We applied this method to a large sample of medium X-ray flux sources: the AXIS+XWAS sample. We detected with a 99.9% significance an unresolved Fe $K\alpha$ emission line around 6.4 keV for type 1 and type 2 AGN with an EW ~ 100 eV. However, we find no evidence for any significant broad relativistic emission line in the final average spectra. This result is in agreement with several studies of local AGN showing that a narrow Fe $K\alpha$ emission line, displaying similar characteristics, is almost universally present in the X-ray spectra of nearby AGN. Deviations from a power law around the narrow line are best represented by a reflection component arising from cold or low-ionisation material for type 1 AGN. We estimate an upper limit for the EW of any relativistic line of 400 eV at a 3σ confidence level. In the case of type 2 AGN, we found that a mixture of absorbed power laws is a good fit and there is no need for additional components. The results of the analysis of the type 1 AGN AXIS+XWAS sample have been presented in [Corral et al. \(2008\)](#).
- We applied the averaging method to a fainter flux but higher spectral quality sample (S05). We detected again a narrow emission line around 6.4 keV and no evidence of a broad relativistic line. The type 1 AGN average spectrum is also better described by a mixture of absorbed power laws, which the simulated continuum is composed of, plus a cold reflected component and we estimated an upper limit for a relativistic line EW of 240 eV at 3σ confidence level, a value significantly lower than the one presented in S05 but consistent with the findings in the local universe. In the case of type 2 AGN, we found that the effect of intrinsic absorption was too important to use the simulated continuum as the underlying continuum, but the average spectral shape was well described by a partial covering model. We concluded that the differences in the results presented in S05 and our results must be due to differences between the methods employed.
- We added together all the sources from AXIS+XWAS and the Lockman Hole sample. For the type 1 AGN we obtained a similar result as for the

AXIS+XWAS sample, and an upper limit for the relativistic line of 370 eV at 3σ confidence level. In the case of type 2 AGN, we needed again to fit a partial covering model to account for the effect of the intrinsic absorption, obtaining a similar value for the hydrogen column density but a smaller value for the covering fraction. We searched for dependence of the average spectrum on flux redshift or luminosity by dividing the total samples into three samples of equal quality. We only found dependence of the narrow emission line on luminosity, its EW becoming smaller as the luminosity increases, the so-called Iwasawa-Taniguchi effect. The results corresponding to the total sample are presented in Corral et al. (2011b).

From these results, we can conclude that:

- The average spectral slopes we measure for both studied samples are in excellent agreement with the values obtained from the individual spectral analyses presented in Mateos et al. (2005b) and Mateos et al. (2005a), the lower values for type 2 AGN being due to the larger amount of intrinsic absorption in these sources.
- X-ray absorption is more common and displays larger values for type 2 than for type 1 AGN, as it has been shown in many individual spectral analyses over large X-ray samples. The values we compute for the individual spectra are again consistent with the ones presented in Mateos et al. (2005b) and Mateos et al. (2005a).
- A narrow Fe K α emission line is a common characteristic of AGN up to high redshift as it has been shown it is for local AGN and with an average EW ~ 100 eV (Guainazzi et al. 2006, Nandra et al. 2007). This could allow, in a near future and in the light of new X-ray observatories, to infer redshifts directly from the X-ray data.
- A broad relativistic line, if present, is not stronger for distant AGN than for local AGN. We estimate an upper limit for the relativistic line EW of 370 eV at 3σ confidence level. This might suggest a small amount of material close to the ISCO.
- We find tantalising evidence for the Iwasawa-Taniguchi effect on the narrow line being present also for distant AGN as it is for nearby Seyfert galaxies (Iwasawa and Taniguchi 1993, Bianchi et al. 2007, Page et al. 2004, Nandra et al. 1997).

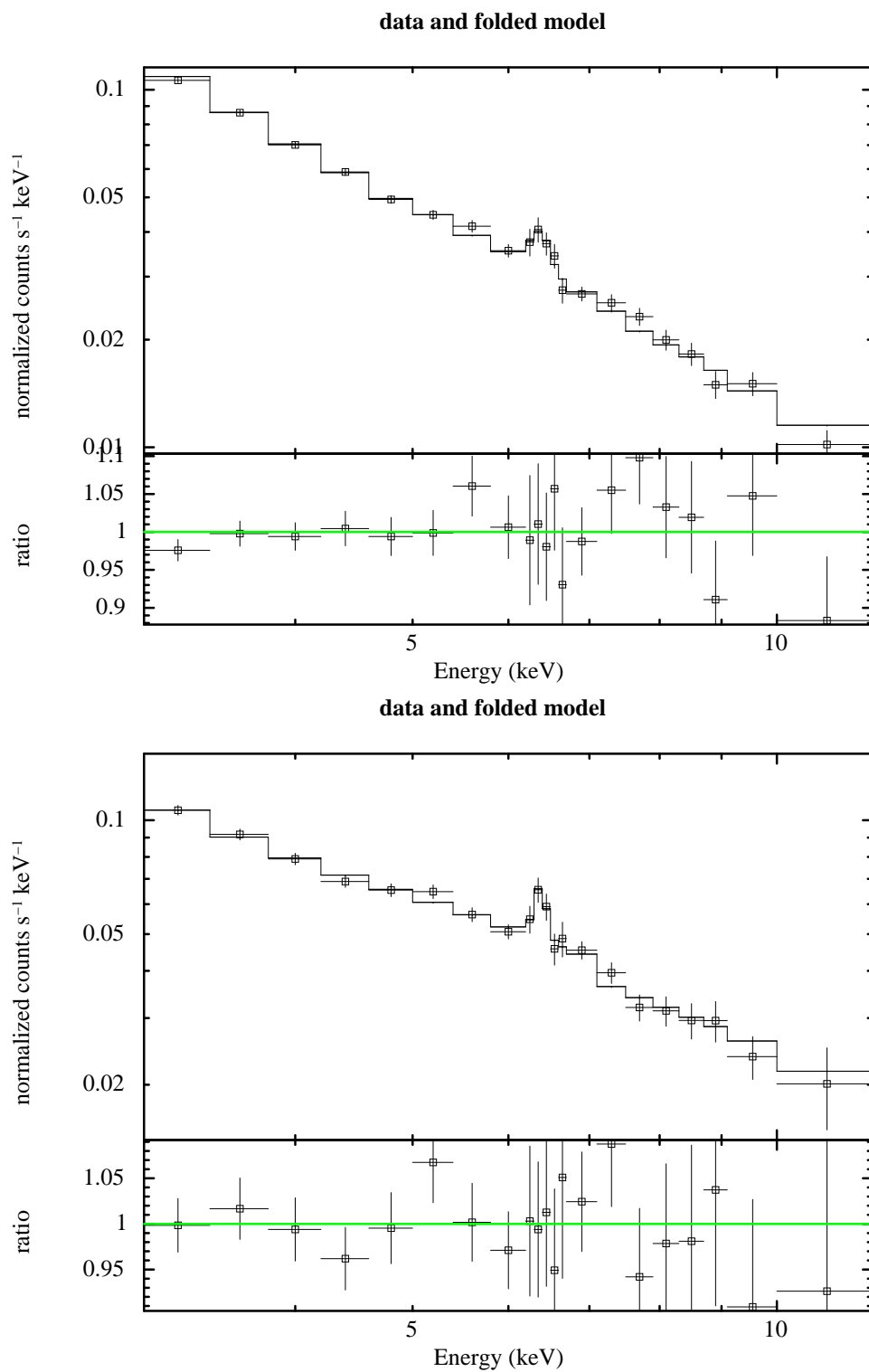


Figure 4.21 **Total sample:** Spectral fit corresponding to the best-fit model for type 1 (top) and type 2 (bottom) AGN.

Table 4.4 Best fit parameters for the spectral fit to the **Total sample** average spectra.

Model	E_{gaus} (keV)	σ_{gaus} (eV)	EW_{gaus} (eV)	Reflection Factor	Inclination Angle (deg)	Intrinsic N_{H} (10^{22} cm^{-2})	Covering Fraction	$\chi^2/\text{d.o.f}$
Type 1 AGN								
Baseline model	6.35 ⁿ	160 ⁿ	180 ⁿ	46/18
Baseline model + pexrav	6.37 ^{+0.07} _{-0.08}	< 160	60 ⁺³⁰ ₋₃₀	0.6 ^{+0.2} _{-0.20}	< 80	15/15
Type 2 AGN								
Baseline model	6.37 ^{+0.09} _{-0.07}	200 ^f	180 ⁺⁷⁰ ₋₇₀	33/18
Partial covering + narrow line	6.37 ^{+0.04} _{-0.04}	< 70	70 ⁺³⁰ ₋₃₀	30 ⁺¹⁴ ₋₁₀	0.4 ^{+0.2} _{-0.2}	8/14

Model parameters not displayed correspond to default values.

ⁿ poor fit does not allow error calculation.

^f fit parameter pegged at hard limit.

^f fixed parameter.

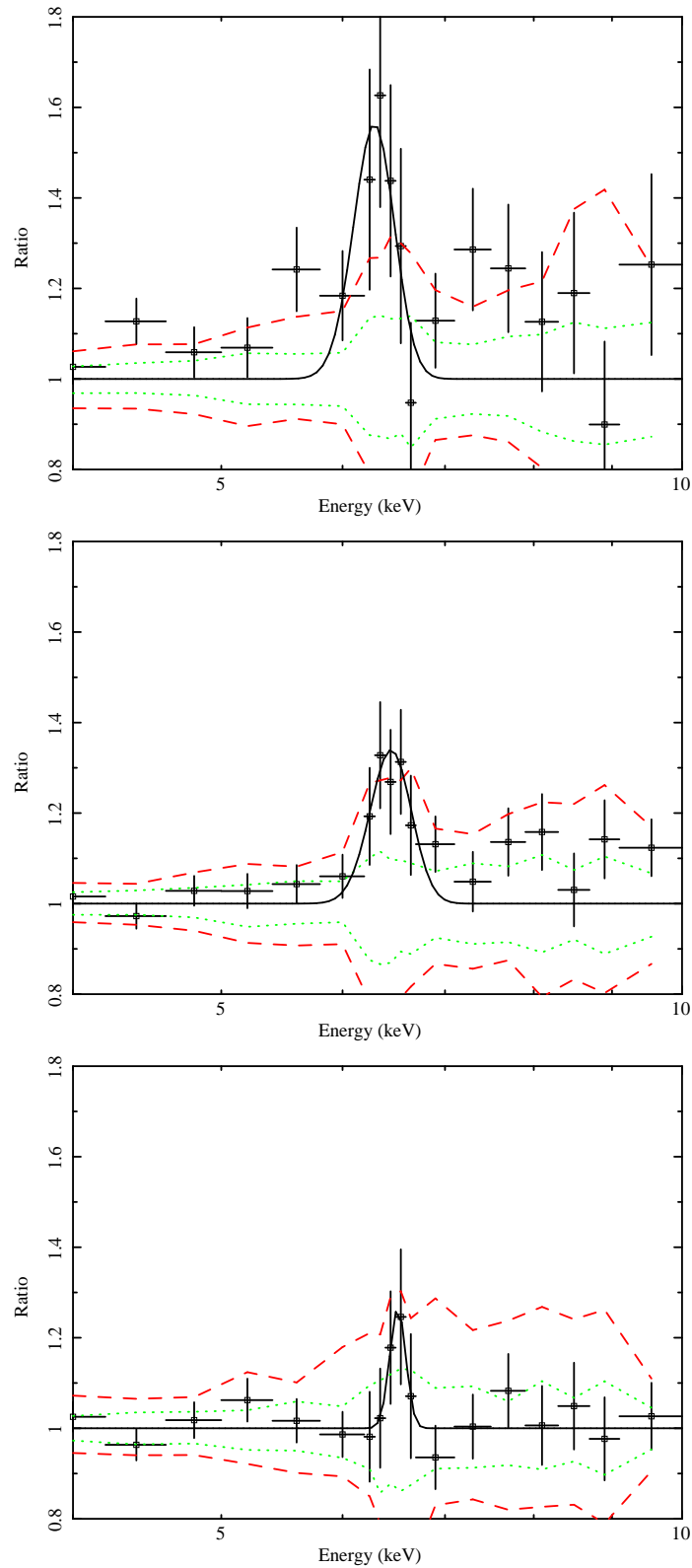


Figure 4.22 **Hard (2-10 keV) Luminosity samples for type 1 AGN in the total sample.** *Top panel:* Average spectrum with Gaussian fit for the low luminosity sample. *Central panel:* Medium Luminosity sample. *Bottom panel:* High Luminosity sample.

Table 4.5 Luminosity sub-samples.

Luminosity Range (erg s^{-1})	Narrow Fe K α EW (eV)	Redshift Range	Narrow Fe K α EW (eV)	Flux Range ($\text{erg cm}^{-2} \text{s}^{-1}$)	Narrow Fe K α EW (eV)
Type 1 AGN					
$3 \times 10^{41} - 2 \times 10^{44}$	270^{+110}_{-100}	0.077 - 0.975	230^{+80}_{-130}	$1 \times 10^{-17} - 3 \times 10^{-14}$	190^{+80}_{-100}
$2 \times 10^{44} - 6 \times 10^{44}$	170^{+50}_{-50}	0.985 - 1.710	200^{+120}_{-110}	$2 \times 10^{-14} - 1 \times 10^{-13}$	210^{+40}_{-60}
$6 \times 10^{44} - 1 \times 10^{47}$	50^{+50}_{-50}	1.712 - 4.450	120^{+70}_{-60}	$1 \times 10^{-14} - 5 \times 10^{-12}$	80^{+70}_{-80}
Type 2 AGN					
$1 \times 10^{40} - 4 \times 10^{43}$	140^{+100}_{-60}	0.017 - 0.205	370^{+110}_{-150}	$7 \times 10^{-16} - 4 \times 10^{-14}$	110^{+150}_{-60}
$4 \times 10^{43} - 1 \times 10^{44}$	140^{+100}_{-90}	0.205 - 0.711	100^{+70}_{-60}	$4 \times 10^{-14} - 3 \times 10^{-13}$	150^{+80}_{-60}
$1 \times 10^{44} - 2 \times 10^{45}$	60^{+40}_{-50}	0.711 - 3.240	190^{+90}_{-130}	$3 \times 10^{-13} - 8 \times 10^{-13}$	50^{+140}_{-50}

Conclusions and future work

Contents

5.1	Conclusions of this thesis	141
5.1.1	Changing-type Seyfert galaxies	141
5.1.2	Average Fe $K\alpha$ emission	143
5.2	Potential extensions of this work	145
5.2.1	Further exploring the Broad Line Region	145
5.2.2	Further constraining the Fe emission	147

The purpose of this thesis is to make progress towards the answer of two of the most relevant and still open questions regarding AGN (Active Galactic Nuclei) physics: the reliability of the AGN unified model and the properties of the AGN Fe $K\alpha$ emission. These two questions have been treated in two different ways. On the one hand, the AGN unified model has been probed by making use of an individual analysis of a small sample of Seyfert galaxies. And on the other hand, the Fe $K\alpha$ emission has been studied statistically by computing its average characteristics over a large sample of AGN.

5.1 Conclusions of this thesis

5.1.1 Changing-type Seyfert galaxies

The simplest unified model for AGN (Antonucci, 1993), assumes that all AGN share a common structure and that the differences among the observed optical spectral characteristics are caused by an orientation effect. In this model, the central SMBH (super massive black hole) is surrounded by an accretion disk/hot electron corona system and then by clouds of turbulent and fast-moving gas (the broad line region, BLR). The dividing line between the accretion disk and the BLR is still unclear, part of the BLR could be composed of accretion disk winds. This accretion disk/BLR system is believed to be surrounded by a torus-shaped structure coplanar with the accretion disk and containing both cold gas and dust and, further away, by a region of slowly-moving and colder clouds of gas (the narrow line region, NLR). As the observers' viewing angle intercepts more and more material, the observed optical spectral types go from type 1 to intermediate types and then to type 2 AGN. The most obvious implication of this model is that

optical type 1 AGN should be unabsorbed in X-rays whereas type 2 AGN should be absorbed.

Although this simple model is consistent with most observations, a number of AGN that appear not to follow this scheme have been found in recent years in X-ray surveys. Several explanations were proposed to account for the X-ray/optical spectral type mismatches. In this thesis work, we focused on the variability scenario. AGN are extremely variable sources and most of these mismatches come from non-simultaneous observations at different wavelengths. Therefore, different observations could catch a source in different absorption states leading to different optical classifications. The adopted strategy in this thesis work was to compile a sample of AGN that had displayed optical spectral changes over the years and to observe them simultaneously in the optical and in X-rays.

Our sample was composed of four Seyfert galaxies: Mrk 993, Mrk 6, NGC 7603 and Mrk 1018. All these sources changed their optical spectral types in time scales of years. Our simultaneous optical/X-rays observations show that variable absorption could account for the spectral changes in three cases: Mrk 6, NGC 7603 and Mrk 1018. However, in the case of Mrk 993, the optical/X-ray type mismatch cannot be explained by invoking variability. We found that for this source, the measured intrinsic column density obtained from the X-ray spectra is not enough to be responsible for the reddening derived from the optical spectrum. We therefore concluded that, for this source, the quite large computed Balmer decrement must be an intrinsic property of the central engine (in particular the BLR) rather than be caused by obscuration (Corral et al., 2005). One possibility is that, given that Mrk 993 is a low luminosity AGN ($L_x \sim 7 \times 10^{41} \text{ erg s}^{-1}$), the conditions within its BLR could be different from other more luminous AGN. Its bolometric luminosity is that of a more luminous AGN ($L_{bol} \sim 2.6 \times 10^{44} \text{ erg s}^{-1}$), but it has been estimated from the [OIII] luminosity, which can be contaminated by a star-burst contribution and therefore, its Eddington ratio could be overestimated. In the case of Mrk 1018, the type 1 optical spectral type turned out to be consistent with the non-detection of absorption by cold gas in X-rays. In this case, its optical spectral changes could be caused by a change in the amount of intervening material in time scales of years. This kind of variability has been reported for a number of AGN (Risaliti et al., 2002; Elvis et al., 2004; Risaliti and Elvis, 2004; Risaliti et al., 2007). Mrk 6 and NGC 7603 showed a much more complex behaviour, although the simultaneous optical and X-rays observations are consistent with each other. The reported changes in their optical spectral types could be caused by changes in the BLR itself. These two sources display double-peaked profiles in their broad optical emission lines. These shapes are believed to be produced within the accretion disk so that they would be very much affected by changes in the ionising continuum, common among AGN. Within the double-peaked emitters scenario proposed by Cao and Wang (2006), these changes in the primary emission would affect the conditions within the

accretion disk/BLR system that would affect the ionised absorbers within those regions and thus the line emission (Corral et al., 2011a).

In summary, the population of changing-type Seyfert galaxies seems to be composed of a mixture of different kinds of sources, most of which display complex and very likely variable absorption, rather than being a class of sources themselves. All these results show that extreme caution must be exercised when extracting any conclusions from non-simultaneous observations at different wavelengths.

5.1.2 Average Fe $K\alpha$ emission

Spectroscopy is the heart of Astrophysics. Spectral features, like emission and absorption lines, are the main, and often unique, tools to diagnose the conditions in distant sources. Emission and absorption lines in X-rays, given the X-rays penetrating ability, give us an unique opportunity to study the innermost regions of AGN. The Fe $K\alpha$ emission line is the most observed X-ray emission line in AGN. Its central energy and shape depend on the ionisation state of the line emitting material and its proximity to the SMBH. A narrow Fe $K\alpha$ line centred around 6.4 keV, and thus likely coming from neutral material located far from the SMBH, has been found to be ubiquitous among local Seyfert galaxies. However, its properties for most luminous and more distant AGN are still poorly constrained. Besides, its shape should be distorted by General Relativity effects if there is a component emitted close enough to the SMBH. However, this relativistically broadened shape has only been detected in a modest number of cases. A shocking but very exciting result was presented in Streblyanska et al. (2005). In that work the authors constructed average spectra for type 1 and type 2 AGN from a medium-size sample and found an extremely large relativistically broadened Fe $K\alpha$ emission line in both cases, at odds with theoretical predictions and observations of local AGN. This result has remained controversial during the years, but there has been either no definite confirmation or rejection for such a strong relativistically broadened line in distant AGN.

The strategy of this thesis work has been to compile as many X-ray distant AGN spectra as possible in order to construct an average AGN spectrum and from that, to extract the average Fe $K\alpha$ line properties. Moreover, by dividing the sample into different samples, the evolution of the line properties as well as their dependence on other AGN properties, such as the AGN luminosity, can be derived. The sample used in Streblyanska et al. (2005) was also considered, and average spectra were also constructed for the same objects but using the novel methods proposed in this thesis in order to probe these earlier results. In this way, we could test whether the differences, if any, between ours and previous results are due to differences in the averaging method and/or to differences in the sample properties.

The first sample used to develop the new averaging method presented in this thesis work is composed of two surveys: the AXIS (An XMM-Newton International survey) and XWAS (XMM-Newton Wide Angle Survey) amounting to more than 600 AGN with spectroscopic redshifts. A narrow Fe $K\alpha$ emission line with an EW of ~ 100 eV is found to be a common characteristic of type 1 and type 2 AGN, in agreement with local AGN studies. In the case of type 1 AGN, a reflection component likely coming from cold and distant material is also detected. The amount of reflection and the narrow Fe $K\alpha$ width and EW are consistent with both the line and the reflection component arising from the same distant and cold material. No relativistic Fe $K\alpha$ emission line component is significantly detected in the type 1 AGN average spectrum. An upper limit for its contribution is estimated to be 400 eV at the 3σ confidence level. For type 2 AGN, a mixture of absorbed power laws plus a narrow Fe $K\alpha$ line turned out to be the best-fit model.

A similar result was obtained in the case of the [Streblyanska et al. \(2005\)](#) sample, the Lockman Hole sample. In the case of type 1 AGN, a much restrictive upper limit for a relativistic emission line contribution of ~ 240 eV was found. In the case of type 2 AGN, the larger amount of absorption in the individual spectra forced us to fit a partial covering model to the averaged spectrum. We concluded that the difference between our results and the ones presented in [Streblyanska et al. \(2005\)](#) must be due to the differences in the averaging method rather than differences in the samples used. Our method does not make use of grouped spectra, as in [Streblyanska et al. \(2005\)](#), that can introduce artificial features in the average spectrum. Besides, we deal with continuum features around the Fe $K\alpha$ region in a more careful way.

We finally combined the two samples in order to study the dependence of the Fe $K\alpha$ line properties on other source properties such as luminosity or redshift. No evolution of the line properties is found, whereas a decrement in the narrow line EW as the X-ray luminosity increases, and maybe in the amount of cold reflection, is marginally detected, the so-called “Iwasawa-Taniguchi effect”. Our results favour the “receding-torus” scenario, in which the covering fraction of the torus would decrease as the luminosity increases.

For the combined sample averaged spectra, we compute an average narrow Fe $K\alpha$ line EW of ~ 100 eV for type 1 and type 2 AGN. For type 1 AGN, we estimated an upper limit for the relativistic line contribution of 370 eV at the 3σ confidence level. These results are in excellent agreement with the ones obtained from local AGN ([Nandra et al., 2007](#)). The upper limit for the relativistic line contribution is also in agreement with recent theoretical models that predicts a maximum Fe $K\alpha$ EW of ~ 300 eV ([Ballantyne, 2010](#)).

Other stacking/averaging analyses have been presented in recent years for local (de La Calle Pérez et al., 2010) and more distant (Chaudhary et al., 2010) AGN. The results presented in those works are also in excellent agreement with the ones obtained in this thesis work, although the Iwasawa-Taniguchi effect remains poorly constrained.

The summary of the main results obtained by using our averaging method are:

- A Fe $K\alpha$ narrow emission line of $EW \sim 100$ eV is a common characteristic of all kinds of AGN up to high redshifts ($z \sim 1.5-2$ and $\sim 0.5-1$ for type 1 and type 2 AGN, respectively) as it is for local studied AGN.
- The narrow emission line EW, and probably the amount of cold reflection, seems to decrease as the AGN luminosity increases, as it is also found for local AGN.
- The EW of any relativistic contribution to the Fe $K\alpha$ line, if present, must be lower than ~ 400 eV, in agreement with theoretical models.

5.2 Potential extensions of this work

The results from the study of Changing-type Seyfert galaxies, in all but one case, are roughly consistent with the simplest versions of the unified model combined with complex and likely variable absorbers. These results have also shown us the importance of studying a particular kind of sources: double-peaked emitters. In the case of the Fe $K\alpha$ emission, our results are consistent with what it was expected from theoretical models, although the line properties are still not well constrained.

5.2.1 Further exploring the Broad Line Region

Out of the four Changing-type Seyfert galaxies studied during this thesis work, two are double-peaked emitters. Double-peaked emitters are AGN that show double-peaked profiles in their optical/UV broad emission lines. The origin of this double-peaked emission is still a matter of debate. Double-peaked sources are more commonly observed in RL AGN (mostly showing a type 1.5 optical spectrum) but not in very powerful radio sources. Several models have been proposed to explain this emission: a binary SMBH (Gaskell, 1983), a biconical outflow of matter (Zheng et al., 1990), a collection of anisotropically illuminated clouds (Wanders et al., 1995), and emission from the accretion disk (Chen and Halpern, 1989). Although none of these models is able to reproduce all the observed characteristics of these kind of sources, the most widely accepted one is emission from the accretion disk (see for example Eracleous and Halpern 2003 for a comparison between the different models proposed).

The accretion disk emission model has been very successful in reproducing the double-peaked line shape and, above all, its variability by making use of optical monitoring of double-peaked sources. However, since all AGN should have an accretion disk, it fails to explain the small fraction of observed double-peaked emitters ($\sim 20\%$ of radio-loud sources, and only $\sim 3\%$ of the whole AGN population). Besides, the viscous power that can be extracted from the accretion disk has been found to be insufficient to account for the observed line luminosities in several cases. This means that extra-illumination of the line emitting region within the disk is necessary to explain the line emission (see [Strateva et al. 2008](#) and references therein). One possible solution to the former problem could be differences in the observers' viewing angle. If we see the disk nearly or completely face-on, we will only see single-peaked profiles. In the case of very powerful radio sources, the contribution of the jet emission would outshine the disk/BLR system emission thus hiding any double-peaked emission. However, this still does not explain why double-peaked emission is not observed in all radio-quiet or moderately radio-loud type 1.5 AGN.

One possible solution to the accretion disk model illumination problem was suggested by [Cao and Wang \(2006\)](#). The authors proposed that the extra-illumination of the accretion disk comes from slowly moving jets or from very massive outflows ($N_H > 10^{23} \text{ cm}^{-2}$) in the case of moderately RL and RQ AGN, respectively. In RQ AGN, the double-peaked emission would be only observed if these outflows of partially ionised material are present. This hypothesis can be tested by searching for absorption signatures from this ionised material in X-rays. Ionised absorption, with column densities in the 10^{21} to 10^{22} cm^{-2} range, is commonly detected in a fraction of Seyfert galaxies, although high spectral resolution is needed in order to characterise the outflowing material, like the one of the Reflection Grating Spectrometer (RGS) on-board XMM-Newton (see [Blustin et al. 2005](#) for example). In fact, the two double-peaked emitters studied in this thesis work, Mrk 6 and NGC 7603, show signatures of ionised absorption with high column densities. However, the outflowing speed cannot be constrained due to the lack of high resolution data of enough quality. No ionised absorption had been detected in the high-resolution data of broad-line radio galaxies (BLRG) until recently. The first BLRG for which a ionised absorber has been detected in soft X-rays turned out to be a double-peaked emitter, 3C 382 ([Torresi et al., 2010](#)).

The study of these fast and massive outflows could improve our understanding of the disk/BLR system formation and dynamics. Ultra fast outflows (UFOs) have been claimed to be detected in high energy ($\sim 7 \text{ keV}$) spectra for a number of radio-quiet and radio-loud AGN ([Tombesi et al., 2010a,b](#)). These outflows could carry enough mass and energy far away enough so as to affect the host-galaxy environment and thus producing the so-called "AGN feedback". Therefore, double-peaked sources could be an excellent laboratory to study both the innermost AGN structure and the AGN/host-galaxy interaction.

The proposed steps to improve our knowledge about these double-peaked emitters are the following:

- To compile all available EPIC-like spectra of double-peaked emitters in archive coming from targeted observations in order to ensure a minimum data quality. Then, these spectra can be individually analysed and their properties can be compare to “normal” AGN.
- To propose new and long X-ray observations of the double-peaked emitters not yet observed in X-rays, such as Arp 102b, so that high quality RGS-like data can be acquired.
- To develop an averaging method to obtain a high spectral resolution average spectrum of double-peaked emitters in order to check if these sources display absorption characteristics that are different from “normal” AGN.

5.2.2 Further constraining the Fe emission

We successfully constrained the contribution of Fe $K\alpha$ emission to X-ray AGN spectra up to high redshift for type 1 AGN. However, its dependence on the source properties remains poorly unconstrained as well as the presence of a relativistically broadened contribution to the line emission. Besides, none of the samples considered here are complete samples, therefore limiting the applicability of our results. In the case of type 2 AGN, the sample size and the spectral quality does not allow us to extract conclusive results. More data of medium to high quality and covering a wider region of the parameter space (lower luminosities and larger redshifts, for example) are needed.

The proposed strategies are the following:

- In order to obtain a better coverage of the parameters space, the XMM-Newton¹ and Chandra² catalogues can be cross-correlated with optical spectroscopic catalogues like the SDSS (Sloan Digital Sky Survey³). For example, The 2XMM-Newton catalogue has already been cross-correlated with the SDSS DR7 (*Data Release 7*) and more than 30000 identifications have been obtained (Pineau et al., 2011). From these identifications, larger and complete samples of AGN can be selected.
- The best luminosity range to search for a relativistic contribution to the Fe $K\alpha$ emission line turned out to be $10^{44} - 10^{45} \text{ erg s}^{-1}$, according to the theoretical predictions presented in Ballantyne (2010).

¹<http://xmm.esac.esa.int/xsa/>

²<http://cxc.harvard.edu/csc/index.html>

³<http://www.sdss.org/>

- In order to constrain the dependence of the line emission on the source properties (such as the SMBH mass or the accretion rate), observations in different wavelengths are needed. Nowadays, there are several projects aimed to construct large samples covering many different wavelengths ranges, like the COSMOS⁴ (*Cosmological Evolution Survey*), CDFS⁵ (*Chandra Deep Field South*) or the ALHAMBRA⁶ (*Advanced Large Homogeneous Area Medium Band Redshift Astronomical*) surveys.
- To increase the number of type 2 AGN of our sample, the X-ray catalogues can be used to select sources at hard X-rays (> 5 keV, for example), a band much less affected by obscuration. These samples selected at hard X-rays can be enlarged and completed by using IR data, also less affected by obscuration.
- In the long term, the X-ray mission currently under study ATHENA (ESA), could allow us for the first time to study the Fe $K\alpha$ emission at high redshifts by analysing individual spectra.

⁴<http://cosmos.astro.caltech.edu/>

⁵<http://www2.astro.psu.edu/niel/cdfs/cdfs-chandra.html>

⁶<http://alhambra.iaa.es:8080/alhambra/>

Bibliography

- Abramowicz, M. A., B. Czerny, J. P. Lasota, and E. Szuszkiewicz (1988), "Slim accretion disks." *ApJ*, 332, 646–658. (Cited on pages 20 and 47.)
- Anders, E. and N. Grevesse (1989), "Abundances of the elements - Meteoritic and solar." *GeCoA*, 53, 197–214. (Cited on page 46.)
- Antonucci, R. (1993), "Unified models for active galactic nuclei and quasars." *ARA&A*, 31, 473–521. (Cited on pages 2, 13, 52, 116, 118 and 141.)
- Antonucci, R. R. J. and J. S. Miller (1985), "Spectropolarimetry and the nature of NGC 1068." *ApJ*, 297, 621–632. (Cited on page 18.)
- Aretxaga, I. and R. Terlevich (1994), "Type transitions in starbursts powered AGN." In *Multi-Wavelength Continuum Emission of AGN* (T. Courvoisier & A. Blecha, ed.), volume 159 of *IAU Symposium*, 438. (Cited on pages 19 and 52.)
- Arnaud, K. A. (1996), "XSPEC: The First Ten Years." In *Astronomical Data Analysis Software and Systems V* (G. H. Jacoby and J. Barnes, eds.), volume 101 of *Astronomical Society of the Pacific Conference Series*, 17–+. (Cited on pages 43, 54, 66, 76 and 97.)
- Baldwin, J. A. (1997), "Broad Emission Lines in Active Galactic Nuclei." In *IAU Colloq. 159: Emission Lines in Active Galaxies: New Methods and Techniques* (B. M. Peterson, F.-Z. Cheng, & A. S. Wilson, ed.), volume 113 of *Astronomical Society of the Pacific Conference Series*, 80. (Cited on page 24.)
- Baldwin, J. A., M. M. Phillips, and R. Terlevich (1981), "Classification parameters for the emission-line spectra of extragalactic objects." *PASP*, 93, 5–19. (Cited on page 62.)
- Ballantyne, D. R. (2010), "The Integrated Relativistic Iron Line from Active Galactic Nuclei: Chasing the Spin Evolution of Supermassive Black Holes." *ApJL*, 716, L27–L30. (Cited on pages xiii, xv, 144 and 147.)
- Balucinska-Church, M. and D. McCammon (1992), "Photoelectric absorption cross sections with variable abundances." *ApJ*, 400, 699. (Cited on page 45.)
- Barcons, X., F. J. Carrera, and M. T. Ceballos (2003), "H1320+551: a type 1.8/1.9 Seyfert galaxy with an unabsorbed X-ray spectrum." *MNRAS*, 339, 757–764. (Cited on pages 18 and 63.)
- Barcons, X., F. J. Carrera, M. T. Ceballos, M. J. Page, J. Bussons-Gordo, A. Corral, J. Ebrero, S. Mateos, J. A. Tedds, M. G. Watson, D. Baskill, M. Birkinshaw, T. Boller, N. Borisov, M. Bremer, G. E. Bromage, H. Brunner, A. Caccianiga, C. S. Crawford, M. S. Cropper, R. Della Ceca, P. Derry, A. C. Fabian,

- P. Guillout, Y. Hashimoto, G. Hasinger, B. J. M. Hassall, G. Lamer, N. S. Loaring, T. Maccacaro, K. O. Mason, R. G. McMahon, L. Mirioni, J. P. D. Mittaz, C. Motch, I. Negueruela, J. P. Osborne, F. Panessa, I. Pérez-Fournon, J. P. Pye, T. P. Roberts, S. Rosen, N. Schartel, N. Schurch, A. Schwope, P. Severgnini, R. Sharp, G. C. Stewart, G. Szokoly, A. Ullán, M. J. Ward, R. S. Warwick, P. J. Wheatley, N. A. Webb, D. Worrall, W. Yuan, and H. Ziaeeepour (2007), “The XMM-Newton serendipitous survey. IV. Optical identification of the XMM-Newton medium sensitivity survey (XMS).” *A&A*, 476, 1191–1203. (Cited on page 108.)
- Bassani, L., M. Dadina, R. Maiolino, M. Salvati, G. Risaliti, R. della Ceca, G. Matt, and G. Zamorani (1999), “A Three-dimensional Diagnostic Diagram for Seyfert 2 Galaxies: Probing X-Ray Absorption and Compton Thickness.” *ApJS*, 121, 473–482. (Cited on pages 18, 52 and 63.)
- Bianchi, S., A. Corral, F. Panessa, X. Barcons, G. Matt, L. Bassani, F. J. Carrera, and E. Jiménez-Bailón (2008), “NGC 3147: a ‘true’ type 2 Seyfert galaxy without the broad-line region.” *MNRAS*, 385, 195–199. (Cited on page 18.)
- Bianchi, S., M. Guainazzi, and M. Chiaberge (2006), “The soft X-ray/NLR connection: a single photoionized medium?” *A&A*, 448, 499–511. (Cited on page 20.)
- Bianchi, S., M. Guainazzi, G. Matt, and N. Fonseca Bonilla (2007), “On the Iwasawa-Taniguchi effect of radio-quiet AGN.” *A&A*, 467, L19–L22. (Cited on pages 132 and 136.)
- Blustin, A. J., M. J. Page, S. V. Fuerst, G. Branduardi-Raymont, and C. E. Ashton (2005), “The nature and origin of Seyfert warm absorbers.” *A&A*, 431, 111–125. (Cited on pages 85 and 146.)
- Bohlin, R. C., B. D. Savage, and J. F. Drake (1978), “A survey of interstellar H I from L-alpha absorption measurements. II.” *ApJ*, 224, 132–142. (Cited on pages 24 and 62.)
- Bongiorno, A., G. Zamorani, I. Gavignaud, B. Marano, S. Paltani, G. Mathez, P. Møller, J. P. Picat, M. Cirasuolo, F. Lamareille, D. Bottini, B. Garilli, V. Le Brun, O. Le Fèvre, D. Maccagni, R. Scaramella, M. Scodreggio, L. Tresse, G. Vettolani, A. Zanichelli, C. Adami, S. Arnouts, S. Bardelli, M. Bolzonella, A. Cappi, S. Charlot, P. Ciliegi, T. Contini, S. Foucaud, P. Franzetti, L. Guzzo, O. Ilbert, A. Iovino, H. J. McCracken, C. Marinoni, A. Mazure, B. Meneux, R. Merighi, R. Pellò, A. Pollo, L. Pozzetti, M. Radovich, E. Zucca, E. Hatziminaoglou, M. Polletta, M. Bondi, J. Brinchmann, O. Cucciati, S. de la Torre, L. Gregorini, Y. Mellier, P. Merluzzi, S. Temporin, D. Vergani, and C. J. Walcher (2007), “The VVDS type-1 AGN sample: the faint end of the luminosity function.” *A&A*, 472, 443–454. (Cited on page 2.)
- Brusa, M., A. Comastri, M. Mignoli, F. Fiore, P. Ciliegi, C. Vignali, P. Severgnini, F. Cocchia, F. La Franca, G. Matt, G. C. Perola, R. Maiolino, A. Baldi, and

- S. Molendi (2003), "The HELLAS2XMM survey. III. Multiwavelength observations of hard X-ray selected sources in the PKS 0312-77 field." *A&A*, 409, 65–78. (Cited on page 18.)
- Brusa, M., R. Gilli, and A. Comastri (2005), "The Iron Line Background." *ApJL*, 621, L5–L8. (Cited on page 94.)
- Cao, X. and T.-G. Wang (2006), "A Physical Model for Active Galactic Nuclei with Double-peaked Broad Emission Lines." *ApJ*, 652, 112–119. (Cited on pages xiii, 75, 83, 91, 142 and 146.)
- Carrera, F. J., J. Ebrero, S. Mateos, M. T. Ceballos, A. Corral, X. Barcons, M. J. Page, S. R. Rosen, M. G. Watson, J. A. Tedds, R. Della Ceca, T. Maccacaro, H. Brunner, M. Freyberg, G. Lamer, F. E. Bauer, and Y. Ueda (2007), "The XMM-Newton serendipitous survey. III. The AXIS X-ray source counts and angular clustering." *A&A*, 469, 27–46. (Cited on page 108.)
- Carrera, F. J., M. J. Page, and J. P. D. Mittaz (2004), "XMM-Newton spectra of hard spectrum Rosat AGN: X-ray absorption and optical reddening." *A&A*, 420, 163–172. (Cited on pages 18, 24 and 63.)
- Chaudhary, P., M. Brusa, G. Hasinger, A. Merloni, and A. Comastri (2010), "Properties of the integrated spectrum of serendipitous 2XMM catalog sources." *A&A*, 518, A58+. (Cited on pages xii and 145.)
- Chen, K. and J. P. Halpern (1989), "Structure of line-emitting accretion disks in active galactic nuclei - ARP 102B." *ApJ*, 344, 115–124. (Cited on pages 23 and 145.)
- Cohen, R. D., R. C. Puetter, R. J. Rudy, T. B. Ake, and C. B. Foltz (1986), "Variability of Markarian 1018 - Seyfert 1.9 to Seyfert 1." *ApJ*, 311, 135–141. (Cited on page 83.)
- Comastri, A., P. Ranalli, K. Iwasawa, C. Vignali, R. Gilli, I. Georgantopoulos, X. Barcons, W. N. Brandt, H. Brunner, M. Brusa, N. Cappelluti, F. J. Carrera, F. Civano, F. Fiore, G. Hasinger, V. Mainieri, A. Merloni, F. Nicastro, M. Paolillo, S. Puccetti, P. Rosati, J. D. Silverman, P. Tozzi, G. Zamorani, I. Balestra, F. E. Bauer, B. Luo, and Y. Q. Xue (2011), "The XMM Deep survey in the CDF-S. I. First results on heavily obscured AGN." *A&A*, 526, L9+. (Cited on pages 95 and 122.)
- Corral, A., X. Barcons, F. J. Carrera, M. T. Ceballos, and S. Mateos (2005), "Simultaneous X-ray and optical spectroscopy of the Seyfert galaxy Mrk 993." *A&A*, 431, 97–102. (Cited on pages x, 91 and 142.)
- Corral, A., X. Barcons, F. J. Carrera, and M. Guainazzi (2011a), "Changing type Seyfert galaxies and the AGN unified model." *submitted to A&A*. (Cited on pages x, xi, 91 and 143.)

- Corral, A., M. J. Page, F. J. Carrera, X. Barcons, R. Della Ceca, S. Mateos, G. Hasinger, and M. G. Watson (2011b), "Average X-ray emission from distant AGN." *submitted to A&A*. (Cited on pages x, xii and 136.)
- Corral, A., M. J. Page, F. J. Carrera, X. Barcons, S. Mateos, J. Ebrero, M. Krumpe, J. A. Schwobe, A. and Tedds, and M. G. Watson (2008), "Average Fe K α emission from distant AGN." *A&A*, 492, 71–80. (Cited on pages x, xi and 135.)
- Cowie, L. L., A. Songaila, E. M. Hu, and J. G. Cohen (1996), "New Insight on Galaxy Formation and Evolution From Keck Spectroscopy of the Hawaii Deep Fields." *AJ*, 112, 839. (Cited on page 2.)
- Crummy, J., A. C. Fabian, L. Gallo, and R. R. Ross (2006), "An explanation for the soft X-ray excess in active galactic nuclei." *MNRAS*, 365, 1067–1081. (Cited on pages 20, 77 and 86.)
- de La Calle Pérez, I., A. L. Longinotti, M. Guainazzi, S. Bianchi, M. Dovčiak, M. Cappi, G. Matt, G. Miniutti, P. O. Petrucci, E. Piconcelli, G. Ponti, D. Porquet, and M. Santos-Lleó (2010), "FERO: Finding extreme relativistic objects. I. Statistics of relativistic Fe K α lines in radio-quiet Type 1 AGN." *A&A*, 524, A50+. (Cited on pages xii, 94 and 145.)
- Dickey, J. M. and F. J. Lockman (1990), "H I in the Galaxy." *ARA&A*, 28, 215–261. (Cited on pages 54, 66 and 84.)
- Dietrich, M., B. M. Peterson, P. Albrecht, M. Altmann, A. J. Barth, P. J. Bennie, R. Bertram, N. G. Bochkarev, H. Bock, J. M. Braun, A. Burenkov, S. Collier, L.-Z. Fang, O. P. Francis, A. V. Filippenko, C. B. Foltz, W. Gaessler, C. M. Gaskell, M. Geffert, K. K. Ghosh, R. W. Hilditch, R. K. Honeycutt, K. Horne, J. P. Huchra, S. Kaspi, M. Kuemmel, K. M. Leighly, D. C. Leonard, Y. F. Malkov, V. Mikhailov, H. R. Miller, A. C. Morrill, J. Noble, P. T. O'Brien, T. D. Oswalt, S. P. Pebley, M. Pfeiffer, V. I. Pronik, B.-C. Qian, J. W. Robertson, A. Robinson, K. S. Rumstay, J. Schmoll, S. G. Sergeev, E. A. Sergeeva, A. I. Shapovalova, D. R. Skillman, S. A. Snedden, S. Soundararajaperumal, G. M. Stirpe, J. Tao, G. W. Turner, R. M. Wagner, S. J. Wagner, J. Y. Wei, H. Wu, W. Zheng, and Z. L. Zou (1998), "Steps toward Determination of the Size and Structure of the Broad-Line Region in Active Galactic Nuclei. XII. Ground-based Monitoring of 3C 390.3." *ApJS*, 115, 185. (Cited on page 64.)
- Done, C., J. S. Mulchaey, R. F. Mushotzky, and K. A. Arnaud (1992), "An ionized accretion disk in Cygnus X-1." *ApJ*, 395, 275–288. (Cited on pages 47 and 56.)
- Doroshenko, V. T. and S. G. Sergeev (2003), "Spectral activity of the Seyfert galaxy Markarian 6 in 1970-1991." *A&A*, 405, 909–915. (Cited on page 65.)
- Eddington, A. S. (1913), "On a formula for correcting statistics for the effects of a known error of observation." *MNRAS*, 73, 359–360. (Cited on page 9.)

- Elvis, M., G. Risaliti, F. Nicastro, J. M. Miller, F. Fiore, and S. Puccetti (2004), "An Unveiling Event in the Type 2 Active Galactic Nucleus NGC 4388: A Challenge for a Parsec-Scale Absorber." *ApJL*, 615, L25–L28. (Cited on pages 19, 52 and 142.)
- Emerson, D. (1999), *Interpreting Astronomical Spectra*. (Cited on page 19.)
- Eracleous, M. and J. P. Halpern (2003), "Completion of a Survey and Detailed Study of Double-peaked Emission Lines in Radio-loud Active Galactic Nuclei." *ApJ*, 599, 886–908. (Cited on page 145.)
- Fabian, A. C. (1979), "Theories of the nuclei of active galaxies." *Royal Society of London Proceedings Series A*, 366, 449–459. (Cited on page 9.)
- Fabian, A. C., K. Iwasawa, C. S. Reynolds, and A. J. Young (2000), "Broad Iron Lines in Active Galactic Nuclei." *PASP*, 112, 1145–1161. (Cited on pages 14, 15 and 21.)
- Fabian, A. C. and G. Miniutti (2005), "The X-ray spectra of accreting Kerr black holes." *ArXiv Astrophysics e-prints*. (Cited on page 94.)
- Fabian, A. C., M. J. Rees, L. Stella, and N. E. White (1989), "X-ray fluorescence from the inner disc in Cygnus X-1." *MNRAS*, 238, 729–736. (Cited on pages 45, 49 and 94.)
- Fabian, A. C. and S. Vaughan (2003), "The iron line in MCG-6-30-15 from XMM-Newton: evidence for gravitational light bending?" *MNRAS*, 340, L28–L32. (Cited on page 94.)
- Fanaroff, B. L. and J. M. Riley (1974), "The morphology of extragalactic radio sources of high and low luminosity." *MNRAS*, 167, 31P–36P. (Cited on page 6.)
- Fath, E. A. (1909), "The spectra of some spiral nebulae and globular star clusters." *Lick Observatory Bulletin*, 5, 71–77. (Cited on page 3.)
- Feldmeier, J. J., W. N. Brandt, M. Elvis, A. C. Fabian, K. Iwasawa, and S. Mathur (1999), "Heavy and Complex X-Ray Absorption toward the Nucleus of Markarian 6." *ApJ*, 510, 167–177. (Cited on page 74.)
- Ferrarese, L. (2002), "Beyond the Bulge: A Fundamental Relation between Supermassive Black Holes and Dark Matter Halos." *ApJ*, 578, 90–97. (Cited on page 2.)
- Ferrarese, L. and D. Merritt (2000), "A Fundamental Relation between Supermassive Black Holes and Their Host Galaxies." *ApJL*, 539, L9–L12. (Cited on page 2.)
- Fiore, F., P. Giommi, C. Vignali, A. Comastri, G. Matt, G. C. Perola, F. La Franca, S. Molendi, F. Tamburelli, and L. A. Antonelli (2001), "The BeppoSAX High Energy Large Area Survey (HELLAS) - II. Number counts and X-ray spectral properties." *MNRAS*, 327, 771–780. (Cited on page 18.)

- Gallimore, J. F., S. A. Baum, C. P. O’Dea, A. Pedlar, and E. Brinks (1999), “Neutral Hydrogen (21 Centimeter) Absorption in Seyfert Galaxies: Evidence for Free-Free Absorption and Subkiloparsec Gaseous Disks.” *ApJ*, 524, 684–706. (Cited on page 64.)
- Gaskell, C. M. (1983), “Quasars as supermassive binaries.” In *Liege International Astrophysical Colloquia* (J.-P. Swings, ed.), volume 24 of *Liege International Astrophysical Colloquia*, 473–477. (Cited on pages 23 and 145.)
- Gaskell, C. M. (2009), “What broad emission lines tell us about how active galactic nuclei work.” *New AR*, 53, 140–148. (Cited on page 23.)
- Gaskell, C. M. and G. J. Ferland (1984), “Theoretical hydrogen-line ratios for the narrow-line regions of active galactic nuclei.” *PASP*, 96, 393–397. (Cited on page 23.)
- Gavazzi, G. and M. Scodeggio (1996), “The mass dependence of the star formation history of disk galaxies.” *A&A*, 312, L29–L32. (Cited on page 2.)
- Gebhardt, K., R. Bender, G. Bower, A. Dressler, S. M. Faber, A. V. Filippenko, R. Green, C. Grillmair, L. C. Ho, J. Kormendy, T. R. Lauer, J. Magorrian, J. Pinkney, D. Richstone, and S. Tremaine (2000), “A Relationship between Nuclear Black Hole Mass and Galaxy Velocity Dispersion.” *ApJL*, 539, L13–L16. (Cited on page 2.)
- George, I. M. and A. C. Fabian (1991), “X-ray reflection from cold matter in active galactic nuclei and X-ray binaries.” *MNRAS*, 249, 352–367. (Cited on page 117.)
- Giacconi, R., H. Gursky, F. R. Paolini, and B. B. Rossi (1962), “Evidence for x Rays From Sources Outside the Solar System.” *Physical Review Letters*, 9, 439–443. (Cited on page 2.)
- Gierliński, M. and C. Done (2004), “Is the soft excess in active galactic nuclei real?” *MNRAS*, 349, L7–L11. (Cited on page 47.)
- Gilli, R., A. Comastri, and G. Hasinger (2007), “The synthesis of the cosmic X-ray background in the Chandra and XMM-Newton era.” *A&A*, 463, 79–96. (Cited on page 2.)
- Goodrich, R. W. (1989), “Spectropolarimetry and variability of Seyfert 1.8 and 1.9 galaxies.” *ApJ*, 340, 190–202. (Cited on page 54.)
- Graham, A. W., P. Erwin, N. Caon, and I. Trujillo (2001), “A Correlation between Galaxy Light Concentration and Supermassive Black Hole Mass.” *ApJL*, 563, L11–L14. (Cited on page 2.)
- Granato, G. L., L. Danese, and A. Franceschini (1997), “Thick Tori around Active Galactic Nuclei: The Case for Extended Tori and Consequences for Their X-Ray and Infrared Emission.” *ApJ*, 486, 147. (Cited on page 18.)

- Greene, J. E. and L. C. Ho (2006), "The MBH-sigma Relation in Local Active Galaxies." *ApJL*, 641, L21–L24. (Cited on page 2.)
- Guainazzi, M. and S. Bianchi (2007), "On the origin of soft X-rays in obscured AGN: answers from high-resolution spectroscopy with XMM-Newton." *MNRAS*, 374, 1290–1302. (Cited on page 20.)
- Guainazzi, M., S. Bianchi, and M. Dovčiak (2006), "Statistics of relativistically broadened Fe K α lines in AGN." *Astronomische Nachrichten*, 327, 1032. (Cited on pages 94, 118, 132 and 136.)
- Guainazzi, M., A. C. Fabian, K. Iwasawa, G. Matt, and F. Fiore (2005), "On the transmission-dominated to reprocessing-dominated spectral state transitions in Seyfert 2 galaxies." *MNRAS*, 356, 295–308. (Cited on page 19.)
- Hasinger, G., T. Miyaji, and M. Schmidt (2005), "Luminosity-dependent evolution of soft X-ray selected AGN. New Chandra and XMM-Newton surveys." *A&A*, 441, 417–434. (Cited on page 2.)
- Hickox, R. C. and M. Markevitch (2006), "Absolute Measurement of the Unresolved Cosmic X-Ray Background in the 0.5-8 keV Band with Chandra." *ApJ*, 645, 95–114. (Cited on page 2.)
- Huchra, J. P., M. S. Vogeley, and M. J. Geller (1999), "The CFA Redshift Survey: Data for the South Galactic CAP." *ApJS*, 121, 287–368. (Cited on pages 53, 75 and 83.)
- Immler, S., W. N. Brandt, C. Vignali, F. E. Bauer, D. M. Crenshaw, J. J. Feldmeier, and S. B. Kraemer (2003), "Probing the Complex and Variable X-Ray Absorption of Markarian 6 with XMM-Newton." *AJ*, 126, 153–157. (Cited on pages 65, 67, 68 and 74.)
- Ivanov, V. D., G. H. Rieke, C. E. Groppi, A. Alonso-Herrero, M. J. Rieke, and C. W. Engelbracht (2000), "Testing the AGN-Starburst Connection in Seyfert Galaxies." *ApJ*, 545, 190–204. (Cited on page 59.)
- Iwasawa, K. and Y. Taniguchi (1993), "The X-ray Baldwin effect." *ApJL*, 413, L15–L18. (Cited on pages 131 and 136.)
- Jiang, P., J. X. Wang, and T. G. Wang (2006), "On the X-Ray Baldwin Effect for Narrow Fe K α Emission Lines." *ApJ*, 644, 725–732. (Cited on page 132.)
- Kinkhabwala, A., E. Behar, M. Sako, M. F. Gu, S. M. Kahn, and F. B. S. Paerels (2003), "Atomic Calculations and Spectral Models of X-ray Absorption and Emission Features From Astrophysical Photoionized Plasmas." *ArXiv Astrophysics e-prints*. (Cited on pages 47 and 56.)
- Kollatschny, W., K. Bischoff, and M. Dietrich (2000), "Strong spectral variability in NGC 7603 over 20 years." *A&A*, 361, 901–912. (Cited on pages 75, 79 and 83.)

- Komossa, S. and N. Bade (1998), "Properties of dusty warm absorbers and the case of IRAS17020+4544." *A&A*, 331, L49–L52. (Cited on page 63.)
- Komossa, S. and G. Hasinger (2003), "The X-ray evolving universe: (ionized) absorption and dust, from nearby Seyfert galaxies to high-redshift quasars." In *XEUS - studying the evolution of the hot universe* (G. Hasinger, T. Boller, & A. N. Parmer, ed.), 285. (Cited on page 19.)
- Kormendy, J. and D. Richstone (1995), "Inward Bound—The Search For Supermassive Black Holes In Galactic Nuclei." *ARA&A*, 33, 581. (Cited on page 2.)
- Laor, A. (1991), "Line profiles from a disk around a rotating black hole." *ApJ*, 376, 90–94. (Cited on pages 45, 49, 76, 84, 94 and 118.)
- Longinotti, A. L. and I. de La Calle Pérez (2010), "FERO (Finding Extreme Relativistic Objects): relativistic Iron Kalpha lines in type 1 AGN." *Twelfth International Solar Wind Conference*, 1248, 465–466. (Cited on page 94.)
- Lynden-Bell, D. (1969), "Galactic Nuclei as Collapsed Old Quasars." *Nat*, 223, 690. (Cited on page 9.)
- Magdziarz, P. and A. A. Zdziarski (1995), "Angle-dependent Compton reflection of X-rays and gamma-rays." *MNRAS*, 273, 837–848. (Cited on pages 45, 47, 67 and 116.)
- Magorrian, J. and S. Tremaine (1999), "Rates of tidal disruption of stars by massive central black holes." *MNRAS*, 309, 447–460. (Cited on page 2.)
- Mainieri, V., J. Bergeron, G. Hasinger, I. Lehmann, P. Rosati, M. Schmidt, G. Szokoly, and R. Della Ceca (2002), "XMM-Newton observation of the Lockman Hole. II. Spectral analysis." *A&A*, 393, 425–438. (Cited on page 18.)
- Malizia, A., L. Bassani, M. Capalbi, A. C. Fabian, F. Fiore, and F. Nicastro (2003), "A BeppoSAX observation of MKN6." *A&A*, 406, 105–109. (Cited on page 67.)
- Mateos, S., X. Barcons, F. J. Carrera, M. T. Ceballos, A. Caccianiga, G. Lamer, T. Maccacaro, M. J. Page, A. Schwobe, and M. G. Watson (2005a), "X-ray spectra of XMM-Newton serendipitous medium flux sources." *A&A*, 433, 855–873. (Cited on pages 18, 117 and 136.)
- Mateos, S., X. Barcons, F. J. Carrera, M. T. Ceballos, G. Hasinger, I. Lehmann, A. C. Fabian, and A. Streblyanska (2005b), "XMM-Newton observations of the Lockman Hole IV: spectra of the brightest AGN." *A&A*, 444, 79–99. (Cited on pages 95, 122 and 136.)
- Matt, G., M. Guainazzi, and R. Maiolino (2003), "Changing look: from Compton-thick to Compton-thin, or the rebirth of fossil active galactic nuclei." *MNRAS*, 342, 422–426. (Cited on page 19.)

- Middleton, M., C. Done, and M. Gierliński (2007), "An absorption origin for the soft excess in Seyfert 1 active galactic nuclei." *MNRAS*, 381, 1426–1436. (Cited on pages 20, 77 and 86.)
- Miller, J. M. (2007), "Relativistic X-Ray Lines from the Inner Accretion Disks Around Black Holes." *ARA&A*, 45, 441–479. (Cited on pages 21 and 22.)
- Morrison, R. and D. McCammon (1983), "Interstellar photoelectric absorption cross sections, 0.03-10 keV." *ApJ*, 270, 119–122. (Cited on page 48.)
- Mouri, H. and Y. Taniguchi (2002), "Far-Infrared Census of Starburst-Seyfert Connection." *ApJ*, 565, 786–799. (Cited on page 59.)
- Murphy, K. D. and T. Yaqoob (2009), "An X-ray spectral model for Compton-thick toroidal reprocessors." *MNRAS*, 397, 1549–1562. (Cited on page 21.)
- Mushotzky, R. and G. J. Ferland (1984), "The line continuum luminosity ratio in active galactic nuclei - or, on the 'Baldwin effect'." *ApJ*, 278, 558–563. (Cited on page 132.)
- Nandra, K., I. M. George, R. F. Mushotzky, T. J. Turner, and T. Yaqoob (1997), "On the Dependence of the Iron K-Line Profiles with Luminosity in Active Galactic Nuclei." *ApJL*, 488, L91+. (Cited on pages 132 and 136.)
- Nandra, K., P. M. O'Neill, I. M. George, and J. N. Reeves (2007), "An XMM-Newton survey of broad iron lines in Seyfert galaxies." *MNRAS*, 382, 194–228. (Cited on pages 94, 116, 118, 136 and 144.)
- Nandra, K. and K. A. Pounds (1994), "GINGA Observations of the X-Ray Spectra of Seyfert Galaxies." *MNRAS*, 268, 405. (Cited on pages 18 and 52.)
- Nayakshin, S. and T. R. Kallman (2001), "Accretion Disk Models and Their X-Ray Reflection Signatures. I. Local Spectra." *ApJ*, 546, 406–418. (Cited on page 49.)
- Neufeld, D. A., P. R. Maloney, and S. Conger (1994), "Water maser emission from X-ray-heated circumnuclear gas in active galaxies." *ApJL*, 436, L127+. (Cited on page 9.)
- Osterbrock, D. E. (1981), "Seyfert galaxies with weak broad H alpha emission lines." *ApJ*, 249, 462–470. (Cited on pages 7 and 83.)
- Osterbrock, D. E. (1989), *Astrophysics of gaseous nebulae and active galactic nuclei*. (Cited on pages 6, 23, 24, 59, 62 and 71.)
- Page, K. L., P. T. O'Brien, J. N. Reeves, and M. J. L. Turner (2004), "An X-ray Baldwin effect for the narrow Fe K α lines observed in active galactic nuclei." *MNRAS*, 347, 316–322. (Cited on pages 116, 132 and 136.)

- Page, M. J., I. M. McHardy, K. F. Gunn, N. S. Loaring, K. O. Mason, T. Sasseen, A. Newsam, A. Ware, J. Kennea, K. Sekiguchi, and T. Takata (2003), "X-ray and optical properties of X-ray sources in the 13hr XMM-Newton/Chandra deep survey." *Astronomische Nachrichten*, 324, 101–104. (Cited on page 18.)
- Page, M. J., J. P. D. Mittaz, and F. J. Carrera (2001), "A survey of hard spectrum ROSAT sources - II. Optical identification of hard sources." *MNRAS*, 325, 575–583. (Cited on page 18.)
- Panessa, F. and L. Bassani (2002), "Unabsorbed Seyfert 2 galaxies." *A&A*, 394, 435–442. (Cited on page 18.)
- Panessa, F., F. J. Carrera, S. Bianchi, A. Corral, F. Gastaldello, X. Barcons, L. Bassani, G. Matt, and L. Monaco (2009), "Unabsorbed Seyfert 2 galaxies: the case of 'naked' AGN." *MNRAS*, 398, 1951–1960. (Cited on page 18.)
- Pappa, A., I. Georgantopoulos, G. C. Stewart, and A. L. Zezas (2001), "The X-ray spectra of optically selected Seyfert 2 galaxies: are there any Seyfert 2 galaxies with no absorption?" *MNRAS*, 326, 995–1006. (Cited on pages 18, 19 and 63.)
- Perola, G. C., S. Puccetti, F. Fiore, N. Sacchi, M. Brusa, F. Cocchia, A. Baldi, N. Carangelo, P. Ciliegi, A. Comastri, F. La Franca, R. Maiolino, G. Matt, M. Mignoli, S. Molendi, and C. Vignali (2004), "The HELLAS2XMM survey. VI. X-ray absorption in the 1df AGN sample through a spectral analysis." *A&A*, 421, 491–501. (Cited on page 18.)
- Peterson, B. M. and M. C. Bentz (2006), "Black hole masses from reverberation mapping." *New AR*, 50, 796–799. (Cited on page 8.)
- Petrucci, P. O., G. Ponti, G. Matt, A. L. Longinotti, J. Malzac, M. Mouchet, C. Boisson, L. Maraschi, K. Nandra, and P. Ferrando (2007), "Unveiling the broad band X-ray continuum and iron line complex in Mrk 841." *A&A*, 470, 889–902. (Cited on page 48.)
- Pineau, F.-X., C. Motch, F. Carrera, R. Della Ceca, S. Derrière, L. Michel, A. Schwope, and M. G. Watson (2011), "Cross-correlation of the 2XMMi catalogue with Data Release 7 of the Sloan Digital Sky Survey." *A&A*, 527, A126+. (Cited on page 147.)
- Porquet, D., J. N. Reeves, P. O'Brien, and W. Brinkmann (2004), "XMM-Newton EPIC observations of 21 low-redshift PG quasars." *A&A*, 422, 85–95. (Cited on pages 20 and 47.)
- Rees, M. J. (1984), "Black Hole Models for Active Galactic Nuclei." *ARA&A*, 22, 471–506. (Cited on page 9.)
- Reeves, J. (2003), "XMM-Newton Observations of AGN Iron Line profiles." In *Active Galactic Nuclei: From Central Engine to Host Galaxy* (S. Collin, F. Combes, and

- I. Shlosman, eds.), volume 290 of *Astronomical Society of the Pacific Conference Series*, 35. (Cited on page 117.)
- Reeves, J. N., K. Nandra, I. M. George, K. A. Pounds, T. J. Turner, and T. Yaqoob (2004), "The XMM-Newton Iron Line Profile of NGC 3783." *ApJ*, 602, 648–658. (Cited on page 116.)
- Reeves, J. N., M. J. L. Turner, K. A. Pounds, P. T. O'Brien, T. Boller, P. Ferrando, E. Kendziorra, and S. Vercellone (2001), "XMM-Newton observation of an unusual iron line in the quasar Markarian 205." *A&A*, 365, L134–L139. (Cited on page 117.)
- Reilman, R. F. and S. T. Manson (1979), "Photoabsorption cross sections for positive atomic ions with Z equal to or less than 30." *ApJS*, 40, 815–880. (Cited on page 47.)
- Reynolds, C. S. (1997), "An X-ray spectral study of 24 type 1 active galactic nuclei." *MNRAS*, 286, 513–537. (Cited on page 46.)
- Reynolds, C. S. and M. A. Nowak (2003), "Fluorescent iron lines as a probe of astrophysical black hole systems." *PhR*, 377, 389–466. (Cited on page 94.)
- Risaliti, G. and M. Elvis (2004), "A Panchromatic View of AGN." In *Supermassive Black Holes in the Distant Universe* (A. J. Barger, ed.), volume 308 of *Astrophysics and Space Science Library*, 187. (Cited on pages 20, 52 and 142.)
- Risaliti, G., M. Elvis, G. Fabbiano, A. Baldi, A. Zezas, and M. Salvati (2007), "Occultation Measurement of the Size of the X-Ray-emitting Region in the Active Galactic Nucleus of NGC 1365." *ApJL*, 659, L111–L114. (Cited on pages 19, 52 and 142.)
- Risaliti, G., M. Elvis, and F. Nicastro (2002), "Ubiquitous Variability of X-Ray-absorbing Column Densities in Seyfert 2 Galaxies." *ApJ*, 571, 234–246. (Cited on pages 19, 52 and 142.)
- Risaliti, G., R. Maiolino, and M. Salvati (1999), "The Distribution of Absorbing Column Densities among Seyfert 2 Galaxies." *ApJ*, 522, 157–164. (Cited on pages 18 and 52.)
- Ross, R. R. and A. C. Fabian (1993), "The effects of photoionization on X-ray reflection spectra in active galactic nuclei." *MNRAS*, 261, 74–82. (Cited on page 117.)
- Ross, R. R. and A. C. Fabian (2005), "A comprehensive range of X-ray ionized-reflection models." *MNRAS*, 358, 211–216. (Cited on pages 47 and 48.)
- Salpeter, E. E. (1964), "Accretion of Interstellar Matter by Massive Objects." *ApJ*, 140, 796–800. (Cited on page 9.)

- Schmidt, M. (1963), "3C 273 : A Star-Like Object with Large Red-Shift." *Nat*, 197, 1040. (Cited on page 3.)
- Schurch, N. J., R. E. Griffiths, and R. S. Warwick (2006), "The messy environment of Mrk 6." *MNRAS*, 371, 211–220. (Cited on pages 65 and 68.)
- Sergeev, S. G., V. I. Pronik, E. A. Sergeeva, and Y. F. Malkov, Y. F. Malkov (1999), "Markarian 6 Nucleus since 1992." *ApJS*, 121, 159–169. (Cited on page 65.)
- Seyfert, C. K. (1943), "Nuclear Emission in Spiral Nebulae." *ApJ*, 97, 28. (Cited on page 3.)
- Shull, J. M. and M. van Steenberg (1982), "The ionization equilibrium of astrophysically abundant elements." *ApJS*, 48, 95–107. (Cited on page 47.)
- Smith, D. A. and C. Done (1996), "Unified theories of active galactic nuclei: a hard X-ray sample of Seyfert 2 galaxies." *MNRAS*, 280, 355–377. (Cited on pages 18 and 52.)
- Strateva, I. V., W. N. Brandt, M. Eracleous, and G. Garmire (2008), "A Chandra Look at Five of the Broadest Double-Peaked Balmer Line Emitters." *ApJ*, 687, 869–883. (Cited on pages 75 and 146.)
- Streblyanska, A., G. Hasinger, A. Finoguenov, X. Barcons, S. Mateos, and A. C. Fabian (2005), "XMM-Newton observations of the Lockman Hole. III. A relativistic Fe line in the mean X-ray spectra of type-1 and type-2 AGN." *A&A*, 432, 395–400. (Cited on pages ix, xi, xii, 94, 143 and 144.)
- Tanaka, Y., K. Nandra, A. C. Fabian, H. Inoue, C. Otani, T. Dotani, K. Hayashida, K. Iwasawa, T. Kii, H. Kunieda, F. Makino, and M. Matsuoka (1995), "Gravitationally Redshifted Emission Implying an Accretion Disk and Massive Black-Hole in the Active Galaxy MCG:-6-30-15." *Nat*, 375, 659. (Cited on page 94.)
- Tombesi, F., M. Cappi, J. N. Reeves, G. G. C. Palumbo, T. Yaqoob, V. Braitto, and M. Dadina (2010a), "Evidence for ultra-fast outflows in radio-quiet AGNs. I. Detection and statistical incidence of Fe K-shell absorption lines." *A&A*, 521, A57+. (Cited on page 146.)
- Tombesi, F., R. M. Sambruna, J. N. Reeves, V. Braitto, L. Ballo, J. Gofford, M. Cappi, and R. F. Mushotzky (2010b), "Discovery of Ultra-fast Outflows in a Sample of Broad-line Radio Galaxies Observed with Suzaku." *ApJ*, 719, 700–715. (Cited on page 146.)
- Torresi, E., P. Grandi, A. L. Longinotti, M. Guainazzi, G. G. C. Palumbo, F. Tombesi, and A. Nucita (2010), "First high-resolution detection of a warm absorber in the Broad Line Radio Galaxy 3C 382." *MNRAS*, 401, L10–L14. (Cited on page 146.)

- Tozzi, P., P. Rosati, M. Nonino, J. Bergeron, S. Borgani, R. Gilli, R. Gilmozzi, G. Hasinger, N. Grogan, L. Kewley, A. Koekemoer, C. Norman, E. Schreier, G. Szokoly, J. X. Wang, W. Zheng, A. Zirm, and R. Giacconi (2001), "New Results from the X-Ray and Optical Survey of the Chandra Deep Field-South: The 300 Kilosecond Exposure. II." *ApJ*, 562, 42–51. (Cited on page 18.)
- Tran, H. D., D. E. Osterbrock, and A. Martel (1992), "Extreme spectral variations of the Seyfert galaxy Markarian 993." *AJ*, 104, 2072–2077. (Cited on page 54.)
- Treister, E., C. M. Urry, and S. Virani (2009), "The Space Density of Compton-Thick Active Galactic Nucleus and the X-Ray Background." *ApJ*, 696, 110–120. (Cited on page 2.)
- Tremaine, S., K. Gebhardt, R. Bender, G. Bower, A. Dressler, S. M. Faber, A. V. Filippenko, R. Green, C. Grillmair, L. C. Ho, J. Kormendy, T. R. Lauer, J. Magorrian, J. Pinkney, and D. Richstone (2002), "The Slope of the Black Hole Mass versus Velocity Dispersion Correlation." *ApJ*, 574, 740–753. (Cited on page 2.)
- Trümper, J. E. and G. Hasinger (2008), *The Universe in X-Rays*. (Cited on page 33.)
- Turner, T. J., S. B. Kraemer, I. M. George, J. N. Reeves, and M. C. Bottorff (2005), "Complex X-Ray Absorption and the Fe K α Profile in NGC 3516." *ApJ*, 618, 155–166. (Cited on page 116.)
- Ueda, Y., M. Akiyama, K. Ohta, and T. Miyaji (2003), "Cosmological Evolution of the Hard X-Ray Active Galactic Nucleus Luminosity Function and the Origin of the Hard X-Ray Background." *ApJ*, 598, 886–908. (Cited on page 2.)
- Urry, C. M. and P. Padovani (1995), "Unified Schemes for Radio-Loud Active Galactic Nuclei." *PASP*, 107, 803. (Cited on pages 16 and 17.)
- Wanders, I., M. R. Goad, K. T. Korista, B. M. Peterson, K. Horne, G. J. Ferland, A. P. Koratkar, R. W. Pogge, and J. C. Shields (1995), "The Geometry and Kinematics of the Broad-Line Region in NGC 5548 from HST and IUE Observations." *ApJL*, 453, L87+. (Cited on pages 23 and 145.)
- Wang, J., J. Y. Wei, and X. T. He (2006), "A Sample of IRAS Infrared-selected Seyfert 1.5 Galaxies: Infrared Color $\alpha(60, 25)$ -dominated Eigenvector 1." *ApJ*, 638, 106–119. (Cited on page 64.)
- Wang, J.-M., Y.-M. Chen, C.-S. Yan, C. Hu, and W.-H. Bian (2007), "Suppressed Star Formation in Circumnuclear Regions in Seyfert Galaxies." *ApJL*, 661, L143–L146. (Cited on page 53.)
- Ward, M. J., P. R. Blanco, A. S. Wilson, and M. Nishida (1991), "Infrared spectroscopy of a Cygnus A - Implications for the obscured active nucleus." *ApJ*, 382, 115–120. (Cited on page 18.)

- Ward, M. J., C. Done, A. C. Fabian, A. F. Tennant, and R. A. Shafer (1988), "X-ray observations of IRAS selected Seyfert galaxies and obscuration of the broad-line region." *ApJ*, 324, 767–775. (Cited on pages [v](#), [24](#), [63](#) and [64](#).)
- Woo, J.-H. (2005), *Active black holes and the evolution of their host galaxies*. Ph.D. thesis, AA(Yale University, United States – Connecticut). (Cited on pages [75](#) and [83](#).)
- Worsley, M. A., A. C. Fabian, F. E. Bauer, D. M. Alexander, G. Hasinger, S. Mateos, H. Brunner, W. N. Brandt, and D. P. Schneider (2005), "The unresolved hard X-ray background: the missing source population implied by the Chandra and XMM-Newton deep fields." *MNRAS*, 357, 1281–1287. (Cited on page [2](#).)
- Yaqoob, T. (2006), "Averaging High Redshift X-ray and gamma-ray Spectra of Faint Sources." In *Populations of High Energy Sources in Galaxies* (E. J. A. Meurs and G. Fabbiano, eds.), volume 230 of *IAU Symposium*, 461–462. (Cited on pages [119](#) and [127](#).)
- Yaqoob, T., K. D. Murphy, L. Miller, and T. J. Turner (2010), "On the efficiency of production of the Fe K α emission line in neutral matter." *MNRAS*, 401, 411–417. (Cited on page [21](#).)
- Yu, Q. and Y. Lu (2004), "The Black Hole Mass versus Velocity Dispersion Relation in QSOs/ Active Galactic Nuclei: Observational Appearance and Black Hole Growth." *ApJ*, 610, 93–104. (Cited on page [9](#).)
- Zdziarski, A. A., A. C. Fabian, K. Nandra, A. Celotti, M. J. Rees, C. Done, P. S. Coppi, and G. M. Madejski (1994), "Physical Processes in the X-Ray / Gamma-Ray Source of IC4329A." *MNRAS*, 269, L55+. (Cited on page [11](#).)
- Zdziarski, A. A., W. N. Johnson, C. Done, D. Smith, and K. McNaron-Brown (1995), "The average X-ray / gamma-ray spectra of Seyfert galaxies from GINGA and OSSE and the origin of the cosmic X-ray background." *ApJL*, 438, L63–L66. (Cited on pages [56](#), [67](#) and [116](#).)
- Zheng, W., J. W. Sulentic, and L. Binette (1990), "A double-stream model for line profiles." *ApJ*, 365, 115–118. (Cited on pages [23](#) and [145](#).)